Symmetry breaking and its applications to quantum information processing

by

Akitada SAKURAI

Dissertation

submitted to the Department of Informatics
in partial fulfillment of the requirements for the degree of

Doctor of Philosophy

The Graduate University for Advanced Studies, SOKENDAI
March 2022

Acknowledgement

First and foremost, I would like to express my deepest gratitude to my supervisor, Prof. Kae Nemoto, at the National Institute of Informatics and the Graduate University for Advanced Studies (SOKENDAI) and National Institute of Informatics (NII), for giving me encouragement and support to complete my thesis. I thank her for staying late to discuss with me to conduct my research. In addition, she gave me much guidance on the skills that I need as a researcher in the future.

I would like to thank Associate Prof. Masako Kishida, one of my supervisors, and Associate Prof. Keiji Matsumoto, my sub-supervisor, at SOKENDAI and NII. Also, I am grateful to my reviewers, Prof Leong Chuan Kwek at Centre for Quantum Technologies (CQT) and Prof. Johannes Majer at the University of Science and Technology of China. They are members of my thesis defense. I wish to thank them for their appropriate advice during the review process before submitting this thesis. It has helped me to improve the quality of my doctoral thesis.

I would like to especially thank Dr. V. M. Bastidas, a researcher at NTT Basic Research Laboratories and a visiting professor at NII, and Dr. M. P. Estrellas, a former postdoc at NII and now a researcher at Qilimanjaro Quantum Tech. He collaborates on the first part of the my thesis, and she collaborates on the first and second parts. They have provided me with guidance on writing the paper and composing the presentation slides. Our discussions with them were very profound. Moreover, I could learn from him about my future vision as a researcher besides research activities. Also, Victor helped me a great deal in writing my doctoral thesis. Without their support, it would have been difficult to complete my doctoral thesis.

I wish to thank Dr. W. J. Munro, the group leader of NTT Basic Research Laboratories. He has been a collaborator on all aspects of this research. He provided me with the necessary computer and cluster computer support to carry out our research. He also contributed to improving the quality of all the research.

It is my pleasure to thank Dr. N. L. Piparo and Dr. J. Dias, postdoctoral researchers at NII. The discussions with them at regular meetings were excellent. I would also like to thank them for their advice on my research and other topics.

I am grateful to Shin Nishio and Aoi Hayashi, who are doing their master's degrees at SOKENDAI. They joined us in the middle of the second part of the research. The discussions with them were beneficial in writing this part. I want to thank them for participating in the meeting until late.

I wish to thank Yukiko Sanaka, the secretary of our laboratory. Thanks to her management, I was able to carry out my research smoothly.

I would also like to thank my friend, Masato Fujitake, a Ph.D. student at NII. He gave me much advice in writing Machine Learning part.

Last but not least, I would like to express my deep gratitude to my parents, Shoichiro Sakurai and Chiyo Sakurai. Without their wholehearted support, it would have been impossible to complete my doctoral thesis. Also, I wish to thank my sister Mari Sakurai, and my brother Shiro Sakurai, for their support and patience.

Abstract

The recent developments in quantum technology enable us to realize and control isolated quantum systems with multiple particles and spins with high precision. These systems are called the Noisy Intermediate-Scale Quantum (NISQ) devices and consist of tens to hundreds of qubits. Although the size of these devices suggests computational power superior to their classical counterparts, errors associated with system imperfections seem to be an obstacle to performing advanced quantum processing tasks. It is an open fundamental question of how such devices could harness this expected computational power if that is possible.

In this thesis, we address this question with two different approaches. In these approaches, we will focus on Floquet systems, which are periodically driven quantum systems that have been experimentally demonstrated in many physical systems. Floquet systems are expected to exhibit new phenomena that cannot be seen in equilibrium quantum systems and could be exploited for quantum processors. In particular, we use discrete-time crystals (DTCs), which break the discrete-time translational symmetry (DTTS).

In Chapter 2, we briefly explain DTTS breaking and DTCs in Floquet spin networks and provide the physical concepts and mathematical tools for the following Chapters. We primarily consider 2T-DTCs, which are widely applied to other theoretical models and experimentally demonstrated with several NISQ devices. To simplify the discussion, we introduce its minimum model and carefully derive its 2T-effective Hamiltonian, essential for analyzing DTCs. Using this Hamiltonian, we show the $\mathbb{Z}_2$-Ising symmetry plays an essential role in 2T-DTCs. After that, we explain two different approaches, MBL-DTCs, and pre-thermal-DTCs to understand the stability of the sub-harmonic oscillation on the spin networks, which is a signal of the DTTS breaking. Further, to understand the DTC and its phase transition, we introduce a mapping between the Ising model and the effective Hamiltonian, which governs stroboscopic dynamics. At the end of the Chapter, we review two crucial experiments on DTTS breaking and realizing DTCs using trapped ions and NV centers.

The first part of the thesis proposes two new quantum phases that break the DTTS using a spin network. Chapter 3 shows how regional driving can break the DTTS regionally.

Due to this regionally broken DTTS, two different phases of matter can coexist in one quantum system, despite the interactions throughout the quantum system. We named this novel quantum state "chimeric time crystal" as an analogy to the classical chimeric state. We investigate the chimera time crystal from a microscopic perspective by employing its entanglement entropy at stroboscopic times. We found that while a network exhibits the chimera phase, the entanglement growth is highly suppressed despite long-range interaction. Our results could contribute to the design of the quantum simulator and quantum memories using Floquet systems.

In DTCs, besides the $\mathbb{Z}_2$-Ising symmetry, the spin network has the U(1)-symmetry at stroboscopic times. Chapter 4 introduces a new DTC model breaking the local U(1)-symmetry. We show that as long as the global U(1)-symmetry is preserved, the network can exhibit DTCs for specific initial states. We analyze this model with and without environmental effects and show that the network can exhibit sub-harmonic oscillation with sufficiently long periods, even when the environmental effects being present.

Next, we discuss our discovery that breaking the local U(1)-symmetry in the network induces the time crystal growth that does not appear in the conventional model. We show that time crystal growth can be stabilized due to the environmental effect. To understand its mechanism, we analyze the spectrum of the 2T-effective Liouvillian operator, which governs the stroboscopic dynamics of the dissipative systems. The analysis shows that the time scale of time crystal growth can be estimated by the Liouvillian gap. Further, we investigate negativity (a measure of entanglement commonly used in open systems) of the spin network to understand crystal growth from the microscopic perspective. Our new model allows us to understand the dynamical quantum phases of matter coupled to the environment.

The second part of the thesis proposes a new quantum processor using such dynamically driven systems. Our model is a quantum neural network (QNN) based on two classical computational models, reservoir computation and extreme learning machine. It mainly consists of a classical input layer, a quantum layer, and a classical output layer. The quantum layer is a quantum reservoir providing a huge neural network. The classical input is to pre-process the classical data and then efficiently encodes the data into the quantum reservoir as its initial state. We employ a DTC for the quantum reservoir. To connect the quantum layer to the classical output layer, we insert M-layer, which is a measurement layer to convert the quantum output information to the classical information. The learning process optimizes the classical network between the M-layer and the output layer.

We then apply this new QNN model to classification problems. In particular, we extensively investigate how this model enables pattern recognition of handwritten digits using the MNIST data set and demonstrate that the accuracy reaches 98% with only 14 qubits. We efficiently encode images into quantum states using classical data compression

with only single-qubit operations. Unlike the variational quantum algorithms, our model does not require optimization on the quantum system. This dramatically simplifies the quantum device and its control, and it contributes a significant speed-up of the learning processes. Using DTCs as the quantum layer, we reveal the essential relationship between the quantum neural network's performance and the system's symmetry.

Contents

List of Figures

List of Tables

LIST OF TABLES

Chapter 1

Introduction

1.1 Background

At the end of the 19th century, Max Planck proposed that emitted electromagnetic energy should be quantized to solve the problem of black-body radiation [5]. Soon after, Albert Einstein expanded Planck's idea into quantizing the energy of light. He proposed that light, which in classical mechanics was a wave, behaves like a particle in some cases [6]. Nowadays, it is recognized that their idea was a revolutionary discovery in physics and opened the door to quantum mechanics. In the early stage of quantum mechanics, single and few-body systems such as atoms and elementary particles have played an essential role in discovering these fundamental laws in quantum physics. Niels Bohr, Werner Heisenberg, Erwin Schrodinger, and others revealed unique mechanical laws of quantum mechanics that are unthinkable in classical mechanics [7, 8, 9, 10]. For example, it was shown that atomic energy is discretized in quantum mechanics using a hydrogen atom [7].

At the same time that the fundamental laws of quantum mechanics were being revealed, many new discoveries were founded in studies of many-body systems that follow those new laws. For example, in contrast to classical mechanics, in quantum mechanics, particles are identical [11]. It means that one can not distinguish between each particle. Furthermore, due to the symmetry of quantum states, there are two types of particles: boson particles and Fermi particles. Consequently, the spin-statistics theorem shows two statistical properties: boson statistics [12] and Dirac statistics. Due to the difference in statistical properties, phenomena that cannot be seen in classical systems occur in quantum systems. For instance, a quantum many-body system that obeys boson statistics shows Bose-Einstein condensation [12] in which particles behave as an ideal gas rather than as an individual at ultra-low temperatures. In fact, when helium-4 is cooled to below 2.2K, superfluidity is observed [13]. At present, this superfluidity is considered a kind of Bose-Einstein condensation [13]. Furthermore, since the latter half of the 20th century, Bose-Einstein

condensation has been realized in the laboratory by cooling an ensemble with 10^3 to 10^7 particles to an ultra-low temperature 2×10^{-7}K [14].

With the fusion of new physical laws, quantum mechanics, and statistical physics, the 20th century has seen a significant improvement in quantum statistical physics, both theoretical and experimental, such as discovering quantum phase transitions. In contrast, it was challenging to control quantum dynamics experimentally for a long time. However, in the 21st century, as technology has improved further, it has become possible to control isolated quantum systems with high precision [15, 16, 17, 18, 19]. It indicates one can use these quantum systems as information processors like classical processors in our computer. Thus, these devices are called quantum processors or, commonly said, quantum computers. At the current level of technology, quantum processors can have tens to hundreds of qubits (quantum version of bits). Because these qubits are still affected by the environment, these devices are called the Noisy Intermediate-Scale Quantum (NISQ) devices. So far, several physical systems are proposed as NISQ devices, e.g., superconducting qubits [20, 18, 21], trapped ions [22, 23, 24, 16], cold atoms [25], and others [26]. We have entered the NISQ era, where enough qubits can be controlled with high precision.

1.2 Topic and scope of this thesis

Although NISQ devices have succeeded in performing small quantum computations with quantum gates [27, 28], it is challenging to perform practical algorithms using quantum gate decomposition at the current level due to noise and their scaling. Therefore, it is crucial to explore new applications and new computational models that effectively use the computational power of these devices.

Importantly, NISQ devices have successfully realized quantum many-body systems and dynamics [29, 30, 31, 32]. For example, it can be used to realize states out of equilibrium using the periodically driven systems. These quantum non-equilibrium states are expected to exhibit new and rich physical phenomena that cannot be seen in equilibrium quantum systems [29, 33, 34, 35]. Thus, it indicates that NISQ devices may play an essential role in exploring dynamical quantum phases and new physics with many-body systems.

In addition to exploring new physical phenomena such as the dynamical phases of matter, driven systems are expected to be applied to information processors based on quantum mechanics. Since it is out of the equilibrium system, a state would sufficiently explore the Hilbert space [36]. In other words, such a quantum system is difficult to calculate with a classical computer. In fact, it has been suggested that there is a relationship between phase transitions in non-equilibrium quantum systems and quantum supremacy [36]. However, their application to practical problems remains open-question. Recently, it has been shown that the dynamical phase transition can efficiently perform reservoir computing, one of

the machines [36, 37].

The present thesis addresses the above two different possibilities of NISQ applications by focusing on the symmetry of periodically driven quantum systems. Among the phases of matter in non-equilibrium systems, we employ a **discrete-time crystal (DTC)** breaking **discrete-time translational symmetry (DTTS)** [33]. First, it has opened a new possibility of driven systems. Thus, it is expected that they can use it to explore new physics and to design new quantum phases or non-trivial dynamics. Additionally, because it has been shown that they have a type of network structure with non-trivial complexity in DTCs [38], it is expected to be used as a new type of quantum information processing based on a quantum neural network. Lastly, because this new crystal has been experimentally realized with different platforms [2, 3, 39, 40, 41, 42, 43, 44], our applications would be demonstrated with NISQ devices in the feature.

1.3 Outline of this thesis

This thesis mainly addresses two subjects. In the first part, we propose new phases of matter and exotic phenomena in periodic drive systems breaking DTTS. The second part will propose a new quantum information processing using driven quantum systems for practical problems. The former is discussed in Chapters 3 and 4, and the latter is discussed in Chapter 5.

To help the readers understand our main works, Chapter 2 briefly explains the DTTS breaking and 2T-DTCs in the Floquet spin network using the minimal model, which has been experimentally realized. This Chapter provides the physical concepts and mathematical tools necessary for the following Chapters. For example, to understand the stroboscopic dynamics of the driven network, the Floquet theorem is introduced and applied to find the effective Hamiltonian. Using this Hamiltonian, we show the $\mathbb{Z}_2$-Ising symmetry plays an essential role in 2T-DTCs. Then we explain two different approaches, MBL-DTCs, and pre-thermal-DTCs to show the stability of the DTC phase against parameter fluctuation of the system. In addition, we introduce a mapping between the Ising model and the effective Hamiltonian, which helps to understand the phase transition of the DTC. At the end of the Chapter, we review two crucial experiments on DTTS breaking and realizing DTCs using trapped ions [2] and NV centers [3].

Part 1: Proposal for new dynamical phase of matter breaking the DTTS

Chapter 3 proposes a new exotic phase of matter called a chimera DTC [45], in which two different phases of matter can coexist in one quantum system. We will explain how the

chimer DTC appears using the periodically driven system. In addition, we will consider the von Neumann entropy to understand this chimeric state from a quantum information perspective.

Next, Chapter 4 proposes the new DTC model breaking the local U(1)-symmetry on a spin network. Then, we report a new essential phenomenon called DTC growth due to this symmetry breaking, which is not seen in the conventional model [4]. In this growth, the DTC region at the initial state expands with time, just like the growth of a spatial crystal. Furthermore, we will extend this model to spin networks coupled to an environment. In general, the effects of environmental systems are noise and do not help stabilize the quantum phase. However, we show that the environment can stabilize the DTC growth by considering the symmetry of the whole system, including the environment.

Part 2: Proposal of new application based on quantum dynamics

The second part of the thesis proposes a new quantum processing based on machine learning using such dynamically driven systems. Chapter 5 will show that a quantum system can be used as a reservoir that provides a huge neural network. Then, we will show how to apply such a quantum neural network to pattern recognition's practical problem using the handwritten digits called MNIST dataset [46]. We will see that our algorithm is fully operational even on NISQ devices. Our results predict that quantum information processing with a quantum reservoir will be applied to various practical problems in the future.

Chapter 2

2T-Discrete time crystals (2T-DTCs)

In both classic and quantum physics, the spontaneous symmetry breaking of microscopic levels has yielded significant results in understanding the transitions between phases of matter which is a state's appearance at macroscopic scales [47, 48]. In closed systems, energy conservation is directly related to invariance under continuous translations in time. For a long time, with the exception of relativistic quantum physics [49, 50], space and time have been treated differently in terms of symmetries. However, recently the idea of applying spontaneous symmetry breaking to the time direction symmetry has been proposed.

Subsequently, the symmetry breaking along the time-axis has been proposed on periodically driven quantum systems (or Floquet systems) [33, 51]. In the systems, its Hamiltonian is time periodic with a period T. In other words, the Hamiltonian is invariant under the **discrete time-translational symmetry (DTTS)** with T. Thus, it allow us to consider an exotic state spontaneously breaking breaks the DTTS. In the situation, a macroscopic observable should show the sub-harmonic response with a longer period $n_d T$ ($n_d > 1, n_d \in \mathbb{Z}$). This new phase of matter in the Floquet system is referred to as the **discrete-time crystal (DTC)**. In particular, when the period of sub-harmonic oscillation is two times larger than T ($n_d = 2$), it is called the **2T-DTC**.

Later Chapters use the DTTS breaking and the 2T-DTC to introduce new models and apply them to quantum information processing. Thus, in the present Chapter, we briefly explain the DTTS and the 2T-DTC using a simple model to understand its physics and introduce mathematical tools for the late Chapters. In the last section, we also show the recent experiments on DTCs. Several review papers have been published on time-axis symmetry breaking and the resulting time crystals, including the DTCs [52, 53, 54]. We refer to the interested reader to these References for more details.

2.1 Symmetry breaking and quantum Ising model

Before considering the symmetry breaking along the temporal axis, let us briefly review concepts of symmetry and symmetry breaking in this section. Two concepts are fundamental and play essential roles in revealing physics in many areas ranging from condensed matter physics to particle physics [55, 56, 57]. For example, in quantum physics, symmetries determined a transition between states.

2.1.1 Basic idea of symmetry breaking in quantum mechanics

In quantum mechanics, symmetry is determined by the Hamiltonian of the system. When the system's Hamiltonian is invariant under some unitary operator, the system has symmetry related to the operation. Similarly, if a state is invariant under this operator, the state has this symmetry. Similar to the symmetry, the Hamiltonian determines its steady states. For example, the ground state is the steady-state with the lowest energy. Thus, it is natural to assume that these states have the same system symmetry. However, surprisingly, even if a system has symmetry, its ground state does not have symmetry. It is known as spontaneous symmetry breaking at the ground state.

The concept of symmetry breaking is mainly used in quantum phases of matter and particle physics. For example, spontaneous symmetry breaking plays an essential role in Cooper pairs of superconductivity [56] and the Higgs mechanism giving weight to elementary particles [57]. A phase of matter is a way of describing a state at the macroscopic scale. While symmetry lies on the microscopic scale. Usually, due to the different scales, these physical laws are independent of each other. However, spontaneous symmetry breaking of states leads to phase transitions at macroscopic scales. Therefore, understanding the symmetry of quantum states is significant at the microscopic and macroscopic scales.

2.1.2 Symmetry breaking using the Ising-model

To understand the basic concepts of spontaneous symmetry breaking at the ground state, let us see it using the simplest model. As an example, we employ a quantum one-dimensional Ising model with N-spins. It is given by,

$$\hat{H}_{\text{Ising}} = -J \sum_{l=1}^{N-1} \sigma_l^z \sigma_{l+1}^z - Jg \sum_{l=1}^{N} \sigma_l^x, \tag{2.1}$$

where σ_l^μ with $\mu \in \{x, y, z\}$ are the usual Pauli operators at the l-th site. Here, a parameter J is a coupling constant. Next, the second term of $\hat{H}_{\text{Ising}}$ represents transverse-field, and the parameter g is a dimensional coupling. In this section, we consider both parameters

are positive ($J, g > 0$). To find the symmetry of the $\hat{H}_{\text{Ising}}$, let us consider a following transformation,

$$\hat{X}\sigma_l^x\hat{X}^\dagger = \sigma_l^x, \quad \hat{X}\sigma_l^z\hat{X}^\dagger = -\sigma_l^z, \tag{2.2}$$

where $\hat{X} = \prod_l \sigma_l^x$ is a unitary operator. Thus, under this transformation, the Hamiltonian is invariant, $\left[\hat{H}_{\text{Ising}}, \hat{X}\right] = 0$. In other words, the system $\hat{H}_{\text{Ising}}$ has the $\mathbb{Z}_2$-Ising symmetry given by the operator $\hat{X}$. This symmetry is crucial in this thesis, which will appear in 2T-DTCs discussed next and in the new models introduced in later Chapters.

Now, let us find the ground state of $\hat{H}_{\text{Ising}}$. To simplify the discussion, we consider the two opposing extreme limits $g \gg 1$ and $g \ll 1$.

First, when $g \gg 1$, the transverse-field is dominant. Thus, in the extreme limit, its ground state is simply,

$$|g_0\rangle = |+\rangle_0 \otimes |+\rangle_1 \otimes \cdots \otimes |+\rangle_N = |++\cdots+\rangle, \tag{2.3}$$

where $|+\rangle_l = (|0\rangle_l + |1\rangle_l)/\sqrt{2}$ is the eigenstate of σ_l^x . Here, $|0\rangle_l$ and $|1\rangle_l$ are eigenstates of σ_l^z with eigenvalues ± 1. Thus, the ground state is invariant under the $\mathbb{Z}_2$-Ising symmetry transformation.

Next, when $g \ll 1$, since the first term is dominant, in the extreme limit, there are two ground states, as follows,

$$|g_1\rangle = |00\cdots0\rangle, \quad |g_2\rangle = |11\cdots1\rangle. \tag{2.4}$$

Importantly, two ground states are connected by the $\mathbb{Z}_2$-Ising symmetry transformation, $\hat{X}|g_1\rangle = |g_2\rangle$. At the thermodynamic limits, the system will always choose one or other of the states as its ground state, thus, the $\mathbb{Z}_2$-Ising symmetry is broken. In general, it is refereed to as a spontaneous breaking of the $\mathbb{Z}_2$-Ising symmetry at the ground state.

In this Ising model, the spontaneous symmetry breaking shows ordering along the z-axis at the macroscopic scale. To see this, let us consider the total magnetization along the z-axis: $\hat{M}_z = (\sum_l \sigma_l^z)/N$. First, when the ground state has the $\mathbb{Z}_2$-Ising symmetry, its magnetization is close to zero, for instance, $\langle g_0|\hat{M}_z|g_0\rangle = 0$. Thus, when $g \gg 1$, the z-axis component of the magnetization is disordered. On the contrary, when $g \ll 1$, it is ordered. For example, when either $|g_1\rangle$ or $|g_2\rangle$ is realized as the ground state, magnetizations are non-zero: $\langle g_1|\hat{M}_z|g_1\rangle = 1$ and $\langle g_2|\hat{M}_z|g_2\rangle = -1$. It can be interpreted as a phase transition from a disordered phase to an ordered phase due to spontaneous symmetry breaking.

For more details on spontaneous symmetry breaking in quantum systems and quantum phase transitions, see the textbook [58].

2.2 Time translational symmetry breaking (TTSB)

In the introduction, we have briefly explained the intimate relation between DTTS and DTCs. However, here, we explain it again and more precisely.

2.2.1 Continuous Time Transnational Symmetry (CTTS) breaking

The first idea of the symmetry breaking for the temporal axis (t-axis) and the resulting new crystalline order referred to as the time crystal have been proposed by Frank Wilczek as the analogy to crystalline order in space [59]. Thus, initially, it was considered as a phase of matter in thermal equilibrium. However, soon it was analytically shown that such an exotic phase of matter predicted by original Wilczek's model could not be realized as the ground state of a manybody Hamiltonian. Furthermore, Bruno proposed a no-go theorem that theoretically rules out the existence of time crystals in equilibrium systems, as originally proposed by Wilczek [60].

Since Bruno's no-go theorem is restricted to a specific model, and does not rules out the general idea of the time crystals, a new type of the time crystalls were proposed by Wilzeck and others [61, 62]. However, the no-go theorem is generalized by Watanabe and Oshikawa [63]. Until then, the definition of time translation symmetry was a bit ambiguous. So they gave a precise definition based on spatial translational symmetry which is a important aspect for crystalline order in space. They define the continuous-time translational symmetry (CTTS) by using the following correlation function of the integrated order parameter $\hat{\Phi} = \int_V dx^d \hat{\phi}(\vec{x}, 0)$,

$$\frac{1}{V^2} \lim_{V\to\infty} \langle e^{i\hat{H}t} \hat{\Phi} e^{-i\hat{H}t} \hat{\Phi} \rangle \to f(t) \tag{2.5}$$

where $\hat{\phi}(\vec{x}, 0)$ is a local order parameter, V is the volume and $\hat{H}$ is the Hamiltonian of the system in $d+1$ dimensions. Note that the order parameter is the spatial average over d spatial dimensions. Now, when the state breaks the CTTS, then the correlation function should show the periodic oscillation with time t. However, they also shown that at zero temperature, when the interactions decay with a power-law r^α with $\alpha > 0$, the ground-state correlation function satisfies the following inequality,

$$\frac{1}{V^2} |\langle 0|\hat{\Phi} e^{-i(\hat{H}-E_0)t} \hat{\Phi}|0\rangle - \langle 0|\hat{\Phi}^2|0\rangle| \leq C \frac{t}{V} \tag{2.6}$$

where E_0 is the ground energy and C is a constant dependent on $\hat{\Phi}$ and $\hat{H}$ but not on t and V. This means that for any fixed time t, the correlation function $f(t)$ remains constant in the thermal limit $V \to \infty$.

2.2.2 Discrete Time Transnational Symmetry (CTTS) breaking

However, the generalized no-go theorem that forbids spontaneous CTTS breaking at equilibrium systems does not exclude the possibility of the time-translational symmetry breaking in non-equilibrium quantum systems. Actually, some time after it has been proposed a new time crystal using a Floquet system whose Hamiltonian is time-periodic with period T: $\hat{H}(t) = \hat{H}(t+T)$. The system is described by a time-periodic Hamiltonian and thus, it is not invariant under CTTS. Instead of that, it has a discrete-time translational symmetry (DTTS) with the period T. Thus, in the new phase, the state breaks the DTTS, and as a result, some observable shows the sub-harmonic response with a period $n_d T$ that is multiple integer of the driving period T, as follows,

$$\langle \Psi(n_d T)|\hat{O}|\Psi(n_d T)\rangle = \langle \Psi(0)|\hat{O}|\Psi(0)\rangle \tag{2.7}$$

where $|\Psi(0)\rangle$ is an initial state. Such a new time crystal is referred to as discrete time crystal (DTC) or Floquet time crystal.

2.3 Minimal model of 2T-DTCs

To understand the 2T-DTC in more details, let us consider a simple and more concrete model. As the model, we employ a periodically spin network with N-sites and its time-periodic Hamiltonian with a period $T = T_1 + T_2$,

$$\hat{H}(t) = \begin{cases} \hat{H}_1 = \hbar g(1-\epsilon)\sum_l \sigma_l^x & (0 \le t < T_1) \\ \hat{H}_2 = \sum_{lm} J_{lm}^z \sigma_l^z \sigma_m^z + \sum_l W_l^z \sigma_l^z & (T_1 \le t < T), \end{cases} \tag{2.8}$$

where σ_l^μ with $\mu \in \{x, y, z\}$ are the usual Pauli operators at the l-th site. The above model has been widely demonstrated in several papers [1, 64] and, furthermore it has been experimentally realized using trapped ions [2]. Obviously, the above Hamiltonian is invariant under the DTTS.

Now, let us see more details of the system governed Eq. 5.31. The first Hamiltonian $\hat{H}_1$ is the individual spin rotation along the x-axis over the entire network with uniform angle $\theta = g(1-\epsilon)T_1/2$, as follows,

$$e^{-i\theta\sum_l \sigma_l^x} = \prod_l \left(\cos(\theta)\,\hat{\mathbb{I}}_l - i\sin(\theta)\,\sigma_l^x\right). \tag{2.9}$$

Now, to obtain a sub-harmonic response from the time-dependent Hamiltonian $\hat{H}(t)$, in

general one should set g to be $2gT_1 = \pi$. Letter we will see the reason. When $\epsilon = 0$, the above rotation gives the perfect π-rotation, as follows,

$$e^{-i\frac{\pi}{2}\sum_l \sigma_l^x} = (-i)^N \prod_l \sigma_l^x \equiv \hat{X}. \tag{2.10}$$

and it is the same as the spin flips by operator $\hat{X}$. Here, we note that the square of the operator returns the identity ($\hat{X}^2 = \hat{\mathbb{I}}$). In addition, under the operator $\hat{X}$, the Pauli matrices transforms as,

$$\hat{X}\sigma_l^x\hat{X}^\dagger = \sigma_l^x, \quad \hat{X}\sigma_l^y\hat{X}^\dagger = \sigma_l^y, \quad \hat{X}\sigma_l^z\hat{X}^\dagger = -\sigma_l^z. \tag{2.11}$$

It means that $\hat{X}$ is a representation of the $\mathbb{Z}_2$-Ising symmetry transformation [58]. Here, we note that it is the same operator defined in section 2.1 for the $\mathbb{Z}_2$-Ising symmetry transformation the except for the phase. Later we will see that this symmetry is intimately related to the discrete-time translational symmetry.

Next, the second Hamiltonian $\hat{H}_2$ represents the spin network with the long-range interactions with a disorder potential. Here, J_{lm}^z is the coupling constant between l-th and m-th sites and defines the connectivity of the network. Because the interaction term consists of two sigma operators along the z-axis, it is invariant under the $\mathbb{Z}_2$-Ising symmetry. Next, W_l^z is the on-site energy at l-th site and is randomly chosen from the uniform distribution $W_l \in [0, W]$ with the strength of the disorder W. Because of the diagonal disorder, the network $\hat{H}_2$ breaks the $\mathbb{Z}_2$-Ising (parity) symmetry.

2.4 Effective Hamiltonian and Symmetry

Due to the DTTS breaking, the stroboscopic dynamics of the system governed by Eq 5.31 will exhibit the sub-harmonic oscillation with 2T. Thus, to understand the stroboscopic dynamic, we employ the Floquet theory which is discussed in detail in Appendix B.2.

In the Floquet theory, the stroboscopic dynamics given by a unitary operator for one periods called the Floquet operator,

$$\hat{F} = \mathcal{T}\exp\left(-\frac{i}{\hbar}\int_0^T \hat{H}(\tau)d\tau\right) = e^{-\frac{i}{\hbar}\hat{H}^{\text{eff}}T}. \tag{2.12}$$

where $\mathcal{T}$ is a time ordering operator. Here, the exponent argument $\hat{H}^{\text{eff}}$ is a Hermitian operator and can be interpreted as the Hamiltonian, which governs the dynamics at the stroboscopic times $t = nT$ with an integer n. Thus, $\hat{H}^{\text{eff}}$ is called the effective Hamiltonian. This approach to understanding the stroboscopic dynamics of periodically driven quantum

systems, using the effective Hamiltonian, will be used throughout this thesis.

Now, because of the interesting in the sub-harmonic oscillation with $2T$, let us derive the effective Hamiltonian for double periods, which governs the dynamics stroboscopic times $t_n = 2nT$ with an integer n. Because the square of the Floquet operator maps a state to the state two periods later, the Hamiltonian can be obtained from $\hat{F}^2$, as follows, $\hat{H}^{\text{2T-eff}} = i\hbar \ln(\hat{F}^2)/2T$. Now, $\hat{F}^2$ is given by

$$\hat{F}^2 = \exp\left[-\frac{i}{\hbar}\hat{H}_2 T_2\right] \exp\left[-\frac{i}{\hbar}\hat{H}_1 T_1\right] \exp\left[-\frac{i}{\hbar}\hat{H}_2 T_2\right] \exp\left[-\frac{i}{\hbar}\hat{H}_1 T_1\right]. \tag{2.13}$$

However, generally, it is not easy to write the above unitary in terms of the single Hamiltonian, which is necessary to find the effective Hamiltonian.

2.4.1 Trivial case ($\epsilon = 0$)

To get some intuition of 2T-DTCs, here let us consider the trivial case in which $\epsilon = 0$. As we saw in the above section, now the time evolution under the first Hamiltonian $\hat{H}_1$ is the same as the spin flip operator $\hat{X}$. As a result, the square of the Floquet operator $\hat{F}^2$ can be written as,

$$\begin{aligned}
\hat{F}^2 &= \exp\left[-\frac{i}{\hbar}\hat{H}^{\text{2T-eff}}_{\epsilon=0}(2T)\right] \\
&= \exp\left[-\frac{i}{\hbar}\hat{H}_2 T_2\right] \exp\left[-\frac{i}{\hbar}\hat{H}_1 T_1\right] \exp\left[-\frac{i}{\hbar}\hat{H}_2 T_2\right] \exp\left[-\frac{i}{\hbar}\hat{H}_1 T_1\right] \\
&= \exp\left[-\frac{i}{\hbar}\hat{H}_2 T_2\right] \hat{X} \exp\left[-\frac{i}{\hbar}\hat{H}_2 T_2\right] \hat{X} \\
&= \exp\left[-\frac{i}{\hbar}\hat{H}_2 T_2\right] \exp\left[-\frac{i}{\hbar}\hat{X}\hat{H}_2\hat{X} T_2\right] \\
&= \exp\left[-\frac{i}{\hbar}\left(\hat{H}_2 + \hat{X}\hat{H}_2\hat{X}^\dagger\right) T_2\right]
\end{aligned} \tag{2.14}$$

where we use $\hat{X}^\dagger = \hat{X}$ except a phase, and $\left[\hat{H}_2, \hat{X}\hat{H}_2\hat{X}^\dagger\right] = 0$. Here, in $\hat{X}\hat{H}_2\hat{X}^\dagger$, we see the spin-flip, as follows,

$$\hat{X}\left(\sum_l W_l^z \sigma_l^z\right)\hat{X}^\dagger = \sum_l W_l^z \hat{X}\sigma_l^z\hat{X}^\dagger = -\sum_l W_l^z \sigma_l^z. \tag{2.15}$$

It means that the perfect π-rotation ($\hat{X}$) changes the sign of the disorder term. As a result, one can analytically obtain the effective Hamiltonian $\hat{H}^{\text{2T-eff}}_{\epsilon=0}$, as follows,

$$\hat{H}^{\text{2T-eff}}_{\epsilon=0} = \frac{\hbar T_2}{T}\sum_{l,m} J^z_{l,m}\sigma^z_l\sigma^z_m. \tag{2.16}$$

Now, we see that the effective Hamiltonian derived in the above has the $\mathbb{Z}_2$-Ising symmetry (parity) which was absent in $\hat{H}_2$. It indicates that parity is conserved at every even (odd) period.

2.4.2 Presence of a small error ($\epsilon \ll 1$)

Above, we have derived the effective Hamiltonian for $\epsilon = 0$ and seen it has the parity symmetry. To see the imperfect driving effect, let us consider the presence of the small error $\epsilon \ll 1$. Using the high-frequency expansion, one can approximately derive the effective Hamiltonian, as follows,

$$\hat{H}_\epsilon^{\text{2T-eff}} \approx \frac{\hbar T_2}{T}\sum_{l,m} J_{lm}^z \sigma_l^z \sigma_m^z - \frac{\hbar\pi\epsilon T_2}{2T}\sum_l J_{lm}^z \sigma_l^x \sigma_m^y - \frac{\hbar\pi\epsilon}{4T}\sum_l \left[(\cos\theta_l + 1)\,\sigma_l^x + \sin\theta_l \sigma_l^y\right] \tag{2.17}$$

where, $\theta_l = 2W_l T_2$.

Here, we assume that $J_{lm}^z \epsilon \ll 1$ to ignore the second term in the above effective Hamiltonian. Later, we will see that the error is responsible for melting the DTC order. To understand the symmetry of the above Hamiltonian, we decompose it into two components, $\hat{H}_\epsilon^{\text{2T-eff}} = \hat{H}_{\epsilon=0}^{\text{2T-eff}} + \hat{H}_\epsilon$:

$$\hat{H}_\epsilon = -\frac{\hbar\pi\epsilon}{4T}\sum_l \left[(\cos\theta_l + 1)\,\sigma_l^x + \sin\theta_l \sigma_l^y\right] \tag{2.18}$$

By comparing it to Eq. (2.16), we see that the small error ϵ induces the transverse magnetic field ($\hat{H}_\epsilon$) along the x and y-axis. We see that $\hat{H}_\epsilon$ breaks the $\mathbb{Z}_2$-Ising symmetry of Eq. (2.11). Despite of it, in a rotated frame, the system can recover the symmetry. To find the frame, first let us simplify the Hamiltonian, as follows,

$$\begin{aligned}\hat{H}_\epsilon &= -\frac{\hbar\pi\epsilon}{4T}\sum_l \sqrt{2(1+\cos\theta_l)}\left[\frac{(\cos\theta_l+1)}{\sqrt{2(1+\cos\theta_l)}}\sigma_l^x + \frac{\sin\theta_l}{\sqrt{2(1+\cos\theta_l)}}\sigma_l^y\right] \\ &= -\frac{\hbar\pi\epsilon}{4T}\sum_l \sqrt{2(1+\cos\theta_l)}\left[\cos\tilde{\theta}_l\sigma_l^x + \sin\tilde{\theta}_l\sigma_l^y\right]\end{aligned} \tag{2.19}$$

where the new angle $\tilde{\theta}_l$ satisfies the relation $\tan\tilde{\theta}_l = \sin\tilde{\theta}_l/\left(\cos\tilde{\theta}_l + 1\right)$. Now, let us consider an unitary operator,

$$\hat{V}_{\tilde{\theta}} = \exp\left[-i\sum_l \tilde{\theta}_l \sigma_l^z\right] \tag{2.20}$$

In the rotated frame defined by $\hat{V}_{\tilde{\theta}}$, the induced field $\hat{H}_\epsilon$ can be written as

$$\hat{V}_{\tilde{\theta}}\hat{H}_\epsilon\hat{V}_{\tilde{\theta}}^\dagger = -\frac{\hbar\pi\epsilon}{4T}\sum_l \sqrt{2(1+\cos\theta_l)}\sigma_l^x \tag{2.21}$$

We see that it has parity symmetry. Here, we note that $\hat{H}_{\epsilon=0}^{\text{2T-eff}}$ does not change under the this transformation. Thus, in the frame, the effective Hamiltonian $\hat{H}_R^{\text{2T-eff}} = \hat{V}_{\tilde{\theta}}\hat{H}_\epsilon^{\text{2T-eff}}\hat{V}_{\tilde{\theta}}^\dagger$ has the $\mathbb{Z}_2$-Ising symmetry. Correspondingly, the Hamiltonian $\hat{H}_\epsilon^{\text{2T-eff}}$ has the $\mathbb{Z}_z$ Ising-like symmetry given by $\hat{V}_{\tilde{\theta}}\hat{X}\hat{V}_{\tilde{\theta}}^\dagger$.

2.5 2T-DTCs

Now, let us see emergence of the 2T-DTC in our system by using the effective Hamiltonian derived above. To get some intuition, we first consider the trivial case ($\epsilon = 0$). Using it, we will show that the magnetization dynamics can be used as an order parameter for 2T-DTC, and an initial state should break the parity for the system to exhibit the sub-harmonic response. Then, we will examine how the periodicity of the sub-harmonic response is robust against the error ϵ.

2.5.1 Trivial case ($\epsilon = 0$)

Previously, we have derived the 2T-effective Hamiltonian $\hat{H}_{\epsilon=0}^{\text{2T-eff}}$ for $\epsilon = 0$ and seen that it has the $\mathbb{Z}_2$-Ising symmetry. It means that the parity is preserved at every even ($t = 2nT$) and odd ($t = (2n+1)T$) periods, and can use parity as an order parameter to observe the DTC. One of the measures of parity is the expectation value of the magnetization, and we employ it.

Now, let us see the dynamics of the local magnetization $\langle\sigma_l^Z(nT)\rangle$. Suppose, we have a initial state $|\Psi(0)\rangle$, then the magnetization at even periods is the same as its initial value, as follows,

$$\begin{aligned}\langle\sigma_l^z(2nT)\rangle &= \text{Tr}\left[\hat{F}^{2n}\hat{\rho}(0)\left(\hat{F}^{2n}\right)^\dagger\sigma_l^z\right] \\ &= \text{Tr}\left[e^{-\frac{i}{\hbar}\hat{H}_{\epsilon=0}^{\text{2T-eff}}}\hat{\rho}(0)e^{+\frac{i}{\hbar}\hat{H}_{\epsilon=0}^{\text{2T-eff}}}\sigma_l^z\right] \\ &= \langle\sigma_l^z(0)\rangle\end{aligned} \tag{2.22}$$

where $\hat{\rho} = |\Psi(0)\rangle\langle\Psi(0)|$ and we used $\left[\hat{H}_{\epsilon=0}^{\text{2T-eff}}, \sigma_l^z\right] = 0$. At odd periods, the expectation

value of the magnetization is given by,

$$\begin{aligned}\langle \sigma_l^z \left((2n+1)T\right)\rangle &= \mathrm{Tr}\left[\hat{F}^{2n+1}\hat{\rho}(0)\left(\hat{F}^{2n+1}\right)^\dagger \sigma_l^z\right] \\ &= \mathrm{Tr}\left[\hat{F}^{2n}\hat{\rho}(0)\left(\hat{F}^{2n}\right)^\dagger \hat{F}^\dagger \sigma_l^z \hat{F}\right] \\ &= -\langle \sigma_l^z(0)\rangle\end{aligned} \tag{2.23}$$

where we used $\hat{X}\sigma_l^z\hat{X} = -\sigma_l^z$.

The above result means that when the initial state, e.g. $|\Psi\rangle = |00\cdots\rangle$, breaks the parity and initial magnetization is no-zero, the magnetization dynamics exhibits the sub-harmonic oscillation with two times longer periods of the Hamiltonian [33, 38]. It indicates that breaking the $\mathbb{Z}_2$-Ising symmetry leads to the sub-harmonic oscillation with period 2T. In other words, the dynamics of the magnetization breaks the DTTS, and such the state is called the **DTC** or **2T-DTC**. Furthermore, we have seen that the spin-flip operator or the parity operator in the Hamiltonian Eq. (5.31) plays an essential role for the system to break the DTTS and to exhibit the sub-harmonic oscillation with period 2T.

2.5.2 MBL-DTCs

When $\epsilon = 0$, as seen in above, the magnetisation dynamics of the system governed by Eq. (5.31) shows a sub-harmonic oscillation. However, to conclude that this system is a DTC, we need to show that the periodicity of the sub-harmonic oscillations of the magnetization stable against parameter changes in the Hamiltonian.

Here, let us see the sub-harmonic response of the model Eq. (5.31) discussed in above in a different way by looking at the eigenstates of the Floquet operator. Here, to simplify the discussion, we assume that there is only nearest neighbours interactions and the absence of the disorder $W = 0$. It means that the second Hamiltonian of Eq. (5.31) is simply given by

$$\hat{H}_2 = \sum_{\langle i,j\rangle} J_{ij}^z \sigma_i^z \sigma_j^z. \tag{2.24}$$

where $\langle i,j\rangle$ means only taking the nearest neighbour pair of i,j. Now, when $\epsilon = 0$, the Floquet operator is given by

$$\hat{F} = \exp\left[-i\sum_{\langle i,j\rangle} J_{lm}^z T_2 \sigma_l^z \sigma_m^z\right]\hat{X}. \tag{2.25}$$

To find its eigenstate, first let us see the eigenstates of $\hat{H}_2$. Because there is only σ_l^z operators in the interactions $\hat{H}_2$, eigenstates of $\hat{H}_2$ can be labelled by its eigenstates

$|0/1\rangle_l$ and the eigenvalue $m_l = \pm 1$. Among them, we focus on the two eigenstates $|\mathbf{m}\rangle = |00\cdots0\rangle$ and $|-\mathbf{m}\rangle = |11\cdots1\rangle$ with the same eigenvalue $E_{\text{int}} = \sum_{\langle i,j\rangle} J_{ij}^z$. Next, using the two states, let us introduce two new states $|\pm\rangle_{\mathbf{m}} = (|\mathbf{m}\rangle \pm |-\mathbf{m}\rangle)$. Here, these states $|\pm\rangle_{\mathbf{m}}$ are the eigenstates of $\hat{X}$, as follows,

$$\hat{X}|\pm\rangle_{\mathbf{m}} = \hat{X}\left(|\mathbf{m}\rangle \pm |-\mathbf{m}\rangle\right) = \left(|-\mathbf{m}\rangle \pm |\mathbf{m}\rangle\right) = \pm|\pm\rangle_{\mathbf{m}} \tag{2.26}$$

where we used $\hat{X}|\pm\mathbf{m}\rangle = |\mp\mathbf{m}\rangle$. Finally, we conclude that the eigenstates of the Floquet operator $\hat{F}$ are given by $|\pm\rangle_{\mathbf{m}}$ with eigenvalues $\pm e^{-iE_{\text{int}}T_2}$. These states are cat states, which are a superposition of two microscopically distinct states. As a result, when the initial state is either $|\mathbf{m}\rangle$ and $|-\mathbf{m}\rangle$, it evolves periodically with a period $2T$.

Now, how stable is its periodicity against perturbations such as an error ϵ? Here, the strong disorder induces many-body localization (Floquet MBL) in driven systems [65, 66, 67] and plays an important role. In general, a periodically driven system is eventually thermalized to the thermal state with the infinite temperature [68, 69, 70, 71, 72, 73, 74, 75, 76] where the time-averaged expectation value of the system for longer times is the same as the expectation value using the thermal state. This indicates that if the cat states mentioned above are fragile, the DTC phase may become unstable. However, in the presence of the strong disorder, it is shown that the system can avoid heating and does not thermalize. Furthermore, when the system shows the (Floquet) MBL, the change of eigenstates due to perturbation is small within a local length scale [77, 78, 79]. Therefore, Floquet MBL protects the cat states being the eigenstates of the Floquet operator. Hence, the system with the strong disorder exhibits a stable and rigid DTC, and the state is specifically called the **MBL-DTC** [33]. More details on MBLs are available from Ref. [33, 1].

2.5.3 Prethermal DTCs

In this present section, let us reconsider the DTCs in terms of an effective Hamiltonian. The effective Hamiltonian of the Floquet operator tells us the dynamics of a periodically driven system at stroboscopic times. However, in general, it is impossible to find the exact effective Hamiltonian ($\hat{H}^{\text{eff}}$) analytically from the Floquet operator. Here, we note that in the present section we use $\hat{H}^{\text{eff}}$ and $\hat{H}_F$ with the same meaning, which is the exponential argument of the Floquet operator. Thus, one should use a series expansion to find the effective Hamiltonian ($\hat{H}^{\text{eff}}$) or the Floquet Hamiltonian ($\hat{H}_F$). Generally, to keep the unitary, the Magnus expansion is used. It is given by,

$$\hat{H}_F = \sum_{n=0}^{\infty} \Omega_n(T) T^n, \tag{2.27}$$

where T is a driving period, and Ω_n is an expansion coefficient. Its details are discussed in Appendix B.2.2. For example, the Hamiltonian of the lowest order is referred to as the time-averaged Hamiltonian. The expansion has been widely used to predict new phenomena in periodically driven quantum systems.

However, in the limit where the system's size becomes infinity, such as the scenario of quantum phases of matter, the Magnus expansion does not converge and diverge, except for some trivial cases such as a non-interaction system. Furthermore, because of the breaking of the energy conservation in Floquet systems, it is thermalized and reaches an equilibrium state at infinite temperature, known as Floquet ETH (see Appendix B.2.3). Thus, in MBL-DTCs, the strong disorder is crucial in avoiding this thermalization due to the MBL effect. As a result, as we saw above, a strong disorder system can exhibit DTC even in driven systems.

However, there is not always a strong disorder in a system. For example, when the strength of the interaction is stronger than that of the disorder, it may not be possible to get the MBL effect. Thus, we will show that even in the absence of the strong disorder, systems can exhibit a sub-harmonic oscillation or show the DTC phase.

When the frequency of the driven system is sufficiently high, importantly, it is shown that there is an order n_0 at where one can assume $\exp\left(-i\hat{H}_F T\right) \approx \exp\left(-i\hat{H}_F^{(n_0)} T\right)$, where $\hat{H}_F^{(n_0)} = \sum_{n=1}^{n_0} \Omega_n T^n$ is a Magnus expansion up to the n_0-order. Here, we note that the assumption is valid within a time scale $t \ll e^{\mathcal{O}(\omega)}$, where ω is the frequency of a system. Therefore, as long as a time within this scale, the state seems to be thermalized through the effective Hamiltonian up to the n_0-th order. Furthermore, since the time scale is exponentially long, it can reach its thermalized state. Since this thermalized state is not an actual thermal state, after a time beyond this time scale, the state relaxes to an equilibrium state at an infinite temperature. This two-step thermalization is called Floquet pre-thermalization. [80, 81, 82, 83, 84].

Now, the prethermal regime may allow the system with errors to exhibit the stable sub-harmonic oscillation with two periods. To see it, let us see the magnetization at even periods ($t = 2nT$) with a small error $\epsilon \ll 1$,

$$
\begin{aligned}
\langle \sigma_l^z(2nT) \rangle &= \mathrm{Tr}\left[\hat{F}^{2n}\hat{\rho}(0)\left(\hat{F}^{2n}\right)^\dagger \sigma_l^z\right] \\
&\approx \mathrm{Tr}\left[\hat{V}_{\tilde{\theta}}^\dagger e^{-\frac{i}{\hbar}\hat{H}_R^{\text{2T-eff}}2nT}\hat{V}_{\tilde{\theta}}\hat{\rho}(0)\hat{V}_{\tilde{\theta}}^\dagger\left(e^{-\frac{i}{\hbar}H_R^{\text{2T-eff}}2nT}\right)^\dagger \hat{V}_{\tilde{\theta}}\sigma_l^z\right] \\
&\approx \mathrm{Tr}\left[e^{-\frac{i}{\hbar}\hat{H}_R^{\text{2T-eff}}2nT}\hat{\tilde{\rho}}(0)\left(e^{-\frac{i}{\hbar}H_R^{\text{2T-eff}}2nT}\right)^\dagger \hat{V}_{\tilde{\theta}}\sigma_l^z\hat{V}_{\tilde{\theta}}^\dagger\right] \\
&\approx \mathrm{Tr}\left[\hat{\tilde{\rho}}(2nT)\sigma_l^z\right]
\end{aligned}
\tag{2.28}
$$

where we used $[\hat{V}_{\tilde{\theta}}, \sigma_l^z] = 0$. Here we use the following transformation,

$$\hat{V}_{\tilde{\theta}} \hat{F}^2 \hat{V}_{\tilde{\theta}}^\dagger = e^{-\frac{i}{\hbar} H_R^{\text{2T-eff}} 2T}. \tag{2.29}$$

Thus, the state $\hat{\tilde{\rho}}(0) = \hat{V}_{\tilde{\theta}} \hat{\rho}(0) \hat{V}_{\tilde{\theta}}^\dagger$ is the initial state in the rotating frame and its time-evolution is given by the effective Hamiltonian $\hat{H}_R^{\text{2T-eff}}$.

We now consider that the system immediately relaxes to the thermal state of the effective Hamiltonian with the lower order, as follows

$$\langle \sigma_l^z (2nT) \rangle \approx \text{Tr} \left[\hat{\tilde{\rho}}_{\text{pre}} \sigma_l^z \right] \tag{2.30}$$

where $\hat{\tilde{\rho}}_{\text{pre}}$ is the thermal density matrix for $\hat{H}_R^{\text{2T-eff}}$ at some temperature $\tau \neq \infty$. Here we empathize that it does not mean that the state itself is the same as the pre thermal state. As we saw, the thermal state is different from the true thermal state of the Floquet system, and it is stable state with a exponentially longer time ($\sim e^{\text{O}(\omega)}$). It means that the magnetization can be represented by the thermal state $\hat{\tilde{\rho}}_{\text{pre}}$. Now, using the pre-thermal state, the magnetization at the odd periods can be obtained by,

$$\begin{aligned} \langle \sigma_l^z \left((2n+1)T \right) \rangle &= \text{Tr} \left(\hat{F}^{2n+1} \hat{\rho}(0) (\hat{F}^{2n+1})^\dagger \sigma_l^z \right) \\ &\approx \text{Tr} \left(\hat{\tilde{\rho}}_{\text{pre}} \hat{F}^\dagger \sigma_l^z \hat{F} \right) \\ &\approx -\langle \sigma_l^z (2nT) \rangle \end{aligned} \tag{2.31}$$

where we use $[\hat{H}_2, \sigma_l^z] = 0$ and $\hat{X} \sigma_l^z \hat{X}^\dagger = -\sigma_l^z$.

We have seen that in the system Eq. (5.31), the magnetization dynamics breaks the discrete-time translational symmetry of the Hamiltonian with the period T. As a result, it shows two times longer periods ($2T$). Furthermore, the periodicity is robust to the small error ϵ. We can conclude that the system (5.31) shows the DTC phase when the initial state breaks parity. Here, the method used to show the existence of DTCs assumes that the state is in a pre-thermal regime. Hence, such DTCs are called the **prethermal DTCs** [85].

2.6 Simple theoretical description of 2T-DTCs

In this section, let us reconsider 2T-DTCs analytically. As we saw above, we have assumed that after a certain time τ_{pre}, states at even periods $t = 2nT$ reaches the state $\hat{\tilde{\rho}}_{pre}$, which is the (pre-) thermal state of the Hamiltonian $\hat{H}_R^{\text{2T-eff}}$. As a result, its magnetization can be

given by $\langle\sigma_l^z(2nT)\rangle \approx \mathrm{Tr}\left[\hat{\tilde{\rho}}_{pre}\sigma_l^z\right]$. Here, $\hat{H}_R^{\text{2T-eff}}$ is given by

$$\hat{H}_R^{\text{2T-eff}} = \frac{\hbar T_2}{T}\sum_{l,m} J_{lm}^z \sigma_l^z\sigma_m^z - \frac{\hbar\pi\epsilon}{4T}\sum_l \sqrt{2(1+\cos\theta_l)}\sigma_l^x, \tag{2.32}$$

for $J_{lm}^z T \ll 1$. Thus, to understand its phase transition and reveal the physics behind 2T-DTCs, let us first investigate the dynamics of Eq. (2.32).

2.6.1 Dynamics and characteristic parameters of the Ising model

To understand the dynamics of Eq. (2.32), let us simplify it by assuming the nearest-neighborhood interactions with the coupling constant $J_0^z > 0$ and the absence of the disorder ($W = 0$). As a result, the Hamiltonian becomes the simplest model referred to as the ZZ-Ising model [86], similar to the system defined in Section 2.1. Thus, it is given by

$$\hat{H}_{\text{ZZ-Ising}} = \hbar J\sum_l \sigma_l^z\sigma_{l+1}^z - \hbar g\sum_l \sigma_l^x, \tag{2.33}$$

where $J(= J_0^z T_2/T)$ is the coupling constant, and $g(= \pi\epsilon/2T)$ is the amplitude of the transverse magnetic field. The driving error ϵ induces the transverse magnetic field in this model.

Here, we note that, unlike in Section 2.1, the signs of the parameters J, g are different. Thus, to make the following discussion easier, let us consider a non-trivial transformation of the Hamiltonian $\hat{H}_{\text{ZZ-Ising}}$, where these parameters are reversed ($J, g \to -J, -g$). Because the dynamics of this system are not given by the Hamiltonian $\hat{H}_{\text{ZZ-Ising}}$, but by its unitary $\hat{U} = \exp(-i\hat{H}_{\text{ZZ-Ising}}t)$, where t is a time, one can consider the inversion of the time parameter $t \to -t$, as follows,

$$\hat{U} = \exp(-i\hat{H}_{\text{ZZ-Ising}}t) = \exp\left\{-i\left(-\hat{H}_{\text{ZZ-Ising}}\right)(-t)\right\}. \tag{2.34}$$

Here, we note it is not a strict time-reversal operation for spin systems defined in quantum mechanics [11]. The above transformation indicates that as long as we keep in mind that the time parameter is reversed, the system's dynamics can be characterized by $-\hat{H}_{\text{ZZ-Ising}}$. Furthermore, we will expand on this. Thus, as long as the Hamiltonian is used to investigate the dynamical properties, one can use the reversed Hamiltonian $\left(-\hat{H}_{\text{ZZ-Ising}}\right)$. Thus, now, it is identical to the Ising model in Section 2.1$\left(\hat{H}_{\text{Ising}} = -\hat{H}_{\text{ZZ-Ising}}\right)$.

To investigate its dynamics, we need to choose an initial state. Previous works have suggested that to obtain 2T-DTCs, the initial state has to break the parity symmetry in the case of short-range interactions. Thus, we consider the simplest initial state $|\Psi(0)\rangle = |00\cdots0\rangle$ which maximally breaks the parity, as an example.

As we saw in Section 2.1, its eigenstates can be characterized by parity symmetry. Similarly, this symmetry can be used to understand its dynamics. First, when $J \gg g$, there are parity symmetric eigenstates, i.e., $|00\cdots0\rangle$ and $|11\cdots1\rangle$ for $g = 0$. It indicates that the initial state $|\Psi(0)\rangle$ is almost dynamically frozen in this regime ($J \gg g$). As a result, parity or magnetization is preserved for a long time. Contrary, if $J \ll g$, its eigenstates become parity symmetric, i.e., $|++\cdots+\rangle$ and $|--\cdots-\rangle$ for $J = 0$. Thus, the dynamics of initial states breaking the parity symmetry such as $|\Psi(0)\rangle$ can not be stable. Consequently, its magnetization dynamics are also not stable.

The above analysis indicates that the magnetization dynamics of the Ising model can be characterized by a parameter $\delta_{\text{Ising}} \sim g/J$ that is the balance between the transverse magnetic field and the two-body interaction. And there is a critical point: $\delta_{\text{Ising}} \sim 1$.

2.6.2 Characteristic parameter δ_x for 2T-DTCs

From the above estimation, one can characterise 2T-DTC phase by a parameter δ_x,

$$\delta_x \sim \frac{\epsilon\pi}{2J_0^z T_2}. \tag{2.35}$$

We see that as the interaction strength increases, the DTC phase becomes more stable. Furthermore, it indicates that to get the 2T-DTC, the system should be the many-body spin system in which spins are interacting.

Previously, we have assumed the absence of the disorder. Here, let us expand the parameter δ_x to that of a system with the disorder. From Eq. (2.32), the magnetization dynamics at a l-the site can be characterised by a parameter $\delta_x^{(l)}$, as follows,

$$\delta_x^{(l)} \sim \frac{\epsilon\pi}{4|J_0^z|T_2}\sqrt{2\left(1+\cos 2W_l T_2\right)}. \tag{2.36}$$

We note here that the above parameters are site-dependent. Therefore, we introduce the concept of ensemble and define the parameters of the disordered system as the ensemble average of the above parameters over the disorder as follows,

$$\delta_x = \overline{\left\langle \delta_x^{(l)} \right\rangle} \tag{2.37}$$

where $\overline{\langle\cdots\rangle}$ means taking the ensemble average over the disorder realization.

2.6.3 Initial state of 2T-DTCs and the total number of domain walls

Next, let us reconsider the requirement for the initial state to get a stable 2T-DTC. In conventional models, the total magnetization is used to measure the parity symmetry

breaking. Furthermore, it is used to measure the initial states of 2T-DTCs. However, this measure does not work for some initial states. For example, consider two initial states $|\Psi\rangle_1 = |0_1 0_2 \cdots 0_L 1_1 1_2 \cdots 1_L\rangle$ and $|\Psi\rangle_2 = |0_1 1_1 0_2 1_2 \cdots 0_L 1_L\rangle$, where $2L = N$. The total magnetizations of both initial states are the same $M_{1/2} = 0$. However, the dynamics of the initial state $|\Psi\rangle_2$ show the stable sub-harmonic oscillation with 2T, but that of the state $|\Psi\rangle_1$ is unstable [64, 44].

Let us use the inference based on the Ising model again to get a better measure. When $J \ll g$, the stability of the state dynamics would be characterized by the number of spin flips in the initial state. Thus, let us use the total number of domain walls of the basis states $\hat{\mathcal{N}}$ [38] to evaluate initial states. Here, it tells us the number of spin flips in states. Therefore, we believe that when it is smaller, the sub-harmonic oscillation of the system is more stable. For instance, the total number of domain walls for the initial states, $|\Psi\rangle_1$ and $|\Psi\rangle_2$, are $\mathcal{N}_1 = 1$ and $\mathcal{N}_2 = (N-1)/2$, respectively. Thus, the state $|\Psi\rangle_1$ is available as the initial state of 2T-DTC. Contrary, the state $|\Psi\rangle_2$ will show random dynamics [64]. Thus, $\hat{\mathcal{N}}$ can be used to evaluate the initial stat of 2T-DTCs.

2.6.4 Phase diagram of 2T-DTCs

Now, there is a critical point at $\delta_x \sim 1$, after and before, where the dynamics would dramatically be changed. If $\delta_x \ll 1$, the system should show the stable DTC with a longer lifetime due to the presence of cat eigenstates of the Floquet operator. Contrary, when $\delta_x \gg 1$, the state does not show a stable sub-harmonic response or it collapses rapidly. However, because of the presence of the $\mathbb{Z}_2$-Ising like symmetry of the 2T-effective Hamiltonian, the state at the longer time should be different from the thermal state. Thus, in the presence of the strong disorder case, the state is called the **symmetry unbroken MBL** [1, 87].

Lastly, let us consider the second term effect in Eq. (2.17). Previously, when both the interaction strength and the error are small, we can assume that the second term effect is much smaller than the transverse magnetic field $\hat{H}_\epsilon$. Contrary, if both parameters are large, we can expect that it contributes to dynamics dominantly. Here, we see that the term is complicated two-body interaction and breaks the both $\mathbb{Z}_2$-Ising symmetry and the U(1)-symmetry. As a result, we expect that the state will be thermalized in $\epsilon|J_0^z| \gg 1$ regime.

The above results can be summarized in a phase diagram as shown in Fig. 2.1. Here, the blue line shows the critical line ($\delta_x \sim \epsilon/|J_z^0| \sim 1$) between the 2T-DTC phase and the symmetry unbroken MBL phase. Similarly, the red line ($\epsilon|J_0^z| \sim 1$) divides the thermal phase and the other two phases. We note that the diagram is a very rough drawing based on a simplistic model of our effective Hamiltonian. Nevertheless, our theoretical results

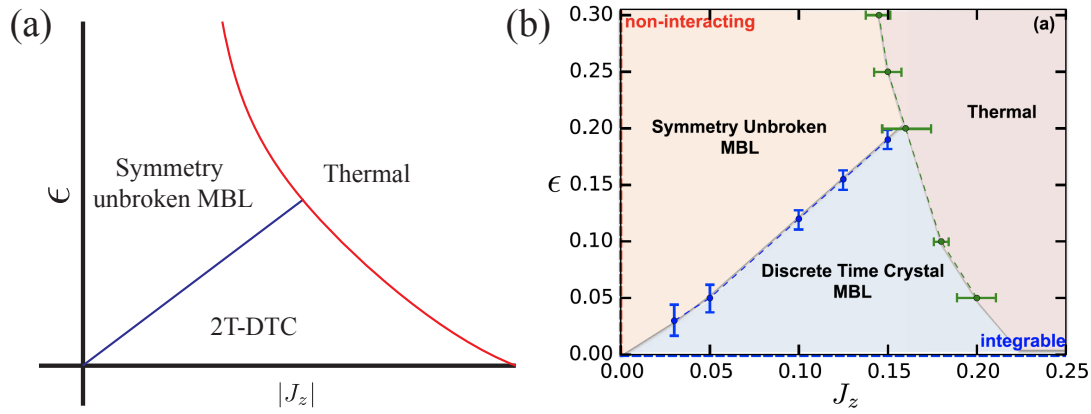

Figure 2.1: Phase diagram of the 2T-Discrete time crystal: (a) Exhibits the phase diagram as a function of the coupling strength $|J_0^z|$ and the rotational error ϵ. The result is theoretically obtained using the simple 2T-DTC model defined by Eq. (5.31). The red (blue) line shows the critical line between the 2T-DTC and the symmetry unbroken MBL (thermal). (b) Illustrates the phase diagram numerically obtained [1].

nicely reflect the characteristics of the diagrams obtained from numerical calculations [1]. They used the same model we used to obtain the numerical results, but note that the parameter definitions are a bit different from ours.

Here, we also mention the recent research on the phase diagram investigated by N. V. Yao, et al [1] . In 2021, a comment to the paper that introduced this phase diagram was appeared on the arXiv [64]. In the original work [1], they assumed that the initial state can take a generic state as long as it breaks the parity and is short correlated. However, recent work [64] numerically demonstrated that for some initial states such as a random state $|01011\cdots01\rangle$, the two-period sub-harmonic response rapidly disappears, even when the parameter values of the system are in the region giving rise to the MBL-DTC phase. Furthermore, they claim that their results indicate the absence of MBL-DTCs using trapped ions reported in 2017 [2]. N.V. Yao and et al. have recently put a reply to this on the arXiv [88]. From these discussions, it can be said that DTC research is a very hot topic and is very active.

In this Chapter, we have seen 2T-DTCs with respect to two different models, MBL-DTCs and prethermal DTCs. Here, we briefly note that several models breaking the discrete (continuous) time translation symmetry have been proposed:e.g., disordered photonic time crystals [89], quantum time crystals on isolated Heisenberg magnet [90]. For example, it has been reported that a time-crystal structure appears as a symmetry protected topological phase using a topological insulator, called Topological Time Crystals [91]. In

addition, there are researches on DTC coupled with the environment system [92, 93, 94]. Furthermore, there is a proposal of the new DTC caused the environment effect [95].

2.7 Recent experiments on 2T-DTCs

Previously we have investigated the 2T-DTC both analytically and numerically. Now, let us briefly review the recent experiments on the 2T-DTCs. Recently, as quantum technology has improved, it has become possible to realize quantum systems that can be controlled at a sufficient level. As a result, quantum systems exhibiting sub-harmonic responses have been observed on several experimental platforms: e.g., nuclear spins in molecules [39], super-fluid quantum gases [40], ordered dipolar many-body systems [41], and silicon doped with phosphorus. Furthermore, recently, the realization of DTCs using quantum gates on superconducting qubits has been reported [42, 43, 44]. Google group used a programmable superconducting circuit and demonstrated the 2T-DTCs for random Bit-strings (initial states). In the next section, among them, we will review the two first DTC experiments on trapped ions [2] and NV-centers [3] reported in 2017.

2.7.1 Trapped ions

In 2017, J. Zhang. et al. reported the first observation of discrete-time crystals in a spin chain using trapped atomic ions [2]. They used hyperfine clock states of a $^{171}\mathrm{Yb}^{+}$ ion, $|F=0, m_F=0\rangle$ and $|F=0, m_F=1\rangle$, to prepare the effective spin-1/2 states denoted $|\uparrow\rangle_z$ and $|\downarrow\rangle_z$, where F and m_F are the hyper-fine and Zeeman quantum numbers, respectively. They prepared a chain with ten ions in a linear radiofrequency Paul trap.

To observe the DTC, they experimentally realized the system governed by the following Hamiltonian,

$$\hat{H}(t) = \begin{cases} \hat{H}_1 = g(1-\epsilon)\sum_l \sigma_l^y & \text{time } T_1 \\ \hat{H}_2 = \sum_{lm} J_{lm}\sigma_l^x\sigma_m^x & \text{time } T_2 \\ \hat{H}_3 = \sum_l D_l\sigma_l^x & \text{time } T_3. \end{cases} \tag{2.38}$$

Here, the first Hamiltonian is the strong driving, and it can be performed by using the optical Raman transition between two spin states. To break the DTTS, they tuned the Rabi frequency g to be $2gT_1 = \pi$ with the error ϵ. Next, the second term has the spin-spin interaction. Using the spin-dependent optical dipole force, they approximately generate the a tun-able long-range Ising interaction $J_{lm} \propto J_0/|l-m|^\alpha$, where α ranges from $\alpha = 0$ to $\alpha = 3$ [96]. Finally, the third Hamiltonian represents a program-able strong disorder along the z-axis encoded by the AC Stark Shift using the off-resonant tightly focused laser

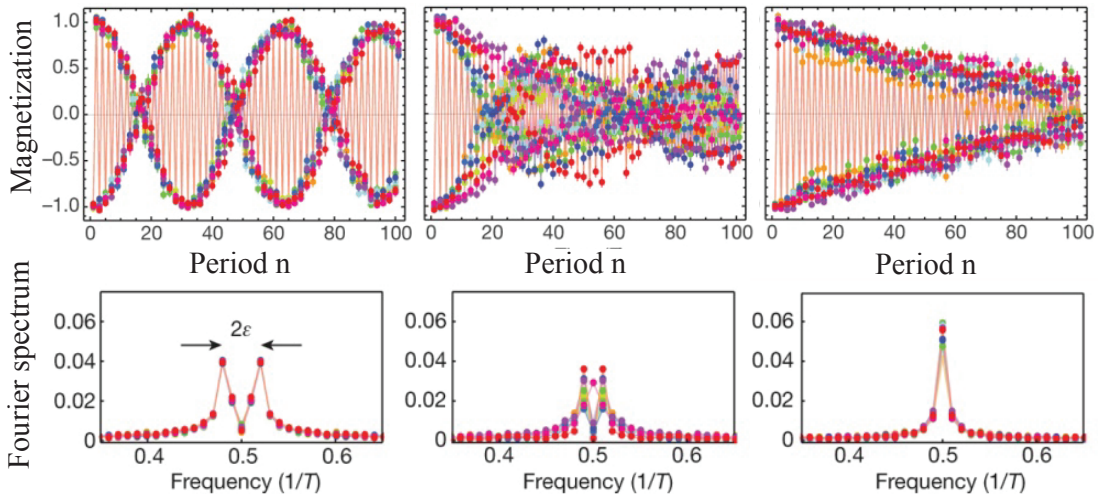

Figure 2.2: Observation of the 2T-DTC using trapped ions. The top panels shows the magnetization dynamics at stroboscopic times. The corresponding Fourier spectrum are shown in the bottom panels. In the experiment, to see the rigidity of the sub-harmonic response to imperfection of the rotation pulse, they set ϵ to be $\epsilon = 0.03$. In the experiment, to get the MBL effect, they used the diagonal disorder $WT_3 = \pi$. Finally, to get the long-range interaction, they set $2J_0T_2 = 0.072$ with $\alpha = 1.51$. The plot is take from Ref [2].

beam [97].

To observe the DTC, they initialized a state to be $|\Psi(0)\rangle = |+\rangle = \frac{1}{\sqrt{2}}(|0\rangle + |1\rangle)$ and observed a magnetization along the x-axis at the stroboscopic times $t = nT$ which gives the time-correlation function,

$$\langle \sigma_l^x(nT)\rangle = \langle \Psi(0)|\sigma_l^x(nT)\sigma_l^x(0)|\Psi(0)\rangle. \tag{2.39}$$

They measured the magnetization with 100 Floquet periods. The experimental results of the magnetization dynamics and its Fourier spectrum for several conditions are shown in Fig. 2.2.

In the absence of disorder and interaction, the sub-harmonic oscillations of the magnetization are very brittle to spin-flip errors, as shown in the leftmost panel of Fig. 2.2. While, in the presence of the interactions, magnetization dynamics shows the sub-harmonic oscillation, and as a result, its Fourier spectrum peaks at $1/2$-frequency (1/T). It indicates that the interacting spin system can break the DTTS, unlike the non-interaction spin ensemble.

Their results measured the DTTS breaking and the resulting DTC signal in trapped ions. The experiment was performed with high precision. Thus, even with the small

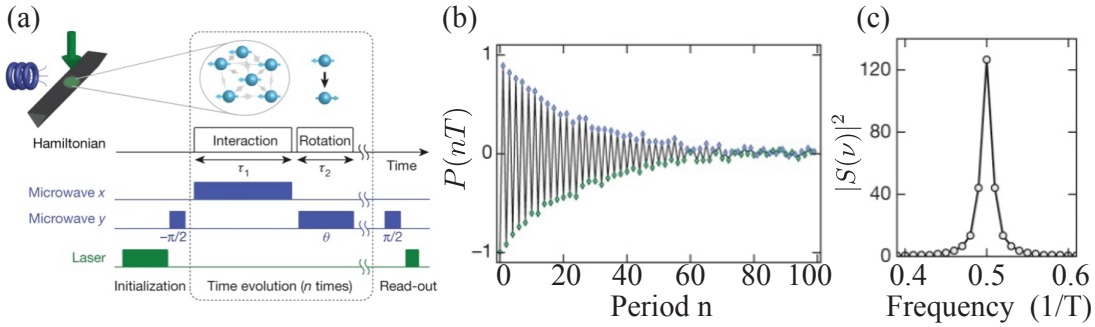

Figure 2.3: Experimental set-up and observation of the DTC in NV-centers. (a) Exhibits the NV-centers in a nanobeam fabricated from black diamond and the pulse sequence to generate the DTC phase. In the experiment, they prepared the initial state $|\Psi(0)\rangle = (|m_s = 0\rangle + |m_s = -1\rangle)/\sqrt{2}$ using a microwave. Panels (b) and (c) show the stroboscopic dynamics of the spin polarization along the x-axis and corresponding Fourier spectrum with imperfect rotation ($\theta = 1.034\pi$). The plot is take from Ref [3].

size of the system, the results are very important for comparison with the theoretical aspects. However, the analysis of the experimental results with trapped ions is still under debate [64].

2.7.2 NV Centers in diamond

Here, we present the experimental observation of the DTTS breaking and the DTC in a platform with numerous spins, which is closer to a true many-body system. Choi. et al. realized the 2T-DTC in 2017 using the nitrogen-vacancy (NV) spin impurities in diamond at room temperature [3]. In NV-center, each nitrogen-vacancy has an $S = 1$ spin, and they used external driving to prepare an effective two-level sub-system. States of their two-level system are spanned by states $|m_s = 0\rangle$ and $|m_s = -1\rangle$. Their diamond samples have a high purity of nitrogen-vacancy (45 p.p.m.), and as a result, they have realizes the system with about one million spins ($\sim 10^6$NV).

Using strong resonant microwave filed to control the individual spins, they prepared the following effective time-dependent Hamiltonian,

$$\hat{H}(t) = \sum_l \Omega_x(t) S_l^x + \Omega_y(t) S_l^y + \Delta_l S_l^z + \sum_{lm} \frac{J_{lm}}{r_{lm}^3} \left(S_l^x S_m^x + S_l^y S_m^y - S_l^z S_m^z\right) \tag{2.40}$$

where S_l^μ ($\mu = x, y, z$) are general Pauli matrices. Here, $\Omega_{x/y}$ are the Rabi frequency of the microwave driving, and they use $\Omega_y(t)$ with $\tau_2 = \theta/\Omega_y$ to rotate the spin ensemble with

nearly perfect π pulses ($\theta \approx \pi$). And, Δ_l is a disordered on-site field with approximate standard deviation. During $\tau_1 \ll \tau_2$, the spin ensemble is coupled via the long range interactions J_{lm}/r_{lm}^3. Thus, these two pulses define the Floquet operator with the total period $T = \tau_1 + \tau_2$. Fig. 2.3(a) illustrates the pulse sequence used in the experiment.

To break the DTTS, they prepared a superposition state as an initial state: $|\Psi(0)\rangle = (|m_s = 0\rangle + |m_s = -1\rangle)/\sqrt{2}$ and measured the the normalized polarization $P(nT)$ along the x-axis with 100 Floquet periods.

The results of polarization with imperfect π-rotation ($\theta = 1.034\pi$) are exhibited in Fig. 2.3 (b). They also found the corresponding Fourier spectra $S(\nu) = \sum_n P(nT)e^{i2\pi n\nu}$ shown in Fig. 2.3 (c). They successfully observed the signal of the DTC phase breaking the DTTS using NV-centers even with the error in the rotation. Hence, the important point of their experiment is that they measured the DTTS breaking and the 2T-DTC in the large system ($\sim 10^6$ NV) that is closer to true many-body systems.

2.8 Conclusion

In the present Chapter, we have briefly reviewed the DTTS breaking, and the resulting new phase of matter called the DTC phase. We have demonstrated the simple model of the 2T-DTC and shown its magnetization dynamics exhibits the sub-harmonic response with 2T concerning two different ways, such as the MBL effects and the pre-thermalization. We have seen that for DTTS breaking, and the appearance of DTCs, the parity symmetry (or $\mathbb{Z}_2$-Ising symmetry) of the 2T-effective Hamiltonian of the Floquet system and the initial state are essential. We also have reviewed the experiments on the 2T-DTC. The tools used in this Chapter will be essential in the following Chapters to understand the DTTS breaking in those proposed models.

Furthermore, we have shown that in this simple model, the collapse of the DTC phase leads to the two different phases of matter, such as the symmetry broken MBL and the thermal state. In particular, the existence of this thermalized phase is essential in scenarios where the complexity of this quantum system is applied. The existence of these different classes of quantum phases will be meaningful when considering applications of the complexity of this periodically driven system.

Part I

Proposal for new dynamical phase of matter breaking the DTTS

Chapter 3

Chimera Discrete Time Crystal

In periodically driven systems, one can realize a state spontaneously breaking the discrete-time translational symmetry (DTTS), and consequently, some observable show sub-harmonic response with integer times longer period of the driving. For example, as we saw in the previous Chapter, in a periodically driven spin network with the ZZ-interactions, by applying the spin-rotation pulse, the magnetization dynamics exhibits the periodic oscillation with two times longer period of the driving, so-called the 2T-Discrete Time Crystal (**2T-DTC**) phase.

When a state shows the DTC phase, the periodicity of the sub-harmonic response is rigid to slight changes of parameters in the Hamiltonian. For instance, in the 2T-DTC case, the 2T-periodicity of the magnetization dynamics is robust to a rotational error. In the previous models, it has been considered that the rotational error is uniform across the entire system.

However, the present Chapter considers the spin network under periodic driving with site-dependent errors. This new freedom allows us to break the DTTS differently and design a new phase of matter. In classical mechanics, the non-linear dynamics show an exotic phase of matter in which synchronized and unsynchronized phases coexist [98], and it is known as the chimera phase. Similarly, such exotic phases of matter have been found in the semi-classical regime [99]. However, because of the absence of non-linearity in the quantum dynamics, it is challenging to make the chimera phase in the fully quantum domain.

Nevertheless, the periodically driven network allows one to make a chimera in which multiple phases coexist within the whole system. Here, one of the phases is the DTC phase, and thus, we refer to it as a **chimera DTC** [45]. In the present Chapter, we employ a spin network with two regions and demonstrate the chimera DTC for the extreme case in which regions A and B's error is are drastically different.

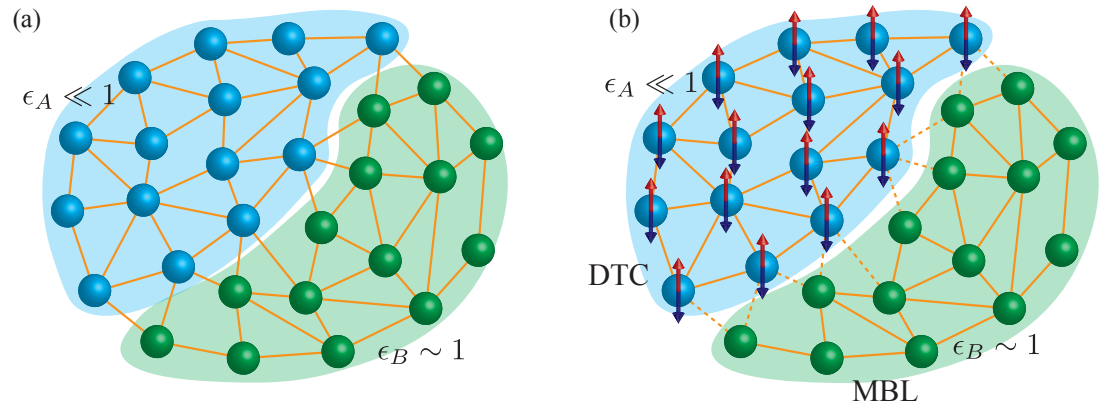

Figure 3.1: Diagram of the chimera DTC on the spin network governed by Eq. (3.1). (a) shows the spin network under the periodic driving. The spin network has two or more regions labeled by the rotational error, such as $\epsilon_{A/B}$. These regions have different errors, and site errors are uniform in each region. In panel (a), the network has two regions A and B, in which we set rotational errors to be close to zero and one, respectively. (b) shows the phases of matter in the network. When the initial state in region A breaks the $\mathbb{Z}_2$-Ising symmetry, region A exhibits a DTC phase. On the contrary, region B is the MBL ferromagnetic state. As a result of two different regional rotational errors, two regions are effectively decoupled at the stroboscopic times.

3.1 Model

As mentioned in the introduction, we are interested in periodically driven spin networks with two domains under the effect of by different errors in the driving (so-called the regional error). Thus, we consider the following time-dependent Hamiltonian with period $T = T_1 + T_2$ for the periodically driven spin network with N-sites,

$$\hat{H}(t) = \begin{cases} \hat{H}_1 = \hbar g(1-\epsilon_A) \sum_{l\in A} \sigma_l^x + \hbar g(1-\epsilon_B) \sum_{l\in B} \sigma_l^x & (0 \le t < T_1) \\ \hat{H}_2 = \hbar \sum_{lm} J_{lm}^z \sigma_l^z \sigma_m^z + \hbar \sum_l W_l^z \sigma_l^z & (T_1 \le t < T), \end{cases} \tag{3.1}$$

where σ_l^μ with $\mu \in \{x, y, z\}$ are the usual Pauli operators at the l-th site. The first Hamiltonian $\hat{H}_1$ represents the individual spin rotation along the x-axis with the same amplitude g. To break the discrete time translational symmetry, we set g to be $2gT_1 = \pi$, similarly to other 2T-DTC models [33, 2, 3]. Now, as we mentioned, to define two regions in the network, we put two different regional errors ϵ_A and ϵ_B in the driving, as shown in Fig. 3.1. As a result, two regions are characterized by the different rotation angle. In this Chapter, to see the effect of the regional error efficiently, we assume that the error

ϵ_A is close to zero ($\epsilon_A \ll 1$), contrary, the error ϵ_B is close to one ($\epsilon_B \sim 1$). When the regional error in region A is exactly zero ($\epsilon_A = 0$), then the time evolution under the first Hamiltonian flips spins in region A,

$$\hat{X}_A = e^{-i\frac{\pi}{2}\sum_{l\in A}\sigma_l^x} = \prod_{l\in A}\sigma_l^z, \tag{3.2}$$

where $l \in A$ means sites in region A. This operator can be seen as the regional spin-flip operator and regional $\mathbb{Z}_2$-Ising symmetry (parity) ore region A with $\hat{X}_A\hat{X}_A^\dagger = \hat{\mathbb{I}}$

Next, J_{lm}^z defines the connectivity between l-th and m-th sites over the network. Here, we emphasize that there is no restriction on the range of couplings between sites; in other words, there is the interaction between the two regions. Next, W_l^z is the on-site energy at l-th site and is uniformly distributed $[0, W]$ with the strength of the disorder W. In later sections, we will see that the MBL effect of this diagonal disorder stabilizes the phases in this network.

3.2 Effective Hamiltonian and Symmetry

Due to the time-periodicity of the system, we can apply Floquet theory to it to understand its physics and dynamics at stroboscopic times. Since our model is similar to the DTC model discussed in the previous Chapter, we expect that our system shows sub-harmonic oscillation with a period that is twice the driving period T. Given the 2T-periodicity of the DTC phase, we find the effective Hamiltonian for two periods, $\hat{H}^{\text{eff}}_{2\text{T},\epsilon_A,\epsilon_B}$, which gives the dynamics at the stroboscopic times $t = 2nT$. The Hamiltonian can be obtained from the square of Floquet as follows, $\hat{H}^{\text{2T-eff}}_{\epsilon_A,\epsilon_B} = i\hbar\ln(\hat{F}^2)/2T$. In our model, $\hat{F}^2$ is given by,

$$\hat{F}^2 = \exp\left[-\frac{i}{\hbar}\hat{H}_2T_2\right]\exp\left[-\frac{i}{\hbar}\hat{H}_1T_1\right]\exp\left[-\frac{i}{\hbar}\hat{H}_2T_2\right]\exp\left[-\frac{i}{\hbar}\hat{H}_1T_1\right]. \tag{3.3}$$

But, in general, it is difficult to obtain the effective Hamiltonian from the above equation. Therefore, in the following, we will look at the effective Hamiltonian for several combination of ϵ_A and ϵ_B.

3.2.1 Trivial case ($\epsilon_A = 0$ and $\epsilon_B = 1$)

Since we are interested in the parameter regime $\epsilon_A \ll 1$ and $\epsilon_B \sim 1$, to get some intuition let us first consider the extreme case in which $\epsilon_A = 0$ and $\epsilon_B = 1$. Then the time evolution under the first Hamiltonian $\hat{H}_1$ is the same as the spin flip operator ($\hat{X}_A$) of region A defined in Eq. (3.2). As a result, the square of the Floquet operator ($\hat{F}^2$) can be written

as,

$$\begin{aligned}\hat{F}^2 &= \exp\left[-\frac{i}{\hbar}\hat{H}_{0,1}^{\text{2T-eff}}(2T)\right] \\ &= \exp\left[-\frac{i}{\hbar}\hat{H}_2 T_2\right]\exp\left[-\frac{i}{\hbar}\hat{H}_1 T_1\right]\exp\left[-\frac{i}{\hbar}\hat{H}_2 T_2\right]\exp\left[-\frac{i}{\hbar}\hat{H}_1 T_1\right] \\ &= \exp\left[-\frac{i}{\hbar}\hat{H}_2 T_2\right]\hat{X}_A\exp\left[-\frac{i}{\hbar}\hat{H}_2 T_2\right]\hat{X}_A \\ &= \exp\left[-\frac{i}{\hbar}\hat{H}_2 T_2\right]\exp\left[-\frac{i}{\hbar}\hat{X}_A\hat{H}_2\hat{X}_A T_2\right] \\ &= \exp\left[-\frac{i}{\hbar}\left(\hat{H}_2 + \hat{X}_A\hat{H}_2\hat{X}_A^\dagger\right)T_2\right]\end{aligned} \tag{3.4}$$

where we used $\hat{X}_A^\dagger = \hat{X}_A$ except a phase, and $\left[\hat{H}_2, \hat{X}_A\hat{H}_2\hat{X}_A^\dagger\right] = 0$. Similarly to the 2T-DTCs previously discussed, in $\hat{X}_A\hat{H}_2\hat{X}_A^\dagger$, we see that the operator $\hat{X}_A$ generates spin flip in region A, as follows,

$$\hat{X}_A\left(\sum_{l\in A} W_l^z\sigma_l^z\right)\hat{X}_A^\dagger = \sum_{l\in A} W_l^z\hat{X}\sigma_l^z\hat{X}_A^\dagger = -\sum_{l\in A} W_l^z\sigma_l^z. \tag{3.5}$$

Furthermore, we also see that,

$$\hat{X}_A\left(\sum_{\substack{l\in A\\ m\in B}} J_{lm}^z\sigma_l^z\sigma_m^z\right)\hat{X}_A^\dagger = \sum_{\substack{l\in A\\ m\in B}} J_{lm}^z\left(\hat{X}_A\sigma_l^z\hat{X}_A^\dagger\right)\sigma_m^z = -\sum_{\substack{l\in A\\ m\in B}} J_{lm}^z\sigma_l^z\sigma_m^z \tag{3.6}$$

The above results means that the regional π-rotation generates the effective time reversal transformation to the interaction between two region A and B. As a result, one can exactly obtain the effective Hamiltonian, as follows,

$$\hat{H}_{0,1}^{\text{2T-eff}} = \frac{\hbar T_2}{T}\sum_{l,m\in\text{A}} J_{lm}^z\sigma_l^z\sigma_m^z + \frac{\hbar T_2}{T}\sum_{l,m\in\text{B}} J_{lm}^z\sigma_l^z\sigma_m^z + \frac{\hbar T_2}{T}\sum_{l\in\text{B}} W_l^z\sigma_l^z. \tag{3.7}$$

Due to the effective time-reversal, the interactions between two regions disappears in the above effective Hamiltonian. In other words, the two regions are completely decoupled at even periods.

Now, let us explore the symmetries of the above Hamiltonian. First, due to the diagonal disorder, the original Hamiltonian breaks the $\mathbb{Z}_2$-Ising symmetry generated by the operator $\hat{X} = \prod_l \sigma_l^x$. However, the 2T-effective Hamiltonian above has a $\mathbb{Z}_2$-Ising symmetry generated by the operator $\hat{X}_\text{A} = \prod_{l\in A}\sigma_l^x$. As a result, the system preserves the regional parity of $\hat{X}_A$ at even or odd periods. On the contrary, region B breaks the

regional $\mathbb{Z}_2$-Ising symmetry generated by $\hat{X}_{\mathrm{B}} = \prod_{l\in B}\sigma_l^x$ due to the remaining diagonal disorder W_l in Eq. (3.7), unlike 2T-DTCs previously discussed.

3.2.2 Presence of a small error ($\epsilon_A \ll 1$)

The next step is to consider a small error in region A ($\epsilon_A \ll 1$), which acts as a perturbation. Using the high-frequency expansion, one can approximately obtain the effective Hamiltonian as follows,

$$\begin{aligned}\hat{H}^{\text{2T-eff}}_{\epsilon_A,1} \approx{}& \frac{\hbar T_2}{T}\sum_{l,m\in A} J^z_{lm}\sigma^z_l\sigma^z_m - \frac{\hbar\pi\epsilon_A T_2}{2T}\sum_{\substack{l,m\in A\\ l\neq m}} J^z_{lm}\sigma^z_l\sigma^y_m \\ &+ \frac{\hbar T_2}{T}\sum_{l,m\in B} J^z_{lm}\sigma^z_l\sigma^z_m + \frac{\hbar T_2}{T}\sum_{l\in B} W_l\sigma^z_l \\ &- \frac{\hbar\pi\epsilon_A}{4T}\sum_{l\in A}\left[\Big(\cos\hat{\Theta}_l + 1\Big)\sigma^x_l + \sin\hat{\Theta}_l\sigma^y_l\right],\end{aligned} \tag{3.8}$$

where $\hat{\Theta}_l = 2W_lT_2 + 2\sum_{m\in B} J^z_{lm}T_2\sigma^z_m$. In the previous section, we saw that when $J^z_{lm}\epsilon_A \gg 1$, the second interaction term breaks the 2T-DTC order and consequently the state is eventually thermalized. Thus, in the following discussion, we assume that $J^z_{lm}\epsilon_A \ll 1$ unless otherwise, similarly to the similar to 2T-DTCs in the previous Chapter.

Here, to make it simple, we decompose the above Hamiltonian into three components, $\hat{H}^{\text{eff}}_{\epsilon_A,2T} = \hat{H}_{\mathrm{A}} + \hat{H}_{\mathrm{B}} + \hat{H}_{\mathrm{AB}}$:

$$\begin{aligned}\hat{H}_{\mathrm{A}} &= \frac{\hbar T_2}{T}\sum_{l,m\in A} J^z_{lm}\sigma^z_l\sigma^z_m \\ \hat{H}_{\mathrm{B}} &= \frac{\hbar T_2}{T}\sum_{l,m\in B} J^z_{lm}\sigma^z_l\sigma^z_m + \frac{\hbar T_2}{T}\sum_{l\in B} W_l\sigma^z_l \\ \hat{H}_{\mathrm{AB}} &= -\frac{\hbar\pi\epsilon_A}{4T}\sum_{l\in A}\left[\Big(\cos\hat{\Theta}_l + 1\Big)\sigma^x_l + \sin\hat{\Theta}_l\sigma^y_l\right],\end{aligned} \tag{3.9}$$

where $\hat{H}_{\mathrm{A/B}}$ are Hamiltonian for each region, and $\hat{H}_{\mathrm{AB}}$ represent the induced interaction between two regions due to the driving. Note that the interaction is highly nontrivial, because the Θ_l contains only operators in region B. We see that the interaction $\hat{H}_{\mathrm{AB}}$ due to the small error ϵ_A is very similar to the effective transverse field in the 2T-DTC effective Hamiltonian of (2.17). And, since $-1 \le \sin\theta, \cos\theta \le 1$ for any θ, in the Hamiltonian $\hat{H}_{\mathrm{AB}}$, the interaction term of $\sigma^x_{l\in A}$ dominates over that of $\sigma^y_{l\in A}$. However, we can see the difference between them. In the presence model, the interaction term induced by the small error ϵ_A is not only single operator but also two-body interactions between two region.

Now, in the presence of the small error ϵ_A, the $\mathbb{Z}_2$-Ising symmetry of region A is broken due to the effective interaction $\hat{H}_{\rm AB}$. However, in a rotated frame, the Hamiltonian recovers the $\mathbb{Z}_2$-Ising symmetry. To see it, first let us simplify the induced interaction $\hat{H}_{\rm AB}$, as follows,

$$\begin{aligned}\hat{H}_{\rm AB} &= -\frac{\hbar\pi\epsilon_A}{4T}\sum_{l\in A}\left[\left(\cos\hat{\Theta}_l+1\right)\sigma_l^x+\sin\hat{\Theta}_l\sigma_l^y\right]\\ &= -\frac{\hbar\pi\epsilon_A}{4T}\sum_{l\in A}\sqrt{2\left(1+\cos\hat{\Theta}_l\right)}\left(\frac{\cos\hat{\Theta}_l+1}{\sqrt{2\left(1+\cos\hat{\Theta}_l\right)}}\sigma_l^x+\frac{\sin\hat{\Theta}_l}{\sqrt{2\left(1+\cos\hat{\Theta}_l\right)}}\sigma_l^y\right)\\ &= -\frac{\hbar\pi\epsilon_A}{4T}\sum_{l\in A}\sqrt{2\left(1+\cos\hat{\Theta}_l\right)}\left(\cos\hat{\tilde{\Theta}}_l\sigma_l^x+\sin\hat{\tilde{\Theta}}_l\sigma_l^y,\right)\end{aligned} \tag{3.10}$$

where the new angle $\hat{\tilde{\Theta}}_l$ reads

$$\tan\hat{\tilde{\Theta}}_l=\frac{\sin\hat{\Theta}_l}{\cos\hat{\Theta}_l+1}. \tag{3.11}$$

Here we would like to emphasize that all the previous algebraic manipulations are possible because $\hat{\Theta}_l$ commutes with operators in region A. Let us consider a rotated frame given by the unitary operator $\hat{V}_A$,

$$\hat{V}_{\rm A}=\exp\left[-i\sum_{l\in A}\tilde{\Theta}_l\sigma_l^z\right]. \tag{3.12}$$

In that frame, the Hamiltonians $\hat{H}_A$ and $\hat{H}_B$ in the $2T$-effective Hamiltonian do not change, but the induced interaction $\hat{H}_{AB}$ is now written as

$$\begin{aligned}\hat{H}^{\rm R}_{\rm AB} &= \hat{V}_{\rm A}\hat{H}_{\rm AB}\hat{V}_{\rm A}^\dagger\\ &= -\frac{\hbar\pi\epsilon_A}{4T}\sum_{l\in A}\left(\sqrt{2\left(1+\cos\hat{\Theta}_l\right)}\right)\sigma_l^x,\end{aligned} \tag{3.13}$$

Thus, in the frame, the effective Hamiltonian has the $\mathbb{Z}_2$-Ising symmetry. Consequently, the effective Hamiltonian (3.1) in the original frame has the $\mathbb{Z}_2$ Ising like symmetry generated by $\hat{X}_A^R=\hat{V}_A\hat{X}_A\hat{V}_A^\dagger$.

Previously, we have seen the symmetry of region B by looking at the effective Hamiltonian Eq. (3.7) for $\epsilon_A=0$ and $\epsilon_B=1$. Here, we consider the own symmetry of region B for small error $\epsilon_A\ll 1$. Surprisingly, region B has local U(1)-symmetry at any time,

independent of the regional error ϵ_A. This means that the local magnetization of region B is preserved at any times, $[\sigma^z_{l\in B}, \hat{H}(t)] = 0$.

3.2.3 Presence of the driving in region B ($\epsilon_B \sim 1$)

Now, let us consider that ϵ_B is not exactly one, has a small value ($\epsilon_B \lesssim 1$). Because the corresponding rotation angle is too small, $\frac{\pi(1-\epsilon_B)}{2} \ll 1$, its effect to the Hamiltonian should be small, as follows,

$$\hat{H}^{\text{2T-eff}}_{\epsilon_A,\epsilon_B} = \hat{H}^{\text{2T-eff}}_{\epsilon_A,1} + \hbar\frac{\pi(1-\epsilon_B)T_1}{2T}\sum_{l\in B}\sigma^x_l \tag{3.14}$$

where we use the high-frequency expansion again. As a result of the second term, the U(1)-symmetry of region B is broken. Consequently, the local magnetisation is not the conserved quantity anymore.

3.3 Chimera Discrete Time Crystalline Order (Chimera DTC)

Previously, we have derived the effective Hamiltonian for two periods and seen emergent symmetries. In this section, let us investigate the phases of matter in the two regions based on these symmetries. Since we are interested in quantum phases in non-equilibrium quantum systems, the choice of the initial state is also important. Here, we assume that there is no correlation between the two regions at the initial time. The assumption is experimentally reasonable because it can be easily realized in many devices, such as trapped ions and superconducting qubits. Thus, the initial state can be written as the tensor product of the two states: $|\Psi(0)\rangle = |\Psi(0)\rangle_{\text{A}} \otimes |\Psi(0)\rangle_{\text{B}}$, where $|\Psi(0)\rangle_{\text{A/B}}$ are the initial states of regions A and B, respectively.

3.3.1 Trivial case ($\epsilon_A = 0, \epsilon_B = 1$)

To understand the phase of matter in two regions, let us first consider the extreme case where $\epsilon_A = 0$ and $\epsilon_B = 1$ as we discussed in section 3.2.1. In this case, the effective Hamiltonian for two periods is given by Eq. (3.7). Due to the perfect π-rotation in region A, the two regions are completely decoupled at the stroboscopic times. It means that since there is no correlation between the two regions initially, we can investigate the time evolution of the two regions separately.

First, let us see the phase of matter in region B. Since its regional error is precisely one ($\epsilon_B = 1$) or there is no drive acting on A, there is the local U(1)-symmetry at any time in region B, and thus the local magnetization is preserved. Thus, there are two possible quantum phases in region B in terms of the initial state. When the initial state of region B, $|\Psi(0)\rangle_{\mathrm{B}}$, breaks the parity symmetry and has a non-zero longitudinal magnetization, the phase of matter of region B is ferromagnetic. On the contrary, if the initial state is s symmetric under parity transformations, the longitudinal magnetization is zero and the system is in the paramagnetic phase.

Next, let us explore which kind of phase of matter is present in region A. Given the similarity between our model and the DTC model discussed in the previous Chapter, we expect region A exhibits the DTC phase. Thus, as similar to the previous DTC model, we consider the initial state of region A, $|\Psi(0)\rangle_{\mathrm{A}}$ breaking the parity symmetry and having the non-zero longitudinal magnetization $\langle\sigma_l^z\rangle \neq 0$. Now, at even periods $t = 2nT$, the local magnetization in region A returns to the initial value, as follows,

$$\begin{aligned}\langle\sigma_{l\in A}^z(2nT)\rangle &= \mathrm{Tr}\left(\hat{F}^{2n}\hat{\rho}(0)(\hat{F}^{2n})^\dagger\sigma_{l\in A}^z\right)\\ &= \mathrm{Tr}\left(e^{-\frac{i}{\hbar}\hat{H}^{\text{2T-eff}}_{\epsilon_A,\epsilon_B=1}2nT}\hat{\rho}(0)e^{\frac{i}{\hbar}\hat{H}^{\text{2T-eff}}_{\epsilon_A,\epsilon_B=1}2nT}\sigma_{l\in A}^z\right)\\ &= \langle\sigma_{l\in A}^z(0)\rangle\end{aligned} \tag{3.15}$$

where we have used $\left[\hat{H}^{\text{2T-eff}}_{\epsilon_A,\epsilon_B=1},\sigma_{l\in A}^z\right] = 0$. Contrary, at odd periods $t = (2n+1)T$, the magnetization change it sign, as follows

$$\begin{aligned}\langle\sigma_{l\in A}^z\left((2n+1)\,T\right)\rangle &= \mathrm{Tr}\left(\hat{F}^{2n+1}\hat{\rho}(0)(\hat{F}^{2n+1})^\dagger\sigma_{l\in A}^z\right)\\ &= \mathrm{Tr}\left(\hat{\rho}(2nT)\hat{F}^\dagger\sigma_{l\in A}^z\hat{F}\right)\\ &= -\langle\sigma_{l\in A}^z(0)\rangle\end{aligned} \tag{3.16}$$

where we have used $[H_2,\sigma_{l\in A}^z] = 0$ and $\hat{X}_A\sigma_{l\in A}^z\hat{X}_A^\dagger = -\sigma_{l\in A}^z$. These results indicate that the local magnetization dynamics shows a sub-harmonic oscillation with period $2T$. This means that in region A the magnetization dynamics breaks the discrete translational symmetry in time from the time-periodic Hamiltonian Eq. (3.1) and the system is in the DTC phase, as we expected.

The above results indicate that there are two completely different phases of matter in the same network: the DTC phase for region A and the ferromagnetic/paramagnetic phase for region B. Remarkably, two phases of matter stably coexist in space despite there are long-range interactions across the network. Here, we refer to such a unique DTC phase as the **chimera DTC** [45], analogous to Chimera states of classical systems in which synchronized and unsynchronized phases coexist [98, 100, 101, 102]. However, in this

section, we have considered a minimal example to simplify the discussion. So, in the following sections, we will discuss each quantum phase in more detail.

3.3.2 Absence of the disorder ($WT = 0$)

Previously, we have considered the trivial case with $\epsilon_A = 0$ to get some intuition of the phase in region A and shown that it exhibits a DTC phase. Here, let us consider the presence of a small error $\epsilon_A \ll 1$. At the even periods, $t = 2nT$, the order parameter or the expectation value of the magnetization in region A is given by

$$\begin{aligned} M_A(2nT) &= \mathrm{Tr}\left(\hat{F}^{2n}\hat{\rho}(0)(\hat{F}^{2n})^\dagger\sigma^z_{l\in A}\right) \\ &\approx \mathrm{Tr}\left(\hat{V}_A^\dagger e^{-\frac{i}{\hbar}\hat{H}_R^{\text{2T-eff}}(2nT)}\hat{V}_A\hat{\rho}(0)\hat{V}_A^\dagger e^{\frac{i}{\hbar}\hat{H}_R^{\text{2T-eff}}(2nT)}\hat{V}_A\sigma^z_{l\in A}\right) \\ &\approx \mathrm{Tr}\left(\hat{\tilde{\rho}}(2nT)\sigma^z_{l\in A}\right) \end{aligned} \tag{3.17}$$

where we have used $[\hat{V}_A, \sigma^z_{l\in A}] = 0$ and $[\hat{V}_A, \hat{\rho}(0)] = 0$. Here, we have used the following transformation,

$$\hat{V}_A\hat{F}^2\hat{V}_A^\dagger = e^{-\frac{i}{\hbar}\hat{H}_R^{\text{2T-eff}}2T}. \tag{3.18}$$

In other wards, $\hat{H}_R^{\text{2T-eff}}$ is the 2T-effective Hamiltonian in the rotated frame by $\hat{V}_A$. Thus, $\hat{\tilde{\rho}}(0) = \hat{V}_A\hat{\rho}(0)\hat{V}_A^\dagger$ is the initial state in the rotated frame and its time-evolution is given by the new effective Hamiltonian $\hat{H}_R^{\text{2T-eff}}$.

We now assume that as similar to the DTC phase discussed in the previous Chapter [85], the system immediately relaxes to the thermal state of the $\hat{H}_R^{\text{2T-eff}}$ with the lower order, as follows,

$$M_A(2nT) \approx \mathrm{Tr}\left(\hat{\tilde{\rho}}(2nT)\sigma^z_{l\in A}\right) \approx \mathrm{Tr}\left(\hat{\tilde{\rho}}_{\text{pre}}\sigma^z_{l\in A}\right), \tag{3.19}$$

where $\hat{\tilde{\rho}}_{\text{pre}}$ is the thermal density matrix for $\hat{H}_R^{\text{2T-eff}}$ at some temperature $\tau \neq \infty$ [80, 81, 82, 83, 84]. It means that the macroscopic observable of the system after the certain time can be given by the thermal state $\hat{\tilde{\rho}}_{\text{pre}}$: $M_A(2nT) \approx \mathrm{Tr}\left(\hat{\tilde{\rho}}_{\text{pre}}\sigma^z_{l\in A}\right)$. Here, we note that it does not mean that the state is the same as the thermal state.

Now, at the odd periods $t = 2n + 1$, the expectation value is given by

$$\begin{aligned} M_A(2n+1) &= \mathrm{Tr}\left(\hat{F}^{2n+1}\hat{\rho}(0)(\hat{F}^{2n+1})^\dagger\sigma^z_{l\in A}\right) \\ &= \mathrm{Tr}\left(\hat{\tilde{\rho}}_{\text{pre}}\hat{F}^\dagger\sigma^z_{l\in A}\hat{F}\right) \\ &\approx -M_A(2n) \end{aligned} \tag{3.20}$$

where we use $[\hat{H}_2, \sigma^z_{l\in A}] = 0$ and $\hat{X}_A\sigma^z_{l\in A}\hat{X}_A^\dagger = -\sigma^z_{l\in A}$. Thus, from the above results,

we see that the expectation value of the magnetization has a period 2T and it breaks the discrete-time translational symmetry of the Hamiltonian (3.1) with period T. It indicates that when the initial state of region A breaks the $\mathbb{Z}_2$-Ising symmetry of the effective Hamiltonian, there is the DTC phase in region A.

3.3.3 Critical point of Chimera DTCs

Previously, we have shown that region A exhibits the DTC phase, and the phase is robust to a small error $\epsilon_A \ll 1$. Furthermore, as we saw, the magnetization dynamics is effectively governed by the Hamiltonian $\hat{H}_{\mathrm{R}}^{\text{2T-eff}}$ being parity symmetric. Here, let us investigate a critical point of the DTC phase at which the discrete crystalline order start melting. To explore this point, we apply the same approach used in section 2.6, in which the effective Hamiltonian is mapped to the Ising model to chimeric DTCs. When $\epsilon_A \ll 1$, the dynamics in region A is given by the following terms of the effective Hamiltonian in the rotated frame:

$$\begin{aligned}\hat{H}_{R,A}^{\text{2T-eff}} &= \hat{H}_A^R + \hat{H}_{AB}^R \\ &\approx \frac{\hbar T_2}{T}\sum_{l,m\in A} J_{lm}^z \sigma_l^z \sigma_m^z - \frac{\hbar\pi\epsilon_A}{4T}\sum_{l\in A}\left(\sqrt{2\left(1+\cos\hat{\Theta}_l\right)}\right)\sigma_l^x .\end{aligned} \tag{3.21}$$

Now, similarly to the 2T-DTC, the dynamics in region A can be characterized by a parameter δ_x,

$$\delta_x^{(l)} \sim \frac{\epsilon_A \pi}{4|J_0^z|T_2}\sqrt{2\left(1+\cos\hat{\Theta}_l\right)} \tag{3.22}$$

where J_0^z is the order scale of the spin-spin interactions. A similar analysis can be seen in the research on phase transitions in the random Ising model [103, 104]. In absence of the disorder, the region B has an effect on region A through the parameter, $\hat{\Theta}_l = 2T_2\sum_{m\in B} J_{lm}^z\sigma_m^z$. To understand this in more detail, let us suppose the interaction is the nearest neighbor. Consequently, the value of $\hat{\Theta}_l$ should be small and can be ignored. Then, the above parameter is approximately given by

$$\delta_x \sim \frac{\epsilon_A\pi}{2|J_0^z|T_2}, \tag{3.23}$$

Here, we note that unlike Eq.(3.22) it is site-independent. In general, the interaction is not only nearest neighbor, but also long-range with exponential decay. When there are long-range interactions in the system, it is known that the critical point shifts in the Ising model [105].

Finally, as the Hamiltonian Eq. (3.21) looks like a one dimensional quantum Ising chain with a transverse field modulated by the region B, there is a critical point at $\delta_x^c \sim 1$.

Thus, it is expected that the behavior of DTC changes dramatically before and after this critical point. If $\delta_x \ll 1$, region A should show the stable DTC phase with a longer lifetime, which is associated with the ferromagnetic phase. Contrary, when $\delta_x \gg 1$: i.e., $\epsilon_A \gg 1$, region A should be quickly thermalized, and the sub-harmonic response can not be because the effective Hamiltonian Eq. (3.21) is in the paramagnetic phase and there is no long-range order. While if $\epsilon \sim 1$, the magnetization dynamics in region A may show the sub-harmonic oscillation. However, even if that, the oscillation is unstable, and the DTC phase collapses rapidly.

3.3.4 Strong diagonal disorder and MBL phases

Previously, we have shown that there is a pre-thermal DTC in region A in the absence of the diagonal disorder. Here, let us consider the disorder effect. As we saw above, when the interaction J^z_{lm} is small, the DTC in region A might not be stable. However, in the presence of a strong disorder, it is expected that the DTC gets stable due to many-body localization (MBL) [65, 66, 67].

In the previous section, we introduce the parameter δ_x to characterise the DTC phase in region A. However, in the presence of the strong disorder, we need to take into account its randomness. Thus, we update the parameter as follows,

$$\overline{\langle \delta_x \rangle} \sim \frac{\epsilon_A \pi}{4|J^z_0|T_2} \overline{\left\langle \sqrt{2 + \sin 2\hat{\Theta}_l} \right\rangle} \tag{3.24}$$

where $\overline{\langle \cdots \rangle}$ is the ensemble average over the disorder realizations.

Next, let us investigate the disorder effect in region B. If the error of region B is close to one but not exactly one ($\epsilon_B \sim 1$), there is a driving in region B. In the absence of the disorder, because the periodic driving heats up the region B, the ferromagnetic phase in region B is unstable. However, in the presence of a strong disorder, the phase becomes the MBL phase and it is stable.

3.4 Numerical results

Previously, we have analytically investigated our model and shown that two different phases of matter that coexist in the same network, so-called the chimera DTC. Here, we numerically investigate the chimera DTC to understand its stability to the parameter changes in the Hamiltonian and reveal the physics behind the model.

3.4.1 Parameter setting

First, let us define the parameters used in our numerical calculations. We employed a spin system arranged in a one-dimensional array, as shown in Fig. 3.2. Here, we consider long-range interactions between the spins given by $J^z_{lm} = J_0/|l-m|^\alpha$ at sites l and m , where J_0 is the coupling constant and α determines the range of the interaction. The parameter α can be chosen between 0 to ∞ and allows us to consider various network's connectivity, e.g., the nearest-neighbor networks ($\alpha = \infty$) and the fully connected network ($\alpha = 0$). Furthermore, as it is illustrated in Fig. 3.2, we consider a spin network with $N = 8$ sites where sites $l = 0, 1, 2, 3$ belong to region A while the remaining sites belong to region B. Unless otherwise stated, we use the spin network.

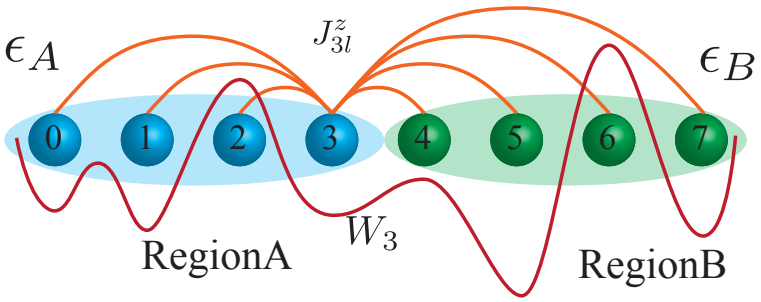

Figure 3.2: A $N = 8$ sites spin chain where we apply regional drives with errors labeled by $\epsilon_{A/B}$. A π-rotation with small error $\epsilon_A \ll 1$ is applied on region A having sites $l = 0, 1, 2, 3$. While a small rotation pulse is applied on the reaming spites (region B). On the chain, sites are under the effect of diagonal disorder W_l and are coupled via the long-range interaction $J^z_{lm} = J^z_0/|l-m|^\alpha$, where J_0 is the coupling constant and α is the interaction decay rate.

3.4.2 Absence of the disorder ($WT = 0$)

First, let us investigate the stability of the chimera DTC phase in the absence of the disorder. To simplify the discussion, we assume $\epsilon_B = 1$ and explore the stability of the DTC phase of region A. Here, we consider a initial state fully polarized along the z-axis: $|\Psi(0)\rangle_z = |00\cdots0\rangle_{\rm A} \otimes |00\cdots0\rangle_{\rm B}$. In this case, region B preserves the local magnetization at the stroboscopic times. Thus region B shows the static ferromagnetic phase, as we discussed above.

As we saw, the DTC phase in region A can be characterized by the parameter $\delta^{(l)}_x$ defined in the above section. Here, in our numerical model, J^z_0 is the strength of the

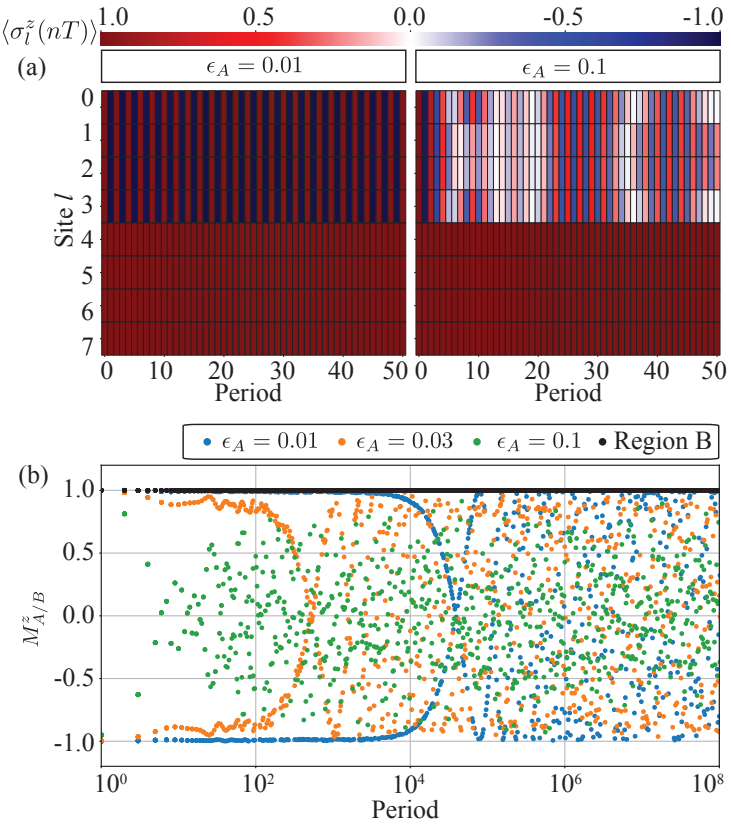

Figure 3.3: Short time-scale dynamics (a) of the local magnetization $\sigma_l^z(nT)$ for the chimera DTC with a small error $\epsilon_A = 0.01$ and a strong error $\epsilon_A = 0.1$. Here, we set ϵ_B to be $\epsilon_B = 1$. And we have chosen $gT = \pi$, $J_0T = 0.2$ with $\alpha = 1.51$ and $WT = 0$. (b) shows the long time-scale dynamics of the regional magnetization $M^z_{A/B}$ for different errors $\epsilon_A = 0.01, 0.03$ and 0.1.

spin-spin interaction. In the following sections, we will investigate DTC robustness with respect to **the rotational error** ϵ_A, **the interaction strength** and **the interaction range** (α).

3.4.2.1 Robust against drive imperfections (ϵ_A) and size effect (N)

The parameter δ_x is proportional to the rotational error ϵ_A. It means that as ϵ_A increases, the parameter δ_x gets larger. Consequently, the effective Hamiltonian Eq. (3.21) undergoes a transition from ferromagnetic to paramagnetic phase and the DTC becomes unstable. To see it, we calculate the local magnetization dynamics at the stroboscopic times in a short time-scale for small and large errors ($\epsilon_A = 0.01, 0.1$) and show the results in Fig 3.3 (a). Here, we consider the strongly interacting ($J_0T = 0.1$) spin-network. First, as we

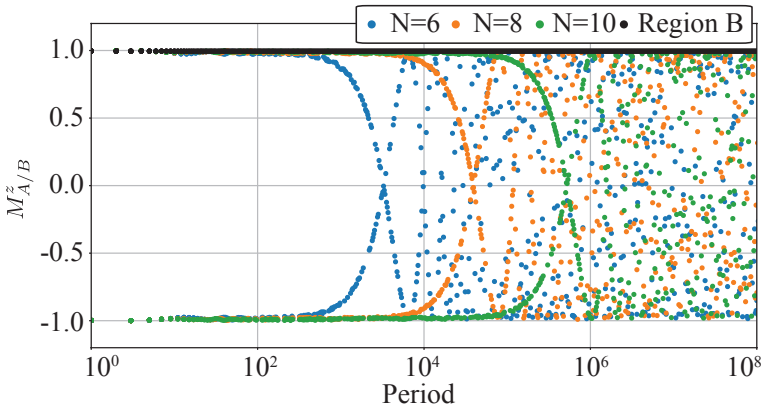

Figure 3.4: The long-time dynamics of regional magnetization $M^z_{A/B}$ for different system sizes $N = 6, 8$ and 10. Here, we have chosen $\epsilon_A = 0.01$, $\epsilon_B = 1$, $J^z_0 T = 0.2$ with $\alpha = 1.51$ and $WT = 0$.

expected, region B exhibits the ferromagnetic phase. When the error ϵ_A is sufficiently small, the effective Hamiltonian Eq. (3.21) is in the ferromagnetic phase and region A clearly shows the sub-harmonic oscillation in the magnetization dynamics with 2T. As a result, two different phases of matter coexist in the same network. Contrary, when the error is large, the sub-harmonic osculation rapidly decays, and consequently, the time crystalline order in region A melts.

To explore the dynamics in more detail, we calculate the stroboscopic dynamics of the regional magnetization defined by,

$$M^z_{A/B}(nT) = \frac{\sum\limits_{l \in A/B} \langle \sigma^z_l(nT) \rangle}{N_{A/B}} \tag{3.25}$$

where $N_{A/B}$ is the number of sites in each region. The results of regional magnetization in long-times with three different error ($\epsilon_A = 0.01, 0.03$ and 0.1) are shown in Fig 3.3 (b). It is clearly shown that the sub-harmonic response in region A becomes more unstable as the error increases. If the error is small, the DTC phase has an exponentially long lifetime. However, as the error increases, the lifetime of the DTC gets smaller, and the DTC phase melts quickly.

In the context of the phases of matter, it is crucial to investigate the long-time dynamics for different system sizes to investigate finite size effects. The results of the regional magnetization for the several sizes $N = 6, 8$ and 10 are shown in Fig 3.4. It is clear that as the system size increases, the DTC becomes more stable and has a longer lifetime.

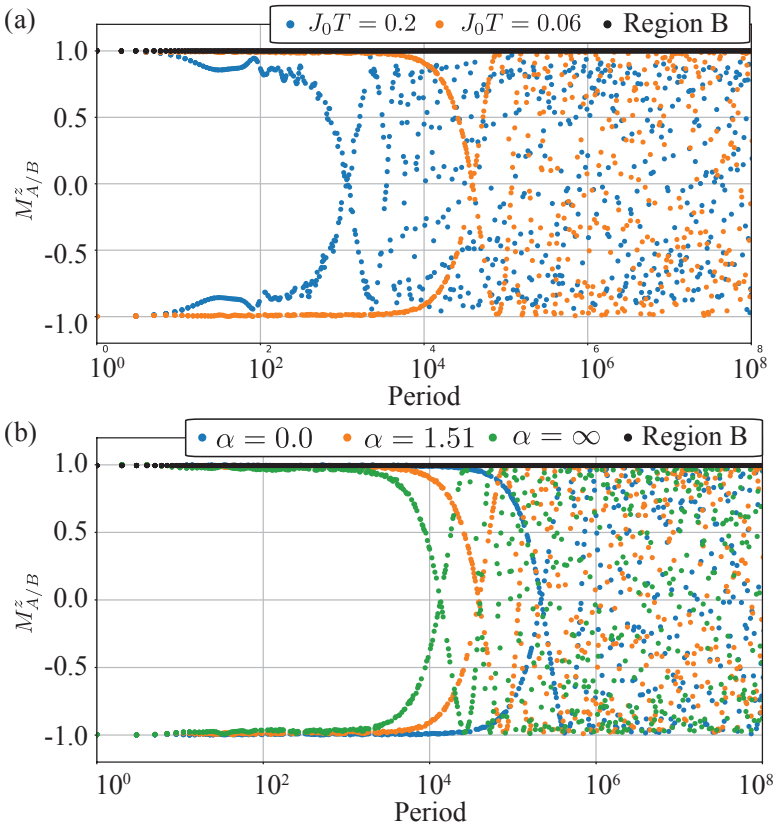

Figure 3.5: (a) shows the long-time dynamics of the regional magnetization $M^z_{A/B}$ for weak ($J^z_0T = 0.06$) and strong ($J^z_0T = 0.1$) interactions . (b) illustrates the long- time dynamics of the regional magnetization $M^z_{A/B}$ for strong interaction with $\alpha = 0, 1.51$ and $\alpha = \infty$. In both panels, we have chosen $\epsilon_A = 0.01$, $\epsilon_B = 1$ and $WT = 0$.

3.4.2.2 Interaction strength (J_0) and its range (α)

Above, we have investigated the resilience of the Chimera DTCs against driving errors. Here, we will see that the manybody effects can stabilize the chimeric DTCs. As the strength of the interaction increases, the parameter δ_x becomes smaller. As a result, we can estimate that the DTC becomes more stable in the strong interaction strength regime. To see its effect, we consider weak interaction ($J^z_0T = 0.06$) and strong interaction ($J^z_0T = 0.2$) cases and Fig 3.5 (a) exhibits local magnetization dynamics at the stroboscopic times in long-times. As we saw in section 3.3.3, as the interaction strength increases, the many-body effect becomes more dominant. As a result, the stroboscopic system tends to preserve the U(1)-symmetry of the many-body interaction. It means that during the time evolution, the system tends to be polarized along the z axis at stroboscopic times. Thus, the chimera

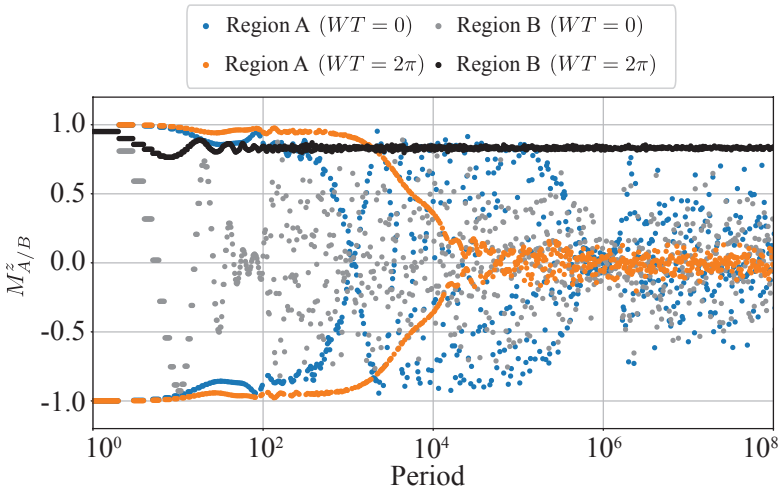

Figure 3.6: Long-time dynamics of regional magnetization $M^z_{A/B}$ for different disorder strengths $WT = 0$ and $WT = 2\pi$. Here, we have chosen driving errors $\epsilon_A = 0.01$, $\epsilon_B = 0.9$ and $J_0T = 0.06$ with $\alpha = 1.51$. The results strongly suggest that the stability of the DTC phase in region A is due to the MBL effect in the weakly coupled spin network.

DTC phase has a longer lifetime, as shown in Fig. 3.5 (a).

As we defined α in section 3.4.1, it effectively determines the connectivity of the spin-network. Thus, one can expect that the critical point shifts depending on α, as similar to that in the Ising model [105]. To see the α effect, we show the long-time dynamics of the regional magnetization for the several connectivity ($\alpha = 0.0, 1.51$, and ∞) in Fig 3.5 (b). Here, $\alpha = 0$ and $\alpha = \infty$ are extreme cases in which the networks are the all-to-all coupling and the nearest-neighbor coupling, respectively. We see that as α decreases, the DTC phase becomes more stable. Furthermore, the result shows that chimera DTC has the longest lifetime for all-to-all coupling ($\alpha = 0$).

3.4.3 Strong disorder ($WT = 2\pi$)

Previously, we have numerically investigated the chimera DTC from the magnetization dynamics of our Chimera DTC in the absence of the diagonal disorder. Now, in the present section, let us investigate the diagonal disorder effect on the chimera DTC. As we discussed in the section 3.3.4, the disorder affects both regions A and B. Thus, we consider regional errors to be $\epsilon_A = 0.03$ and $\epsilon_B = 0.9$ and weakly interacting network ($J_0T = 0.06$). Furthermore, to explore the role of disorder in a systematic way, we compare the magnetization dynamics for the absence of the disorder ($WT = 0$) and the strong disorder $WT = 2\pi$, respectively. Here we employ the same initial state $|\Psi(0)\rangle_z$ as

we used in the previous section.

Fig. 3.6 depicts the regional magnetization of regions A and B without and with the diagonal disorder. Here, for disorder strength $WT = 2\pi$, we take an ensemble average over 100 disorder realizations. In the absence of the disorder and due to the value of the error $\epsilon_B = 0.9$, the spins in region B oscillate with the same frequency in short-time dynamics. Contrary, in the strong disorder regime, magnetization in region B is effectively preserved at stroboscopic times due to the MBL effect. It means that the strong disorder stabilizes the magnetization in region B.

Similarly, the DTC in region A is stabilized by the strong disorder, as shown in Fig. 3.6. To understand the mechanism, let us evaluate the parameter $\langle\overline{\delta_x}\rangle$ for the strong disorder, defined by Eq.(3.24). Because the parameter is the ensemble averaged value, we calculate the ensemble average of $\cos\hat{\Theta}_l$. For simplicity, when we ignore the interactions, we obtain $\Theta_l = 2W_lT_2$, and the ensemble average $\langle\overline{\cos\hat{\Theta}_l}\rangle \sim 0$. As a result, the transverse field in the effective Hamiltonian gets smaller, and the DTC phase in region A becomes stable.

3.5 Chimera phase with quantum information point of view

Previously, we have analytically and numerically seen the chimera phase in the magnetization dynamics. Here, let us investigate the chimera phase from a microscopic perspective by calculating quantum entanglement of the state. In the present model, because of the two different quantum phases coexisting in the same space, let us investigate the entanglement between the two regions. Since the system is a closed system, we employ von Neumann entropy which is used to measure the entanglement of pure states [106, 107]. Here, the entropy between two regions A and B is given by,

$$S_B(t) = -\mathrm{Tr}_B\left[\hat{\rho}_B(t)\mathrm{In}\hat{\rho}_B(t)\right] \tag{3.26}$$

where $\hat{\rho}_B(t) = \mathrm{Tr}_A\left[\hat{\rho}(t)\right]$ is the reduced density matrix of the region B and can get by tracing out the degree of freedom in Region A from the total density matrix $\hat{\rho}(t) = |\Psi(t)\rangle\langle\Psi(t)|$.

3.5.1 Error in initial states and effective interaction suppression and

Previously, we have employed the state fully polarised along z-axis as the initial state $|\Psi(0)\rangle_z = |\Psi(0)\rangle_{\mathrm{A}}\otimes|\Psi(0)\rangle_{\mathrm{B}}$. When $\epsilon_B = 1$, because $\left[\hat{H}_B, \hat{H}^{\text{2T-eff}}_{\epsilon_A,1}\right] = 0$ and $\hat{H}_B|\Psi(0)\rangle_{\mathrm{B}} = E_B|\Psi(0)\rangle_{\mathrm{B}}$, the bipartite entanglement between two regions can not be generated in the dynamics. Therefore, it is impossible to explore the microscopic dynamics via entanglement

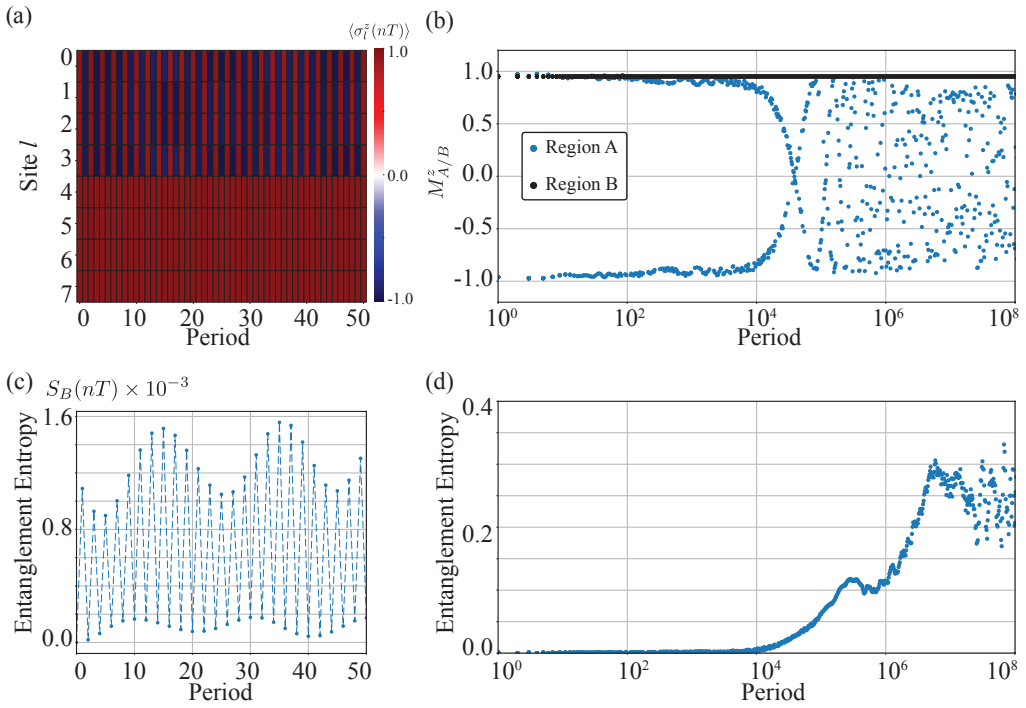

Figure 3.7: (a) and (c) depict the stroboscopic dynamics of the local magnetization $\langle\sigma_l^z(nT)\rangle$ and the entanglement $S_B(nT)$ for the new initial state $|\Psi(0)\rangle_{z,\theta}$ with $\theta = 0.1\pi$. In (b) and (c), we show the long-time dynamics of the regional magnetization $M^z_{A/B}$ and the entanglement entropy. In all panels, we have chosen $\epsilon_A = 0.01$, $\epsilon_B = 1$, $J_0T = 0.2$ with $\alpha = 1.51$ and $WT = 0$.

in the chimeric phase using this initial state.

However, there should always be a small error in the implementation of the initial state in experiments. Thus, here we investigate effect of the error in the initial state preparation to the chimera DTC from the microscopic perspective via entanglement, and we consider a simple model of our initial state as follows,

$$|\Psi(0)\rangle_{z,\theta} = e^{-i\sum_l \frac{\theta}{2}\sigma_l^x}|\Psi(0)\rangle_z \tag{3.27}$$

where θ is the error.

The results of the stroboscopic dynamics of the local magnetization and the entanglement entropy in short times are shown in Fig. 3.7 (a) and (c), respectively. First, the magnetization results indicate that even there is an error in the initial state preparation, as long as region A initially has the non-zero magnetization, its magnetization dynamics shows sub-harmonic oscillation with 2T. As shown in the entanglement dynamics in Fig. 3.7 (c), it seems to indicate that entanglement is low at the even periods and high at

odd periods. Thus, we see that the Floquet operator $\hat{F}$ generates the entanglement between two regions. However, as we saw in section 3.2, the interaction between two regions is strongly suppressed in the effective Hamiltonian associated to the square of the Floquet operator. Indeed, when $\epsilon_A = 0$, two regions are completely decoupled. Consequently, the entanglement entropy between two regions also oscillates with the same period of the magnetization as the entanglement is low at even periods and high at odd periods.

Fig. 3.7 (b) and (d) show the long-time dynamics of the regional magnetization and the entanglement entropy. Despite the error in the initial state preparation, we see that region A shows a stable DTC phase with a long lifetime. The entropy results show that the entanglement generation due to the dynamics is strongly suppressed until a certain long time. It reflects the stable existence of the ordered phases of regions A and B in the macroscopic regime. From a macroscopic point of view, after the DTC phase of region A collapsed, it looks like only region A undergoes a transition into a new quantum phase, e.g., thermal equilibrium. Contrary to this, the phase of matter in Region B remains stable. However, in the macroscopic perspective, as the DTC phase of region A begins to decay, the entropy increases. After the DTC is completely melted, the entropy value saturates and is slightly fluctuating.

3.5.2 Strong disorder ($WT = 2\pi$)

Here, let us see the state dynamics under strong disorder $WT = 2\pi$. To take into account the randomness of the disorder, we consider the ensemble average of the entanglement entropy $\overline{\langle S_B \rangle}$ as similar to the ensemble average of the magnetization, which is defined by,

$$\overline{\langle S_B(t) \rangle} = \frac{1}{N_r} \sum_{r}^{N_r} S_B^{(r)}(t), \tag{3.28}$$

where N_r is the total number of the realizations of disorder and $S_B^{(r)}(t)$, is the von Neumann entropy for a single realization at time t. The entropy is used as the measurement of the bipartite entanglement for the pure state. But, in the case, Eq. (3.28) is an assemble of it. Thus, we note that the ensemble value does not tell us the amount of the entanglement of the state anymore. However, we use it to get the tendency of the entanglement growth.

Here, we consider regional errors to be $\epsilon_A = 0.03$ and $\epsilon_B = 0.9$ and weakly interacting network ($J_0 T = 0.06$) as we used in section 3.4.3. Fig. 3.8 exhibits the ensemble entanglement entropy of the new initial states for different error $\theta = 0, 0.1\pi$ and 0.2π. Similarly to the disorder-free case, while region A shows the DTC phase, the amount of entanglement entropy generation is little for all initial errors (θ). When the DTC phase is melting, the entropy increases until the DTC phase is completely melted. Eventually, the entanglement entropies converge to different values that tend to increases as the error in

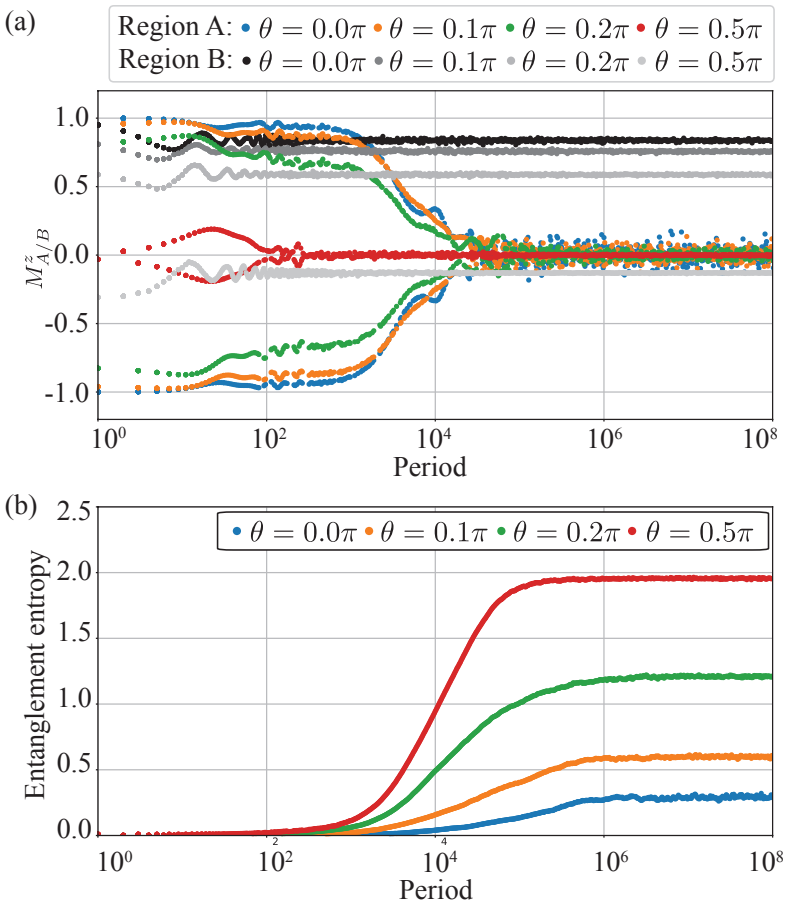

Figure 3.8: Long-time dynamics of ensemble average of the regional magnetization $\langle\overline{M^z_{A/B}}\rangle$ (a) and the ensemble entanglement entropy $\langle\overline{S}\rangle_{\rm B}$ (b) for the new initial state $|\Psi(0)\rangle_{z,\theta}$ with several errors $\theta = 0.0, 0.1\pi, 0.2\pi, 0.5\pi$. In both panels, we have chosen $\epsilon_A = 0.01$, $\epsilon_B = 0.9$, $J_0 T = 0.2$ with $\alpha = 1.51$ and $WT = 2\pi$.

the initial state increases. We will see more details below.

It is important to compare our results with generic thermal and many-body localized states where the ensemble average of the entanglement entropies are predicted to be $\langle\overline{S}\rangle \sim [N \ln 2 - 1]/2 \approx 2.3$ [108] and $\langle\overline{S}\rangle \sim \ln 2 \approx 0.69$ [109], respectively. As we saw, the ensemble entanglement entropy in long times depends on the initial state or the error (θ) in the initial state preparation. When $\theta = 0$, the initial state is the ferromagnetic phase. Thus, in region B, the tunneling time due to the transverse magnetic filed becomes longer. Furthermore, because of strong disorder, the heating due the transition is highly prevented. As a results, the entanglement entropy even after long-times is too small. Contrary, in the presence of the small error $\theta = 0.1\pi$ and 0.2π, ensembles are in between the MBL

and the thermal state. As the initial state of region B approaches the disordered state, the number of ordered states that can be prevented from melting by the MBL effect decreases, so the final ensemble entropy value gets close to the value of thermalization, as shown in the result for $\theta = 0.5\pi$.

3.6 Conclusion

In the present Chapter, we have analytically and numerically investigated a periodically driven spin network under a regional driving. We have shown that quantum phases of matter on the network can be manipulated and demonstrated the chimera DTC in which two different phases of matter stably coexist in the same network. We have also evaluated its entanglement entropy to investigate the chimera phase from a microscopic perspective. Interestingly, in the chimera DTCs, entanglement is highly suppressed despite the long-range interactions over the spin network. It suggests that the chimera state may be used to control sub-networks on a spin network. We believe that our results, in which interactions in the network are strongly suppressed by local driving, will contribute greatly to the design of analog quantum simulators and quantum memories using DTCs.

Chapter 4

XX-DTC and DTC growth

Previously, we investigated the 2T-DTC phase on the periodically driven spin-1/2 network where nodes (spins) are coupled via the ZZ-Ising interactions. In this Chapter, we refer to the 2T-DTCs previously discussed as the **ZZ-DTC** to distinguish the new type of DTC we will introduce in this section. In ZZ-DTC models, the effective Hamiltonian for two periods has a **parity symmetry** (also known as $\mathbb{Z}_2$-Ising symmetry). The symmetry tells us essential information such as the order parameter and plays an essential role in our choice of the initial state to observe the DTC phase on the network. For instance, when the initial state is fully polarized along the z-axis, the magnetization dynamics exhibit a sub-harmonic oscillation with a period that is twice longer than that of the Hamiltonian, which is a clear signature of the 2T-DTC phase.

Besides the $\mathbb{Z}_2$-Ising symmetry, the effective Hamiltonian for two periods has another symmetry called the U(1)-symmetry. As a result, the local longitudinal magnetizations are (quasi-) conserved quantities at the stroboscopic times. Furthermore, that is one of the reasons why one can use magnetization as the order parameter of the 2T-DTC. Importantly, it was experimentally checked using tapped ions [110].

However, there are two types of the U(1)-symmetry, global and local, resulting in total and local magnetization conservation, respectively. In previous studies of (ZZ-) DTCs [33, 110, 3, 38, 4], the difference between the two symmetries was not apparent because the ZZ-interactions have both symmetries. Thus, this Chapter will consider a new spin network breaking the local U(1)-symmetry but having global symmetry.

The present Chapter will show three crucial results on the new network with periodic driving. First, we will show that even when the local U(1)-symmetry is broken in the network, the magnetization dynamics can exhibit stable sub-harmonic oscillation. We show that the global U(1)-symmetry plays an essential role in stabilizing the DTCs.

Next, we will extend our model to the system weakly coupled to an environment. Generally, the noise from the environment destroys the state's purity. Consequently, the

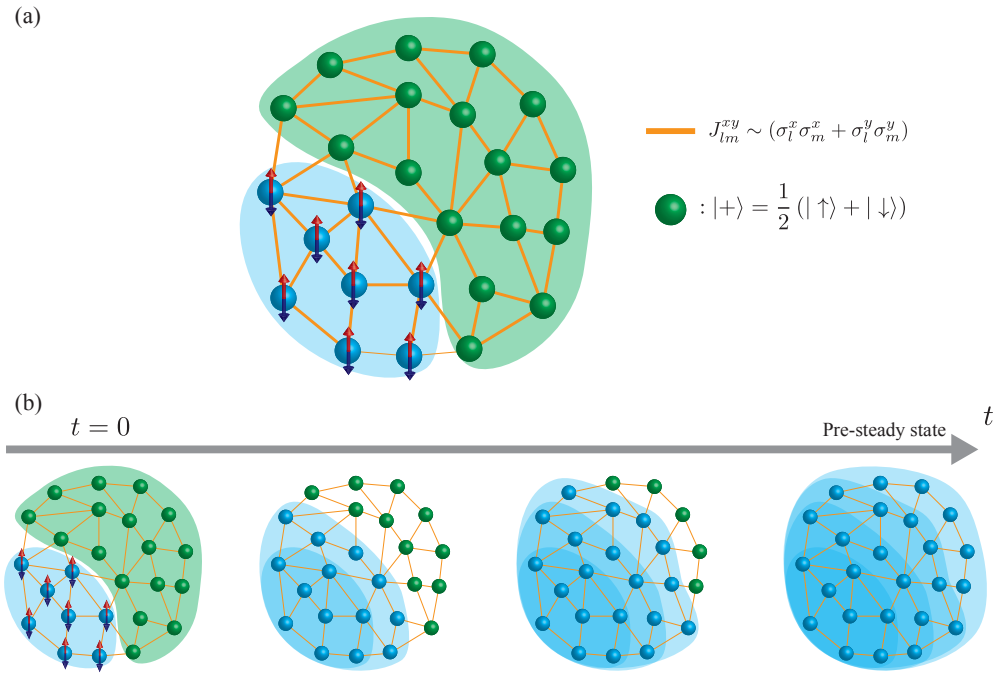

Figure 4.1: (a) Illustrates the initial state we are interested in, and the schematic spin network for our model in which spins are connected via XX-interactions. Our initial state has two regions characterized by different symmetries. The blue region is a state breaking the $\mathbb{Z}_2$-symmetry (parity). Contrary, the green regions is symmetric under the parity. (b) Illustrates the time evolution of the above initial state under our time periodic Hamiltonian (4.1).

phase of matter collapses. However, if we design the system including the environment to have the global U(1)-symmetry, we show that the dissipative system can exhibit the sub-harmonic response with 2T.

Lastly, to see the physics behind the difference between global and local symmetries on the network, we explore the dynamics of a new initial state being in-homogeneous. Specifically, we consider an initial state having two well-defined regions. One of them is prepared in the ferromagnetic state, and the rest is in the para-magnetic state, respectively, as shown in Fig 4.1 (a). Using the initial state, we will show that the DTC can grow, similar to the crystal growth in the space [4]. By comparing the dynamics in the closed system and the system coupled to the environment, we show that the entire system eventually becomes a DTC phase due to the dephasing effect, as illustrated in Fig 4.1 (b).

4.1 Model

As mentioned in the introduction above, this Chapter considers a new periodically driven spin network with N-sites coupling with XX-Ising interactions. Our new time-dependent Hamiltonian with period $T = T_1 + T_2$ is given by,

$$\hat{H}(t) = \begin{cases} H_1 = \hbar g(1-\epsilon)\sum_l \sigma_l^x & (0 \le t < T_1) \\ H_2 = \hbar \sum_{lm} J_{lm}^{xx}\left(\sigma_l^x\sigma_m^x + \sigma_l^y\sigma_m^y\right) + \hbar\sum_l W_l^z\sigma_l^z & (T_1 \le t < T), \end{cases} \tag{4.1}$$

where σ_l^μ with $\mu \in \{x, y, z\}$ are the usual Pauli operators at the l-th site. Since we are interested in the discrete time-translation symmetry breaking, we set g to be $gT_1 = \pi/2$ and a parameter ϵ represents a rotational error, similar to the ZZ-DTC. Importantly, when $\epsilon = 0$, the time evolution of the first Hamiltonian is the same as the parity transformation operator $\hat{X} = \prod_l^N \sigma_l^x$. Next, the coupling J_{lm}^{xx} determines the connectivity of the network between l-th and m-th sites, and W_l^z is the disorder at the l-th site given by the uniform distribution $W_l \in [0, W]$ with the strength of the disorder W.

4.2 Effective Hamiltonian and Symmetry

To investigate the stroboscopic dynamics of the new model, we can apply the Floquet theory to it, similar to the conventional DTCs. In the present section, we will derive the effective Hamiltonian and find its emergent symmetry necessary later. Since we expect our model to show the sub-harmonic oscillation with a period twice longer than the period of the driving, we derive the 2T-effective Hamiltonian.

4.2.1 Trivial case ($\epsilon = 0$ and $W = 0$)

Generally, it is difficult to analytically find the effective Hamiltonian from the Floquet operator with an rotational error ϵ. But as we saw in the ZZ-DTC discussion, one can get some intuition form the the 2T-effective Hamiltonian for the trivial case $\epsilon = 0$. Using Eq.(4.1), the square of the Floquet operator can be written as

$$\begin{aligned} \hat{F}_{\epsilon=0}^2 &= e^{-\frac{i}{\hbar}\hat{H}_2T_2}e^{-\frac{i}{\hbar}\hat{H}_1T_1}e^{-\frac{i}{\hbar}\hat{H}_2T_2}e^{-\frac{i}{\hbar}\hat{H}_1T_1} \\ &= \exp\left[-i\left(\sum_{lm} J_{lm}^{xx}\left(\sigma_l^x\sigma_m^x + \sigma_l^y\sigma_m^y\right) + \sum_l W_l^z\sigma_l^z\right)T_2\right] \\ &\quad \exp\left[-i\left(\sum_{lm} J_{lm}^{xx}\left(\sigma_l^x\sigma_m^x + \sigma_l^y\sigma_m^y\right) - \sum_l W_l^z\sigma_l^z\right)T_2\right] \end{aligned} \tag{4.2}$$

where, we use the fact that the Hamiltonian $\hat{H}_1$ dynamics are same as the perfect π-rotation.

However, unlike the conventional ZZ-DTCs, in this case its difficult to obtain the effective Hamiltonian due to the disorder. Generally, the XX-interaction term and diagonal disorder does not commute with each other,

$$\left[\sum_{lm} J_{lm}^{xx}\left(\sigma_l^x\sigma_m^x+\sigma_l^y\sigma_m^y\right), \sum_l W_l\sigma_l^z\right] = \begin{cases} = 0 & W_l \text{ are } l\text{-independent} \\ \neq 0 & \text{others} \end{cases} \tag{4.3}$$

Thus, to get some intuition or to avoid the difficulty above, we consider the absence of the disorder $W = 0$, and now it is possible to analytically obtained the $2T$-effective Hamiltonian, as follows,

$$\hat{H}^{\text{2T-eff}}_{\epsilon=0,W=0} = \frac{\hbar T_2}{T}\sum_{lm} J_{lm}^{xx}\left(\sigma_l^x\sigma_m^x+\sigma_l^y\sigma_m^y\right) \tag{4.4}$$

where we user $\hat{H}^{\text{2T-eff}} = i\hbar\ln(\hat{F}^2)/2T$. Here, the above Hamiltonian breaks local U(1)-symmetry, as expected. Thus, the local magnetization is no longer a conserved quantity at the stroboscopic times. However, it is still invariant under the global U(1)-symmetry, giving the total magnetization conservation. Next, as similar to ZZ-DTCs, the above Hamiltonian has the $\mathbb{Z}_2$-Ising symmetry (more precisely, it is invariant under the transformation $\sigma_l^x \to \sigma_l^x$, $\sigma_l^y \to -\sigma_l^y$ and $\sigma_l^z \to -\sigma_l^z$).

4.2.2 Presence of the small error ($\epsilon \ll 1$)

Next, to see the rotational error effect, let us consider a small error $\epsilon \ll 1$. By treating the error as a perturbation, one can approximately obtain the effective Hamiltonian, as follows,

$$\hat{H}^{\text{2T-eff}}_{\epsilon,W=0} \approx \frac{\hbar}{2}\sum_{lm} J_{lm}^{xx}\left(\sigma_l^x\sigma_m^x+\sigma_l^y\sigma_m^y\right) + \frac{\epsilon\pi\hbar}{4}\sum_{l\neq m} J_{lm}^{xx}\sigma_l^z\sigma_m^y - \frac{\epsilon\pi\hbar}{2}\sum_l \sigma_l^x, \tag{4.5}$$

where we take the first order of the Baker-Campbell-Hausdorff formula [111]. Remarkably, despite the imperfect π-rotation, the above Hamiltonian (approximately) has the $\mathbb{Z}_2$-Ising symmetry.

4.3 XX-DTCs in closed systems

Previously, we have derived the 2T-effective Hamiltonian in the previous section and seen the emergence of the $\mathbb{Z}_2$-Ising symmetry. The present section analytically and numerically

investigates the stroboscopic dynamics of magnetization. We will show that our model can exhibit a sub-harmonic oscillation with $2T$, similar to the ZZ-DTCs.

Similar to the previous section, we first consider the typical case. We then investigate the case where there is an error in the rotational pulse and see the Robustness of the sub-harmonic response.

4.3.1 Trivial case ($\epsilon = 0$ and $W = 0$)

The emergence of the parity symmetry at periodic times tells us an order parameter and a choice of initial states to get the 2T-DTC phase on the new network. Hence, It is natural to consider local magnetization dynamics $\sigma_l^z(nT)$ as an order parameter of the DTC phase and a state breaking the parity symmetry as an initial state, similar to ZZ-DTCs.

Thus, let us consider an initial state $\hat{\rho}(0) = |\Psi(0)\rangle\langle\Psi(0)|$ breaking the parity and see its local magnetization dynamics. The local magnetization at even periods $t = 2nT$ is given by

$$\begin{aligned}\langle\sigma_l^z(2nT)\rangle &= \mathrm{Tr}\left(\hat{F}^{2n}\hat{\rho}(0)(\hat{F}^{2n})^\dagger\sigma_l^z\right) \\ &= \mathrm{Tr}\left(\hat{\rho}(2nT)\sigma_l^z\right).\end{aligned} \tag{4.6}$$

Similarly, at odd periods $(t = (2n+1)T)$, it is given by,

$$\begin{aligned}\langle\sigma_l^z((2n+1)T)\rangle &= \mathrm{Tr}\left(\hat{F}^{2n+1}\hat{\rho}(0)(\hat{F}^{2n+1})^\dagger\sigma_l^z\right) \\ &= \mathrm{Tr}\left(\hat{\rho}(2nT)F^\dagger\sigma_l^z\hat{F}\right) \\ &= -\mathrm{Tr}\left(\hat{\rho}(2nT)e^{\frac{i}{\hbar}\hat{H}_2T_2}\sigma_l^z e^{-\frac{i}{\hbar}\hat{H}_2T_2}\right)\end{aligned} \tag{4.7}$$

Now, unlike the ZZ-DTCs, because our network breaks the local U(1)-symmetry, $[\hat{H}_2, \sigma_l^z] \neq 0$, and in general,

$$\langle\sigma_l^z\left((2n+1)T\right)\rangle \neq -\langle\sigma_l^z((2n)T\rangle \tag{4.8}$$

Consequently, in the new model, the local magnetizations can not be used as the order parameter to see the 2T-DTC.

However, because of the global U(1)-symmetry in the new network, the total magnetization is preserved, $[\hat{H}_2, \sum_l \sigma_l^z] = 0$. Thus, the total magnetization $M(t) = \sum_l\langle\sigma_l^z(t)\rangle/N$ at odd and even periods satisfies,

$$M\left((2n+1)T\right) = -M\left(2nT\right) \tag{4.9}$$

It indicates that the total magnetization can be used as the order parameter of the new model.

Here, we note that when the initial state has is fully polarized along the z-axis such as $|\Psi(0)\rangle = |00\cdots0\rangle$, then the local magnetization satisfies,

$$\langle\sigma_l^z((2n+1)T)\rangle = -\langle\sigma_l^z(2nT)\rangle, \tag{4.10}$$

due to the magnetization conservation. It means that we can still use the local magnetization as the order parameter as long as the initial state is homogeneous, similar to the ZZ-DTCs. To distinguish it from the conventional ZZ-DTCs, we refer to the new one as the **XX-DTC**.

4.3.2 In the presence of the small error ($\epsilon \ll 1$)

Now, let us see our system in the presence of the small error to demonstrate that it shows the 2T-DTC phase. Similar to the absence of the error, the total magnetization at the even period can be given by,

$$\begin{aligned} M(2nT) &= \frac{1}{N}\mathrm{Tr}\left(\hat{F}_{\epsilon,W=0}^{2n}\,\hat{\rho}(0)(\hat{F}_{\epsilon,W=0}^{2n})^\dagger\sum_l\sigma_l^z\right) \\ &= \frac{1}{N}\mathrm{Tr}\left(\hat{\rho}(2nT)\sum_l\sigma_l^z\right) \\ &\approx \frac{1}{N}\mathrm{Tr}\left(\hat{\rho}_{\mathrm{pre}}\sum_l\sigma_l^z\right) \end{aligned} \tag{4.11}$$

Here, we expect that after a certain time (the characteristic time associated to the prethermal state) [54], the state reaches the thermal state of $\hat{H}_{\epsilon,W=0}^{\text{2T-eff}}$ as similar to the conventional ZZ-DTCs. Thus, the macroscopic observables of the system after the certain time can be given by the thermal state $\hat{\bar{\rho}}_{\mathrm{pre}}$.

Next, at the odd periods, the expectation value can be written, as follows,

$$\begin{aligned} M\left((2n+1)T\right) &= \frac{1}{N}\mathrm{Tr}\left(\hat{F}_{\epsilon,W=0}^{2n+1}\hat{\rho}(0)(\hat{F}_{\epsilon,W=0}^{2n+1})^\dagger\sum_l\sigma_l^z\right) \\ &= \frac{1}{N}\mathrm{Tr}\left(e^{-\frac{i}{\hbar}\hat{H}_{\epsilon,W=0}^{\text{2T-eff}}T}\hat{\rho}(2nT)e^{\frac{i}{\hbar}\hat{H}_{\epsilon,W=0}^{\text{2T-eff}}T}\hat{F}\sum_l\sigma_l^z\hat{F}^\dagger\right) \\ &\approx -M(2nT), \end{aligned} \tag{4.12}$$

where we used $\hat{F}\sum_l\sigma_l^z\hat{F}^\dagger \approx -\sum_l\sigma_l^z$. The above result indicates that, even there is the small error in the rotation, our network sill exhibits the sub-harmonic oscillation in the magnetization dynamics. Thus, the network is in the DTC phase.

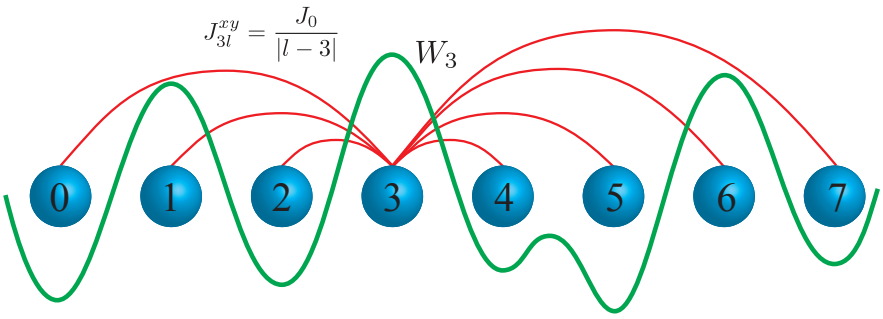

Figure 4.2: (a) Illustrates the one-dimensional arranged spin chain used in the numerical calculation to simulate our model. To account for the complexity of the network, we consider a long-range interaction $J_{lm}^{xx} = \frac{J_0}{|l-m|^\alpha}$ with the coupling strength J_0 and the decay rate α. Later this Chapter, we couple the system with a Markovian environment giving the dephasing effect.

4.3.3 Disorder effect

Now, let us consider the disorder effect. In the trivial case ($\epsilon = 0$), we still get the 2T-oscillation in the magnetization dynamics because the disorder is diagonal. Next, if ϵ is non-zero because the diagonal disorder does not commute with the XX-interaction, it leads to the additional terms in the effective Hamiltonian. Consequently, the effective Hamiltonian is no longer invariant under parity. Nevertheless, the disorder effect that appears in the effective Hamiltonian should be proportional to the error ϵ and the difference $(W_i - W_j)$ between the values of the disorder at different sites i-th and j-th sites. Thus, when the error is small enough ($\epsilon \ll 1$), and the disorder is not too strong, one can observe a stable DTC phase.

4.4 Numerical experiments of closed XX-DTCs

Previously, we have analytically seen that our network exhibits the sub-harmonic response in the stroboscopic dynamics of the magnetization and shown that it is the DTC phase. Here, we numerically evaluate XX-DTC by looking at the magnetization dynamics at the stroboscopic times $t = nT$.

4.4.1 Parameter setting

To investigate the dynamics numerically, we employ the simple spin network in which spins are arranged in a one-dimensional chain shown in Fig. 4.2 as an example. We set the

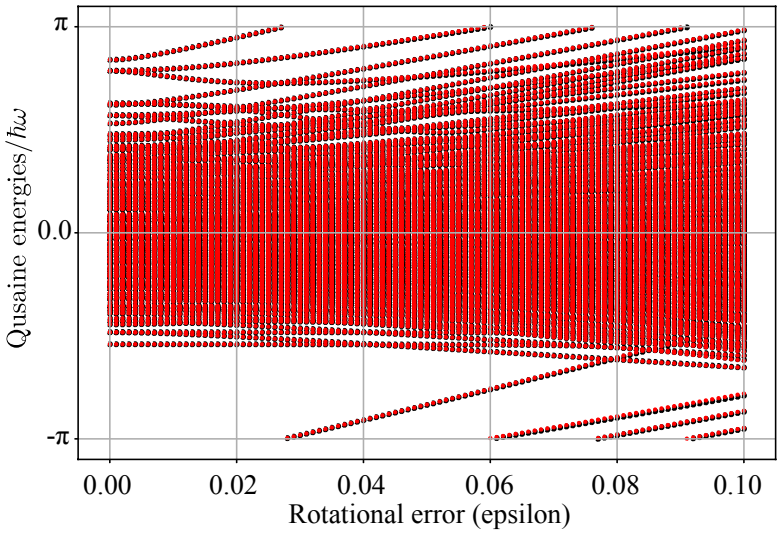

Figure 4.3: Depicts the quasienergy spectrum as a function of the rotational error ϵ for a chain with $N = 8$. The red and black dots represent analytical and numerical results, respectively. The analytical quasienergies are obtained from the approximate $2T$-effective Hamiltonian (4.5). We set $J_0T/2\pi = 0.2$ with $\alpha = 1.51$ and $WT/2\pi = 0$.

coupling between spins to be $J^{xx}_{lm} = J_0/|l-m|^\alpha$ where indexes l and m indicate the sites. Here, J_0 and α are the strength and range of the spin-spin interaction, respectively. The parameter α can be chosen between 0 to ∞ and produce various networks, e.g., a network with coupling between nearest neighbors ($\alpha = \infty$) and the fully connected network ($\alpha = 0$). Here, we choose $\alpha = 1.51$, an experimentally used value in trapped ions [2] and NV-centers in diamonds at room temperature [3], giving long-range interactions across the entire network.

4.4.2 Qusi-energy spectrum

Because we proposed a new DTC model and derive its effective Hamiltonian using the Baker-Campbell Hausdorff formula, it is important to check the quality of the approximation. Thus to evaluate the approximate effective Hamiltonian, we numerically calculated the quasi-energies of the square of the Floquet operator ($\hat{F}^2$), giving the $2T$-effective Hamiltonian. Because the eigenvalues and eigenstates of the Floquet operator can represent the stroboscopic dynamics of any state, we believe that it is sufficient to study the effect of approximation on them. Here, the quasienergies $-\hbar\pi/T < \epsilon_l < \hbar\pi/T$ are

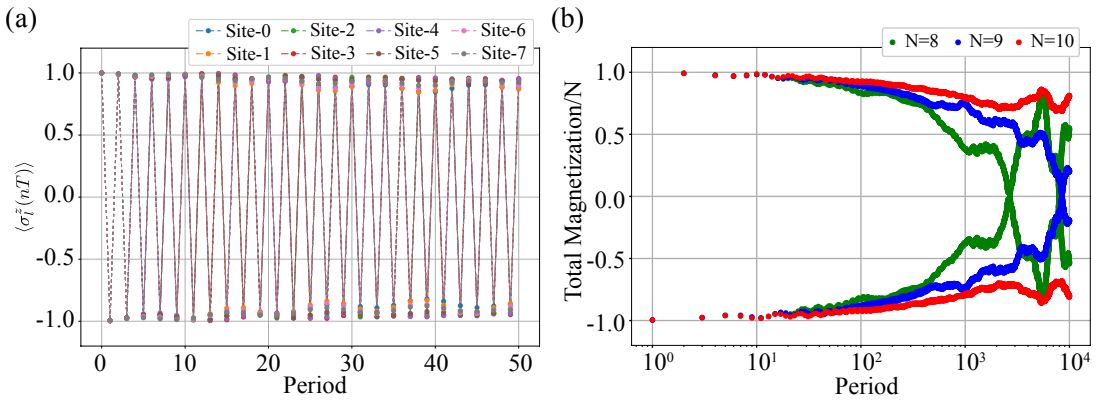

Figure 4.4: (a) Depicts the stroboscopic dynamics of the local magnetization $\langle\sigma_l^z(nT)\rangle$ with $N = 8$ sites in short periods. (b) Shows the stroboscopic dynamics of the scaled total magnetization, $M_z = \sum_l\langle\sigma_l^z(nT)\rangle/N$ for the several sizes $N = 8, 9$ and 10. Here, we have set $\epsilon = 0.03$, $J_0T/(2\pi) = 0.2$ with $\alpha = 1.51$ and $WT/(2\pi) = 0$.

eigenvalues of the Floquet operator, as follows,

$$\hat{F}^2|\Phi_l\rangle = e^{-i\epsilon_l(2T)/\hbar}|\Phi_l\rangle, \tag{4.13}$$

where $|\Phi_l\rangle$ is a corresponding eigenstate.

Fig. 4.3 shows a quasi-energy with different rotational errors ranging from 0 to 0.1. It indicates that when the rotational error is small ($\epsilon \leq 0.04$), the approximate Hamiltonian is sufficiently accurate to obtain the dynamics of the original Hamiltonian. As the error increases, the displacement between the red and black dots is bigger. However, our approximation remarkably works well even at the large error $\epsilon \sim 0.1$.

4.4.3 Stroboscopic dynamics of magnetization

Now, let us see the stroboscopic dynamics of the magnetizations. We employ an initial state $|\Psi(0)\rangle = |00\cdots0\rangle$ that breaks the parity symmetry. First, we see the dynamics in early periods to see its oscillation with $2T$ and check its robustness to the rotational error $\epsilon = 0.03$. As shown in Fig. 4.4 (a), even when there is a small error in the rotation, the local magnetization still shows the sub-harmonic oscillation with $2T$, similarly to that of the ZZ-DTC.

Next, we calculate the magnetization dynamics with different system sizes to see the size effect. Fig. 4.4 (b) shows the time evolution of the normalized total magnetization at long times for different system sizes $N = 8, 9$ and 10. The result means that as the system size increases, the two-period oscillation of the magnetization becomes more stable, or

there is the size effect. Thus, these results show that even in the spin network coupled via the XX-interactions, there is a stable DTC phase in the region where ϵ is small.

4.5 Dissipative XX-DTCs

We have seen that network dynamics should preserve the parity ($\mathbb{Z}_2$-Ising symmetry) and the global U(1)-symmetry at the stroboscopic times to get the stable DTC phase. Recently, the stability of the DTCs under coupling to an external has been investigated theoretically [112, 94, 113, 114, 115] and experimentally [116]. Thus this section extends our XX-DTC model to the system interacting with a Markovian environment [117]. Furthermore, by looking at the symmetry of the entire system, including the environment, we will show that it exhibits stable sub-harmonic oscillation even though our model is affected by the environment.

4.5.1 Lindblad Equation for XX-DTCs

Since we are interested in the system interacting with the environment, we use the density matrix $\hat{\rho}(t)$ of the system rather than the state $|\Psi(t)\rangle$ of the system. In the case, the dynamics of the system can be represented by the Lindblad equation [118, 119], as follows,

$$\begin{aligned}\frac{d}{dt}\hat{\rho}(t) &= -\frac{i}{\hbar}\left[\hat{H}(t), \hat{\rho}(t)\right] + \hat{\mathcal{D}}[\hat{\rho}(t)] \\ &= \hat{\mathcal{L}}\left[\hat{\rho}(t)\right]\end{aligned} \tag{4.14}$$

where $\mathcal{D}[\hat{\rho}(t)]$ is the dissipative term due to the environment, and $\hat{\mathcal{L}}[\cdot]$ is the Liouvillian operator of the system. See Appendix D for details of the dissipative terms in quantum and spin systems coupled to environmental systems.

4.5.2 Symmetry in dissipative systems

In general, the dissipative effect ($\hat{\mathcal{D}}$) or the environment effect are treated as noise that breaks the quantum state of a closed system ($\hat{H}$). However, in our work, we take a different approach in which we extend the symmetry determining the phase of matter of the closed system governed by $\hat{H}$ to that of the dissipative system, including the environment, which is generated by $\hat{\mathcal{L}}$. In other words, we try to define the phase of matter of the dissipative system based on the symmetry of the total system. Specifically, we require the reservoir to have the exact symmetry of the $2T$-effective Hamiltonian at $\epsilon = 0$, and as a result,

we expect that the dissipative network can exhibit the sub-harmonic response with 2T at longer periods.

Thus, let us discuss the symmetry in the dissipative systems in this section. To understand the symmetry of the system governed by the Lindblad equation, we use the super-operator formalism, in which the equation can be written as,

$$\frac{d}{dt}|\hat{\rho}(t)\rangle\rangle = \hat{\hat{\mathcal{L}}}|\hat{\rho}(t)\rangle\rangle, \tag{4.15}$$

where $|\hat{\rho}\rangle\rangle$ is the vector form of the density matrix in the extended Hilbert space $\mathcal{H}\otimes\mathcal{H}$. More details are explained in the Appendix D.4. In this formalism, one can treat the dynamics of the density matrix in a similar way to that of the state in closed system.

Let us extend the symmetry in a closed system to dissipative systems using super-operator formalism [118, 119]. We assume that a system $\hat{H}$ is invariant under the symmetry $\hat{S}$, as follows,

$$\hat{S}^\dagger \hat{H} \hat{S} = \hat{H}. \tag{4.16}$$

Now, in the super-operator formalism, the Liouvillian operator $\hat{\hat{\mathcal{L}}}_{\text{Uni}}$ associated to the unitary dynamics governed by the Hamiltonian $\hat{H}$ is give by,

$$i\hbar\hat{\hat{\mathcal{L}}}_{\text{Uni}} = \hat{H}\otimes\hat{\mathbb{I}}_{2^N} - \hat{\mathbb{I}}_{2^N}\otimes\hat{H}^T, \tag{4.17}$$

where $\hat{H}^T$ is the transpose of $\hat{H}$, and $\mathbb{I}_N$ is the $2^N\times 2^N$-dimensional identity operator.

Then the symmetry transformation in closed systems can be extended in the super-operator formalism, as follows,

$$\begin{aligned} i\hbar\hat{\hat{\mathcal{L}}}_{\text{Uni}} &= \hat{H}\otimes\hat{\mathbb{I}}_{2^N} - \hat{\mathbb{I}}_{2^N}\otimes\hat{H}^T \\ &= \left(\hat{S}^\dagger\hat{H}\hat{S}\right)\otimes\hat{\mathbb{I}}_{2^N} - \hat{\mathbb{I}}_{2^N}\otimes\left(\hat{S}^\dagger\hat{H}\hat{S}\right)^T \\ &= \left(\hat{S}^\dagger H S\right)\otimes\hat{\mathbb{I}}_{2^N} - \hat{\mathbb{I}}_{2^N}\otimes\left(\hat{S}^T\hat{H}^T\hat{S}^*\right) \\ &= \hat{\hat{\mathcal{S}}}^\dagger(\hat{H}\otimes\hat{\mathbb{I}}_{2^N} - \hat{\mathbb{I}}_{2^N}\otimes\hat{H}^T)\hat{\hat{\mathcal{S}}} \\ &= \hat{\hat{\mathcal{S}}}^\dagger\left(i\hbar\hat{\hat{\mathcal{L}}}_{\text{Uni}}\right)\hat{\hat{\mathcal{S}}}. \end{aligned} \tag{4.18}$$

From the above, we see that the symmetry operator in the super-operator formalism can be given by

$$\hat{\hat{\mathcal{S}}} = \hat{S}\otimes\hat{S}^* \tag{4.19}$$

where $\hat{S}^*$ is the complex conjugate of $\hat{S}$ [120, 121, 122].

Now, we extend the above notation to a dissipative system. It means that when the total

system, including an environment, has the symmetry, its Liouvillian operator $\hat{\hat{\mathcal{L}}}$ should be invariant under the symmetric transition, as follows,

$$\hat{\hat{\mathcal{S}}}^{\dagger}\hat{\hat{\mathcal{L}}}\hat{\hat{\mathcal{S}}} = \hat{\hat{\mathcal{L}}}. \tag{4.20}$$

Here, note that we assume that this Liouvillian operator has both unitary and dissipative terms. More details of the symmetry and corresponding conserved quantities in the open system, including the dissipative systems, are discussed in Ref. [122].

4.5.3 Dephasing effect

From the analysis of closed systems, we have seen that the global U(1)-symmetry and $\mathbb{Z}_2$-Ising symmetry are essential for the DTC to be stable. Now, to get a stable DTC under the environmental effect, we extend these two symmetries to the total system, including the environment. Here, in the dissipative system, these symmetries are represented by the super-operator formalism as follows,

$$\begin{aligned} \hat{\hat{\mathcal{U}}}_{\theta} &= \hat{U}_{\theta} \otimes \hat{U}_{\theta}^{*} \\ \hat{\hat{\mathcal{X}}} &= \hat{X} \otimes \hat{X}^{*} \end{aligned} \tag{4.21}$$

where $\hat{U}_{\theta} = e^{-i\theta\sum_l \sigma_l^z}$ with a global phase θ and $\hat{X}$ are the global U(1)-symmetry and $\mathbb{Z}_2$-Ising symmetry operators in the closed systems.

The most straightforward candidate of a dissipative term with $U(1)$-symmetry would be an interaction in the Pauli matrix along the z-axis (σ_l^z). Thus, one of the simple is the dephasing effect given by,

$$\hat{\mathcal{D}}[\hat{\rho}(t)]_{\text{deph}} = \sum_l \left[\gamma_l \sigma_l^z \hat{\rho}(t) \sigma_l^z - \hat{\rho}(t)\right], \tag{4.22}$$

with the site-dependent dephasing strength γ_l. In this work, we consider the site-independent strength $\gamma_l = \gamma$. Now, in the super-operator formalism, the dissipator of Eq. (4.14) can be written by,

$$\hat{\hat{\mathcal{D}}}_{\text{deph}} = \frac{\gamma}{2}\sum_l \left(\sigma_l{}^z \otimes \sigma_l{}^z - \hat{\mathbb{I}}_{2^N} \otimes \hat{\mathbb{I}}_{2^N}\right) \tag{4.23}$$

Remarkably, the dephasing term has the $\mathbb{Z}_2$-Ising symmetry and the U(1)- symmetry defined by Eq. (4.21), as we required. Furthermore, we note that in many solid-state quantum systems, dephasing is the dominant dissipative factor.

4.5.4 XX-DTCs with dephasing effect

Now, let us see the XX-DTC on the dephasing network. Our total Liouvillian is given by,

$$\hat{\mathcal{L}}_t\hat{\rho}(t) = -\frac{i}{\hbar}[\hat{H}(t), \hat{\rho}(t)] + \mathcal{D}[\hat{\rho}(t)]_{\text{deph}}, \tag{4.24}$$

where $\hat{H}(t)$ is the Hamiltonian (4.1). Here, the subscript of $\hat{\mathcal{L}}_t$ means time-dependent of the Liouvillian due to the that of our Hamiltonian. Correspondingly, the Liouvillian super-operator $\hat{\hat{L}}_t$ is given by,

$$\hat{\hat{L}}_t = -\frac{i}{\hbar}\left\{\hat{H}(t)\otimes\hat{\mathbb{I}}_{2^N} - \hat{\mathbb{I}}_{2^N}\otimes\left(\hat{H}(t)\right)^T\right\} + \gamma\sum_l\left(\sigma_l^z\otimes\sigma_l^z - \hat{\mathbb{I}}_{2^N}\otimes\hat{\mathbb{I}}_{2^N}\right). \tag{4.25}$$

Here, we note that since our Hamiltonian is time periodic, thus our Liouvillian super-operator shows the same periodicity $\hat{\hat{\mathcal{L}}}_t = \hat{\hat{\mathcal{L}}}_{t+T}$. As a result, one can apply the Floquet theory to the dissipative system to understand the dynamics at the stroboscopic times. The dissipative dynamics is generated by the dynamical map $\hat{\hat{\Phi}}_T$ associated with the period T,

$$\hat{\hat{\Phi}}_T = \overleftarrow{\mathcal{T}} e^{\int_0^T \hat{\hat{\mathcal{L}}}_\tau d\tau} = e^{\hat{\hat{\mathcal{L}}}_T^{\text{eff}}T}, \tag{4.26}$$

where $\hat{\hat{\mathcal{L}}}_T^{\text{eff}}$ is referred to as the effective Liouvillian super-operator giving the dynamics at the stroboscopic times. More details on the Floquet theory for the dissipative systems are discussed in the Appendix D.5

Before considering the dynamics, here we assume that during the spin rotation $\hat{H}_1$, the dephasing effect can be neglected. We believe the assumption is acceptable because in many experiments the pulse can be applied in short time which is much smaller than the time scale of the dephasing. Thus, now, the time-dependent Liouvillian super-operator can be written as,

$$\hat{\hat{\mathcal{L}}}_t = \begin{cases} \hat{\hat{\mathcal{L}}}_1 = -\frac{i}{\hbar}\left(\hat{H}_1\otimes\hat{\mathbb{I}}_{2^N} - \hat{\mathbb{I}}_{2^N}\otimes\hat{H}_1^T\right) & 0 \le t < T_1 \\ \hat{\hat{\mathcal{L}}}_2 = -\frac{i}{\hbar}\left(\hat{H}_2\otimes\hat{\mathbb{I}}_{2^N} - \hat{\mathbb{I}}_{2^N}\otimes\hat{H}_2^T\right) + \gamma\sum_l\left(\sigma_l^z\otimes\sigma_l^z - \hat{\mathbb{I}}_{2^{(2N)}}\right) & T_1 \le t < T \end{cases} \tag{4.27}$$

where, $\hat{\mathbb{I}}_{2^{(2N)}} = \hat{\mathbb{I}}_{2^N}\otimes\hat{\mathbb{I}}_{2^N}$. Remarkably, remarkably the dynamical map generated by $\hat{\hat{\mathcal{L}}}_1$ corresponds to the super-operator ssociated to the spin flip operator defined in Eq. (4.21), as follows,

$$\hat{\hat{\Phi}}_1 = e^{\hat{\hat{\mathcal{L}}}_1 T_1} = e^{-i\left(\hat{H}_1\otimes\hat{\mathbb{I}}_{2^N} - \hat{\mathbb{I}}_{2^N}\otimes\hat{H}_1^T\right)} = \hat{X}\otimes\hat{X}^* \tag{4.28}$$

where we used $\left[\hat{H}_1 \otimes \hat{\mathbb{I}}_{2^N}, \hat{\mathbb{I}}_{2^N} \otimes \hat{H}_1^T\right] = 0$.

4.5.5 Sub-harmonic oscillations with the dephasing effect

Now, similarly to the DTC in the closed system, we use the Floquet theory to investigate the dynamics at the stroboscopic times. Given the double periodicity of the DTC, let us find the effective Liouvillian super operator $\hat{\hat{\mathcal{L}}}^{\text{2T-eff}}$ associated to the dynamical map $\hat{\hat{\Phi}}_T^2$ for $2T$. As a result, in the absence of rotation error $\epsilon = 0$, one can get the effective Liouvillian for $2T$, as follows,

$$\hat{\hat{\mathcal{L}}}^{\text{2T-eff}}_{\epsilon=0} = -\frac{i}{\hbar}\left\{\hat{H}^{\text{2T-eff}}_{\epsilon=0} \otimes \hat{\mathbb{I}}_{2^N} - \hat{\mathbb{I}}_{2^N} \otimes \left(\hat{H}^{\text{2T-eff}}_{\epsilon=0}\right)^T\right\} + \frac{\gamma}{2}\sum_l \left({\sigma_l}^z \otimes {\sigma_l}^z - \hat{\mathbb{I}}_{2^{2N}}\right). \quad (4.29)$$

This Liouvillian operator is invariant under both the global U(1)-symmetry and $\mathbb{Z}_2$-Ising symmetry. As a result, the dissipative system preserves the magnetization at times $t = 2nT$,

$$\left[\hat{\hat{\Phi}}_T^{2n}, \hat{\hat{\mathcal{M}}}\right] = 0, \quad (4.30)$$

where $\hat{\hat{\mathcal{M}}}$ is the super-operator corresponding to the total magnetization $\hat{M} = \sum_l \sigma_l^z$ [123].

Now, steady states $|\hat{\rho}_{\mathbf{m}}\rangle\rangle$ and $|\hat{\rho}_{-\mathbf{m}}\rangle\rangle$ are fully polarized state along the z-axis, as follows,

$$\hat{\rho}_{\mathbf{m}} = |00\cdots0\rangle\langle00\cdots0|, \quad \hat{\rho}_{-\mathbf{m}} = |11\cdots1\rangle\langle11\cdots1|, \quad (4.31)$$

whose total magnetization are N and $-N$, respectively [123]. This is very similar to the behavior of ZZ-DTC and XX-DTC in closed systems. Here, at times T the operator given in Eq. (4.28) maps the state $\hat{\rho}_{\mathbf{m}}$ to $\hat{\rho}_{-\mathbf{m}}$ and vice versa. As a result, when the initial state is either $|\hat{\rho}_{\mathbf{m}}\rangle\rangle$ and $|\hat{\rho}_{-\mathbf{m}}\rangle\rangle$, then its magnetization dynamics exhibits a sub-harmonic oscillation with period 2T similarly to the XX-DTC in the closed system.

Next, even in the presence of a small error in the rotation, since the effective Hamiltonian still has the parity ($\mathbb{Z}_2$) Ising symmetry and the global U(1)-symmetry as we saw in the previous section, one can observe the DTC phase for longer periods. However, the error also affects the dephasing term, and it induces a new dissipative term breaking these symmetries. Consequently, the error destroys the some symmetries and the state gradually explores all the symmetry multiplets reaches a completely mixed state.

4.5.6 Numerical experiments of XX-DTCs with dephaing

Lastly, let us numerically investigate the XX-DTC under the dephasing. Previously, we have considered the $N = 8$ model with a rotation error $\epsilon = 0.03$ to see the DTC phase rigidity against the error. In the closed system, its computational space is $2^N = 2^8 = 256$.

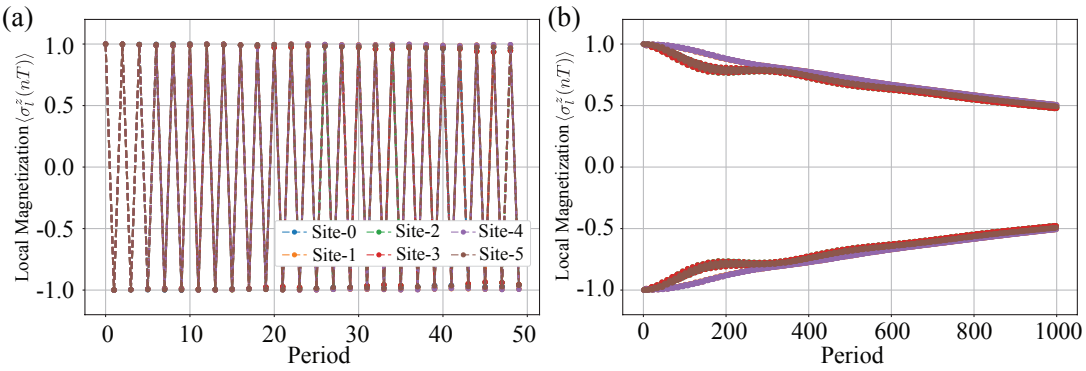

Figure 4.5: (a) Shows the stroboscopic dynamics of the local magnetization $\langle\sigma_l^z(nT)\rangle$ for $N = 6$ sites under the dephasing rate $\gamma T = 0.02$ in short periods. (b) Illustrates the long-time dynamics of the total magnetization, $M_z = \sum_l \langle\sigma_l^z(nT)\rangle/N$ in longer periods. Here, we have set $\epsilon = 0.01$, $J_0 T/(2\pi) = 0.2$ with $\alpha = 1.51$ and $WT/(2\pi) = 0$.

However, in the Liouvillian dynamics, because we use the super-operator formalism, we need more computational space, approximately $2^{2N} = 2^{2\times 8} \sim 7.0 \times 10^5$ which is the same as that of 16-sites in the closed system. Our purpose is to investigate a macroscopically accessible quantity such as the magnetization dynamics from the microscopic point of view. We also believe that the results of small systems can provide some understanding of the behavior of macroscopic physical quantities in large systems. Thus, in our calculation, we employ a small system with $N = 6$ sites to explore dynamical properties and correspondingly consider a small error $\epsilon = 0.01$ to see its robustness.

Now, Fig. 4.5 shows the local magnetization dynamics for the initial state $|\Psi(0)\rangle = |00\cdots0\rangle$ under the dephasing effect $\gamma T = 0.02$ with the rotational error $\epsilon = 0.01$. The leftmost panel in Fig. 4.5 indicates that magnetization dynamics show sub-harmonic oscillation with 2T in the short periods even in the presence of the rotational error and dephasing effect similarly to the XX-DTC in the closed system. Due to the rotational error resulting in the global U(1)-symmetry breaking at the longer periods, the DTC phase gradually melts. However, the sub-harmonic response survives, even at the longer periods ($n \sim 10^3$), which is much longer than the dephasing time scale $1/\gamma \sim 10^2$, as shown in Fig. 4.5 (b).

4.6 DTC Growth (DTCG)

In the previous section, we have seen that the DTC phase could appear on the new network breaking the local U(1)-symmetry. Our result means that as long as a spin network (approximately) preserves the global U(1)-symmetry at the stroboscopic times,

the networks could exhibit stable sub-harmonic oscillation, i.e., the DTC phase. This section investigates the essential difference between our model and previous models due to the network's local U(1)-symmetry breaking. Thus, this section employs a new initial state and investigates its dynamics to find differences.

4.6.1 Initial state and DTC seed

As we previously discussed in Chapter 2, to get the DTC phase, an initial state should break the parity, e.g., the ferromagnetic state $|\Psi(0)\rangle = |00\cdots0\rangle$. Contrary, if the initial state is parity symmetric, e.g., a para-magnetic state $|\Psi(0)\rangle = |++\cdots+\rangle$, it does not exhibit the sub-harmonic oscillation, where $|+\rangle = (|0\rangle + |1\rangle)/\sqrt{2}$. These states have global symmetry, such as global U(1)-symmetry and parity symmetry. Moreover, as we have seen in the previous section, the global symmetry of states helps the network breaking the local symmetry exhibit stable sub-harmonic oscillations. Therefore, we consider that to see the effects of local symmetry breaking in a network, the symmetry of the initial state needs to be broken locally as well.

Thus, this section employs a new initial state which regionally breaks the parity symmetry to investigate the network's local U(1)-symmetry breaking effect. In other words, there are two regions in the initial state where the parity symmetry is preserved while the other region breaks it. To simplify the discussion, we consider a simple initial state dividing the network into two well-defined regions, referred to as region A and region B. First, as an initial state of region A, we employ the ferromagnetic state $|00\cdots0\rangle_{\mathrm{A}}$, breaking the parity symmetry. If the whole network is covered by region A, region A's dynamics breaks the discrete time-translational symmetry, and the state is the DTC phase. Thus, we refer to the initial state on the region A as the **DTC seed**. Next, we chose the para-magnetic state as the initial state $|++\cdots+\rangle_{\mathrm{B}}$ for region B, preserving the parity symmetry. Thus, the total initial state of the entire network is given by $|\Psi(0)\rangle = |00\cdots0\rangle_{\mathrm{A}} \otimes |++\cdots+\rangle_{\mathrm{B}}$.

In the conventional ZZ-DTC model, we expect the two regions to be preserved during the time evolution due to local U(1)-symmetry (in the absence of rotational error case) on the spin network. Contrary, in our network, as discussed in the previous section, the two regions will be mixed under the dynamics due to the network's local U(1)-symmetry breaking.

4.6.2 DTC Growth in closed systems

First, let us explore the dynamics of the new initial state in the closed system. In the numerical model with $N = 6$, we consider a state $|\Psi(0)\rangle = |000\rangle_{\mathrm{A}} \otimes |+++\rangle_{\mathrm{B}}$ as the initial state. We show the stroboscopic dynamics of the local magnetization $\langle\sigma_l^z(nT)\rangle$ for the new initial state in Fig. 4.6 (a) and (b). result depicted in Fig. 4.6 (a), we see that

the magnetization dynamics at each site are not stable compared to the previous initial state $|\Psi(0)\rangle = |000\cdots0\rangle$. The XX-interactions J_{lm}^{xx} allows the population transfer in the network. As a result, the sub-harmonic oscillation with $2T$ or the DTC region initially located at region A propagates to region B in a short time-scale as shown in Fig 4.6 (b). Thus, we refer to this spread of the DTC phase as **DTC growth**, and the initial state on the region A as the **DTC seed**.

The aforementioned results show that magnetization dynamics cannot be stabilized in a finite closed quantum system even after a long time. Here, one can also consider the above phenomenon as a thermalization of the stroboscopic dynamics governed by the effective Hamiltonian Eq. (4.5) for the new initial state. It means that if the system size is large enough to show thermalization, once the state reaches a equilibrium state (at discrete times), there should be no dynamics except for small fluctuations from a macroscopic point of view. In the aforementioned case, the dynamics for even periods $t = 2nT$ shows that the magnetization initially located in region A spread to the entire system. If the effective Hamiltonian system shows thermalization, then eventually the magnetization will stop spreading, and since the total amount of magnetization is constant and there are no special sites, the entire system should show the DTC phase. This point is not addressed enough in the present work. However, we are confident that the scenario is sufficiently reasonable from above results and the previous DTC studies.

4.6.3 DTC Growth with quantum perspective

Previously, we have seen that the initial population located at region A spread over the whole network due to the XX-interaction. Here, we focus on the time evolution of the corresponding quantum state and investigate the relationship between the growth process in magnetization, which is a macroscopic physical quantity, and the microscopic state. To investigate the time evolution of the quantum state, we consider the entanglement between two regions, A and B. As we saw in chimera DTCs, if the quantum system is isolated or closed, one can use the Von Neumann entropy to measure the entanglement of pure bipartite states. However, in the next Chapter, we will investigate the DTC Growth on the dissipative network. Thus, we employ the negativity between two regions A and B, which can be used to measure entanglement between two regions in dissipative systems [124, 125]. Here, the negativity $\mathcal{N}_B$ of the subspace B is defined as

$$\mathcal{N}_B = \frac{\left(||\hat{\rho}^{\Gamma_B}||_1 - 1\right)}{2}, \tag{4.32}$$

where $\hat{\rho}^{\Gamma_B}$ is the partially transposed density matrix $\hat{\rho}$ with respect to subspace B (region B) with $||\hat{X}||_1 = \mathrm{Tr}\sqrt{\hat{X}^\dagger \hat{X}}$ being the trace norm. Fig 4.6 (c) shows the results of the

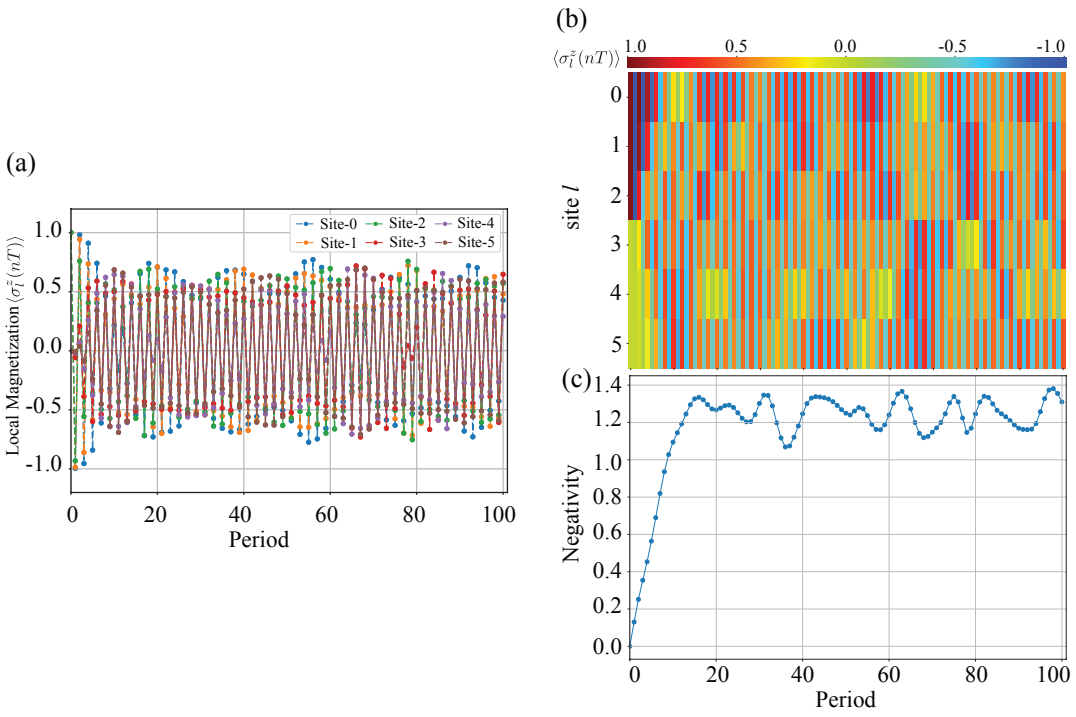

Figure 4.6: (a) and (b) Sxhibit the stroboscopic dynamics of the local magnetization $\langle\sigma_l^z(nT)\rangle$ for DTC growth in the closed system. The panel (b) clearly shows the population propagation on the network due to the XX interactions that allow the hopping of spin flips. In (c), we show the corresponding dynamics of the negativity. We have used a state $|\Psi(0)\rangle = |000\rangle_{\rm A} \otimes |+++\rangle_{\rm B}$ as our initial state. Here, we have chosen, $J_0T/(2\pi) = 0.2$ with $\alpha = 1.51$ and $WT/2\pi = 0.0$.

dynamics of the negativity at the stroboscopic times. During the DTC propagation, the entanglement between two regions increases over time. However, after a certain period, it saturates with fluctuation. The number of period ($n \sim 10$) tells us the time scale of the DTC propagation. Since the state remains pure and bounds at the edge of the spin network, the population transfer reflects and causes interference. In this situation, the negativity fluctuates, and consequently, the magnetization dynamics do not reach a steady state.

4.7 DTC Growth (DTCG) on the dissipative network

As we saw in the previous section, we have seen DTC growth, where the DTC region expands in a short time scale due to the XX interactions that allows for spin flip hopping.g. However, because of the finite size of the system, the numerical results show that the entire system does not exhibit a stable DTC phase at longer periods due to reflections

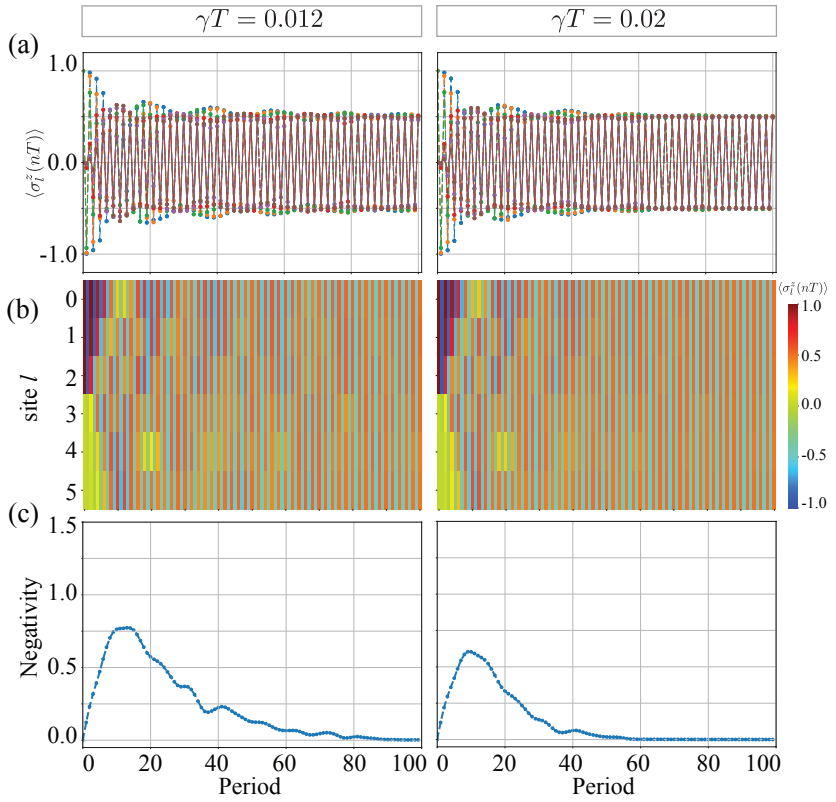

Figure 4.7: We show the stroboscopic dynamics of the local magnetization $\langle \sigma_l^z(nT) \rangle$ for DTC growth for two different dephasing rates $\gamma T = 0.012$ and 0.02 in (a) and (b), respectively. The corresponding dynamics of the negativity is shown in (c). We have used a state $|\Psi(0)\rangle = |000\rangle_{\rm A} \otimes |++\rangle_{\rm B}$ as our initial state. We set $J_0 T/(2\pi) = 0.2$ with $\alpha = 1.51$ and $WT/(2\pi) = 0$ with $\epsilon = 0.0$.

at the spin chain boundaries and interference. These effects are caused by the purity of the quantum state. Here, the environmental effect such as the dephasing might help the system to suppress the magnetization interference due to the loss of phase information or coherence. Thus, when the network is coupled with an environment, one might obtain a homogeneous DTC phase at the steady-state by suppressing the interference using the dephasing effect, even in a finite system. Here, we consider the network that we used in the previous section, and systematically explore the effect of dephasing.

In Fig 4.7, we show the numerical results for the local magnetization dynamics $\langle \sigma_l^z(t) \rangle$ and negativity $\mathcal{N}(nT)$ at the stroboscopic times $t = nT$ with two different dephasing rates $\gamma T = 0.012$ and 0.02. In both cases, the DTC seed initially at region A propagate under the time evolution. Correspondingly, the negativity increases in a short time scale and peaks at a certain time. Unlike the case of the closed system discussed above, the negativity begins

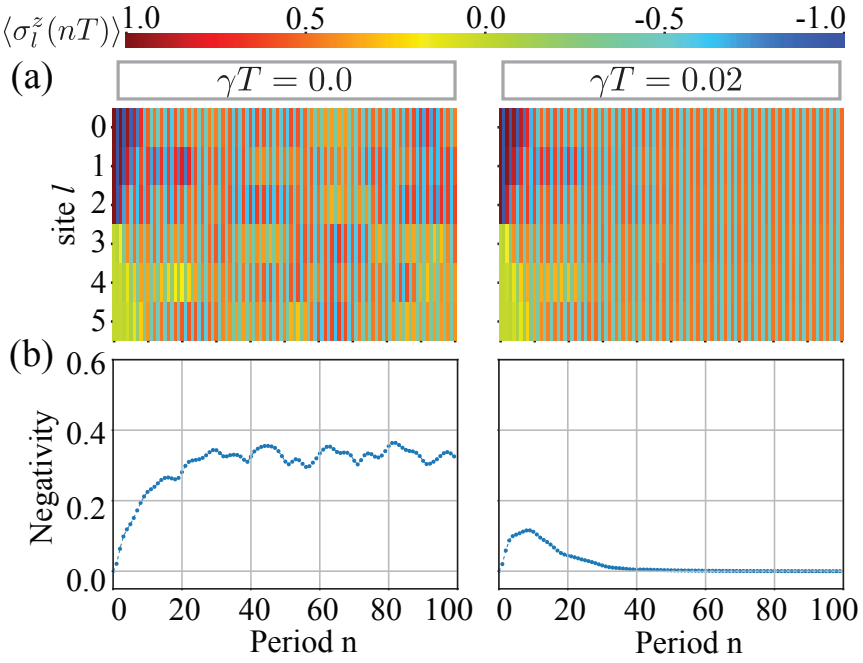

Figure 4.8: We show the DTC growth on the dissipative spin network with a dephasing rate $\gamma T = 0.02$ for a mixed initial state in region B. The panel (a) depicts the dynamics of the local magnetization at the stroboscopic times for a initial state $\hat{\rho}(0) = |000\rangle_{\rm A}\langle 000| \otimes \hat{\rho}(0)_B$, where $\hat{\rho}(0)_B$ is the full mixed state of region B. Correspondingly, the panel (b) plots the stroboscopic dynamics of the negativity. We set $J_0 T/(2\pi) = 0.2$ with $\alpha = 1.51$, $WT/(2\pi) = 0$ with $\epsilon = 0.01$. These results are from our recent article published in Ref. [4].

to decrease and converge to zero due to the dephasing. As a result, the state gradually loses its purity over time and reaches the steady-state that shows sub-harmonic oscillation with period $2T$, as shown in Fig 4.7(a). In general, as the dephasing rate increases, the purity of the state is lost more quickly, and the system reaches a steady-state in a shorter time scale. Thus, as shown in Fig 4.7, the low dephasing rate needs more periods (n) to stabilize the DTC phase.

Above, we have demonstrated the DTC growth for the pure initial state and shown the population transfer due to the XX-interaction, and the dephasing stabilizes the magnetization dynamics. However, it is not clear that dephasing is a key ingredient required to get a stable DTC for a longer time. To investigate it more efficiently, we consider a new initial state where region B is a completely mixed state: $\hat{\rho}_B(0) = \mathbb{I}_{M_B}/M_B$, as an example, where $M_B = 2^3$ is the Hilbert space size of region B. Since region B has no phase information or coherence, DTC may not grow.

We show the result of the local magnetization and the negativity for the new initial

state with two different dephasing rates $\gamma T = 0$, and 0.02 in Fig 4.8. The magnetization results indicate that although the initial state in region B is the completely mixed state, the DTC state initially on region A can grow in a short time scale. Similarly to the results in Fig 4.8, the DTC region spreads over the entire chin and becomes stable due to the dephasing effect.

The above results for the two initial states indicate that the presence of the DTC seed is more crucial for DTC growth than the purity of the quantum state at the initial time. The result of the mixed initial state indicates that the DTC can grow even if the state has already lost its purity due to the environmental noise before the DTC seed spreads. Thus, we can observe that DTC growth even in large systems where the DTC state takes a long time to propagate in comparison to the decoherence time scale.

4.8 Time Scale of the DTC Growth

Previously, we have seen the DTC growth on our network due to the spin hopping and the dephasing. This indicates that the physics behind the DTC growth is intimately related to the Liouvillian operator $\hat{\hat{L}}_T^{\text{eff}}$. Here, to understand the DTC growth in more detail, we investigate the structure of the effective Liouvillian operator.

4.8.1 Effective Liouvillian gap for periodic dissipative systems

First, since effective Liouvillian operator is time-independent and gives the dynamics at the stroboscopic times $t = nT$, the density matrix $\hat{\rho}(nT)$ can be written in terms of its eigenstates and eigenvalues [126], as follows,

$$\begin{aligned}\hat{\rho}(nT) = \left(\hat{\hat{\Phi}}_T\right)^n |\hat{\rho}(0)\rangle\rangle &= \sum_l e^{\Lambda_l nT} c_l |\Lambda_l^R\rangle\rangle \\ &= c_0^{(0)} |\Lambda_0^R\rangle\rangle + \sum_{l\neq 0} c_l e^{\Lambda_l nT} |\Lambda_l^R\rangle\rangle,\end{aligned} \tag{4.33}$$

where, $c_l = \langle\langle \Lambda_l^L | \hat{\rho}(0)\rangle\rangle$, and $|\Lambda_l^{L/R}\rangle\rangle$ are left/right eigenvectors of the effective Liouvillian operator $\hat{\hat{L}}_T^{\text{eff}}$ with the eigenvalue Λ_l. Now, we introduce an order among the eigenvalues as $\text{Re}(\Lambda_0) \geq \text{Re}(\Lambda_1) \geq \cdots \geq \text{Re}(\Lambda_{2^{2N}})$. Next, the state $|\Lambda_0^R\rangle\rangle$ with $\Lambda_0 = 0$ is called the steady state and is denoted by $\hat{\rho}^{(ss)}$. It means that the state does not change under the time evolution,

$$\hat{\hat{L}}_T^{\text{eff}} \hat{\rho}_l^{(ss)} = 0. \tag{4.34}$$

From the expansion, we see that the relaxation time-scale can be estimated by $\tau \sim 1/\Delta$ (unit of T), where Δ is a Liouvillian gap [123, 126, 127],

$$\Delta = -\text{Re}(\Lambda_1), \tag{4.35}$$

which is the negative real part of the second largest eigenvalue Λ_1 of the Liouvillian operator.

4.8.2 DTC growth time-scale (τ_{DTC})

Now, let us consider the DTC growth time scale (τ_{DTC}) that tells us the time scale for the DTC region initially at region to A spread the whole network and the magnetization interference to be settled and stabilized. Thus, there are two steps in the DTC growth: the propagation of the DTC state and the DTC stabilization. We have seen the first step and its time scale in the negativity dynamics in the above section. The time scale can be determined by the propagation speed, which is related to the hopping strength similar to the state transfer [128]. The time scale of stabilization is related to the dissipation time of the system. However, in our model, stabilization due to the dephasing takes longer than state propagation. Thus we can estimate τ_{DTC} from the stabilization time scale or the relaxation time scale. It means that we can use the Liouvillian gap Δ as a measure to estimate τ_{DTC}.

Now, let us see more details. Given the 2T-periodicity of the DTC, we consider the effective Liouvillian operator $\hat{\hat{L}}_{\text{eff}}^{2T}$ and spectral gap. As we saw in the previous section, when $\epsilon = 0$, the operator is analytically obtained by Eq. (D.2). In general, it can be numerically obtained from

$$\hat{\hat{L}}_{2T}^{\text{eff}} = \frac{1}{2T} \ln\left(\mathcal{T} e^{\int_0^{2T} \hat{\hat{L}}_\tau d\tau}\right) = \frac{1}{2T} \ln\left(\hat{\hat{\Phi}}_T^2\right), \tag{4.36}$$

where we use the periodicity of the Liouvillian operator $\hat{\hat{L}}_t = \hat{\hat{L}}_{t+T}$ to perform the integration. In numerical calculations, we used the above equation to find the Liouvillian operator and gap, e.g. in the case of diagonal disorder as we will see in the next section.

Now, as an example, let us numerically find the eigenvalues of the effective Liouvillian with $\gamma T = 0.02$ that is used in Fig. 4.7. We show the results in Fig. 4.9. First, remarkably, because our system preserves the total magnetization at even periods $t_n = 2nT$, there are multiple steady-states which are different from the fully mixed state ($\hat{\rho}_{\text{th}} = \hat{\mathbb{I}}/2^N$), as we expected. As a result, the DTC phase still exists even the system reaches the steady-state. From the results, we see that the Liouvillian gap is $\Delta = 0.02$ (in units of $1/T$). Correspondingly, the relaxation time is $\tau/T \sim 1/\Delta T = 50$. While, from the

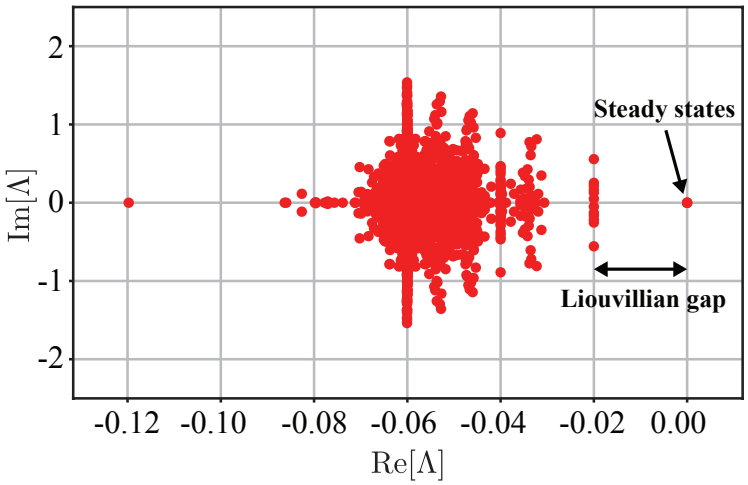

Figure 4.9: Spectrum of the 2T-effective Liouvillian operator $\hat{\hat{L}}^{2T}_{\text{eff}}$ for the $N = 6$ spin network with dephasing rate $\gamma T = 0.02$: Red dots are complex eigenvalues Λ of $\hat{\hat{L}}^{2T}_{\text{eff}}$. We set $J_0 T/(2\pi) = 0.2$ with $\alpha = 1.51$, $WT/(2\pi) = 0$ with $\epsilon = 0.01$. Because of the U(1)-symmetry of $\hat{\hat{L}}^{2T}_{\text{eff}}$, there are multiple steady states. The plot is taken from our recent article Ref. [4].

magnetization and negativity dynamics, we can estimate the DTC growth time scale to be around $\tau_{\text{CG}}/T = 40 \sim 60$. We see that the estimated time-scale obtained by analyzing the Liouvillian gap explains the time scale of the DTC growth.

4.9 Disorder effect on DTC Growth

Previously, we have investigated the DTC growth time-scale τ_{CG} and seen that it is determined measured by the Liouvillian gap Δ. In the above analysis, we have considered the absence of the diagonal disorder to simplify the discussion. Here let us investigate the DTC growth in the presence of the disorder. When there is a strong disorder, it is known that it induces the Floquet Anderson localization [129]. Consequently, the crystal growth might be suppressed due to the localization effect. In this section, we investigate the disorder effect using the Liouvillian gap.

When one derives the Lindblad master equation, it is assumed that the system of interest is weakly coupled to a Markovian environment. In our work, we implicitly assume that the dephasing rate is much lower than the characteristic energy scale of our system. Actually, in the numerical simulation, we set the network's hopping strength to satisfy the condition. However, in the presence of a strong disorder, the coupling might be effectively become negligible due to the localization phenomena. Consequently, the aforementioned

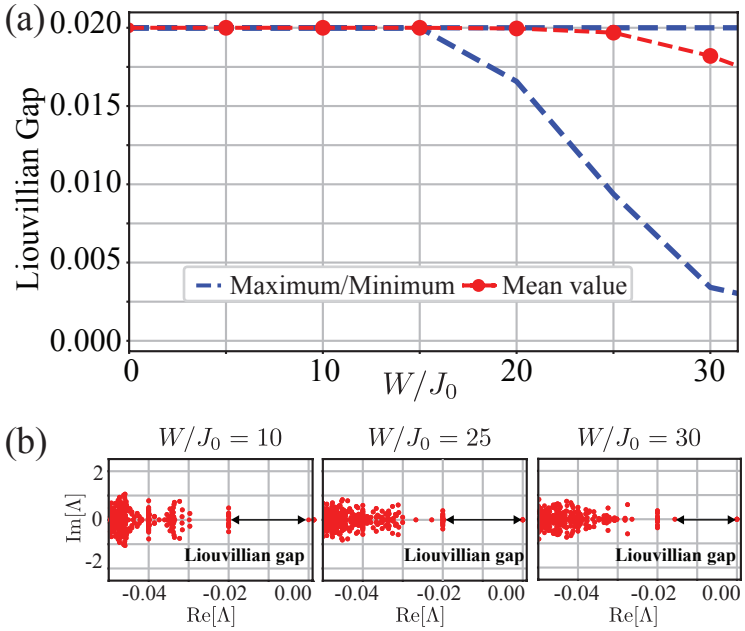

Figure 4.10: Liouvillian gap Δ of the spin chain with $N = 6$ sites under the effect of disorder. (a) Liouvillian gap for several realizations of disorder with strengths ranging from $WT_2/(2\pi) = 0$ to the maximum value π. The red dots and dashed line represent the average value of the Liouvillian gap with 200 disorder realizations. The blue band is the width between the maximum and minimum values of the Liouvillian gap. (b) Spectrum of the Liouvillian for one disorder realization for different strength of the disorder $W/J_0 = 10, 25$ and 30. In both (a) and (b), we set $\gamma T = 0.02$, and $J_0 T/(2\pi) = 0.2$ with $\alpha = 1.51$. These plot are taken our published article Ref. [4].

condition might be broken at stroboscopic times $t = 2nT$. It means that there is a critical strength of the disorder W_c. Before and after the critical point, the Liouvillian spectrum and the Liouvillian gap should dramatically change.

4.9.1 Numerical experiment

In this section, we explore properties of the Liouvillian gap for the several disorder strength and show the result in Fig. 4.10. To deal with the randomness of the disorder, we calculate the average value of the Liouvillian gap (the red dashed line) and the minimum and maximum values (the blue dashed lines) for the several disorder strength with 200 disorder realization. The result shows that the time scale for DTC growth is not affected by the disorder up to a specific strength $W_c/J_0 \sim 15$. Contrary, in the strong disorder region $W \gg W_c$, the Liouvillian gap may take a smaller value due to the effective suppression of the hopping.

Here, let us take a closer look at the Liouvillian gap near the critical point. To explore spectral properties of the Liouvillian that determine the steady state, we depict the spectrum close to the lowest real part for several disorder strengths $W/J_0 = 10, 25$ and 30 in Fig. 4.10. We see that the structure around the gap does not change up to $W/J_0 \sim 15$. Contrary, when the disorder strength is larger than the critical points ($W \gg W_c$), the Liouvillian operator structure gradually changes. As a result, the gap becomes smaller, and the DTC growth becomes slow.

4.9.2 Theoretical analysis using the simplest model

Now, let us investigate the disorder effect on the crystal growth more analytically. Here, we show how the hopping strength effectively decreases due to the disorder effect. To simplify the discussion, we consider a small system with two sites (N=2), and its the time-dependent Hamiltonian is given by,

$$H^{(s)}(t) = \begin{cases} \hbar g \left(\sigma_1^x + \sigma_2^x\right) & 0 \leq t < T_1 \\ \hbar J_0 \left(\sigma_1^x \sigma_2^x + \sigma_1^y \sigma_2^y\right) + \hbar W_1 \sigma_1^z + \hbar W_2 \sigma_2^z & T_1 \leq t < T \end{cases}, \tag{4.37}$$

where $2gT_1 = \pi$. The first Hamiltonian gives the parity operator, $\hat{X} = \sigma_1^x \sigma_2^x$. Next, W_l with $l = 1, 2$ are the diagonal disorder amplitudes at each site and we assume $W_2 > W_1$.

To obtain the $2T$-effective Hamiltonian, we begin with the square of the Floquet operator. Using the spin rotation properties, it can be written as

$$\begin{aligned} \hat{F}^2 &= e^{-i\left\{J_0\left(\sigma_0^x\sigma_1^x+\sigma_0^y\sigma_1^y\right)+W_1\sigma_1^z+W_2\sigma_2^z\right\}T_2}\hat{X}e^{-i\left\{J_0\left(\sigma_0^x\sigma_1^x+\sigma_0^y\sigma_1^y\right)+W_1\sigma_1^z+W_2\sigma_2^z\right\}T_2}\hat{X} \\ &= e^{-i\left\{J_0\left(\sigma_0^x\sigma_1^x+\sigma_0^y\sigma_1^y\right)+W_1\sigma_1^z+W_2\sigma_2^z\right\}T_2}e^{-i\left\{J_0\left(\sigma_0^x\sigma_1^x+\sigma_0^y\sigma_1^y\right)-W_1\sigma_1^z-W_2\sigma_2^z\right\}T_2} \\ &= e^{-i\left\{J_0\left(\sigma_0^x\sigma_1^x+\sigma_0^y\sigma_1^y\right)+(W_2-W_1)\sigma_2^z\right\}T_2}e^{-i\left\{J_0\left(\sigma_0^x\sigma_1^x+\sigma_0^y\sigma_1^y\right)-(W_2-W_1)\sigma_2^z\right\}T_2} \\ &= e^{-i\left\{J_0\left(\sigma_0^x\sigma_1^x+\sigma_0^y\sigma_1^y\right)+W_g\sigma_2^z\right\}T_2}e^{-i\left\{J_0\left(\sigma_0^x\sigma_1^x+\sigma_0^y\sigma_1^y\right)-W_g\sigma_2^z\right\}T_2}, \end{aligned} \tag{4.38}$$

where we use $[\sum_l \sigma_l, J_0\left(\sigma_0^x\sigma_1^x + \sigma_0^y\sigma_1^y\right)] = 0$. Here, $W_g = W_2 - W_1$ is a gap of the disorder for two sites, and it characterises the disorder effect.

Since the total number of expiation are preserved at every even and odd periods, we consider a subspace for the one excitation. In this subspace, our system is a two level system, when we consider a the basis set

$$|10\rangle = \begin{pmatrix} 1 \\ 0 \end{pmatrix}, \quad |01\rangle = \begin{pmatrix} 0 \\ 1 \end{pmatrix}, \tag{4.39}$$

for the new subspace. In this basis, the $2T$-effective Hamiltonian reads

$$\hat{H}_{2T}^{\text{eff}} = \begin{pmatrix} \varepsilon_0 & K \\ K^* & \varepsilon_1 \end{pmatrix}, \tag{4.40}$$

where $\varepsilon_{0/1}$ are real, and K is a complex effective coupling, respectively. The effective hopping strength is characterized by the absolute value of the off-diagonal term $|K|$.

Now, let us find the effective Hamiltonian in the one-excitation subspace. Within the subspace, Eq. (4.38) can be written as,

$$\hat{F}^2 = e^{-i(2J_0\sigma^x + W_g\sigma^z)T_2} e^{-i(2J_0\sigma^x - W_g\sigma^z)T_2}, \tag{4.41}$$

where σ^μ ($\mu \in x, y, z$) are the Pauli matrices for the two level system. Since the system is the two level system, we exactly derive the effective Hamiltonian from the above equation, as follows,

$$\hat{H}_{2T}^{\text{eff}} = -\frac{c\hbar\left(\sqrt{(2J_0)^2 + W_g^2}\sigma^x - W_g \sin(a)\sigma^y\right)}{2T\sqrt{(2J_0)^2\cos^2(a) + W^2}}, \tag{4.42}$$

where we used the composition law of the group SU(2). Here the two parameters a and c are given by

$$\begin{aligned} a &= -T_2\sqrt{(2J_0)^2 + W_g^2} \\ \cos(c) &= 1 - \frac{2(2J_0)^2}{(2J_0)^2 + W_g^2}\sin^2(a), \end{aligned} \tag{4.43}$$

respectively.

The above Hamiltonian is exact, but it is difficult to see the disorder effect. Thus to see it more efficiently, let us consider the two situations, small and strong disorder strength. First, we assume that the disorder strength is small. Then the Hamiltonian becomes,

$$\hat{H}_{2T}^{\text{eff}} \approx \hbar J_0\left(1 - \frac{{W_g}^2T^2}{6}\right)\sigma^x + \frac{J_0W_gT}{2}\sigma^y, \tag{4.44}$$

The result is the same as that obtained by using the Baker-Campbell-Hausdorff formula at the lowest order. Then, in the weak disorder regime, the hopping strength is

$$|K| \sim J_0\sqrt{1 - \frac{(W_gT)^2}{12}} \leq J_0. \tag{4.45}$$

It means that its value decreases as the disorder gap increases, as we expected.

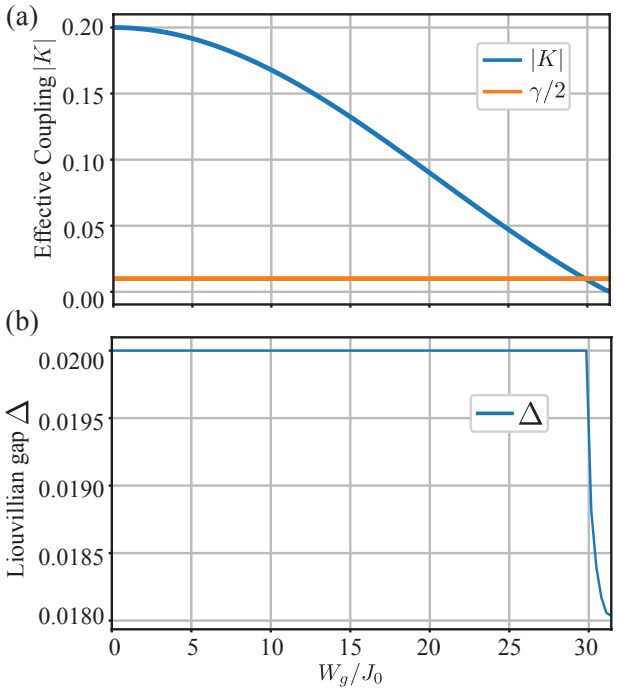

Figure 4.11: Effective coupling $|K|$ and Liouvillian gap Δ for a $N = 2$ coupled spins under the effect of disorder. (a) The effective coupling $|K|$ for disorder strengths ranging from $W_g T_2/(2\pi) = 0$ to π. We show the corresponding Liouvillian gap in (b), In (a) and (b), we set $\gamma T = 0.02$, and $J_0 T/(2\pi) = 0.2$. The plots are taken from Ref. [4].

Nest, we find the large disorder gap ($W_g \gg 1$). Now the Hamiltonian is given by,

$$\hat{H}^{\text{eff}}_{2T} \approx \frac{2\hbar J_0}{W_g T}\left(\frac{\sin(2W_g T_2)}{2}\sigma^x - \sin\left(W_g T_2\right)^2 \sigma^y\right), \tag{4.46}$$

and the corresponding coupling strength is

$$|K| \sim \frac{2J_0|\sin(W_g T_2)|}{W_g T} \ll J_0. \tag{4.47}$$

Surprisingly, the above Hamiltonian and $|K|$ works even for the small gap $W_g \ll g$ except for $W_g = 0$. Now, as W_g increases, we see that the effective coupling strength decreases, and it gets smaller than the dephasing rate at the certain critical strength W_c. From Eq. (4.46), for the given dephasing rate γ, the critical point is roughly estimated as,

$$W_c \sim \frac{\pi}{T_2}\left(1 - \frac{\gamma}{(2J_0 + \gamma)}\right). \tag{4.48}$$

It indicates that for the $N = 2$ case, the critical point is in the strong disorder regime. Thus, we expect that the Liouvillian gap is constant until the diagonal disorder gap reaches the critical point. Then, when disorder strength is larger than the critical disorder, the Liouvillian gap gets smaller. Lastly, we numerically evaluate the above estimation with the hopping strength $J_0T/(2\pi) = 0.2$ and the dephasing rate $\gamma T = 0.02$. First, from the equation obtained above, the critical point for this condition is about $W_c/J_0 \sim 29.9$. Next, we numerically find the effective coupling $|K|$ for several gaps and show the result in Fig. 4.11. We see that as the gap increases, the effective coupling $|K|$ decreases. At a certain gap, it crosses the value γ. Correspondingly, when the diagonal disorder strength is smaller than the critical point, the Liouvillian gap is constant. However, when it exceeds the point, the gap gets smaller. Form Fig. 4.11, the critical gap is about $W_c/J_0 \sim 30$. The agreement between numerical and theoretical results is good. Here, we note that the critical point is much bigger than the $N = 6$ case ($W_c/J_0 \sim 15$). We have to point out that the above model has more sites, long-range interactions, and higher excitation sectors that can shift the critical point.

4.10 Conclusion

This Chapter demonstrated that a spin network breaking the local U(1)-symmetry can exhibit the sub-harmonic oscillations with the double periodicity of the driving. By extending the $\mathbb{Z}_2$-symmetry and the global U(1)-symmetry of the effective Hamiltonian, which are necessary to obtain the stable 2T-DTCs, to the Liouvillian operator of the dissipative system, we showed that a network with dephasing effect can exhibit stable sub-harmonic oscillation. Furthermore, we investigated an essential difference between spin networks preserving and breaking the local symmetry by looking at the stroboscopic dynamics of a new initial state. We firstly demonstrated the DTC growth using the hybrid states, which do not appear in the conventional models. By comparing different initial states, we showed that the DTC seed is crucial to observe the growth and that the purity of the initial state does not play a role in this phenomenon. By analyzing the spectrum of the $2T$-effective Liouvillian operator, we showed that the Liouvillian gap can measure the time scale of DTC growth. Additionally, we investigated DTC growth in the presence of diagonal disorder. Until a specific strength of the disorder, the time scale of DTC growth does not change. However, when the strength of the disorder exceeds a certain critical point, it is slow growth due to the effect of Anderson localization. As a result, its time scale (or the Liouvillian gap) becomes longer (or smaller). We believe that this DTC growth will help generate stable DTCs coupled to the environment and understand new dynamical quantum phases of matter.

Part II

Proposal of new application based on quantum dynamics

Chapter 5

Quantum Reservoir Extreme Learning Machine (QRELM)

When simulating quantum systems on classical computers, the computation time increases exponentially as the size of the system increases. It implies that the dynamics of quantum systems are more complex than classical systems. R. Feynman pointed out that computers based on quantum mechanics may have more computational power than classical computers [130]. Around the same time, Benioff [131] and others have a similar idea. Subsequently, Deutsch [132] proposed a gate model for quantum computer as an extension of the classical Turing machines to quantum systems. It consists of a quantum version of bits called **qubits** (quantum states) and **quantum gates** (operators) which are the quantum counterparts of classical bits and logical gates, respectively. An essential result of this gate model of quantum computation is that its universality has been shown, i.e., any quantum computation can be performed [133].

Although various efficient quantum algorithms [134, 135] have been developed to be run on quantum computers, the implementation of error-correcting codes is inevitable since quantum computers imitate classical Turing machines [136, 137]. Furthermore, to use the aforementioned algorithms for practical problems, many logical qubits are required. However, at the current level of technology, quantum processors have tens to hundreds of qubits affected by noise (**Noisy Intermediate-Scale Quantum (NISQ)** devices): such as superconducting qubits [20], trapped ions, cold atoms [25], and others [26]. Therefore, it is essential to investigate the applications on NISQ devices.

A quantum neural network was proposed as a different approach to exploit the intrinsic quantum complexity of quantum systems. Initially, it was proposed in the context of artificial intelligence to explain the brain's cognitive functions with quantum effects [138, 139]. Nowadays, it is used in the contents of **quantum machine learning (QML)** as an analogy to classical neural networks used in **machine learning (ML)**. Recently, QML has

been extensively investigated because it has been shown that quantum neural networks can be optimized by **Variational Quantum Algorithms (VQAs)** [140, 141, 142, 143, 144, 145] which is widely used to optimized a quantum circuit. The algorithm is a hybrid of quantum and classical computers that can efficiently solve problems based on variational principle and is expected to run on NISQ devices. However, optimization of the quantum circuits has several issues, and one of them is the scalability. Furthermore, the noise effect is inescapable on quantum circuit model.

Recently, **Quantum Reservoir Computing (QRC)** [146, 147, 148] and **Quantum Extreme Learning Machine (QELM)** have been receiving much attention to overcome the difficulties of VQAs. In QRC, the quantum system generates a huge neural network, and this algorithm does not require any optimization in the quantum part. Furthermore, because QRCs can be designed as analog quantum computing, it is expected that the noise effect can be suppressed compared to the circuit model [149]. However, since the quantum state is collapsed by measurement, it is not clear that QRC has a memory effect similar to classical RC. Thus, QELM has recently proposed applying quantum neural networks to pattern recognition tasks. However, it has been challenging to address practical tasks with enormous input, such as images.

The presence Chapter proposes a new machine learning model based on QRCs and ELM and refers to it as **Quantum Reservoir Extreme Learning Machine (QRELM)**. In the model, quantum systems are used as a reservoir producing a complex neural network similar to QRCs. We propose a systematic way to encode the classical image into a quantum state using the classical information compression technique and demonstrate the classification of handwritten digits in the MNIST data set. In this Chapter, we investigate the performance of our computational model by comparing it with different quantum systems. As a significant result, we show by using driven quantum systems (Floquet systems), our model does not require as much complexity as conventional quantum processors require, such as quantum supremacy. For instance, the Floquet system records over **98%** with 14-qubits for testing data (unknown data). We believe that this new QRC opens up new avenues for future computing with quantum complexity.

5.1 Introduction of Machine Learning (CML) and Classical Neural Network (CNN)

We will briefly explain machine learning and classical neural network in this section for readers unfamiliar with them.

5.1.1 Machine learning (ML)

Machine learning (ML) is a type of **artificial intelligence (AL)** which is a technology that allows computers to perform intellectual actions such as language understanding and reasoning on behalf of humans. Among them, ML is the technology to achieve human-like learning ability on computers. In ML, a computer learns from "training data" and uses the learning results to perform some task.

There are three types of ML depending on the learning style: **supervised learning**, **unsupervised learning**, and **reinforcement learning** [150, 151]. First, supervised learning is a learning method that learns connection between input and output using the previously prepared input-output pairs (labeled training data). Contrary, unsupervised learning is a method of learning the characteristics of the training data without output (labels). Finally, reinforcement learning is a method that does not need training data but learns to maximize the reward (or cost) depending on the purpose. In this Chapter, mainly, we focus on supervised learning.

Typical supervised learning applications are **regression** and **pattern recognition**, as shown in Fig. 5.1 (b) and (c). Regression is a kind of function approximation technique. Computers learn the connection between input and output during the ML and find an approximate function. While pattern recognition is a technology that finds specific rules from given data and assigns them to predetermined clusters. Here, we note that sometimes, pattern recognition is referred to as classification, and a machine learning device is referred to as a classifier. An example of a simple problem in pattern recognition is the classification of two-dimensional scatter plots. Another famous problem is the classification of handwritten digits called the MNIST dataset [46]. This Chapter proposes a new classifier using quantum systems that exploit the power of quantum systems to solve a classification problem.

5.1.2 Classical neural network (CNN)

Machine learning is a "methodology" in computer science, and thus to actually perform it, one needs mathematical models. One of them is a **neural network** (model). This section will introduce two neural network models: the **simple perceptron**, which is the

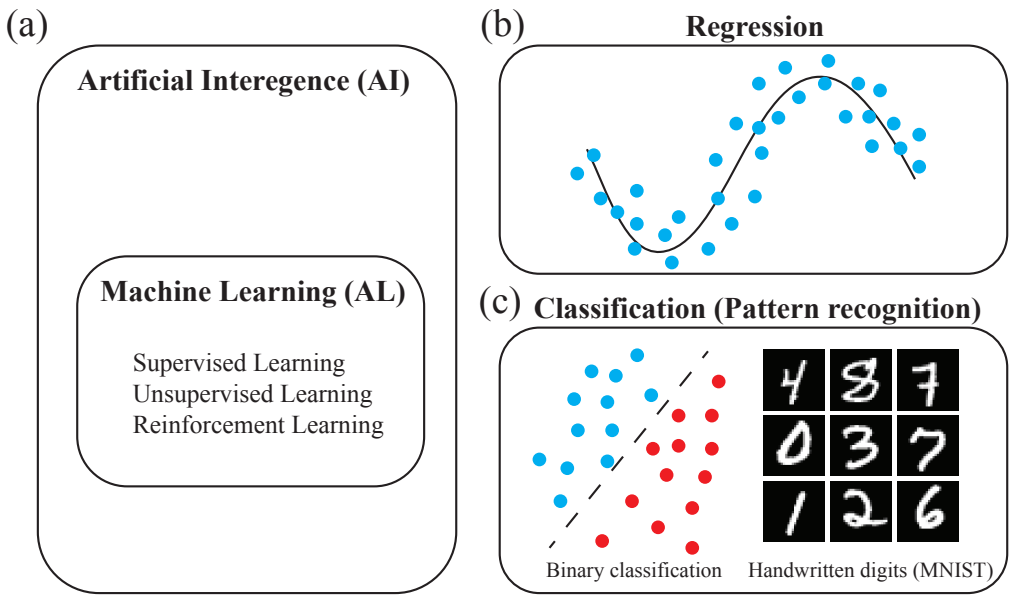

Figure 5.1: Overview of Artificial Intelligence (AI) and Machine Learning (ML): ML is the subclass of AI. Supervised learning is the subfield of ML and mainly used to regression (b) and classification problems (c). Regression analysis is a statistical processes for estimating the relationship between inputs and outputs. The left panel of (c) is the binary classification being linearly separable. The right panel of (c) is hand written digits (MNIST).

most basic and most straightforward, and the **deep neural network (DNN)**.

Initially, the **simple perceptron** is proposed to model **neuron** activity in the brain [152, 153]. Nowadays, it is recognized as a concrete model for performing machine learning. The simple perceptron consists of a weighted summation, and a non-linear function (an **activation function**) called a step function, as shown in Fig. 5.2. For example, let us consider the binary classification (such as true or false). When there are n-inputs $(x_1, \cdots, x_n)$ and one output (y), the output of the simple perceptron is represented by

$$y = f\left(\sum_l^n w_l x_l + b\right) \tag{5.1}$$

where w_l and b are **weights** and a **bias**, and $f(\cdot)$ is the step function. Because of the step function, y can be taken a value from 0 to 1. The weights w_l $(l = 0, 1, \cdots, n)$ are initialized to be small random numbers and updated as follows,

$$w_l^{(n+1)} = w_l^{(n)} - \eta(t - y)x_l \tag{5.2}$$

where $w_0 = b$, t is the desired output (labels), and $0 < \eta < 1$ is a teaching rate. The model

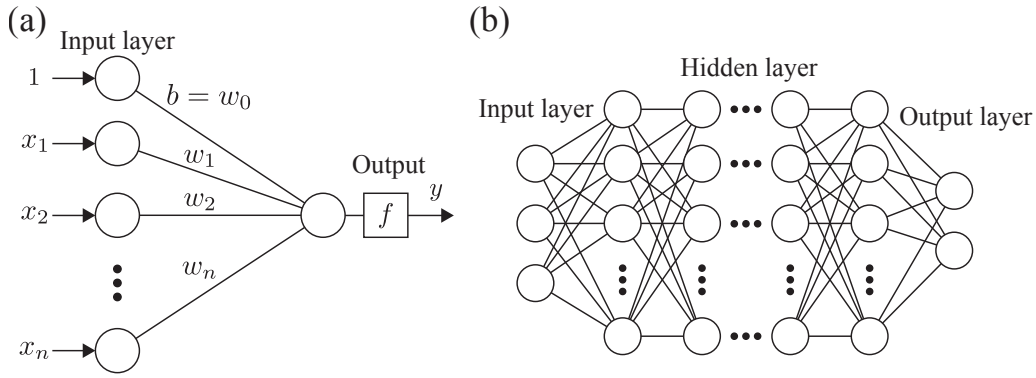

Figure 5.2: Illustration of the simple perceptron and a neural network. (a) Shows the simple perceptron with n-inputs $(x_1, x_2, \cdots, x_n)$ and one output y. The perceptron sums up weighted inputs and returns output through the activation function. (b) Illustrates the conceptual model of the neural network used in deep learning.

can lean the training data by optimizing the weights and bias. Here, we note that since the connection between input and output is a network, the simple perceptron is a neural network.

Despite the simple mechanism, it is theoretically shown to solve any linearly separable problems by the simple perceptron model. Contrary, the only linear transformation (a linear network) does not have the power or expressiveness to solve nonlinear problems such as the classification of handwritten number images.

As an improvement of the simple perceptron, **multilayer perceptron** was proposed. In this model, many neuron layers connect to another layer via an activation. Its structure is more similar to the network of neurons in the brain. By increasing the number of layers, the representation capability of the neural network is increased. As a result, nonlinear separation problems can be solved. Theoretically, a feed-forward neuronal network can represent any continuous function with arbitrary accuracy. It is known as the "**universal approximation theorem**" [154, 155]. However, practically, to get a high expressiveness, a **deep neural network** is used in many applications, and it is called **deep learning**. Conceptually, the neural network can be represented as

$$y = g_L\left(W_{L-1} \cdot g_{L-1}\left(\cdots W_2 \cdot g_2\left(g_1\left(W_1 \cdot x\right)\right)\right)\right) \tag{5.3}$$

where $W_1, W_2, \cdots, W_{L-1}$ are weight matrices, and g_i are activation functions. Thus, first, it was thought to be challenging to optimize the network because of the large number of parameters such as $W_1, W_2, \cdots, W_{L-1}$. Thanks to backpropagation techniques and improved computational power, AI and neural networks are the most active fields and are

widely used on several problems. Furthermore, it has shown very high performance in several fields.

5.1.3 Support Vector Method (SVM) and Kernel Machine

Finally, we briefly explain a **Support Vector Machine (SVM)**, not a neural network model. It is a learning method that determines the boundaries between data in a feature space, such as a sample in a two-dimensional space.

For example, let us consider n-inputs: $\boldsymbol{x} = (x_1, \cdots, x_n)$, where $\boldsymbol{x} \in \mathbb{R}^n$ (n-dimensional real space). To simplify the discussion, let us consider two classes. First, we define a new function $g(\boldsymbol{x})$, as follows,

$$g(\boldsymbol{x}) = \begin{cases} 1 & f(\boldsymbol{x}) \geq 0 \\ 0 & f(\boldsymbol{x}) < 0. \end{cases} \tag{5.4}$$

Here, $f(\boldsymbol{x})$ is a function deterring the boundary, given by,

$$f(\boldsymbol{x}) = w^T \boldsymbol{x} + b \tag{5.5}$$

where w is the normal vector and b is the offset. Now, the function $g(\boldsymbol{x})$ tells us which class a point belongs to. For example, when a point is above the line $f(\boldsymbol{x})$ ($f(\boldsymbol{x}) \geq 0$), then $g(\boldsymbol{x}) = 1$. Contrary, if a point is bellow the line ($f(\boldsymbol{x}) < 0$), then $g(\boldsymbol{x}) = 0$. By adjusting w and b in $f(\boldsymbol{x})$, the output of $g(\boldsymbol{x})$ can be tuned to match the training data.

Now, in learning section, we use the previously prepared label y, that is the ideal g-value for each point. Suppose we have $\boldsymbol{x}_i$ as the input and y_i as the label for the i-th data. If the classification is successful, the sign of y_i and $f(\boldsymbol{x})$ are unique, so we get,

$$y_i f(\boldsymbol{x}_i) > 0. \tag{5.6}$$

If the classification is successful for all the training data, then the above equation is valid for any y_i ($i = 1, \cdots D$), where D is the total number of training points. However, since there are multiple candidates for $f(\boldsymbol{x})$ (or w and b) that satisfy the above equation, we need a criterion to determine it. So, in general, the distance between the data set of each class and the line $f(\boldsymbol{x})$, the margin, is used as a criterion. In SVM, w and b are optimized to maximize the margin. If readers are interested in the details of SVM optimization, please see the Refs [156].

The simplest SVM is the linear SVM described above. However, this method is unable to solve nonlinear classification problems. Therefore, a nonlinear SVM have been proposed. In this method, the input $\boldsymbol{x}$ is mapped to a higher dimension by a nonlinear

function $\phi(\boldsymbol{x})$. As a result, since the feature space of the input is non-linearly extended to a higher-dimensional space, the classification problem may be solved. However, it is well known that as the feature space becomes higher dimensional, the computational complexity of SVM optimization becomes huge.

To solve the above computational problems, the **Kernel method (Kernel machine)** was proposed [157]. In non-linear SVM optimization, the most computationally expensive part is the inner product $\phi(\boldsymbol{x_l})^T\phi(\boldsymbol{x_m})$. Thus, in the kernel method, the kernel function is defined by $K(\boldsymbol{x_l}, \boldsymbol{x_m}) = \phi(\boldsymbol{x_l})^T\phi(\boldsymbol{x_m})$. However, in the actual calculation, the kernel function is given by a specific formula in terms of inputs $\boldsymbol{x}_l$ and $\boldsymbol{x}_m$, called the kernel trick. For example, in the Gaussian kernel method, the kernel function is given by $K(\boldsymbol{x_l}, \boldsymbol{x_m}) = \exp\left(-|\boldsymbol{x_l} - \boldsymbol{x_m}|^2/\sigma\right)$, where σ is a parameter. As result, it is easier to calculate the kernel function. Furthermore, it is possible that to consider the infinite-dimensional feature space by using the kernel function.

5.2 Quantum Neural Network (QNN) and Quantum Machine Learning (QML)

Because quantum systems and their dynamics are more complex than classical systems, it is believed that neural network models based on quantum mechanics have more computational power than classical ones. Therefore, the presence section briefly reviews perceptron and machine learning within the context of quantum mechanics.

5.2.1 Quantum Perceptron

Initially, **quantum neural networks** was developed to explain the cognitive functions of the brain in terms of quantum effects [138, 139]. However, nowadays, quantum neural networks are used to extend classical neural networks in quantum machine learning. Of course, in this Chapter, we use QNNs in this sense. In 1996, E. Behrman et al. gave an idea of the perceptron using quantum dot molecule coupled to the environment [158]. They demonstrated that the system could train any desired classical and quantum logical gates. They state that quantum neural networks can be powerful computational tools and have advantages over classical neural networks in pattern recognition, missing data, and learning ability.

The general concept of the quantum perceptron was proposed by Altaisky [159]. In his model, neurons are represented by the quantum states, and output is their superposition. For example, when we consider the same problem as seen in the previous section (multiple

inputs and one output), the output of the quantum perceptron is represented by,

$$|y\rangle = \hat{F} \sum_{l}^{n} w_l |x_l\rangle \tag{5.7}$$

where $\hat{F}$ is an unknown unitary operator. Unlike the classical perceptron models, the network is not effective due to the linearity of $\hat{F}$. However, it is believed that the measuring procedure can play the role of the non-linearity [160, 161].

5.2.2 Quantum Circuit Learning (QCL)

QNNs have been extensively investigated recently because their optimization can be performed on quantum circuits. It is called the **Quantum Circuit Learning (QCL)** [162]. In this model, a quantum neural network is used to get desired output and thus optimized by **variational quantum algorithms (VQAs)** [143, 145] being believed to be able to run on small quantum processors called NISQ devices. The algorithms are able to optimize or design quantum circuits using the feed-froward loop with the classical optimizer.

The generic procedure of VQAs are illustrated in Fig. 5.3. The quantum circuit $\hat{U}(\boldsymbol{x})$ prepares a quantum state $|\psi_{\text{in}}(\boldsymbol{x})\rangle$ encoded the training input $\boldsymbol{x}$. This initial state is transformed into an output state by a quantum circuit programmed by parameters $\boldsymbol{\theta} = (\theta_1, \cdots, \theta_m)$: $|\psi_{\text{fi}}(\boldsymbol{x})\rangle = \hat{U}(\boldsymbol{\theta})|\psi_{\text{in}}(\boldsymbol{x})\rangle$. One then needs to measure the expectation value of some observable of the final state such as a bit string of qubits in a computational basis and convert it into a final output using classical data processing $y(\boldsymbol{x}, \boldsymbol{\theta})$. This allows us to calculate the loss function $L(\boldsymbol{\theta})$ that evaluates between the desired output y and the model output, $y(\boldsymbol{x}, \boldsymbol{\theta})$ and update $\boldsymbol{\theta}$ to minimize the function: $\arg\min_{\boldsymbol{\theta}} L(\boldsymbol{\theta})$.

VQAs are expected to apply to combinatorial problems and quantum chemical calculations. For example, **Variational Quantum Eigensolver (VQE)** is proposed to find the ground state of atoms and molecules for quantum chemistry and atomic physics using VQAs [140, 141, 163, 142, 143, 144, 145].

Although VAQs are expected to be an optimizer for quantum machine learning using NISQ devices, it seems that optimizing quantum circuits by classical loops is challenging to scale up. Furthermore, during the classical optimization, one needs to update the parameters $\boldsymbol{\theta}$ follow the gradient to explore the minimum of the cost function $L(\boldsymbol{\theta})$. In some situations, the optimization landscape becomes flat and gradient-based techniques fail, as shown in Fig. 5.3. This problem is known as the **barren plateau** [164, 165]. Simply speaking, it is caused by the fact that the cost function is defined by the expectation value. Because it is a macroscopic physical quantity, the expectation value is insensitive to small changes of quantum states as a system size increases. Consequently, the optimization becomes difficult due to a small cost function gradient.

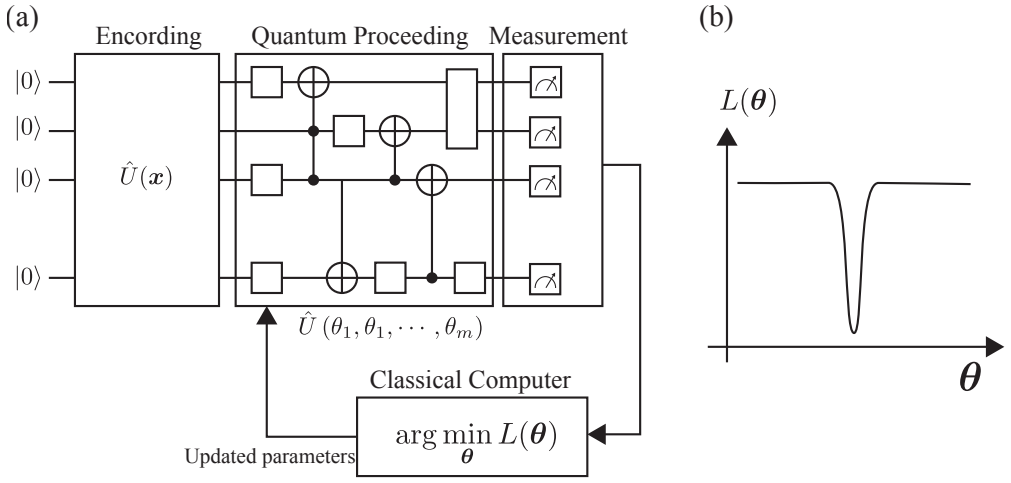

Figure 5.3: A scheme of the Quantum Circuit Learning (QCL) and a Variational Quantum Algorithm (VQA) (a), and landscape of the loss function (b): The unitary operator $\hat{U}(\boldsymbol{x})$ encodes the input data onto qubits. A quantum circuit $\hat{U}(\boldsymbol{\theta})$ parametrized by $\boldsymbol{\theta}$, transforms a quantum input state into an output state.To get the output information from the quantum layer, one measures expectation values on a computational basis. In (b) we depict the loss function $L(\boldsymbol{\theta})$ being necessary to evaluate the quantum circuit. The goal of a VQA algorithm is to update parameters $\boldsymbol{\theta}$ to minimize the loss function using the classical optimizer.

5.2.3 Quantum kernel method

One can consider a quantum kernel method [166, 167] by extending the kernel function to the inner product of quantum states: $K(\boldsymbol{x}_l, \boldsymbol{x}_m) = |\langle\phi(\boldsymbol{x}_m)|\phi(\boldsymbol{x}_l)\rangle|^2$. Generally, the quantum kernel function can be obtained by the unitary operator $\hat{U}$ of the quantum system corresponding to the non-linear map of the classical kernel. It is also used to encode the classical input into the Hilbert space:$|\phi(\boldsymbol{x}_l)\rangle = \hat{U}(\boldsymbol{x}_l)|0\rangle$. Thus, the quantum kernel function can be written as $K(\boldsymbol{x}_l, \boldsymbol{x}_m) = |\langle 0|\hat{U}^\dagger(\boldsymbol{x}_m)|\hat{U}(\boldsymbol{x}_l)|0\rangle|^2$, where $|0\rangle$ is the initial state. Its advantage is that the quantum kernel method does not require optimization of the quantum system. However, to calculate the kernel function, the quantum circuit should implement both the unitary operator for the map and its time reverse [168], which is a challenging point in operation with NISQ devices.

5.3 Quantum Reservoir Computing (RC)

As the section above shows, it is better to avoid tuning or optimizing the quantum system when performing quantum machine learning with NISQ devices. Especially in the

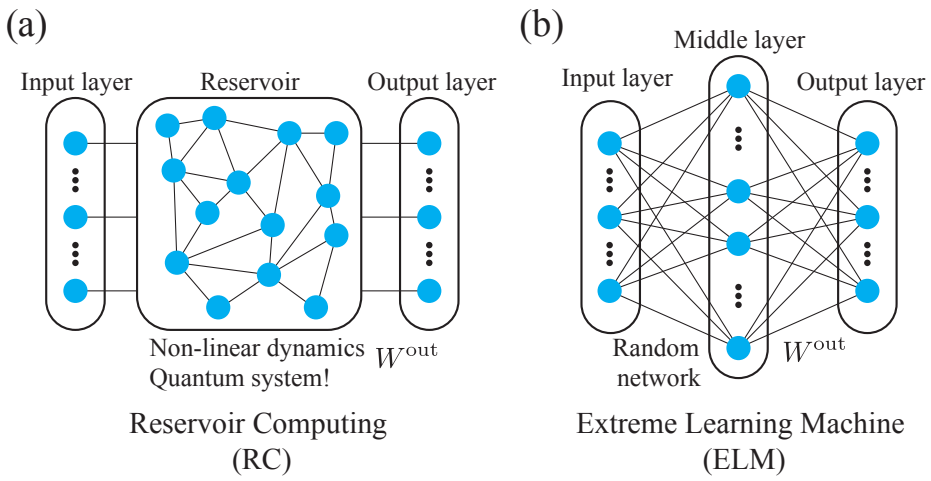

Figure 5.4: Conceptual diagram of reservoir computing (a) and extreme learning machine (b). In both models, the middle layer (reservoir) is connected to a linear classifier (W^{out}). In RC, a network of reservoirs plays the role of a recurrent network. As reservoirs, nonlinear dynamical systems and, recently, quantum systems have been considered.

quantum neural network model, although the network is considered to have sufficient complexity, it is not being used effectively due to noise during optimization. Therefore, research should be carried out to exploit its complexity. One way is quantum reservoir computing. In this section, we will discuss classical and quantum reservoir computing. In addition, we will discuss a Extreme learning Machine, which is an application of QR to static data such as images.

5.3.1 Classical reservoir computing (CRC) and Quantum RC (QRC)

In classical machine learning, to analyze the time-dependent data such as audio data and video efficiently, **Recurrent Neural Networks (RNNs)** were proposed. In RNNs, the output of the neural network unit returns is used as inputs in the next loop. In general, the network consist of an input layer, a recurrent layer, and an output layer, as shown Fig. 5.4 (a). In the learning section, the weight matrices in the recurrent layer and between the recurrent and output layers are optimized. Here, **Reservoir Computing (RC)** is a specific model of the RNNs, in which the recurrent layer is replaced by a huge nonlinear network called the reservoir. Unlike RNNs, it is not necessary to optimize the recurrent layer (reservoir), as shown Fig. 5.4 (a). As a result, it is believed that learning can be performed with much less computational cost.

In recent years, **physical reservoir computing**, in which some physical system replaces this reservoir, has been receiving much attention [169, 170, 171, 172]. Since the physical

system can be used as a computational resource, it is expected to improve energy efficiency and reduce computational costs. In classical systems, analog circuits, fluid dynamics, optical devices, and cultured cells have been investigated.

Like classical reservoirs, quantum systems are expected to be used as reservoirs [147, 148]. Here, to distinguish this model from classical systems, it is referred to as **quantum reservoir computing (QRC)**. As well as classical reservoir computing, quantum reservoir (quantum neural network) is fixed during the optimization. In QRCs, quantum systems are used to get huge neural networks. It is an essential point of QRCs that it may not require any optimization to quantum networks, unlike the QCLs using VQAs. Many different models of QRC have been proposed, e.g., networks of quantum node [146, 173, 172], a single nonlinear oscillator [174] and the Ising Hamiltonian [37].

5.3.2 Extreme learning machine (ELM)

As similar to RC for the temporal data such as movie and voice, **Extreme Learning Machine (ELM)** was proposed for static data, which consists of a huge fixed neural network and a simple classifier [175, 176, 177, 178]. Its conceptual diagram is shown in Fig. 5.4 (b). The input layer $\boldsymbol{u}$ is connected to the huge middle layer x_m $(m = 1, \cdots, N_x)$, as follows

$$x_m = f(\sum_l a_l u_l + b_m) \tag{5.8}$$

where $f(x)$ is a typical activation function such as the step function. Here, $a_l \in \mathbb{R}$ and $b_m \in \mathbb{R}$ are weights and biases between the input layer and the middle layer. In ELM, these parameters a_l, b_m are randomly generated from some probability distribution and are fixed in the optimization loop. Next, the middle layer connects to the output layer with a weight matrix W^{out}, as,

$$y_k = \sum_{m=1}^{N_x} w_{km}^{\text{out}} x_m \tag{5.9}$$

In the learning section, the weight matrix W^{out} are optimized to get the desired output,

$$\min_{W^{\text{out}}} \|\boldsymbol{T} - W^{\text{out}} \boldsymbol{X}\|. \tag{5.10}$$

Here, $\boldsymbol{T} = \left(t^{(1)^T}, \cdots, t^{(N_D)^T}\right)^T$ is the matrix of the desired outputs, and $\boldsymbol{X}$ is a matrix of all inputs of the middle layer, and is given by,

$$\boldsymbol{X} = \begin{pmatrix} x_1(\boldsymbol{u}^{(1)}) & \cdots & x_1(\boldsymbol{u}^{(N_D)}) \\ \vdots & \ddots & \vdots \\ x_{N_x}(\boldsymbol{u}^{(1)}) & \cdots & x_{N_x}(\boldsymbol{u}^{(N_D)}) \end{pmatrix}, \tag{5.11}$$

where N_D is the total number of the training samples. Using the least-squares method, we finally obtain the weight matrix

$$W^{\text{out}} = (\boldsymbol{X}^T \boldsymbol{X})^{-1} \boldsymbol{X}^T \boldsymbol{T}. \tag{5.12}$$

Unlike deep learning, the global minimum can be obtained in ELM.

Like RC, a quantum version of ELM has been proposed [170, 179]. For instance, S. Ghosh applied quantum reservoir computing to a quantum processor and showed that it can recognize entangled quantum states and simultaneously estimate various physical quantities [170]. An ELM using a quantum system is called a quantum ELM (**QELM**) [146, 173, 172, 174, 37, 180].

5.4 Quantum Reservoir Extreme Learning Machine

This section proposes the new machine learning model based on quantum neural networks, a hybrid QRC and classical ELM model. We refer to it as the **Quantum Reservoir Extreme Learning Machine (QRELM)**. Unlike the random neural networks of ELMs and QELMs, this model uses quantum many-body systems and quantum dynamics to generate neural networks. In other words, this model uses the quantum systems as the reservoir generating a non-trivial complex huge network for ELM. Thus, unlike the VQAs and quantum kernel methods, there is no need to optimize or tune the quantum circuits or quantum systems.

Because conventional quantum reservoirs have not dealt with huge classical inputs such as images, they could not be applied to practical problems. To overcome it, we insert a new encoder that can be operated in NISQ and efficiently convert huge classical information into quantum information using classical compression techniques. Thus, our QRELM can treat both classical data and quantum states as input. Unless otherwise noted, we consider classical input data in this section.

A conceptual diagram is shown in Fig. 5.5, which mainly consists of an input layer, a hidden layer, and an output layer. In this model, the input and hidden layers are quantum, and the output layer is classical. A measurement layer referred to as M-layer is inserted to convert quantum and classical information. Each element will be explained later.

5.4.1 Notation of dataset for QRELM

We design QRELM as a supervised learning model to solve classification problems and pattern recognition problems. Thus, there are two sections, learning (training) and inference (testing). The learning section uses the training data to optimize our neural network

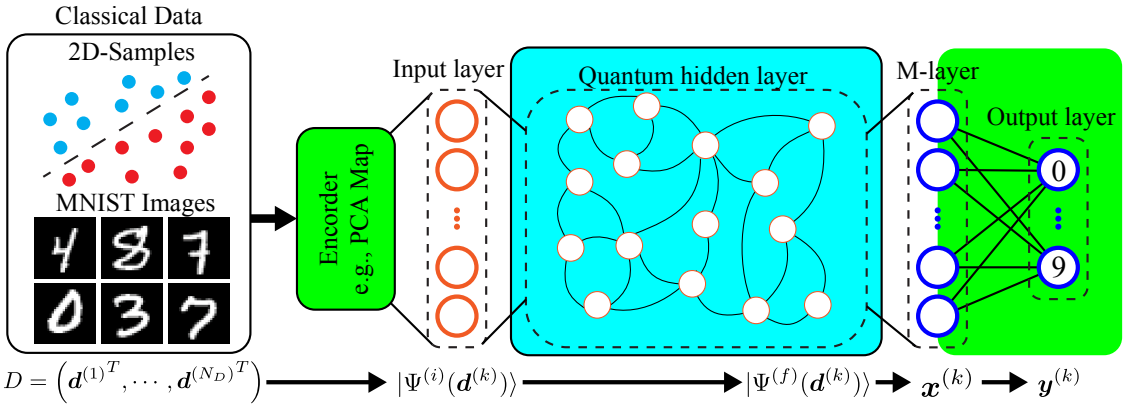

Figure 5.5: Conceptual diagram of Quantum Reservoir Extreme Learning Machine. Classical data $\boldsymbol{d}^{(l)}$ such as a sample and an image encoded into an initial state $|\Psi^{(i)}(\boldsymbol{d}^{(k)})\rangle$ of a quantum system. It changes to a final state $|\Psi^{(f)}(\boldsymbol{d}^{(k)})\rangle$ by the quantum neural network. At the M-layer, a final state is measured on a computational basis, and it converts to $\boldsymbol{x}^{(k)}$ with normalization. In the learning section, the network between $\boldsymbol{x}^{(k)}$ and an output $\boldsymbol{y}^{(k)}$ is classically optimized. Contrary, in the inference, $\boldsymbol{y}^{(k)}$ returns the probability for each class.

to solve a given problem, such as the classification problem. Thus, this section will explain the notation of the data set used in training.

The training dataset contains dataset $\boldsymbol{D}$ of examples, e.g., images, that we want to classify, and corresponding training label set (answers) $\boldsymbol{T}$. Here, $\boldsymbol{D}$ and $\boldsymbol{T}$ are respectively represented by

$$\boldsymbol{D} = \begin{pmatrix} \boldsymbol{d}^{(1)^T} \\ \vdots \\ \boldsymbol{d}^{(k)^T} \\ \vdots \\ \boldsymbol{d}^{(N_D)^T} \end{pmatrix}, \qquad \boldsymbol{T} = \begin{pmatrix} \boldsymbol{t}^{(1)^T} \\ \vdots \\ \boldsymbol{t}^{(k)^T} \\ \vdots \\ \boldsymbol{t}^{(N_D)^T} \end{pmatrix}, \tag{5.13}$$

where $\boldsymbol{d}^{(k)}$ and $\boldsymbol{t}^{(k)}$ are data, and the corresponding label of a k-th example ($k = 1, \cdots, N_D$), and $(a)^T$ is the transpose of a. In this section, we consider a general classification problem with multiple classes. We use the one-hot representation of the training labels, which is commonly used in ML. In this representation, labels can be interpreted as the probability of belonging to each class. For example, if there are two classes, the training labels should be $\boldsymbol{t}^{(k)} = [1, 0]^T$ or $\boldsymbol{t}^{(k)} = [0, 1]^T$. Correspondingly, in the inference

section (or testing), one can interpreter an output $\boldsymbol{y}^{(k)}$ as a probability, as follows,

$$\boldsymbol{y}^{(k)} = \begin{pmatrix} \text{Probability of being the 1st-class} \\ \text{Probability of being the 2nd-class} \end{pmatrix}. \tag{5.14}$$

It implies that output from the final output layer should be fit with probability representation. Therefore, to satisfy this, an activation function has been inserted in our QRELM, as we will see later.

5.4.2 Classification using QRELM

First, if the input data is classical data, it is necessary to encode it into the **(quantum) input layer**, which is a quantum state. The encoding part will be explained in detail in the next section. We use a new encoder to efficiently convert classical information into quantum information. With the new encoding, classical information is stored in the coefficients of the computational basis. For example, consider classical data ($\boldsymbol{d}^{(k)}$) and quantum systems with N-qubits. Now, an initial state with classical information can be written as follows,

$$|\Psi^{(i)}(\boldsymbol{d}^{(k)})\rangle = \sum_l a_l^{(i)}(\boldsymbol{d}^{(k)})|l\rangle, \tag{5.15}$$

where $|l\rangle$ is the computational basis and $a_l^{(i)}$ are its coefficients.

Since this model uses a neural network generated by a quantum reservoir, it can be prepared by the system's dynamics or quantum circuits using gates. Using the neural network, the initial state $|\Psi^{(i)}(\boldsymbol{d}^{(k)})\rangle$ is mapped to a final state $|\Psi^{(f)}(\boldsymbol{d}^{(k)})\rangle$.

To perform optimization in the classical part, converting quantum information into classical information is necessary. Thus, we insert the measurement layer called the **M-layer**. Due to the stochastic nature of quantum states, single-shot measurement cannot provide information on quantum neural networks. Therefore, the layer needs to take a statistic. In this proposal, we measure the population density in the computational. Thus, the M-layer outputs 2^N-classical neurons, by measurement, as follows,

$$\boldsymbol{p}(\boldsymbol{d}^{(k)}) = (p_1, p_2, \cdots, p_{2^N})^T = \left(\left|a_1^{(f)}\right|^2, \left|a_2^{(f)}\right|^2, \cdots, \left|a_{2^N}^{(f)}\right|^2\right)^T, \tag{5.16}$$

where $(\cdots)^T$ means transpose.

It is easily predicted that as the size of the quantum system increases, the population density becomes exponentially smaller: $p_l \sim 1/2^N (lin1, \cdot, 2^N)$. Consequently, the classical optimization becomes unstable. Thus, the M-layer has classical data processing to stabilize the optimization process in the classical part ($\boldsymbol{p} \to \boldsymbol{x}$). In this model, we

normalize the population density to have it's average 0 and variance 1, as follows,

$$x_i = \frac{2^N p_l - 1}{\sqrt{2^N \sum_l p_l^2 - 1 + \delta}}, \tag{5.17}$$

where we used $\sum_l p_l = 1$. Here, $\delta = 10^{-7}$ is a parameter to avoid divergence. Finally, the M-layer returns the classical output $\boldsymbol{x}(\boldsymbol{d}^k)$.

The classical neural network connects the M-layer $\boldsymbol{x}(\boldsymbol{d}^{(k)})$ and the output layer $\boldsymbol{y}(\boldsymbol{d}^{(k)})$ in the classical part. In the inference part, the output layer returns the probability of belonging to each class. While in the training part, we optimize the network using classical techniques using the label ($\boldsymbol{t}^{(k)}$).

5.4.3 Quantum reservoir and Quantum hidden layer in QRELM

In the QRELM, a quantum reservoir provides a huge neural network defined by Altaisky's representation [159]. For example, an initial state can be written as a vector using computational basis, as follows,

$$|\Psi^{(i)}(\boldsymbol{d}^{(k)})\rangle = \begin{pmatrix} a_1^{(i)} \\ a_1^{(i)} \\ \vdots \\ a_{2^N}^{(i)} \end{pmatrix} = \begin{pmatrix} \mathrm{Re}(a_1^{(i)}) + i\mathrm{Im}(a_1^{(i)}) \\ \mathrm{Re}(a_2^{(i)}) + i\mathrm{Im}(a_2^{(i)}) \\ \cdots \\ \mathrm{Re}(a_{2^N}^{(i)}) + i\mathrm{Im}(a_{2^N}^{(i)}) \end{pmatrix} \tag{5.18}$$

where $a_l^i \in \mathbb{C}$ are complex values. Similarly, in the computational basis, a unitary $\hat{U}$ generated by QR is written as,

$$\hat{U} = \begin{pmatrix} u_{11} & u_{12} & \cdots & u_{12^N} \\ u_{21} & u_{22} & \cdots & u_{22^N} \\ \vdots & \vdots & \ddots & \vdots \\ u_{2^N 1} & u_{2^N 2} & \cdots & u_{2^N 2^N} \end{pmatrix} \tag{5.19}$$

where $u_{lm} \in \mathbb{C}$ are complex values. Thus, the unitary transformation between the initial state $|\Psi^{(i)}(\boldsymbol{d}^{(k)})\rangle$ and a final state $|\Psi^{(f)}(\boldsymbol{d}^{(k)})\rangle$ by the unitary matrix $\hat{U}$ can be written as

$$|\Psi^{(f)}\rangle = \hat{U}|\Psi^{(i)}\rangle \rightarrow a_l^{(f)} = \sum_m^{2^N} u_{lm} a_m^{(i)} \tag{5.20}$$

By comparing the above transformation with Eq. (5.1), we can see that it is equivalent to a classical neural network, except that there is no activation function and the values are

complex. However, as we saw above, the measurement process can be seen as a nonlinear activation function for a probability amplitude: $p_l = f(a_l) = |a_l|^2$.

In general, as quantum system's size increases, its unitary size exponentially increases. Thus, using the large quantum reservoir, it is possible to generate an exponentially huge neural network. Additionally, since unlike VQAs, the quantum part is fixed, our model is a kind of ELM.

5.4.4 Classical neural network and optimization in QRELM

In our model, we connect between the M-layer and the output-layer via a classical neural network $\boldsymbol{W}$ refereed to as **one layer neural network (ONN)**. Thus, $x_l^{(k)}$ linearly transforms to $u_l^{(k)}$, as follows,

$$u_l^{(k)} = \sum_{i=1}^{2^N} x_i^{(k)} w_{il} + b_l \tag{5.21}$$

where $\boldsymbol{B} = (b_1, \cdots, b_m)$ is a bias vector. To interpreter the output layer as probability of each classes, we use the soft-matrix function as an activation function,

$$y_l^{(k)} = g(u_l^{(k)}) = \frac{\exp\left(u_l^{(k)}\right)}{\sum_i \exp\left(u_i^{(k)}\right)}. \tag{5.22}$$

Unlike the classical ELMs and other QELMs, since our model includes the non-linear activation function (soft-matrix), it is impossible to use the least-squares method to find the global minimum. Therefore, we use a **gradient method**, which can find a minimum of a given function. Compared to the least-squares method, the gradient method may require a longer time for learning because it iterates until the solution converges. Furthermore, one might expect that a global minimum cannot be found. However, in the QRELM, since feature space is sufficiently expanded by the quantum system and the optimized network is linear, we believe that the convergence theorem [181] and the universal approximation theorem [154, 155] efficiently work. Thus, that learning will be completed in a finite number of iterations, and a minimum value will be obtained. Furthermore, due to recent improvements in classical optimization algorithms, we believe that a solution with this amount of computation can be obtained with sufficient speed.

To optimize the ONN using the gradient method, we need to define a cost function or loss function that evaluates the difference between the outputs $\boldsymbol{y}$ and training labels $\boldsymbol{t}$. While various cost functions have been proposed for different tasks, we use cross-entropy, which is widely used for multi-class classification problems,

$$L^{(k)} = -\sum_{l}^{N_c} t_l^{(k)} \ln\left(y_l^{(k)}\right) \tag{5.23}$$

where N_c is the total number of classes. This function takes a smaller value as the distribution of $\boldsymbol{y}^{(k)}$ is closer to the label $\boldsymbol{t}^{(k)}$.

To optimize the above loss function. we employ the simplest and most widely used the **stochastic gradient descent (SGD)**. From this algorithm, the update process of the weight matrix $\boldsymbol{W}$ and bias vector $\boldsymbol{B}$ are given by,

$$\begin{aligned} w_{ij}^{(\text{new})} &= w_{ij}^{(\text{old})} - \eta \frac{\partial L^{(k)}}{\partial w_{ij}} \\ b_{i}^{(\text{new})} &= b_{i}^{(\text{old})} - \eta \frac{\partial L^{(k)}}{\partial b_{i}} \end{aligned} \tag{5.24}$$

where $L^{(k)}$ is the loss function of the output $\boldsymbol{y}^{(k)}$ of k-th sample, and η is a learning rate $(0 < \eta < 1)$. Here, we note that there are, of course, other optimization algorithms. Using a modified algorithm of the basic SGD, the performance of the QRELM may change. However, in this Chapter, we use it to simplify the classical part.

The loss function $L^{(k)} = L(\boldsymbol{y}^{(k)})$ is a function of an output $\boldsymbol{y}$ which is a function of the M-layer output $\boldsymbol{x}$. Thus, applying the chain rule, we have

$$\begin{aligned} \frac{\partial L^{(k)}}{\partial w_{ij}} &= x_i^{(k)}(y_j^{(k)} - t_j^{(k)}) \\ \frac{\partial L^{(k)}}{\partial b_i} &= (y_i^{(k)} - t_i^{(k)}), \end{aligned} \tag{5.25}$$

where $x_i^{(k)} \in \boldsymbol{x}^{(k)} (i = 1, \cdots 2^N)$ is the output at the M-layer.

Furthermore, in this study, we use the mini-batch method to speed up the optimization and to avoid local minimum. We randomly extract M-training data ($M < N_D$) and update the parameters, where N_D is the total number of the training data, and M is the mini-batch size. With this as a set, update the parameters iteratively until the cost function converges. Here, a loss function is now the average of the loss function for each sample: $L = \sum_{k=1}^{M} L^{(k)}/M$. Using the new loss function, the derivatives for the weight matrix and the bias are given by

$$\begin{aligned} \frac{\partial L}{\partial w_{ij}} &= \frac{1}{M} X^T \cdot \begin{pmatrix} \vec{y}^{(1)} - \vec{t}^{(1)} \\ \vdots \\ \vec{y}^{(M)} - \vec{t}^{(M)} \end{pmatrix} \\ \frac{\partial L}{\partial b_i} &= \frac{1}{M} \sum_{l}^{M} \frac{\partial L_l}{\partial b_i} \end{aligned} \tag{5.26}$$

where $X = \left(\left(\boldsymbol{x}^{(1)}\right)^T, \cdots, \left(\boldsymbol{x}^{(M)}\right)^T\right)^T$. Here we note that, the derivative for the weight matrix is written in the matrix representation.

5.5 Encoder in the QRELM and PCA Map

When using quantum systems as a classifier, an unavoidable part is encoding classical data into quantum states. If there is a fault-tolerant quantum computer, one can use an arbitrary quantum state such as the entangled state to encode classical information such as images [182, 183]. Because one can use the entire Hilbert space, which is generally much bigger than the classical data size, one can encode all classical data information into a quantum state with a few qubits [182, 183].

However, in NISQ devices, it is hard to prepare an arbitrary quantum state such as an entangled state due to the noise effect. On the contrary, the fidelity of a single gate is very high in NISQ devices. Thus, using product states prepared with single quantum gates is more reasonable to encode classical data. Additionally, we believe that the complexity generated by the dynamics of a quantum system is essential, so the initial states do not need to be already complex such as entangled states. This approach is similar to encoders proposed in image processing research using quantum systems [184, 183].

5.5.1 Encoder using the Bloch sphere

First, to simply discussion, let us consider a samples (points) in a two-dimensional space as show in Fig. 5.1 (c) and one qubit. In this case, a k-th points ($\boldsymbol{d}^{(k)}$) are given by two values $(d_1^{(k)}, d_2^{(k)})$. Next, any state of a single qubit can be represented by the Bloch sphere and is written by,

$$|\Psi\rangle = \cos\left(\frac{\theta}{2}\right)|0\rangle + e^{i\phi}\sin\left(\frac{\theta}{2}\right)|1\rangle \tag{5.27}$$

with two angles (θ, ϕ).

Now, it is natural to use a map between two coordinates (d_1, d_2) and two angles (θ, ϕ) as an encoder. Here, the surface of the Bloch sphere is closed, but the data feature space is generally flat. Therefore, to efficiently map a plane to a sphere, we only use the hemispherical surface of the Bloch sphere. The map between the data point $(d_1^{(k)}, d_2^{(k)})$ and two angles $(\theta^{(k)}, \phi^{(k)})$ is give by,

$$\theta^{(k)} \text{ or } \phi^{(k)} = \frac{\pi(d^k_{1\text{ or }2} - \min[\boldsymbol{d}]_{1\text{ or }2})}{(\max[\boldsymbol{d}]_{1\text{ or }2} - \min[\boldsymbol{d}]_{1\text{ or }2})}. \tag{5.28}$$

Here, because the training data set: $\boldsymbol{d} = \left(\boldsymbol{d}^{(1)}, \cdots, \boldsymbol{d}^{(k)}, \cdots\right)$ is given in advance, it is

possible to calculate the minimum $\min[\boldsymbol{d}]_{1\text{ or }2}$ and the maximum $\max[\boldsymbol{d}]_{1\text{ or }2}$ from the training data $(d_1^{(k)}, d_2^{(k)})$ in advance and use them in the inference section (testing).

Now, the initial state of the point $(\boldsymbol{d}^{(k)})$ with N-qubits can be given by,

$$|\Psi^{(i)}(\boldsymbol{d}^{(k)})\rangle = |\Psi\rangle_1(\boldsymbol{d}^{(k)}) \otimes |+\rangle_2 \otimes \cdots \otimes |+\rangle_N. \tag{5.29}$$

Here, we assume that the state except for the first qubits are $|+\rangle_l = (|0\rangle + |1\rangle)/\sqrt{2}$. Alternatively, one can consider a state,

$$|\Psi^{(i)}(\boldsymbol{d}^{(k)})\rangle = |\Psi(\boldsymbol{d}^{(k)})\rangle_1 \otimes |\Psi(\boldsymbol{d}^{(k)})\rangle_2 \otimes \cdots \otimes |\Psi(\boldsymbol{d}^{(k)})\rangle_N. \tag{5.30}$$

Here, we emphasize that a training data $(d_1^{(k)}, d_2^{(k)})$ are non-linearly encoded into a quantum system represented by $\cos\left(\theta^{(k)}/2\right), \sin\left(\theta^{(k)}/2\right)$ and $e^{i\phi^{(k)}}$ in computational basis. It indicates that this encoder generates a non-trivial non-linearity in the classifier.

Lastly, we note that there are different encoding methods [184, 183] similar to Eqs. (5.29) (5.30), but without phases. Thus, unlike these ways, one can encode two classical points into a qubit so that the N-qubits system can maximally encode $2N$ components of classical data in our encoding way.

5.5.2 General classical input and PCA Map

Generally, classical data such as images have more information (such as pixels) than twice the total number of qubits (2N). Thus, in the study of quantum image processing, an encoder has been proposed, using entanglement states with ancillaries [182, 183]. But, in this work, to encode images into quantum states still using single rotations, we need to compress them into $2N$. In addition, in the machine learning, it is not necessary to keep all the information of the classical data.

There are a lot of different classical compression technologies, and one needs to choose the appropriate one for the purpose after understanding the advantages of each. Since the purpose of our work is to develop a classifier, we use the **principal component analysis (PCA)**, which is a linear transformation to the direction that maximizes the variance of the data and does not lose the features of classical data. More detail is explained in Appendix E. We refer to it as a **PCA** map.

For example, let us consider images with $L \times M$ pixels, where $LM \gg N$. An image data labelled k can be written as a LM-dimensional vector: $\boldsymbol{I}^{(k)} = \sum_{l=1}^{LM} c_l^k \boldsymbol{e}_l$. Now, the PCA map complex it to the $2N$-dimensional vectors:$\boldsymbol{I}^{(k)} \approx \sum_{l=1}^{2N} \tilde{c}_l^k \boldsymbol{v}_l$, where $\boldsymbol{v}_l$ are new basis set which nicely reflects information of images. We use these $\tilde{c}_l$ to prepare the initial states of N-qubits. The procedure after the PCA map is the same as that of the two-dimensional case. More precisely, in the PCA map, the first N-principle components

$\tilde{c}_l$ ($l = 1, \cdots, N$) are encoded into θ_l of each qubit, and the remaining components ($l = N+1, \cdots, 2N$) are encoded into their phase ϕ_l.

The role of PCA described above can be viewed as a feature extraction in the QRELM, which efficiently finds features from data such as images. Similar studies have been conducted in classical ELM [185, 186]. The ELM works as an extended classifier in these studies, and feature extraction is done using previously optimized networks, e.g., auto-encoders and convolutional neural networks (CNNs) [187]. Such a model can find features more efficiently, and the classifier can be optimized faster by ELM than other classifiers. We believe in the classification task, it would be more efficient to optimize feature extraction on a classical computer and avoid optimizing the quantum circuit than complete quantum classifiers.

5.6 Models for quantum reservoirs

In the next section, we will use four different quantum reservoirs to numerically evaluate the dependence of quantum reservoirs on the performance of the QRELM. Here, we introduce the quantum reservoirs we will use.

5.6.1 2T-Discrete Time Crystal

Recently, in the study of quantum reservoir computing, it was pointed out that dynamical phase transitions can improve reservoir computing performance [37]. Similarly, we expect that the dynamical phase can generate a non-trivial neural network for the QRELM.

To see the phase transition effect on the QRELM performance, we employ the discrete-time crystals discussed in the Chapter 2 as a reservoir. It is a periodically driven system with N sites and its time-periodic Hamiltonian with a period $T = T_1 + T_2$ is given by,

$$\hat{H}(t) = \begin{cases} \hat{H}_1 = \hbar g(1-\epsilon)\sum_l \sigma_l^x & (0 \le t < T_1) \\ \hat{H}_2 = \hbar \sum_{lm} J_{lm}^z \sigma_l^z \sigma_m^z & (T_1 \le t < T), \end{cases} \tag{5.31}$$

where σ_l^μ with $\mu \in \{x, y, z\}$ are the usual Pauli operators at the l-th site. Here, J_{lm}^z are the coupling strength between l-th and m-the sites. In this numerical experiments, we employ $J_{lm}^z = J_0/|l-m|^\alpha$, where J_0 is the coupling constant and α is the decay rate.

As we saw in Chapter 2, the 2T-DTC shows a phase transition from the (MBL or pre-thermal) DTC phase to the MBL or the thermal state by changing the parameter ϵ. Because of the absence of the disorder, our model shows the phase transition between the pre-thermal DTC and the thermal state. Thus, we expect that the model can evaluate

how the performance of the QRELM changes due to the phase transition. Furthermore, recently, a new complexity discovery has been reported in 2T-DTC, which is called scale-free networks [38]. They showed that at the critical point, the point where the DTC phase melts, its effective Hamiltonian shows scale-free in the graph representation. In classical reservoir calculations, it is known that the performance improves at the edge of chaos which lies between the chaos due to nonlinear dynamics and periodic dynamics. Moreover, it has been recently reported that neural networks are scale-free in reservoirs when the dynamics property shows the edge of chaos. Therefore, although the state dynamics are linear in quantum mechanics, the scale-free nature of 2T-DTC is expected to contribute significantly to the performance of the QRELM.

Because of the periodically driven system, one can apply the Floquet theorem to Eq. (5.31), as discussed in Chapter 2. Here, the Floquet operator, which is the unitary operator for one period, is given by,

$$\hat{F} = \mathcal{T} \exp\left(-\frac{i}{\hbar}\int_0^T \hat{H}(\tau)d\tau\right) = e^{-\frac{i}{\hbar}\hat{H}_1 T_1} e^{-\frac{i}{\hbar}\hat{H}_2 T_2} \tag{5.32}$$

where $\mathcal{T}$ is a time ordering operator.

5.6.2 Circular unitary ensemble (CUE)

Recently, several papers have been published that claim to experimentally demonstrate the quantum superiority in programmable quantum circuits [20, 188]. Quantum supremacy refers to the ability of a quantum processor to perform a given task more efficiently than a classical one [189]. They used a random sequence of gates to sample the **Haar-random** quantum states. These states are uniformly distributed with Haar measure in the Hilbert space [189]. Thus it is considered to be difficult to simulate on a classical computer.

Similarly, we consider a unitary operator sampled from all unitary matrices with Haar measure. It is known as the **circular unitary ensemble (CUE)** [190, 191]. Here, we note that by using sampled unitary operators from the CUE and acting them to a fixed quantum state, one can generate Haar-random states. It means that to generate a unitary operator in CUE, one needs to use random quantum gates [192] as similar to gates in supremacy experiments [20]. Thus, we believe that a unitary in the CUE has the same complexity as that of quantum supremacy. In the QRELM process, we chose a unitary operator $\hat{U}_{\text{CUE}}$ from the CUE and used it as a quantum reservoir.

The CUE is ensemble of all unitary matrices with Haar measure. For example, consider the CUE for $2^N \times 2^N$-unitary. Now, mathematically, its probability distribution

$P(\theta_1, \theta_2, \cdots, \theta_{2^N})$ of the eigenvalues is given by,

$$P(\theta_1, \theta_2, \cdots, \theta_{2^N}) \sim \prod_{1 \leq k < \leq 2^N} \left| e^{i\theta_k} - e^{i\theta_j} \right|^2 \tag{5.33}$$

where $e^{i\theta_k}$ with $0 \leq \theta_k < 2\pi$ for $k = 1, \cdots, 2^N$ are the eigenvalues of $\hat{U}_{\text{CUE}}$. In the numerical experiment, to generate a unitary operator sampled from the CUE, we use the QR decomposition [193].

5.6.3 Non-interacting spin systems

We believe that many-body interactions can improve the performance of quantum neural networks because they allow states to explore widely in Hilbert space. Thus, let us consider the spin network without any many-body interaction to explore this point efficiently. In other words, the system can be interpreted as a system with N-free spins. Its unitary $\hat{U}_{\text{S-CUE}}$ is constructed by the tensor product of small unitary operators $\hat{U}_{SU(2)}$,

$$\hat{U}_{\text{S-CUE}} = \hat{U}_{SU(2)} \otimes \hat{U}_{SU(2)} \otimes \cdots \otimes \hat{U}_{SU(2)} \tag{5.34}$$

where $\hat{U}_{SU(2)}$ is a sampled unitary from the CUE of single qubits. Thus, the above unitary represents the N-qubits system without many-body interactions. We refer to the system as the S-CUE model.

5.6.4 Cauchy random Hamiltonian (Cauchy model)

Any unitary operator can be expressed as $\hat{U} = e^{-i\hat{G}}$ using the Hermitian matrix $\hat{G}$. In quantum mechanics, this matrix corresponds to the system's Hamiltonian with appropriate units ($\hat{G} = \hat{H}t/\hbar$, where t is time). From the graphic representation [38], one can consider that the Hamiltonian represents a transition network between quantum neurons. Here, consider one artificial unitary whose $\hat{G}$ follows a Cauchy distribution. Here, its density function is given by,

$$f(x; x_0, \gamma) = \frac{1}{\pi\gamma} \left[\frac{\gamma^2}{(x - x_0)^2 + \gamma^2} \right], \tag{5.35}$$

where x_0 and γ are the location parameter and the scale parameter, respectively. To simplify the discussion, we chose x_0 and γ to be $x_0 = 0$ and $\gamma = 1$, which is known as the standard distribution. Therefore, each element G_{lm} $(l \leq m)$ of the Hamiltonian can be represented by,

$$G_{lm} = x + iy, \quad \text{and} \quad G_{ml} = G_{lm}^*, \tag{5.36}$$

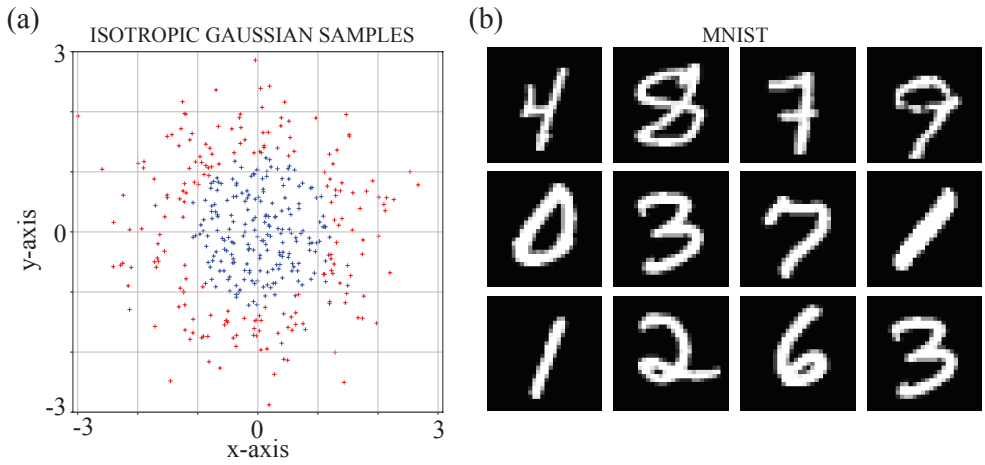

Figure 5.6: Isotopic Gaussian Samples (IGS) in 2D-space (a) and digit images of MNIST dataset in which there are 60,000 images as for training and 10,000 images for testing (b).

where $x, y \in f(x; 0, 1)$ and G^*_{lm} means the complex conjugate of G_{lm}. Here, we note that since G is a Hermitian, when $l = m$, the imaginary part is zero ($y = 0$). The main characteristic of the Cauchy distribution is that it has a large spread, namely having a long tail. Consequently, some configurations are more strongly coupled than others. This property is clearly different from the unitary operator $\hat{U}_{\text{CUE}}$, where all quantum states are treated equally, and thus we believe the cauchy model can represent more natural physical systems.

5.7 Numerical experiments

We have seen that quantum reservoir provides a huge neural network. We believed that the performance of the QRELM is dependent on its complexity. Thus, in the this section, we will evaluate the performance of QRELM with four different quantum reservoirs by numerical experiments.

5.7.1 Non-linear separability in QRELM

Because of the enormous feature space of the neural network generated by the quantum reservoir, we believe the QRELM can solve the non-linear classification problems, similar to the non-linear SVM. Thus, we consider the classification of the isotropically Gaussian distributed samples (IGS) with two classes (red and blue) in two-dimensional space, as shown in Fig. 5.6. This classification problem has been used widely in other QR and QML studies [194, 168].

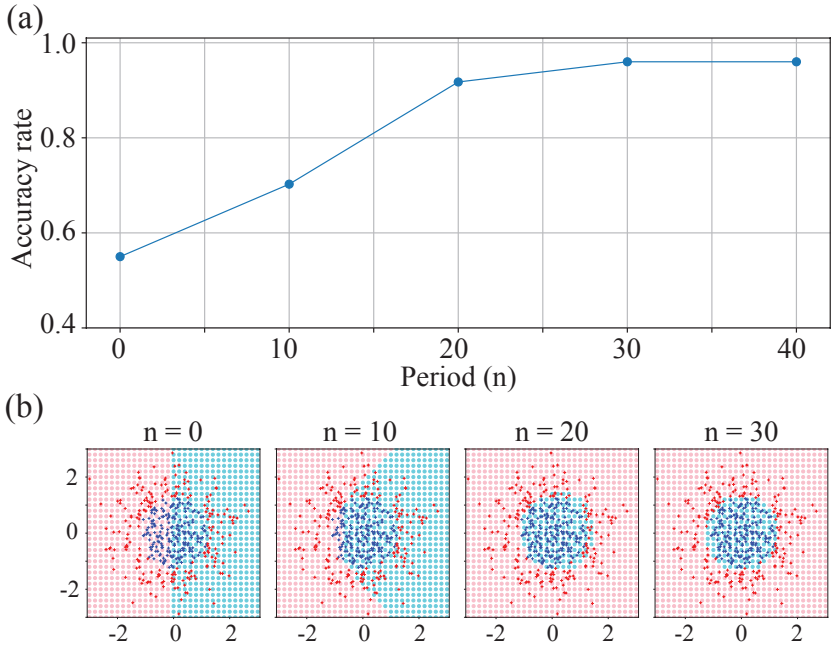

Figure 5.7: Performance of the 2T-DTC against IGS: the training accuracy rate of the classification vs. periods (a), and the classification results for different periods $nT = 0, 10, 20$ and 30 (b). The parameter are set as $J_0^z T = 0.06$ and $\epsilon = 0.02$ with $\alpha = 1.51$.

We employ the 2T-DTC with 6-sites as an example to demonstrate IGS classification. With the experiment in trapped ions [2] in mind, we set each parameter to $\epsilon = 0.02$ and $J_0 T = 0.06$ with $\alpha = 1.51$. Fig. 5.7 (b) shows the classification accuracy versus the number of periods (n). We see that the quantum system must be sufficiently time-evolved to obtain a neural network with high expressive power from the quantum system. For example, at $nT = 0$, the representativeness of the network is very poor, and only linear separation is possible. On the contrary, at $nT = 30$, the network has much representativeness to classify IGS with nearly 100%.

Since the QRELM has one classical optimized neural network, it is guaranteed to solve any linear separation problem. Contrary, it is opaque for non-linearity problems. But, the above result implies that combining the linear classifier with the quantum neural network giving huge feature space, can solve non-linear problems. The mechanism is very similar to that of the non-linear SVM.

5.7.2 Comparison of the performance of four QRs using MNIST

The above demonstration with IGS shows that the QRELM can solve non-linear problems. However, because the previous example is too simple to evaluate the quantum system

	Training accuracy				Testing accuracy			
	DTC	CUE	CAU	S-CUE	DTC	CUE	CAU	S-CUE
Average	0.998	0.998	0.998	0.755	0.973	0.973	0.975	0.752
Best	0.998	0.999	0.998	0.802	0.974	0.974	0.976	0.794

Table 5.1: Performance of four quantum reservoirs against MNIST. The result of DTC is for $\epsilon = 0.02$. Here, the average and the best records are taken for 90 and 100 epochs. The parameter are set as $J_0^z T = 0.06$ with $\alpha = 1.51$

dependency of the performance, here we apply it to a more complex problem, classification of the MNIST dataset [46], which is closer to real-world issues. This data set consists of digit images from 0 to 9, as shown in Fig. 5.6 (b). There are 60,000 images for training and 10,000 images for testing.

Although the handwritten digits are 784-dimensional input vectors, they can be efficiently represented with about 20 principal components using the PCA. Thus, to encode them into quantum states efficiently, we consider $N = 11$ qubits. It means that $2^{11} = 2048$ neurons from the quantum network are used to optimize the classical network. We employ four quantum reservoirs explained in the previous section to see the system dependency.

Next, let us explain the setup for the 2T-DTC model. Like the previous classification, with the experiment in the trapped ions in mind, we employ the weak coupling $J_0^z T = 0.06$ with $\alpha = 1.51$. Given the previous results of the IGS classification with 2T-DTCs, to generate the sufficiently complex neural network, we consider the Floquet operator with 100 periods ($\hat{F}^{100}$). In this section, we consider the 2T-DTC at the critical point, as am example. As discussed in Chapter 2, the critical point of the 2T-DTC are characterised by the parameter $\delta_x = \epsilon\pi/J_0^z T \sim 1$, thus we consider the 2T-DTC with a rotational error $\epsilon = 0.02$, where $\delta_x = 1.05$.

Results of the QRELM performance for all reservoirs are summarized in Table 5.1. Here, the average and best accuracy are taken from 90 to 100 epochs.

First, let us see the performance of the CUE and the Cauchy models. Both models are well-trained, as shown in Table 5.1, and their testing accuracy rate is sufficiently high, over 97.0%. Here, it is interesting to compare our results with the classical classifiers. However, since QRELM uses a quantum system as a neural network, it is difficult to find its classical counterpart directly. Thus to simplify the comparison, we compare our results with the classical ELM (CELM) with $784 - 2048 - 10$ neurons. Here, a random neural network is classically generated between an input and a hidden layer in the CELM. To keep the conditions the same as in QRELM, we also use the soft-max function and optimize it with SGD. The performance of the CELM are about 100% (training) and 95.5% (testing), respectively. It implies that our quantum random neural network in QRELM has more

expressive power than the CELM.

Interestingly, the CUE model is better than the Cauchy model in the training part. However, the Cauchy model performs better than the CUE model in the test section. It indicates that the Cauchy model has less overfitting than the CUE model for the MIST dataset. We believe that its property comes from the difference of the quantum neural networks. Since the QRELM performance depends on several factors such as quantum systems, activation functions, classical classifiers, and classification problems, it is hard to evaluate slight differences between models. However, we would like to point out the following point. There is no specific configuration because the CUE model can generate Haar-random states. In other words, all configuration is treated equally. While, in the Cauchy model, the transition strength of some configurations becomes higher than others due to the long tail of the Cauchy distribution. As a result, the distribution of the neurons' values also takes a more spread form. It is similar to the initialization problem of the neural network in ML [195, 196] and ELM [110]. In other words, we can expect that individual neurons in the Cauchy model have high expressive power.

Next, let us see the performance of the S-CUE model. To encode the classical information (MNIST digit images) to quantum information, we use one-qubit gates (rotation gates). Thus, because the unitary $\hat{U}_{\text{S-CUE}}$ randomly rotates each qubit, the encoding information at the initial state may be broken. Consequently, as shown in Table 5.1, the the S-CUE model doesn't work well in training and testing.

Finally, let us briefly see the performance of the 2T-DTC. We see that the performance of the test at the critical point of the 2T-DTC is comparable to the CUE model, as shown in Table. 5.1. It indicates that the dynamics of quantum many-body systems can be used to generate a neural network with high-expressive power without using random quantum circuits, which are challenging to implement in NISQ, such as random gates.

5.7.3 ϵ-dependence of 2T-DTCs and ZZ-Ising model

In the previous section, we have seen the performance of the 2T-DTC at the critical point. This section will further investigate the performance of the quantum neural network generated by 2T-DTC and investigate the ϵ-dependence of its quantum neural network. Additionally, we will use the Ising model introduced in Chapter 2, which effectively governs the discrete-time dynamics of 2T-DTCs to investigate 2T-DTCs. We will show that the rotational error ϵ and the U(1)-symmetry play essential roles in 2T-DTCs to generate a quantum neural network with high expression power.

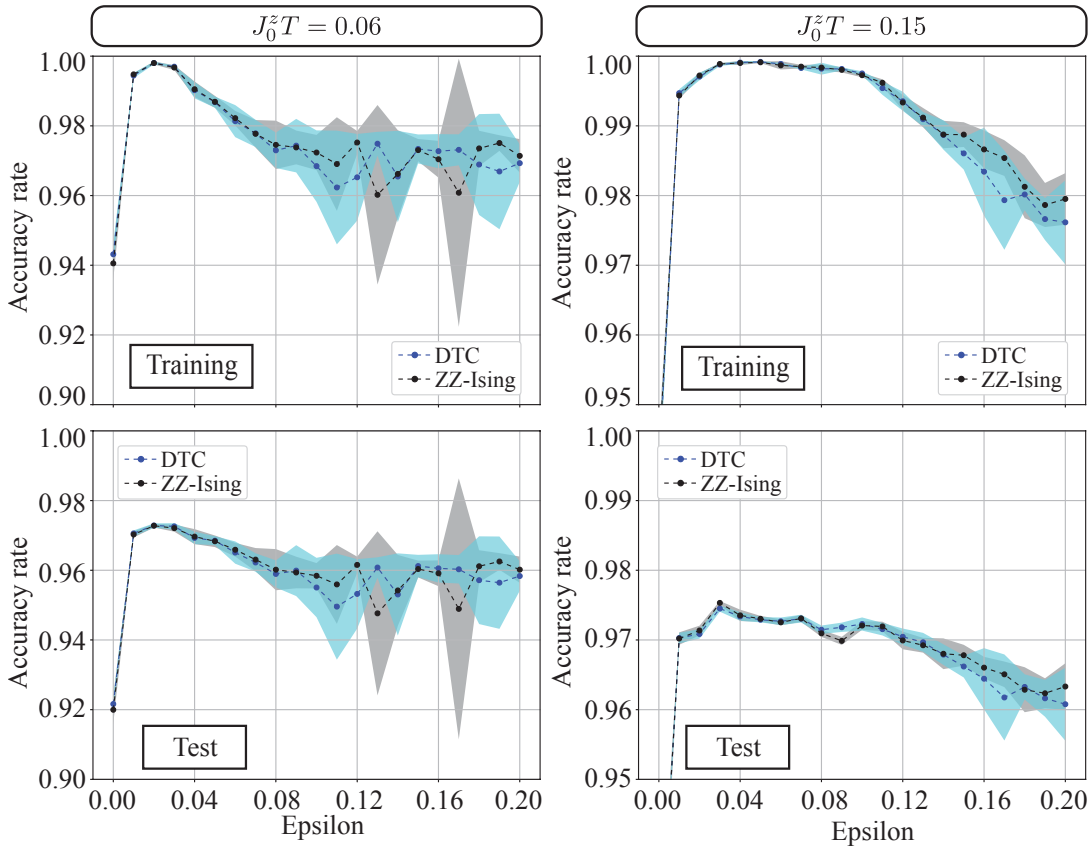

Figure 5.8: Accuracy rates of the 2T-DTC and the ZZ-Ising with $N = 11$ sites. The black and blue lines show the average accuracy rates for the 2T-DTC and the ZZ-Ising models with different rotational errors ranging from $\epsilon = 0.0$ to $\epsilon = 0.2$, and the blue and gray shadows are the corresponding standard deviations. We consider the weak ($J_0^z T = 0.06$) and strong ($J_0^z T = 0.15$) interactions. Here, the average and the standard deviation are taken for 90 and 100 epochs.

2T-DTCs

To investigate the ϵ-dependency in detail, we set its range from $\epsilon = 0.0$ to $\epsilon = 0.2$. Here, since the parameter δ_x is the balance between the rotation error ϵ and the interaction J_0^z, we compare the performance of 2T-DTCs with weak ($J_0^z T = 0.06$) and strong ($J_0^z T = 0.15$) interactions cases to obtain further numerical evidence. The expected critical point is around $\epsilon = 0.01 \sim 0.02$ and $\epsilon = 0.04 \sim 0.05$ for each strength, respectively.

Results are shown in Fig. 5.8. We see that in both interaction strength, training, and testing performance become high around its critical point. Furthermore, interestingly, the strong coupling case tends to have better performance than that of weaker coupling overall, and optimization fluctuations of the linear classifier tend to be smaller. The performance

decreases in both weak and strong interactions as rotational error becomes stronger. It shows that although not all rotational errors will result in better performance, by adjusting the 2T-DTC to a critical point, a strong quantum neural network can be generated without using random quantum gates.

ZZ-Ising model

As we saw in Chapter 2, the parameter δ_x is obtained from the ZZ-Ising model analogy. Thus, it might be possible to investigate the rotational error effect via the Ising model. Since we are considering DTCs without the diagonal disorder, the corresponding ZZ-Ising model has a transverse field in the x-axis direction,

$$\hat{H}_{\text{ZZ-Ising}} = \frac{\hbar T_2}{T} \sum_{lm} \frac{J_0^z}{|l-m|^\alpha} \sigma_l^z \sigma_m^z - \frac{\hbar \pi \epsilon}{2T} \sum_l \sigma_l^x \tag{5.37}$$

where ϵ and J_0^z use the same values as the DTC.

The results are shown in Fig. 5.8. As expected, for a small rotational error regime, including the critical point, the performance trends of the DTC and the ZZ-Ising models are almost identical. In contrast, for a large rotational error regime, because the approximation using the Ising model breaks, there is also a difference in the classification performance of the two. But, similar to the DTC, the ZZ-Ising results also show poor performance as the strength of the one-body interaction increases. These results indicate that the ZZ-Ising model can perform the QRELM easier than the 2T-DTC on NISQ devices.

U(1)-symmetry breaking the role of transverse magnetic fields

The above results indicate that improving the classification performance in the 2T-DTC is not caused by the higher-order interactions that appeared in the effective Hamiltonian of the Floquet operator. In other words, it would be possible to reveal its mechanism by investigating the effect of transverse magnetic fields in the Ising model. Thus, here we explore the role of the transverse magnetic field.

First, to simplify the discussion, consider the trivial case where $\epsilon = 0$. In this case, the ZZ-Ising model is invariant under the local U(1)-symmetry. As a result, the probability distribution $|a_l^{(f)}|^2$ ($l = 1, \cdots, 2^N$) does not change under the time evolution. To see it more clearly, let us rewrite the probability distribution in terms of correlations of σ_l^z

$(l = 1, \cdots, N)$. For example, $|a_1^{(f)}|^2$ can be written as

$$\begin{aligned} |a_1^{(f)}|^2 &= \left\langle \Psi_f \left| \frac{\hat{\mathbb{I}} + \sigma_1^z}{2} \cdot \frac{\hat{\mathbb{I}} + \sigma_2^z}{2} \cdots \frac{\hat{\mathbb{I}} + \sigma_N^z}{2} \right| \Psi_f \right\rangle \\ &= \frac{1}{2^N} \left(\hat{\mathbb{I}}_{2^N} + \sum_l^N \langle \Psi_f | \sigma_l^z | \Psi_f \rangle + \sum_{l<m} \langle \Psi_f | \sigma_l^z \sigma_m^z | \Psi_f \rangle + \cdots \right) \end{aligned} \tag{5.38}$$

where $\hat{\mathbb{I}}$ and $\hat{\mathbb{I}}_{2^N}$ are 2×2-dimensional and $2^N \times 2^N$-dimensional identities, respectively. As a result, the probability distribution can transform into the stings of the correlations, as follows,

$$\begin{pmatrix} |a_1^{(f)}|^2 \\ |a_2^{(f)}|^2 \\ \vdots \\ |a_{2^N}^{(f)}|^2 \end{pmatrix} \rightarrow \begin{pmatrix} 1 \\ \langle \sigma_1^z \rangle \\ \vdots \\ \langle \sigma_1^z \sigma_2^z \cdots \sigma_N^z \rangle \end{pmatrix}, \tag{5.39}$$

where $\langle \cdots \rangle$ means $\langle \Psi_f | \cdots | \Psi_f \rangle$. In other words, dynamics affect only phase information being not measurable.

Thus, in the ZZ-Ising model, the transverse magnetic field plays a role in breaking the symmetry. As a result, these correlations show non-trivial phenomena. While as discussed in the previous section shows, when the transverse field strength is too large, the one-body interaction injures the encoded information in initial states. Thus, the competition between the strengths of the two-body interaction and the transverse field is essential. In the current case, as long as the parameter δ_x is below the critical point except for the zero, it shows high performance.

5.7.4 nT-dependence of 2T-DTCs

In the IGS classification, we have seen that the performance of the QRELM of DTCs depends on the number of the period (n) of the Floquet operator. Here, we explore this point in a bit more detail with the MNIST dataset. We show the results of the n-dependency of classification accuracy rate for the weakly interacting DTC in Fig. 5.9. If n is small, the quantum states are not sufficiently spread out in the Hilbert space. Thus the performance of the classification is low. Therefore, we can see that it is getting better as time increases. Furthermore, we can see the effect of the one-body interaction in Fig. 5.9. For the large error ($\epsilon = 0.08$), because of the weak interaction, we see that the classification performance is significantly affected by the rotational error in short periods ($n < 30$).

The effect of the one-body interaction discussed above is also explained by the ZZ-Ising model. First, let us consider that the strength of the ZZ-interaction is smaller than

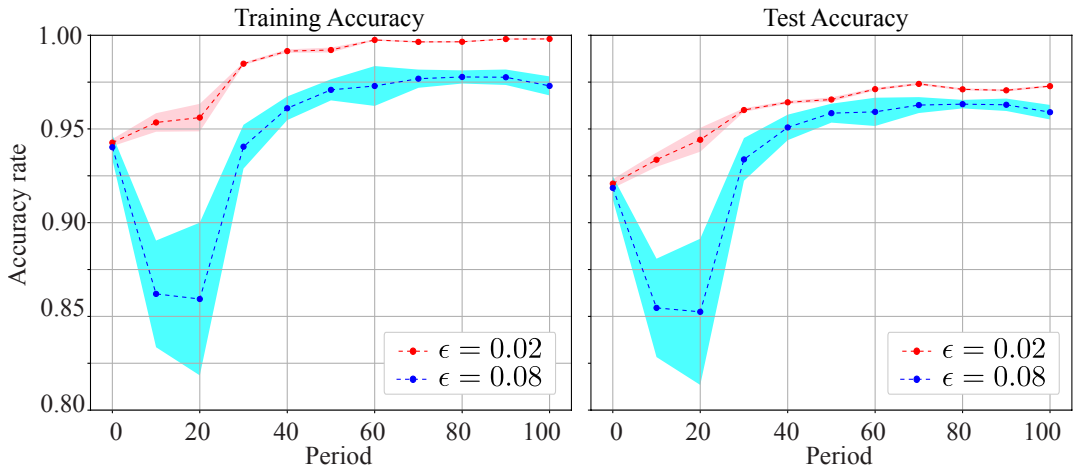

Figure 5.9: Accuracy rates of the 2T-DTC v. s. the total number of Floquet period. The red and blue lines show the average accuracy rates for the 2T-DTC with $\epsilon = 0.02$ and $\epsilon = 0.08$, and the red and blue shadows are the corresponding standard deviations. The parameters are set as $J_0^z T = 0.06$ with $\alpha = 1.51$. Here, the average and the standard deviation are taken for 90 and 100 epochs.

that of the transverse interaction. Thus, let us consider the simplest Ising model,

$$\hat{H} = \lambda \hat{H}_I + \hat{V}, \tag{5.40}$$

where $\lambda \ll 1$ is a parameter. Here, $\hat{H}_I$ and $\hat{V}$ represent the ZZ-interactions and transverse magnetic field along the x-axis. Now, a state can be written as,

$$\begin{aligned} |\Psi(t)\rangle &= e^{-\frac{i}{\hbar}(\hbar\lambda\hat{H}_I + \hbar\hat{V})t}|\Psi(0)\rangle \\ &\approx \left(1 - i\lambda t\hat{H}_I\right) e^{-i\hat{V}t}|\Psi(0)\rangle \\ &\approx e^{-i\hat{V}t}|\Psi(0)\rangle - i\lambda t\hat{H}_I e^{-i\hat{V}t}|\Psi(0)\rangle, \end{aligned} \tag{5.41}$$

for a short time ($t \ll 1$). In the above, since $\lambda \ll 1$, the first term is dominant, it collapses encoded information in initial states. Contrary, because the second term is not one-body interaction and breaks the U(1)-symmetry, it can improve the performance. Thus, for $\lambda \gg 1$, it decreases the performance due to a short time effect. But, because of the second term, it improves its performance over time.

Next, let us consider that the strength of the transverse interaction is smaller than that of the ZZ-interaction. As discussed above, we consider the simplest Ising model given by

$$\hat{H} = \hat{H}_I + \lambda \hat{V}. \tag{5.42}$$

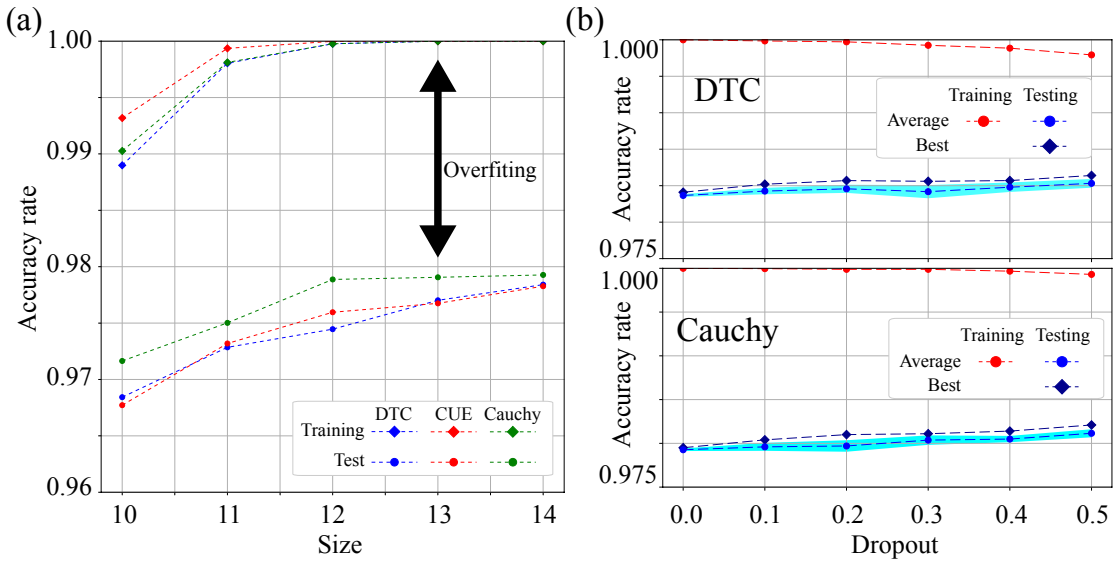

Figure 5.10: (a) Illustrates scaling of the classification performance for each quantum system. Over 12 qubits, the training has saturated to one, and there is severe overfitting where the test does not improve. (b) and (c) Illustrate the accuracy rate of the 2T-DTC and the Cauchy model with dropout. The dropout allows the neural network to perform pseudo ensemble learning. This increases the expressive power of the network and improves test performance. Here, the average and the standard deviation are taken for 90 and 100 epochs.

Then, one can lead a state for a short time ($t \ll 1$),

$$|\Psi(t)\rangle \approx e^{-i\hat{H}_I t}|\Psi(0)\rangle - i\lambda t\hat{V}e^{-i\hat{H}_I}|\Psi(0)\rangle. \tag{5.43}$$

Contrary to Eq. (5.41), now the many-body interaction $\hat{H}_I$ is dominant. Because $\hat{H}_I$ has the local U(1)-symmetry, for a short time, the performance does not change. However, the second term that breaks the symmetry improves the performance as time increases, as shown in Fig.2 for $\epsilon = 0.02$.

5.7.5 Quantum neural network size and Dropout

We believe that quantum systems behave as reservoirs and that exponentially expanding Hilbert Space provides a huge neural network. Therefore, in this last section, we investigate the scaling of performance. The size dependency of performance is shown in Fig. 5.10 (a). It shows that for all quantum systems, the performance of classification increases as the size of the hidden layer, the quantum neural network, increases. As we saw above, the Cauchy model performs better in testing than other quantum systems.

In machine learning, overfitting is a severe problem. It is a situation in which the

Dropout		0.0	0.1	0.2	0.3	0.4	0.5
DTC	ave.	0.979	0.979	0.980	0.979	0.980	0.980
	bes.	0.979	0.980	0.981	0.981	0.981	0.981
Cauchy	ave.	0.979	0.980	0.980	0.980	0.980	0.981
	bes.	0.980	0.980	0.981	0.981	0.981	**0.982**

Table 5.2: Classification performance of the 2T-DTC and the Cauchy model trained with dropout. The parameters of 2T-DTC are the same as in Fig. 5.10. To see the effect of dropout, we considered a dropout rate of 0.0 to 0.5. Here, the average (ave.) and the best records (bes.) are taken for 90 and 100 epochs.

classifier over-adapts to the training data in the training section (optimization). As a result, it loses its expressive power and does not perform well with unseen data such as test data. There are two leading causes of overfitting. First, a model with many parameters and high expressive power. Second, there is not enough training data. In this study, the MNIST dataset we used has 60,000 images for training, which we believe is sufficient. However, since the neural network of a quantum system grows exponentially with size, the linear separator has a huge number of neurons (parameters).

There are two main ways to suppress over-fitting: weight decay and dropout [197]. Weight decay is an old method that penalizes the weight matrix for having large weights in the learning process. However, we employed the dropout for this study. It is a method of learning by randomly erasing neurons. Here, dropout is closely related to ensemble learning. It is a machine learning technology in which multiple models are trained independently, and their outputs are averaged together during inference (testing). Experimentally, this model has been shown to improve the recognition accuracy of neural networks by several percent. In the dropout, because several network structures are realized in the training optimization, it can be interpreted as ensemble learning. We intend to realize a robust network or classifier by combining the quantum neural network and this dropout.

We trained the 2T-DTC and the Cauchy models with 14-qubits with dropouts ranging from 0.0 to 0.5. The classification performance results are shown in Fig. 5.10 (b) and Table 5.2. From the results in Fig. 5.10 (a), we can already see overfitting at 12-qubits, or at $4,096$ neurons. Thus, for 14 qubits with $16,384$ neurons, the network can be optimized even if 50% of the neurons (8192 neurons) are randomly removed. In both models, we see that dropout improves the performance in the test. In the Cauchy distribution model and dropout 0.5, we recorded the best accuracy rate of 98.2% in this experiment.

Our method is effective and efficient compared to other machine learning methods

based on quantum systems [198, 199] in terms of the size of the quantum system and the complexity of the model.

Furthermore, recent ML research has pointed out that the datasets used in classifications such as MNIST have errors in the test labels [200]. This labeling error naturally affects the testing (benchmark). In the case of MNIST, the magnitude of the label error is 0.15 [200]. Given this effect, we believe that our model is very superior.

5.8 Conclusion

We proposed a new powerful machine learning model, the QRELM, which combines a quantum neural network with a classical linear classifier. In this model, the quantum system acts as a reservoir, like a reservoir computer, providing a huge and complex neural network. We have also proposed a new way to encode classical information into quantum states so that this can be run on NISQ devices. We have experimented with several models, 2T-DTC, ZZ-Ising, the Cauchy model and the CUE model, to classify MNIST handwritten digit images. Using the 2T-DTC and the ZZ-Ising model, we found essential factors to design quantum reservoirs, First, if the quantum system has the U(1)-symmetry, its performance does not change. Second, when the system is written by only single rotational operators, its performance gets poor. In this demonstration, we recorded over 98% classification accuracy rates for the 2T-DTC and Cauchy model with 50% dropout. We believe that our result has a great advantage over the ML method using quantum systems and classical ML in terms of computational complexity, simplicity of the model and system sizes [198, 199].

Chapter 6

Summary

Current technology has reached the level where small isolated quantum systems can be realized stably and controlled with high precision. This has led to even greater expectations for the realization of quantum computers. In reality, however, the size of current quantum processors is only a few tens to a few hundred qubits, which is insufficient to run efficient quantum algorithms. These are called NISQ devices, and currently, research on how to use these devices effectively is essential and attracting much attention. One such application is the use of these devices in non-equilibrium quantum systems. Unlike the equilibrium quantum systems, they are not stable, and the quantum state is not in a steady state but shows dynamics. Therefore, this quantum non-equilibrium state is expected to exhibit new and rich physical phenomena not seen in equilibrium quantum systems. Furthermore, it has been reported that non-equilibrium quantum systems can be used as information processing devices to study quantum neural networks and quantum transcendence. Among the various non-equilibrium quantum systems, discrete-time crystals observed in NISQ devices have attracted much attention. This Chapter investigates quantum phases in new non-equilibrium quantum systems and applications of non-equilibrium quantum systems to real-world problems based on these time crystals.

Chapter 2 presented the basic theory and recent research reports on discrete-time crystals, which have recently attracted much attention as a non-equilibrium quantum phase actually observed in NISQ devices. This Chapter shows that the Floquet time crystal using spin systems can be mapped to the quantum Ising model. Using this Ising model, we have given an intuitive, though not rigorous, understanding of the critical phase transition in time crystals from a physical point of view.

In the next part, we proposed two different dynamical phases of matter breaking the DTTS. In Chapter 3, we focused on the fact that in the Floquet time crystal, the breaking of the discrete-time translational symmetry is determined by the rotation angle of the external field. In quantum systems with regions of different rotation angles, we show that, unlike

conventional time crystals, there are two regions where one region breaks the discrete-time translational symmetry and one that does not. We showed that each region is a time crystal and a ferromagnet, indicating that two different quantum phases coexist in this quantum system. We named this exotic quantum system the chimeric time crystal as an analogy to the classical chimeric state. Furthermore, by measuring the entanglement between the two quantum systems using von Neumann entropy, we showed that the entanglement is hardly generated during the quantum phases in the stable two regions.

The next Chapter focused on another symmetry of DTCs, U(1)-symmetry. Conventional models of time crystals have both local and global symmetry, and thus the essential difference is hidden. Therefore, we proposed a new discrete-time crystal model with only global symmetry. We have shown that when the initial state has the global $\mathbb{Z}_2$-Ising (parity) symmetry, it exhibits the sub-harmonic oscillation. Then, we extended our model for the isolated quantum system to a system with decoherence. We have shown that the DTC can exist stably as long as the total system has the U(1)-symmetry, including the environment. As the next step, we explore the fundamental difference between our new and conventional models. We found that when the initial state has both $\mathbb{Z}_2$-symmetry and breaking regions, the DTC region expands due to the local U(1)-symmetry breaking, which is not observed in conventional time crystals, i.e., the time crystal grows. Furthermore, we show that the effect of this environment stabilizes the DTC growth of finite systems. With the new time crystals shown in the two Chapters, we have demonstrated the new possibilities of dynamical quantum phases.

The last Chapter proposed a new QIP (quantum information processing) based on machine learning technology. Because the quantum state is in an exponentially huge Hilbert space and can walk around in the space via quantum dynamics, it can be used as a neural network with high explanation power. However, unlike the classical-quantum network, it seems challenging to optimize the quantum neural network, such as the quantum circuit learning with VQAs. Thus, we proposed a new quantum reservoir computing in which the quantum part is fixed during the optimization. We apply it to the static data and thus refer to it as a quantum reservoir extreme learning machine (QRELM) as an analogy to the classical ELM. We investigated the performance of the QRELM with various quantum systems, including the CUE model and the 2T-DTC. As a classification problem close to a practical problem, we use MNIST data sets. Importantly, we have shown that the performance of 2T-DTC is comparable to that of the randomly chosen unitary $\hat{U}_{\mathrm{CUE}}$ used in the study of quantum supremacy. Based on these results, we proposed two critical factors for the QRELM. In addition, we have shown that over-learning due to the exponential expansion of neural networks by QR can be suppressed by dropout, which is widely used in ML, and high expressiveness of the network can be obtained. We believe we open a new way to use the quantum's complexity as QIP for more practical problems.

Appendix A

Spin Systems and Two level systems

Here, we briefly explain the basics of quantum spin systems that we used in this thesis. We assume that the reader already has an understanding of classical physics. In this Chapter, we will only explain the minimum knowledge and symbols needed to understand this thesis. If readers want to understand the basics of quantum mechanics, we recommend reading Ref. [11, 201].

A.1 Single spin and Two level system

In classical physics, the motion of an object is determined by its initial condition and the equations of motion known as Newton's equation. Here, the classical state is given by its position and velocity. However, in quantum mechanics, its state is represented by a wave function, and physical observables such as positions becomes stochastic.

The dynamics corresponding to classical velocity and position were systematized by Schrodinger's wave mechanics [9]. But, to simplify the following discussion, let us consider the discrete state such as a single spin (two-level system). For understanding the dynamics of such discrete states, Heisenberg's matrix mechanics is effective.

First, the classical spin state is described by two basic states: e.g. $\sigma = \pm 1$ or $s = 0, 1$ [202]. However, in a quantum system, its state should be described by a vector. Given the fact that the two basic states can be distinguished by measurement, they can be described by the following basis vectors as follows,

$$|0\rangle = \begin{pmatrix} 1 \\ 0 \end{pmatrix}, \quad |1\rangle = \begin{pmatrix} 0 \\ 1 \end{pmatrix}. \tag{A.1}$$

Here, the linear space of these vectors is called the Hilbert space, and in this case, the dimension is two. Now, a generic state can be written as the superposition of the two basis

states, as follows,

$$|\Psi\rangle = \begin{pmatrix} \alpha \\ \beta \end{pmatrix} = \alpha|0\rangle + \beta|1\rangle \tag{A.2}$$

where $\alpha, \beta \in \mathbb{C}$ which satisfies $|\alpha|^2 + |\beta|^2 = 1$ to normalize its norm. It tells us that either $|0\rangle$ or $|1\rangle$ can be observed with a probability $|a|^2$ or $|b|^2$. As an analogy to a classical bit, the two-level systems are used as qubits, a bit of the quantum version.

Here, we introduce the nice representation for the qubit called the Bloch sphere. The state is a point on this sphere, which can be given by the two angles θ and ϕ as follows,

$$|\Psi\rangle = \cos\left(\frac{\theta}{2}\right)|0\rangle + e^{i\phi}\sin\left(\frac{\theta}{2}\right)|1\rangle. \tag{A.3}$$

Here, we ignore the global phase.

In quantum mechanics, to know the physical quantities A of a state, we need the corresponding Hermitian matrix $\hat{A}$, and measured values are the eigenvalues of the matrix. Because of the stochastic interpretation of general quantum states, observables are also stochastic. Thus, in many cases, we are interested in the average value $\langle A \rangle$ of the observables, which can be given as follows.

$$\langle A \rangle = \langle \Psi | \hat{A} | \Psi \rangle. \tag{A.4}$$

Here, $\langle A \rangle$ is referred to as the expectation value of $\hat{A}$ for the state $|\Psi\rangle$.

Now, we introduce the Pauli matrices (σ^μ, for $\mu = x, y, z$) which is a sef of three 2×2 complex matrices, as follows,

$$\sigma^x = \begin{pmatrix} 0 & 1 \\ 1 & 0 \end{pmatrix}, \quad \sigma^y = \begin{pmatrix} 0 & -i \\ i & 0 \end{pmatrix}, \quad \sigma^z = \begin{pmatrix} 1 & 0 \\ 0 & -1 \end{pmatrix}. \tag{A.5}$$

These matrices are Hermitian ($(\sigma^\mu)^\dagger = \sigma^\mu$) and unitry ($(\sigma^\mu)^\dagger \sigma^\mu = \sigma^\mu (\sigma^\mu)^\dagger = \hat{\mathbb{I}}$). It is known that the Pauli matrices with the identity matrix ($\mathbb{I}$) are an orthogonal basis of the 2×2 Hermician matrix space, thus any Hermician matrix $\hat{A}$ can be written as

$$\hat{A} = \begin{pmatrix} A_0 + A_z & A_x - iA_y \\ A_x + iA_y & A_0 - A_z \end{pmatrix} = A_0\hat{\mathbb{I}} + A_x\sigma^x + A_y\sigma^y + A_z\sigma^z \tag{A.6}$$

where $A_\mu \in \mathbb{R}$ for $\mu = 0, x, y, z$. It can be shortly written as,

$$\hat{A} = A_0\hat{\mathbb{I}} + \vec{A} \cdot \vec{\sigma} \tag{A.7}$$

where $\vec{\sigma} = (\sigma^x, \sigma^y, \sigma^z)^T$.

In the quantum mechanics, the state dynamics $|\Psi(t)\rangle$ is given by the Shorödinger equation,

$$i\hbar\frac{\partial}{\partial t}|\Psi(t)\rangle = \hat{H}|\Psi(t)\rangle \tag{A.8}$$

where $\hat{H}$ is the Hamiltonian corresponding to the energy. Generally, the Hamiltonian can be both time-independent $\hat{H}(t)$ and dependent $\hat{H}$. Here, let us assume the system is time-dependent and its Hamiltonian is given by,

$$\begin{aligned}\hat{H} &= \hbar\omega_0\hat{\mathbb{I}} + \hbar\omega_x\sigma^x + \hbar\omega_y\sigma^y + \hbar\omega_z\sigma^z \\ &= \hbar\omega_0\hat{\mathbb{I}} + \vec{\omega}\cdot\vec{\sigma},\end{aligned} \tag{A.9}$$

Now, a solution of Eq. (A.8) can be given by,

$$\begin{aligned}|\Psi(t)\rangle &= e^{-\frac{i}{\hbar}\hat{H}t}|\Psi(0)\rangle \\ &= \hat{U}(t)|\Psi(0)\rangle\end{aligned} \tag{A.10}$$

where $|\Psi(0)\rangle$ is an initial state, and $\hat{U} = \exp\left[-\frac{i}{\hbar}\hat{H}t\right]$ is the Unitary operator. Now, using the properties of the Pauli matrices, one can write the unitary operator as follows,

$$\begin{aligned}\hat{U}(t) &= e^{-\frac{i}{\hbar}\hat{H}t} \\ &= e^{-i\omega_0\hat{\mathbb{I}}t - i\vec{\omega}\cdot\vec{\sigma}t} \\ &= e^{-i\omega_0 t}\left(\cos\left(|\vec{\omega}|t\right)\hat{\mathbb{I}} - i\sin\left(|\vec{\omega}|t\right)\vec{n}\cdot\vec{\sigma}\right)\end{aligned} \tag{A.11}$$

where $\vec{n}$ is the unit vector along the $\vec{\omega}$-axis ($\vec{n} = \omega/|\omega|$). Here, we see that ω_0 is the phase information which disappears at the observation level. Thus, in general, the first term is omitted form the Hamiltonian by chaining the origin of the energy.

A.2 Many body systems

Now, let us expand the single spin model to many body (spin) systems. To get some intuition, here we consider two spins as an example. In the case, by using the basis sets of the single spin, its Hilbert space can be represented by the four basis,

$$|0\rangle\otimes|0\rangle = \begin{pmatrix}1\\0\\0\\0\end{pmatrix},\ |1\rangle\otimes|0\rangle = \begin{pmatrix}0\\1\\0\\0\end{pmatrix},\ |0\rangle\otimes|1\rangle = \begin{pmatrix}0\\0\\1\\0\end{pmatrix},\ |1\rangle\otimes|1\rangle = \begin{pmatrix}0\\0\\0\\1\end{pmatrix}, \tag{A.12}$$

where $\otimes$ means the tensor product. Here, we note that sometimes the tensor product is omitted in the short notation, e.g. $|00\rangle \equiv |0\rangle \otimes |0\rangle$. Thus, in general, the Hilbert space for N-spins can be spanned by 2^N states given by

$$\underbrace{|000\cdots0\rangle,\ |010\cdots0\rangle,\ |001\cdots0\rangle, \cdots, |111\cdots1\rangle}_{2^N \text{states}}. \tag{A.13}$$

Now, let us see the operators. First, we expand the operator for the single spin to the many body systems. When $N = 2$, the operator acting on the single spin can be written by,

$$\begin{aligned} \hat{A}_1 &\equiv \hat{A}_1 \otimes \hat{\mathbb{I}} \\ \hat{A}_2 &\equiv \hat{\mathbb{I}} \otimes \hat{A}_2 \end{aligned} \tag{A.14}$$

where the left side are the short notation. While, the operator $\hat{A}_{12}$ acting on the both spins are given by,

$$\text{Two-body operator} = \hat{A}_1 \otimes \hat{A}_2 \tag{A.15}$$

Here, we note that sometimes the tensor product is omitted in the short notation, $\hat{A}_1 \otimes \hat{A}_2 \equiv \hat{A}_1\hat{A}_2$. Similarly, in the N-spins, the operator $\hat{A}_l$ acting on the single spin at l-th site are written as,

$$\hat{A}_l = \underbrace{\hat{\mathbb{I}} \otimes \hat{\mathbb{I}} \otimes \cdots \otimes \hat{\mathbb{I}}}_{l-1} \otimes \hat{A}_l \otimes \underbrace{\hat{\mathbb{I}} \otimes \hat{\mathbb{I}} \otimes \cdots \otimes \hat{\mathbb{I}}}_{N-l} \tag{A.16}$$

And the operator acting on two sites ($l > m$) is

$$\hat{A}_l\hat{A}_m = \underbrace{\hat{\mathbb{I}} \otimes \cdots \otimes \hat{\mathbb{I}}}_{l-1} \otimes \hat{A}_l \otimes \underbrace{\hat{\mathbb{I}} \otimes \cdots \otimes \hat{\mathbb{I}}}_{m-l-1} \otimes \hat{A}_m \otimes \underbrace{\hat{\mathbb{I}} \otimes \cdots \otimes \hat{\mathbb{I}}}_{N-m}. \tag{A.17}$$

Similarly, many-body interactions such as $\hat{A}_1\hat{A}_2\hat{A}_3$ can be defined.

Appendix B

Thermalization of quantum systems and the Floquet systems

In the present section, we briefly review the quantum thermalization and the Floquet theory used to understand the discrete time crystals.

B.1 Quantum thermalization

This section will briefly review the thermal equilibrium state for quantum systems that have frequently appeared in the above Chapters. These topics are rich and are active, with many unresolved issues still to be addressed. Thus, here we only give the basic idea of quantum thermalization and its mathematical representation.

As we know, in classical mechanics, the dynamics is an updated process of the state governed by Newton's Law. If one has all the information (initial position and initial verbosity) about the initial state, one can track the state at any time by Newton's equation of motion. But, when we focus on the matters such as metals, these consist of several elements (particles). Thus it is impossible to solve Newton's equations for all particles simultaneously. Nonetheless, come to think of it, we do not need all information to understand the macroscopic systems. In thermodynamics, we know that these macroscopic states eventually reach the universal state in which there are no changes from the macroscopic point of view. The state is called the thermal equilibrium state. Of course, from a microscopic point of view, there are still dynamics. However, as long as we look at the macroscopic observable, the state seems steady. Thermodynamics is an elegant theory that reveals the universality of this equilibrium state. In this theory, it is shown that the equilibrium state is defined as a universal state determined by a small number of physical quantitative quantities such as temperature T, the number of particles N, the chemical potential μ, and, if necessary, the total magnetization M.

On the contrary, statistical physics is a framework for describing these macroscopic states from a microscopic perspective. However, as we said, it is impossible to solve the equations of motion based on the dynamics from a microscopic point of view because of large systems. Therefore, statistical physics employs probability theory to describe the physical quantities of the thermal equilibrium state of a macroscopic system without precisely solving the microscopic dynamics [203].

Before going to quantum systems, let us consider the thermal equilibrium state in classical statistical physics. As mentioned above, statistical physics uses stochastic models to understand phenomena at the microscopic scale. Various stochastic models, e.g., micro-canonical, canonical, and grand canonical, have been proposed for different problems. In this section, we consider the canonical ensemble model or canonical Gibbs ensemble [204] as an example. The interest (A) system is coupled to a heat bath (B) in this model. And we assume that there are only energy exchanges between the bath and the system. When the system is coupled to the bath with temperature T, then, a probability of the emergence of a state with energy E_l in the system (A) is defined as follows,

$$p_l^{\mathrm{CM}} = \frac{e^{-\beta E_l}}{Z^{\mathrm{CM}}} \tag{B.1}$$

where $\beta = 1/(K_B T)$ and K_B is Boltzmann's constant. Here, the partition function for the normalization is given by,

$$Z^{\mathrm{CM}} = \sum_l e^{-\beta E_l} \tag{B.2}$$

As a results, the expectation value of the physical quantity (A) can be obtained by,

$$\langle A \rangle = \sum_l A_l p_l^{\mathrm{CM}}, \tag{B.3}$$

where A_l are the value of A for the state with the energy E_l.

Now, let us consider the thermal equilibrium state of a quantum system. In a quantum system, generally states can take superposition, and they are not independent. It means that the number of possible states of a quantum system is very rich. Thus, when we apply the concepts of the canonical ensembles to quantum systems, we need to the some coordinate to pick up states representing representative states with the energy E_l. One of the nice way is that one adapts the principle of equal weights of classical statistical physics to the eigenstates of the Hamiltonian $\hat{H}$, which gives the complete set. As in the classical system, the probability of appearance of an energy state $|\phi_l\rangle$ with energy E_l is given by,

$$p_l^{\mathrm{QM}} = \frac{e^{-\beta E_l}}{Z^{\mathrm{QM}}} = \frac{\langle \phi_l | e^{-\beta \hat{H}} | \phi_l \rangle}{Z^{\mathrm{QM}}} = \frac{e^{-\beta \langle \phi_l | \hat{H} | \phi_l \rangle}}{Z^{\mathrm{QM}}} \tag{B.4}$$

where, $|\phi_l\rangle$ is the eigenstate of the Hamiltonian of the system: $\hat{H}|\phi_l\rangle = E_l|\phi_l\rangle$. Likely, the partition function of the quantum system is written as,

$$Z^{\text{QM}} = \sum_l e^{-\beta E_l} = \sum_l \langle\phi_l|e^{-\beta\hat{H}}|\phi_l\rangle = \text{Tr}\left[e^{-\beta\hat{H}}\right], \tag{B.5}$$

where we use the trace. The above probability can be reconstructed by the single density matrix,

$$\hat{\rho}_{\text{eq}}(\beta) = \frac{1}{Z^{\text{QM}}} e^{-\beta\hat{H}}. \tag{B.6}$$

Here, the density matrix sometimes be called the **canonical Gibbs ensemble** or shortly the thermal state of quantum systems. The above density matrix in quantum systems first given by V. Neumann in his research on measurement process in quantum systems as a mixed state that maximizes von Neumann entropy [205]. Later, R. C. Thomson introduced it as a canonical distribution in quantum statistical mechanics as an extension of classical statistical mechanics [206]. Similarly, when there are several conserved quantities $\hat{I}_k$ including the energy , then the thermal state is given by the generalized Gibbs ensemble,

$$\hat{\rho}_{\text{GGE}} = \frac{e^{-\sum_k \lambda_k \hat{I}_k}}{Z_{GGE}}, \tag{B.7}$$

where $Z_{GGE} = \text{Tr}[e^{-\sum_k \lambda_k \hat{I}_k}]$ and λ_k are Lagrange multipliers. Here, it is important to note that although the equilibrium state of quantum states based on the equal weight principle is elegant and seems to be compatible with the conventional notation of quantum mechanics, but we should not forget that it is just a working hypothesis to explain macroscopic physical quantities by stochastic models.

When the system at the infinite temperature ($T = \infty$ or $\beta = 0$), the thermal state equals the fully mixed state $\hat{\rho}_{\text{eq}}(\beta = 0) = \mathbb{I}/\dim\mathcal{H}$, where $\dim\mathcal{H}$ is the dimension of the Hilbert space of the system. It means that all energy eigenstates appear with the same probability.

Recently, it is believed that the above thermal state also can be used to represent the thermal state of the isolated closed quantum state without the heat bath. Here, thermalization in the isolated systems means that the large isolated state should be relax to the equilibrium state with microscopic perspective. The **Eigenstate Thermalization Hypothesis (ETH)** has been proposed to explain why the Gibbs ensemble is valid for the thermal state of isolated quantum systems [207, 208, 209, 210]. At present, this remains a hypothesis, but various numerical results have followed [211].

B.2 Floquet theory and Floquet thermalization

When a system is time periodic, one can use the **Floquet theory** and the systems is called the **Floquet system**. Here, we briefly review the Floquet theory for the quantum systems. Then we will explain the thermalization process of the periodic systems.

B.2.1 Floquet theory

For a genetic time-dependent Hamiltonian $\hat{H}(t)$, the time evolution of a state $|\Psi(t)\rangle$ is given by the time-dependent Schrödinger equation,

$$i\hbar\frac{d}{dt}|\Psi(t)\rangle = \hat{H}(t)|\Psi(t)\rangle. \tag{B.8}$$

While, because of the unitary dynamics in the quantum system, a state at any time t can be written as

$$|\Psi(t)\rangle = \hat{U}(t)|\Psi(0)\rangle, \tag{B.9}$$

where, $|\Psi(0)\rangle$ is the initial state and $\hat{U}(t)$ is the time-evolution (unitary) operator. Combing the above two equations, we get,

$$i\frac{d}{dt}\hat{U}(t) = \hat{H}(t)\hat{U}(t), \tag{B.10}$$

where $\hat{U}(0) = \hat{\mathbb{I}}$ is the identity operator. Now, when the Hamiltonian is time-periodic: $\hat{H}(t+T) = \hat{H}(t)$, the Floquet theory allows us to write the solution of the above equation, as follows,

$$\hat{U}(t) = \hat{P}(t)e^{-\frac{i}{\hbar}\hat{H}_{\mathrm{F}}T} \tag{B.11}$$

where $\hat{P}(t+T) = \hat{P}(t)$ is a time-periodic unitary and $\hat{P} = \hat{\mathbb{I}}$. Here, the Hamiltonian $\hat{H}_{\mathrm{F}}$ is the time-independent Hamiltonian and called the Floquet Hamiltonian. Using the Hamiltonian, the time evolution operator for one period can be written by,

$$\hat{F} \equiv \hat{U}(T) = \mathcal{T}\exp\left(-\frac{i}{\hbar}\int_0^T \hat{H}(\tau)d\tau\right) = e^{-\frac{i}{\hbar}\hat{H}_{\mathrm{F}}T} \tag{B.12}$$

where, $\mathcal{T}$ is a time ordering operator. Here, the one-period unitary is called the Floquet operator and denote $\hat{F}$. Now, we see that the dynamics at stroboscopic times are effectively governed by the Floquet Hamiltonian $\hat{H}_{\mathrm{F}}$, and thus sometime it is referred to as the effective Hamiltonian and is denoted $\hat{H}^{\mathrm{eff}}$. In this Chapter, we use the notation $\hat{H}_F$. While, in later Chapters, we will use $\hat{H}^{\mathrm{eff}}$ to emphasize that the Hamiltonian effectively governs the stroboscopic dynamics.

B.2.2 Magnus Expansion

In Floquet systems, e.g. the DTC, generally it is more interested in the dynamics at stroboscopic time given by the Floquet Hamiltonian. In general, it is difficult to find the Floquet Hamiltonian analytically. However, there is a closed form solution called the **(Floquet-) Magnus expansion** [212, 213, 214] in which the Floquet Hamiltonian can be expanded in terms of powers of T, as follows,

$$\begin{aligned}\hat{H}_{\mathrm{F}} &= \sum_{l} \hat{H}_{F}^{(l)} = \hat{H}_{\mathrm{F}}^{(0)} + \hat{H}_{\mathrm{F}}^{(1)} + \hat{H}_{\mathrm{F}}^{(2)} + \cdots \\ &= \sum_{m=0} \Omega_m T^m.\end{aligned} \tag{B.13}$$

Here, the expansion coefficient Ω_m at the m-th order is given by

$$\Omega_m = \sum_{\sigma} C_{\sigma,m} \int_0^T ds_{m+1} \cdots \int_0^{s_1} ds_1 \left[\hat{H}(t_{\sigma(m+1)}), \left[\hat{H}(t_{\sigma(m)}), \cdots, \left[\hat{H}(t_{\sigma(2)}), \hat{H}(t_{\sigma(1)}\right] \cdots \right]\right] \tag{B.14}$$

where σ is a permutation, and $C_{\sigma,m}$ being,

$$C_{\sigma,m} = \frac{(-1)^{m-\theta[\sigma]}\theta[\sigma]!(m-\theta[\sigma])!}{i^m(m+1)^2 m! T^{m+1}}, \tag{B.15}$$

with $\theta[\sigma] = \sum_{i=1}^{m} \left(\theta(\sigma(i+1)) - \theta(i)\right)$ and the step function $\theta(\cdot)$. For instance, the first two lowest order can be given by,

$$\begin{aligned}\Omega_0 &= \frac{1}{T}\int_0^T ds \hat{H}(s) \\ \Omega_1 &= \frac{-i}{2\hbar T^2}\int_0^T ds_2 \int_0^{s_2} ds_1 \left[\hat{H}(s_2), \hat{H}(s_1)\right].\end{aligned} \tag{B.16}$$

Here, the approximate Hamiltonian at the lowest order,

$$\hat{H}_{\mathrm{F}}^{(0)} = \Omega_0 T^0 = \frac{1}{T}\int_0^T ds \hat{H}(s) \tag{B.17}$$

is the time-averaged Hamiltonian.

From Eq. (B.14), at the m-th order, there is the multiple commutator, as follows,

$$\left[\hat{H}(t_{m+1}), \left[\hat{H}(t_m), \cdots, \left[\hat{H}(t_2), \hat{H}(t_1)\right] \cdots \right]\right] \tag{B.18}$$

It implies that the term may have at most an $(m+2)$-body interaction term. Thus, in general, in the Magnus expansion, it is not possible to write the Floquet-Hamiltonian with

a few-body interaction term.

B.2.3 Floquet ETH

The divergence of the Magnus expansion suggests a very important physical property of the Floquet system. To see it, let us consider the eigenstate of the Hamiltonian $\hat{H}_F$,

$$\hat{H}_F|\phi_l\rangle = \epsilon_l|\phi_l\rangle \tag{B.19}$$

where ϵ_l is the eigenvalue and is called the quasi-energy. Because the eigenstates forms the complete orthonormal set, an initial state $|\Psi(0)\rangle$ can be written in terms of them: $|\Psi(0)\rangle = \sum_l c_l|\phi_l\rangle$. Here, the long-time average of the density matrix at stroboscopic times ($t = nT$) can be given by,

$$\hat{\bar{\rho}} = \lim_{M\to\infty}\frac{1}{M}\sum_{n=0}^{M-1}\rho(nT) = \sum_l |c_l|^2|\phi_l\rangle\langle\phi_l| \tag{B.20}$$

where we assume that there is no degeneracy in the Floquet system.

Here, some numerical results [70, 74] suggest that the expected value of the local physical observable $\hat{A}$ is indistinguishable from that of the thermal equilibrium state $\hat{\rho}_{\text{eq}}(\beta = 0)$ at infinite temperature $\beta = 0$, as follows,

$$\langle\phi_l|\hat{A}|\phi_l\rangle \approx \text{Tr}\Big(\hat{A}\hat{\rho}_{\text{eq}}(\beta = 0)\Big) \tag{B.21}$$

Although it has not been proven whether the result applies to generic quantum many-body systems, it seems to be a general property of non-integrable and periodically driven systems, which is called the Floquet ETH hypothesis. Now, given that this hypothesis is correct, the long-time average of the physical quantity A is as follows,

$$\text{Tr}\Big(\hat{A}\hat{\bar{\rho}}\Big) \approx \text{Tr}\Big(\hat{A}\hat{\rho}_{\text{eq}}(\beta = 0)\Big) \tag{B.22}$$

where we use $\sum_l |c_l|^2 = 1$. It indicates that the generic Floquet system will relax to a thermal equilibrium state at infinite temperature after waiting long enough time.

More details on the Floquet theory and the thermalization of the periodically driven system are available on Ref. [213, 81].

Appendix C

Derivation of the effective Hamiltonian for the chimer DTC

In the Chapter 3, we have used the effective Hamiltonian for two periods to show that our model exhibits the coexistence of two quantum phases, called chimeric DTCs. Here, we analytically derive the effective Hamiltonian $\hat{H}^{\text{2T-eff}}_{\epsilon_A}$ for a non-zero error ϵ_{A}. In the calculation, we assume that ϵ_{A} is the small compared to the coupling constant $J_0^z$and set $\epsilon_{\text{B}} = 1.0$. To find the effective Hamiltonian, we start from the square of the Floquet operator. By definition, in our model, it can be written as

$$\begin{aligned}\hat{F}^2 &= \exp\left[-\frac{i}{\hbar}\hat{H}^{\text{2T-eff}}_{\epsilon_A} 2T\right] \\ &= \exp\left[-\frac{i}{\hbar}\hat{H}_2 T_2\right]\exp\left[-\frac{i}{\hbar}\hat{H}_1 T_1\right]\exp\left[-\frac{i}{\hbar}\hat{H}_2 T_2\right]\exp\left[-\frac{i}{\hbar}\hat{H}_1 T_1\right],\end{aligned} \tag{C.1}$$

where $\hat{H}_1$ and $\hat{H}_2$ are defined in the main text. For convenience, we decompose H_2 as follows,

$$\begin{aligned}\hat{H}_2 &= \hbar\sum_{lm} J^z_{lm}\sigma^z_l\sigma^z_m + \hbar\sum_l W^z_l\sigma^z_l \\ &= \hbar\sum_{lm\in\text{A}} J^z_{lm}\sigma^z_l\sigma^z_m + \hbar\sum_{l\in\text{A}} W^z_l\sigma^z_l + \hbar\sum_{lm\in\text{B}} J^z_{lm}\sigma^z_l\sigma^z_m + \hbar\sum_{l\in\text{B}} W^z_l\sigma^z_l + \hbar\sum_{\substack{l\in\text{A}\\ m\in\text{B}}} J^z_{lm}\sigma^z_l\sigma^z_m.\end{aligned} \tag{C.2}$$

Here, we consider an operator $\hat{O} = \exp\left(-\frac{i}{\hbar}\hat{H}_1 T_1\right)\exp\left(-\frac{i}{\hbar}\hat{H}_2 T_2\right)\exp\left(-\frac{i}{\hbar}\hat{H}_1 T_1\right)$. And using the properties of the spin rotation we rewrite it as follows

$$\begin{aligned}
\hat{O} &= e^{-\frac{i\pi(1-\epsilon_{\mathrm{A}})}{2}\sum\limits_{l\in\mathrm{A}}\sigma_l^x}\exp\left[-i\left(\sum_{lm}J_{lm}^z\sigma_l^z\sigma_m^z+\sum_l W_l^z\sigma_l^z\right)T_2\right]e^{-\frac{i\pi(1-\epsilon_{\mathrm{A}})}{2}\sum\limits_{l\in\mathrm{A}}\sigma_l^x} \\
&= \hat{V}_{\epsilon_A}\exp\left[-i\left(\sum_{lm\in\mathrm{A/B}}J_{lm}^z\sigma_l^z\sigma_m^z-\sum_{\substack{l\in\mathrm{A}\\m\in\mathrm{B}}}J_{lm}^z\sigma_l^z\sigma_m^z-\sum_{l\in\mathrm{A}}W_l^z\sigma_l^z+\sum_{l\in\mathrm{B}}W_l^z\sigma_l^z\right)T_2\right]\hat{V}_{\epsilon_A} \\
&= \hat{V}_{\epsilon_A}\exp\left[-i\left(-\sum_{l\in\mathrm{A}}\frac{\hat{\Theta}_l}{2}\sigma_l^z\sum_{lm\in\mathrm{A}}J_{lm}^z\sigma_l^z\sigma_m^z+\sum_{lm\in\mathrm{B}}J_{lm}^z\sigma_l^z\sigma_m^z+\sum_{l\in\mathrm{B}}W_l^z\sigma_l^z\right)T_2\right]\hat{V}_{\epsilon_A} \\
&= \hat{V}_{\epsilon_A}\exp\left[i\left(\frac{\hat{\Theta}_l}{2}\right)T_2\right]\exp\left[-i\left(\sum_{lm\in\mathrm{A}}J_{lm}^z\sigma_l^z\sigma_m^z+\hat{H}_B\right)T_2\right]\hat{V}_{\epsilon_A},
\end{aligned} \tag{C.3}$$

where $\hat{\Theta}_l = 2W_lT_2+2\sum\limits_{m\in B}J_{lm}^zT_2\sigma_m^z$ and $\hat{V}_{\epsilon_A} = \exp\left(\frac{i\epsilon_{\mathrm{A}}\pi}{2}\sum\limits_{l\in\mathrm{A}}\sigma_l^x\right)$. Here we defined the Hamiltonian containing operators of region B: $\hat{H}_B = \sum\limits_{lm\in\mathrm{B}}J_{lm}^z\sigma_l^z\sigma_m^z+\sum\limits_{l\in\mathrm{B}}W_l^z\sigma_l^z$. Let us define a rotation acting on the operator σ_l^z as follows,

$$\exp\left(-i\sum_{l\in\mathrm{A}}\frac{\hat{\Theta}_l}{2}\sigma_l^z\right)\hat{V}_{\epsilon_A}\exp\left(i\sum_{l\in\mathrm{A}}\frac{\hat{\Theta}_l}{2}\sigma_l^z\right) = \exp\left[\frac{i\epsilon_{\mathrm{A}}\pi}{2}\sum_{l\in\mathrm{A}}\left(\cos\hat{\Theta}_l\sigma_l^x+\sin\hat{\Theta}_l\sigma_l^y\right)\right]. \tag{C.4}$$

Thus,

$$\begin{aligned}
\hat{\mathcal{F}}^2 &= \exp\left[-i\left(\sum_{lm\in\mathrm{A}}J_{lm}^z\sigma_l^z\sigma_m^z\right)T_2\right]\exp\left(-i\sum_{l\in\mathrm{A}}\frac{\hat{\Theta}_l}{2}\sigma_l^z\right)\hat{V}_{\epsilon_A} \\
&\quad\exp\left(i\sum_{l\in\mathrm{A}}\frac{\hat{\Theta}_l}{2}\sigma_l^z\right)\exp\left[-i\left(\sum_{lm\in\mathrm{A}}J_{lm}^z\sigma_l^z\sigma_m^z+2\hat{H}_B\right)T_2\right]\hat{V}_{\epsilon_A} \\
&= \exp\left[-i\left(\sum_{lm\in\mathrm{A}}J_{lm}^z\sigma_l^z\sigma_m^z\right)T_2\right]\exp\left[\frac{i\epsilon_{\mathrm{A}}\pi}{2}\sum_{l\in\mathrm{A}}\left(\cos\hat{\Theta}_l\sigma_l^x+\sin\hat{\Theta}_l\sigma_l^y\right)\right] \\
&\quad\exp\left[-i\left(\sum_{lm\in\mathrm{A}}J_{lm}^z\sigma_l^z\sigma_m^z\right)T_2\right]\exp\left(-i2\hat{H}_BT_2\right)\hat{V}_{\epsilon_A}\,.
\end{aligned} \tag{C.5}$$

When the parameter λ and μ are small, the Baker-Campbell-Hausdorff formula is approximately given by

$$\exp\left(\lambda\hat{X}\right)\exp\left(\mu\hat{Y}\right) \approx \exp\left(\lambda\hat{X}+\mu\hat{Y}+\frac{1}{2}\lambda\mu[\hat{X},\hat{Y}]\right), \tag{C.6}$$

where $\hat{X}$ and $\hat{Y}$ are matrices. By using this equation, one can write

$$\begin{aligned}
&\exp\left(\lambda\hat{X}\right)\exp\left(\mu\hat{Y}\right)\exp\left(\lambda\hat{X}\right)\\
&\quad=\exp\left(\lambda\hat{X}\right)\exp\left(\frac{\mu}{2}\hat{Y}\right)\exp\left(\frac{\mu}{2}\hat{Y}\right)\exp\left(\hat{X}\right)\\
&\quad\approx\exp\left(\lambda\hat{X}+\frac{\mu}{2}\hat{Y}+\frac{\lambda\mu}{4}[\hat{X},\hat{Y}]\right)\exp\left(\lambda\hat{X}+\frac{\mu}{2}\hat{Y}-\frac{\lambda\mu}{4}[\hat{X},\hat{Y}]\right)\\
&\quad\approx\exp\left(2\lambda\hat{X}+\mu\hat{Y}\right).
\end{aligned} \tag{C.7}$$

We here assume that both the couplings J^z_{lm} as well as the error ϵ_A are small. Thus, we can apply the formula discussed above to obtain

$$\begin{aligned}
&\exp\left[-i\left(\sum_{lm\in\mathrm{A}}J^z_{lm}\sigma^z_l\sigma^z_m\right)T_2\right]\exp\left[\frac{i\epsilon_\mathrm{A}\pi}{2}\sum_{l\in\mathrm{A}}\left(\cos\hat{\Theta}_l\sigma^x_l+\sin\hat{\Theta}_l\sigma^y_l\right)\right]\exp\left[-i\left(\sum_{lm\in\mathrm{A}}J^z_{lm}\sigma^z_l\sigma^z_m\right)T_2\right]\\
&=\exp\left[-i\left(2\sum_{lm\in\mathrm{A}}J^z_{lm}\sigma^z_l\sigma^z_m\right)T_2+\frac{i\epsilon_\mathrm{A}\pi}{2}\sum_{l\in\mathrm{A}}\left(\cos\hat{\Theta}_l\sigma^x_l+\sin\hat{\Theta}_l\sigma^y_l\right)\right].
\end{aligned} \tag{C.8}$$

By combining Eqs (C.3), (C.4) and (C.8), finally, we get

$$\begin{aligned}
\hat{H}^{\mathrm{eff}}_{\epsilon_A,2T}\approx&\frac{\hbar T_2}{T}\sum_{l,m\in A}J^z_{lm}\sigma^z_l\sigma^z_m-\frac{\hbar\pi\epsilon_A T_2}{2T}\sum_{\substack{l,m\in A\\ l\neq m}}J^z_{lm}\sigma^z_l\sigma^y_m+\frac{\hbar T_2}{T}\sum_{l,m\in B}J^z_{lm}\sigma^z_l\sigma^z_m\\
&+\frac{\hbar T_2}{T}\sum_{l\in B}W_l\sigma^z_l-\frac{\hbar\pi\epsilon_A}{4T}\sum_{l\in A}\left[\left(\cos\hat{\Theta}_l+1\right)\sigma^x_l\sin\hat{\Theta}_l\sigma^y_l\right]
\end{aligned} \tag{C.9}$$

From this Hamiltonian, we see that the rotation error ϵ_A produces an interaction between regions A and B, and the strength of this interaction is proportional to it. If $\epsilon_\mathrm{A}=0$, this Hamiltonian reduces to

$$\hat{H}^{\mathrm{eff}}_{\epsilon_A=0,2T}=\frac{\hbar T_2}{T}\sum_{\boldsymbol{l},\boldsymbol{m}\in\mathrm{A}}J^z_{lm}\sigma^z_l\sigma^z_m+\frac{\hbar T_2}{T}\sum_{\boldsymbol{l},\boldsymbol{m}\in\mathrm{B}}J^z_{lm}\sigma^z_l\sigma^z_m+\frac{\hbar T_2}{T}\sum_{l\in\mathrm{B}}W^z_l\sigma^z_l, \tag{C.10}$$

which is the same as the exact one obtained from Eq. (C.1) analytically. Obviously, regions A and B are completely decoupled.

Appendix D

Quantum dissipative systems

In the present Chapter, we briefly introduce the formalism to find the dynamics of the quantum dissipative system. In addition, we will explain the super operator form, which is very useful for analyzing the dynamics of dissipative systems.

D.1 Liouvillian-von Neumann equation

Let us start from the closed systems or highly isolated systems from the environment, in which its physical state is represented by a wave function $\Psi(x,t)$ or a state vector $|\Psi(t)\rangle$. And one can calculate it's dynamics by Schrödinger equation which is differential equation. For instance, when the system's Hamiltonian $\hat{H}$ is time independent, the state dynamics is given by

$$i\hbar\frac{d}{dt}|\Psi(t)\rangle = \hat{H}|\Psi(t)\rangle. \tag{D.1}$$

For closed systems, the state vector and the above equation are enough to understand it dynamics.

However, when the system is effected by the environment, it is better to use the density matrix $\hat{\rho}(t) = |\Psi(t)\rangle\langle\Psi(t)|$. Now, in general a different equation for $\hat{\rho}(t)$ can be written as

$$\frac{d}{dt}\hat{\rho}(t) = \hat{\mathcal{L}}[\hat{\rho}(t)]\ , \tag{D.2}$$

where $\hat{\mathcal{L}}$ is called the **Liouvillian operator** and it acts on the operator. The above equation is an analogy to the classical Liouvillian equation in the classical statistics physics. In the absence of the environment, the Liouvillian equation can be obtained form Eq. (D.1), as

follows,

$$\begin{aligned}\frac{d}{dt}\hat{\rho}(t) &= \left(\frac{d}{dt}|\Psi(t)\rangle\right)\langle\Psi(t)| + |\Psi(t)\rangle\left(\frac{d}{dt}\langle\Psi(t)|\right) \\ &= -\frac{i}{\hbar}\left(\hat{H}\hat{\rho}(t) - \hat{\rho}(t)\hat{H}\right) \\ &= -\frac{i}{\hbar}[\hat{H},\hat{\rho}].\end{aligned} \tag{D.3}$$

Thus, the corresponding Liouvillian operator is $\hat{\mathcal{L}}[\hat{\rho}] = -\frac{i}{\hbar}[\hat{H},\hat{\rho}]$ that preserves the unitary in the dynamics. In the other words, it gives the unitary dynamics. Thus, the above differential equation (D.2) has is refereed to as the **Liouville-von Neumann equation**.

D.2 The total system including the system and the environment

Now, let us consider the system coupled to an environment. In this case, the generic total Hamiltonian can be represented by $\hat{H}_{\mathrm{T}} = \hat{H}_{\mathrm{S}} + \hat{H}_{\mathrm{E}} + \hat{H}_{\text{S-E}}$, where $\hat{H}_{\mathrm{S}}$ and $\hat{H}_{\mathrm{E}}$ are the system's and environment's Hamiltonian, and $\hat{H}_{\text{S-E}}$ is the interaction term between the system and the environment. Then, the dynamics of the density matrix for the total system are obtained from Eq. (D.2), as follows,

$$\frac{d}{dt}\hat{\rho}_{\mathrm{T}} = -\frac{i}{\hbar}[\hat{H}_{\mathrm{T}},\hat{\rho}_{\mathrm{T}}] \tag{D.4}$$

However, because the above equation has all degree of the freedom including the environment, it is difficult to obtain the dynamics of the interested system from the above. In many cases, to avoid it, one trace out the environment space in the above equation, and derives the equation for the partial density matrix $\hat{\rho}_S = \underset{\mathrm{E}}{\mathrm{Tr}}\hat{\rho}_{\mathrm{T}}$, which is same as the density matrix of the interested system.

D.3 Lindblad equation

In this Chapter, we assume that our system is weakly coupled to the Markovian environment. In this approximation, the Liouvillian operator can be simply written as,

$$\hat{\mathcal{L}}\left[\hat{\rho}_{\mathrm{S}}(t)\right] = -\frac{i}{\hbar}[\hat{H}_{\mathrm{S}},\hat{\rho}_S(t)] + \mathcal{D}[\hat{\rho}_S(t)]. \tag{D.5}$$

Here, Eq. (D.2) with the above Liouvillian operator is specifically called the **Lindblad equation**. Explicitly, the first term above is the same as that of the Liouville-von Neumann equation for the system. Next, the second term represents non-unitary dynamics due to the environment. Generically, it can be represented as follows,

$$\mathcal{D}[\hat{\rho}_S(t)] = \sum_l \left(\hat{L}_l \hat{\rho}(t) \hat{L}_l^\dagger - \frac{1}{2} \left\{ \hat{L}_l^\dagger \hat{L}_l, \hat{\rho}_S(t) \right\} \right), \tag{D.6}$$

where the operators $\hat{L}_l$ are referred to as the jump operator, and $\left\{\hat{A}, \hat{B}\right\} = \hat{A}\hat{B} + \hat{B}\hat{A}$ is an anti-commutator. If you want more details, Refs. [118, 119] are available.

Next, let us see the more detail of Eq. (D.6) for spin-$1/2$ systems that we are interested in. The generic form of $\mathcal{D}[\hat{\rho}_s(t)]$ is given by,

$$\begin{aligned} \mathcal{D}[\hat{\rho}_S(t)] = & \sum_{l,m} \gamma_{lm}^{\text{emi}} \left(\sigma_l^- \hat{\rho}_S(t) \sigma_m^+ - \frac{1}{2} \left\{ \sigma_k^+ \sigma_m^-, \hat{\rho}_S(t) \right\} \right) \\ & + \sum_{l,m} \gamma_{lm}^{\text{abs}} \left(\sigma_l^+ \hat{\rho}_S(t) \sigma_m^- - \frac{1}{2} \left\{ \sigma_k^- \sigma_m^+, \hat{\rho}_S(t) \right\} \right) \\ & + \sum_{l,m} \gamma_{lm}^{\text{dep}} \left(\sigma_l^z \hat{\rho}_S(t) \sigma_m^z - \frac{1}{2} \left\{ \sigma_k^z \sigma_m^z, \hat{\rho}_S(t) \right\} \right), \end{aligned} \tag{D.7}$$

where $\sigma_l^\pm = (\sigma_l^x \pm i\sigma_l^y)/2$. Here, the first and second terms above represent the **emission** and **absorption** of the energy causing the spin flip. For example, when a two-level system is coupled to the cavity, there is energy exchanging between the system and the cavity via the photon emission and absorption. Next, the last term above is referred to as the **dephasing** term that yields the decay of off-diagonal elements in the density operator.

D.4 Super-operator formalism

The differential equation (D.2) is a completely positive map that preserves the trace of the density matrix. Despite its form is very similar to the Schrödinger equation that is the first-order differentiation, we always have difficulty in solving the equation, because they are matrices. However, it is possible to transform the matrix to the vector which is referred to as the super-operation formalism.

Suppose, the system's density matrix is given by $\hat{\rho} = \sum_{lm} \rho_{lm} |l\rangle \langle m|$ where $|l\rangle$ are states in the Hilbert space $\mathcal{H}$, for instance the computational bases set. Then in the super-operation formalism it is written as a vector, as follows,

$$|\hat{\rho}\rangle\rangle = \sum_{lm} \rho_{lm} |l\rangle \otimes |m\rangle. \tag{D.8}$$

where the matrix elements are $\rho_{lm} = \langle l|\hat{\rho}|m\rangle$. Here we note that the vector above are defined in the extended Hilbert space $\mathcal{H} \otimes \mathcal{H}$, and sometimes the space is called the **Fock-Liouvillian space (FLS)**. For instance, let us consider a single spin in the computational bases. A density matrix is given by

$$\hat{\rho} = \begin{pmatrix} \rho_{00} & \rho_{01} \\ \rho_{10} & \rho_{11} \end{pmatrix}. \tag{D.9}$$

While, its super-operator formalism is

$$|\hat{\rho}\rangle\rangle = \begin{pmatrix} \rho_{00} \\ \rho_{01} \\ \rho_{10} \\ \rho_{11} \end{pmatrix}. \tag{D.10}$$

Similarly, for any operator $\hat{A}$, its vector form is given by

$$|\hat{A}\rangle\rangle = \sum_{lm} A_{lm}|l\rangle \otimes |m\rangle. \tag{D.11}$$

In the space, the scalar product of operators $\hat{A}$ and $\hat{B}$ is defined by,

$$\langle\langle \hat{A}|\hat{B}\rangle\rangle = \text{Tr}[\hat{A}^\dagger \hat{B}]. \tag{D.12}$$

Next, to obtained the Liouvillian operator in the super-operation formalism, let us consider action of an operator. Suppose we have an density operator $\hat{\rho}$ and an operator $\hat{A}$ acts on it from the left side, $\hat{A}\hat{\rho}$. In the super-operator formalism, it cam be written by,

$$\hat{A}\hat{\rho} = \sum_{lm} \rho_{lm} A|l\rangle\langle m| \to \sum_{lm} \rho_{lm} \left(\hat{A} \otimes \mathbb{I}\right) (|l\rangle \otimes |m\rangle) = \left(\hat{A} \otimes \mathbb{I}\right) ||\hat{\rho}\rangle\rangle, \tag{D.13}$$

where $\mathbb{I}$ is the identity operator with the same dimension of $\hat{A}$. Similarly, the right multiplication $\hat{\rho}\hat{A}$ can be written by,

$$\hat{\rho}\hat{A} \to \left(\mathbb{I} \otimes \hat{A}^T\right) ||\hat{\rho}\rangle\rangle, \tag{D.14}$$

where $\hat{A}^T$ is the transpose of $\hat{A}$.

Now, in this extended Hilbert space, the Lindblad equation (D.2) is written as a linear system of coupled ordinary differential equations

$$\frac{d}{dt}|\hat{\rho}(t)\rangle\rangle = \hat{\hat{\mathcal{L}}}|\hat{\rho}(t)\rangle\rangle \tag{D.15}$$

where $\hat{\hat{L}}$ is the Liouvillian super-operator. Because the form is the same as the Schrödinger equation, it is easier to get the intuition of the dynamics form the Liovillian super-operators. For example, when the spin-network is under dephasing, its Liouvillian super-operator can be written as

$$\hat{\hat{\mathcal{L}}} = -\frac{i}{\hbar}\left(\hat{H} \otimes \mathbb{I}_N - \mathbb{I}_N \otimes \hat{H}^T\right) + \gamma \sum_l \left(\sigma_l^z \otimes \sigma_l^z - \mathbb{I}_N \otimes \mathbb{I}_N\right), \tag{D.16}$$

where $\mathbb{I}_N$ is the $(2^N \times 2^N)$-dimensional identity operator, and $\hat{H}$ is the network's Hamiltonian. It can be considered as the system where two individual networks are coupled via the pseudo-interaction: $\gamma \sum_l \sigma_l^z \otimes \sigma_l^z$.

D.5 Floquet Theory for the dissipative system

In Chapter 4.5, we have applied the Floquet theory to the periodic driven spin network interacting with the environment. In this section, we briefly explain the Floquet theory for the dissipative systems.

Let us consider a time dependent Liouvillian operator $\hat{\mathcal{L}}_t$ and dynamics given by,

$$\frac{d}{dt}\hat{\rho}(t) = \hat{\mathcal{L}}_t[\hat{\rho}(t)] \tag{D.17}$$

where $\hat{\rho}(t)$ is the density matrix. As it is not possible to apply Floquet theory in this style, we use the sparse operator formalism in which the dynamics is given by

$$\frac{d}{dt}|\hat{\rho}(t)\rangle\rangle = \hat{\hat{\mathcal{L}}}_t|\hat{\rho}(t)\rangle\rangle \tag{D.18}$$

where $\hat{\hat{\mathcal{L}}}_t$ is the super-operator of the Liouvillian. Now, as we saw in the above section, we can treat the dynamics of the density matrix $\hat{\rho}(t)$ as a vector $|\hat{\rho}(t)\rangle\rangle$, and apply the Floquet theory to it, as similar to a state in closed systems [215].

Now, when the Liouvillian operator is time periodic ($\hat{\hat{\mathcal{L}}}_t = \hat{\hat{\mathcal{L}}}_{t+T}$), the Floquet theory tells us that the density matrix $\hat{\rho}(t)$ at stroboscopic times $t = nT$ can be obtained from,

$$|\hat{\rho}(nT)\rangle\rangle = \hat{\hat{\Phi}}_T^n|\hat{\rho}(0)\rangle\rangle, \tag{D.19}$$

where $\hat{\hat{\Phi}}_T$ is called a dynamical map associated with the period T which corresponds to the Floquet operator in the closed system. Like the Floquet operator, the map can be

obtained by,

$$\hat{\hat{\Phi}}_T = \hat{\overleftarrow{\mathcal{T}}} e^{\int_0^T \hat{\hat{\mathcal{L}}}_\tau d\tau} = e^{\hat{\hat{\mathcal{L}}}_T^{\text{eff}} T}, \tag{D.20}$$

where $\hat{\overleftarrow{\mathcal{T}}}$ is the time-ordering operator. As similar to the effective Hamiltonian of the closed system, the the dynamics at the stroboscopic times $t = nT$ are governed by the effective Liouvillian super-operator,

$$\hat{\hat{L}}_T^{\text{eff}} = \frac{1}{T} \ln \hat{\hat{\Phi}}_T. \tag{D.21}$$

Here, clearly the Liouvillian is time-independent.

Similar to the Magnus expansion of the closed systems, the effective Liouvillian operator can be written as,

$$\hat{\hat{L}}_T^{\text{eff}} = \sum_{n=0}^{\infty} \hat{\hat{L}}_F^{(n)} T. \tag{D.22}$$

For instance, the first term is given by,

$$\hat{\hat{L}}_F^{(0)} = \frac{1}{T} \int_0^T \hat{\hat{\mathcal{L}}}_\tau d\tau. \tag{D.23}$$

More details on the Floquet theory for the open quantum systems and disspative systems are available on Ref. [215, 216]

Appendix E

Principal component analysis (PCA)

In Chapter 5, we mentioned that principal component analysis (PCA) is used to map classical data to quantum states. In this Chapter, we will briefly explain the actual process of PCA. In Chapter 5, we used PCA to decompose handwritten digit data set (MNIST) to perform the QRELM with 11 to 14 qubits.

Suppose, we have D-dimensional classical data set $\mathbf{X}$ with M-samples,

$$\mathbf{X} = \begin{pmatrix} x_{1,1} & x_{1,2} & \cdots & x_{1,D} \\ x_{2,1} & x_{2,2} & \cdots & x_{2,D} \\ \vdots & \vdots & \ddots & \vdots \\ x_{M,1} & x_{M,2} & \cdots & x_{M,D} \end{pmatrix} = \begin{pmatrix} \boldsymbol{x}_1^T \\ \boldsymbol{x}_2^T \\ \vdots \\ \boldsymbol{x}_D^T \end{pmatrix} \tag{E.1}$$

where $\boldsymbol{x}_l$ is a one of the sample labeled by l ($l = 1, \cdots, M$) and $\boldsymbol{x}_l^T$ is the transpose of $\boldsymbol{x}_l$. To find the variance of this data set, we denote the averaged data set as,

$$\bar{\mathrm{X}} = \begin{pmatrix} x_{1,1} - \bar{x}_1 & x_{1,2} - \bar{x}_2 & \cdots & x_{1,D} - \bar{x}_D \\ x_{2,1} - \bar{x}_1 & x_{2,2} - \bar{x}_2 & \cdots & x_{2,D} - \bar{x}_D \\ \vdots & \vdots & \ddots & \vdots \\ x_{M,1} - \bar{x}_1 & x_{M,2} - \bar{x}_2 & \cdots & x_{M,D} - \bar{x}_D \end{pmatrix} = \begin{pmatrix} (\boldsymbol{x}_1 - \bar{\boldsymbol{x}})^T \\ (\boldsymbol{x}_2 - \bar{\boldsymbol{x}})^T \\ \vdots \\ (\boldsymbol{x}_D - \bar{\boldsymbol{x}})^T \end{pmatrix} \tag{E.2}$$

where $\bar{\boldsymbol{x}} = (\bar{x}_1, \cdots, \bar{x}_D)^T$, and $\bar{x}_l = \sum_m^M x_{m,l}/M$. Now, the the covariance matrix ($\boldsymbol{\Sigma}$) representing the variance of the data set is defined by,

$$\boldsymbol{\Sigma} = \mathrm{Var}\left\{\bar{\boldsymbol{X}}\right\} = \frac{1}{M}\bar{\boldsymbol{X}}^T\bar{\boldsymbol{X}} \tag{E.3}$$

where $\boldsymbol{\Sigma}$ is the real symmetric matrix.

The PCA is a linear transformation of a data set to the direction in which its variance

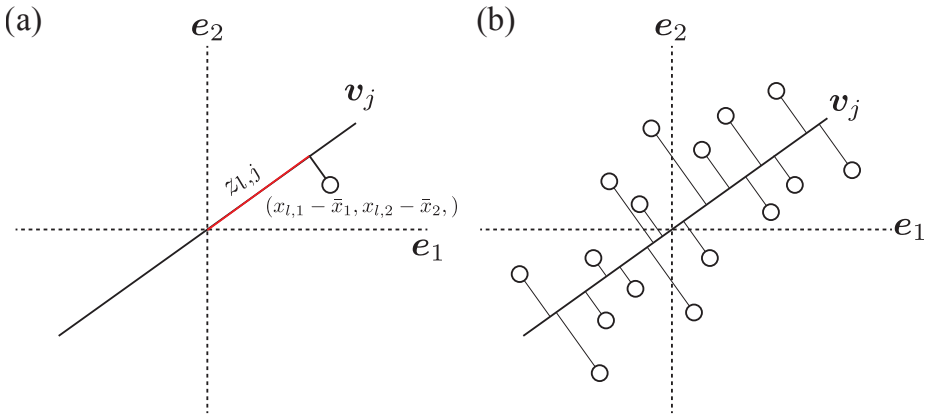

Figure E.1: Basis transformation in vector space (a). The vector represented by $(x_{l,1} - \bar{x}_1, x_{l,2} - \bar{x}_2)$ in the original space stretched by $\boldsymbol{e}_1$ and $\boldsymbol{e}_2$ is represented by $z_{l,j}$ in the new basis vector $\boldsymbol{v}_j$. PCA finds a new basis vector where the data points are the most spread out, i.e., where the variance is the largest (b).

is maximized. In other words, it is the same as the projection to the direction where its variance is maximized. Thus, here we introduce new unite vectors, as follows,

$$\boldsymbol{v}_1 = \begin{pmatrix} v_{1,1} \\ v_{1,2} \\ \vdots \\ v_{1,D} \end{pmatrix}, \quad \boldsymbol{v}_2 = \begin{pmatrix} v_{2,1} \\ v_{2,2} \\ \vdots \\ v_{2,D} \end{pmatrix}, \cdots, \boldsymbol{v}_D = \begin{pmatrix} v_{D,1} \\ v_{D,2} \\ \vdots \\ v_{D,D} \end{pmatrix}. \tag{E.4}$$

where $\boldsymbol{v}_l^T \boldsymbol{v}_m = \delta_{l,m}$. Here, we want to rewrite the data set $\bar{\mathrm{X}}$ using this new axis. For example, the data $(\boldsymbol{x}_j - \bar{\boldsymbol{x}})$ can be written as,

$$\begin{aligned} (\boldsymbol{x}_j - \bar{\boldsymbol{x}}) &= (x_{l,1} - \bar{x}_1)\, \boldsymbol{e}_1 + (x_{l,2} - \bar{x}_2)\, \boldsymbol{e}_2 + \cdots (x_{l,D} - \bar{x}_D)\, \boldsymbol{e}_D \\ &= z_{l,1} \boldsymbol{v}_1 + z_{l,2} \boldsymbol{v}_2 \cdots z_{l,D} \boldsymbol{v}_D \end{aligned} \tag{E.5}$$

where, z_{lj} can be obtained by

$$\begin{aligned} z_{l,j} &= v_{j,1}\,(x_{l,1} - \bar{x}_1) + v_{j,2}\,(x_{l,2} - \bar{x}_2) + \cdots + v_{j,D}\,(x_{l,D} - \bar{x}_D) \\ &= (\boldsymbol{x}_l - \bar{\boldsymbol{x}})^T\, \boldsymbol{v}_j. \end{aligned} \tag{E.6}$$

Similarly, the data points along $\boldsymbol{v}_j$-axis can be given by

$$\boldsymbol{z}_j = \begin{pmatrix} z_{1j} \\ z_{2j} \\ \vdots \\ z_{Nj} \end{pmatrix} = \bar{\mathrm{X}}\boldsymbol{v}_j \tag{E.7}$$

Next, the variance of the data points on the $\boldsymbol{v}_j$-axis is given by

$$\mathrm{Var}\left\{\boldsymbol{z}_j\right\} = \frac{1}{N}\boldsymbol{z}_j^T\boldsymbol{z}_j = \frac{1}{N}\left(\bar{\mathrm{X}}\boldsymbol{v}_j\right)^T\left(\bar{\mathrm{X}}\boldsymbol{v}_j\right) = \boldsymbol{v}_j^T\boldsymbol{\Sigma}\boldsymbol{v}_j \tag{E.8}$$

Now, our purpose is to find a vector $\boldsymbol{v}_j$, such that it maximizes this new variance, while keeping its norm to one. Therefore, one can use the method of Lagrange multiplier to solve it. Here, the Lagrangian function is given as follows

$$L(\boldsymbol{v}_j) = \boldsymbol{v}_j^T\boldsymbol{\Sigma}\boldsymbol{v}_j - \lambda\left(\boldsymbol{v}_j^T\boldsymbol{v}_j - 1\right) \tag{E.9}$$

where λ is a Lagrange multiplier. The derivative of the function with respect to the vector $\boldsymbol{v}_j$ can be written as

$$\frac{\partial L(\boldsymbol{v}_j)}{\partial \boldsymbol{v}_j} = 2\boldsymbol{\Sigma}\boldsymbol{v}_j - 2\lambda\boldsymbol{v}_j = 0 \tag{E.10}$$

Finally, PCA becomes an eigenvalue problem for the covariance matrix of the original data, as follows,

$$\boldsymbol{\Sigma}\boldsymbol{v}_j = \lambda\boldsymbol{v}_j \tag{E.11}$$

where λ can be seen as eigenvalues. Because of the real symmetric matrix $\boldsymbol{\Sigma}$, eigenvalues are real and we introduce an order among the eigenvalues as $\lambda_1 \geq \lambda_2 \geq \cdots \geq \lambda_D$.

Now, remarkably, the variance of the data set on the v-axis is given by

$$\mathrm{Var}\left\{\boldsymbol{z}_j\right\} = \boldsymbol{v}_j^T\boldsymbol{\Sigma}\boldsymbol{v}_j = \lambda_j\boldsymbol{v}_j^T\boldsymbol{v}_j = \lambda_j \tag{E.12}$$

It means that the component linearly transformed by the eigenvector λ_1 with largest eigenvalue $\boldsymbol{v}_1$ has the largest variance, which is called the first principal component. Similarly, the component transformed by eigenvector $\boldsymbol{v}_j$ is called the j-th principle component (j-th PC). Since the eigenvalues gives the variances, the total variance is given by,

$$V_{\text{tot}} = \sum_{l=1}^{D} = \lambda_l \tag{E.13}$$

where it agrees with the total variance of the original data set due to the properties of

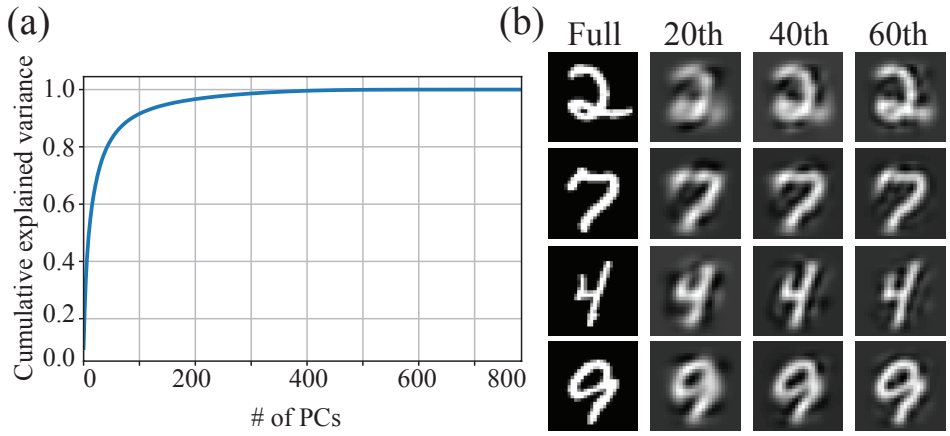

Figure E.2: PCA for handwritten digits provided by MNIST.

the trace. The ratio of the variance of the j principal component to the total variance, $r_j = \lambda_j / V_{\text{tot}}$, is called the contribution of the j-th component. Similarly, the cumulative contribution up to the j-th component is $c_j = \left(\sum_{l=1}^{j} \lambda_l\right) / V_{\text{tot}}$. It tells us the degree of compression of a linear transformation of the original data set by eigenvectors up to the j-th vector $\boldsymbol{v}_j$.

As an example, let's use PCA to decompose a handwritten number image from the MNIST data set. Fig. E.2 (a) shows the cumulative rate against the number of principal components. From this, we can see that the MNIST image can be represented by a sufficiently small vector for the whole. For example, it shows that, about 80% can be represented by the number of 100 PCs. Furthermore, since clear images of digits are not necessary for digit classification, a digit image of about the number of 20 PCs is considered sufficient, as shown in Fig. E.2 (b).

Bibliography

[1] N. Y. Yao, A. C. Potter, I.-D. Potirniche, and A. Vishwanath. Discrete time crystals: Rigidity, criticality, and realizations. *Phys. Rev. Lett.*, 118:030401, Jan 2017.

[2] J Zhang, P W Hess, A Kyprianidis, P Becker, A Lee, J Smith, G Pagano, I.-D. Potirniche, A C Potter, A Vishwanath, N Y Yao, and C Monroe. Observation of a discrete time crystal. *Nature (London)*, 543:217, mar 2017.

[3] Soonwon Choi, Joonhee Choi, Renate Landig, Georg Kucsko, Hengyun Zhou, Junichi Isoya, Fedor Jelezko, Shinobu Onoda, Hitoshi Sumiya, Vedika Khemani, Curt von Keyserlingk, Norman Y. Yao, Eugene Demler, and Mikhail D. Lukin. Observation of discrete time-crystalline order in a disordered dipolar many-body system. *Nature (London)*, 543(7644):221–225, mar 2017.

[4] Akitada Sakurai, Victor M. Bastidas, Marta P. Estarellas, William J. Munro, and Kae Nemoto. Dephasing-induced growth of discrete time-crystalline order in spin networks. *Phys. Rev. B*, 104:054304, Aug 2021.

[5] Max Planck. *The theory of heat radiation*. Courier Corporation, 2013.

[6] Albert Einstein. Über einen die erzeugung und verwandlung des lichtes betreffenden heuristischen gesichtspunkt [adp 17, 132 (1905)]. *Annalen der Physik*, 14(S1 1):164–181, 2005.

[7] Niels Bohr. I. on the constitution of atoms and molecules. *The London, Edinburgh, and Dublin Philosophical Magazine and Journal of Science*, 26(151):1–25, 1913.

[8] W. Heisenberg. Über quantentheoretische umdeutung kinematischer und mechanischer beziehungen. *Zeitschrift für Physik*, 33(1):879–893, Dec 1925.

[9] E. Schrödinger. Quantisierung als eigenwertproblem. *Annalen der Physik*, 384(4):361–376, 1926.

[10] W. Heisenberg. Über den anschaulichen inhalt der quantentheoretischen kinematik und mechanik. *Zeitschrift für Physik*, 43(3):172–198, Mar 1927.

[11] Jun John Sakurai and Eugene D Commins. Modern quantum mechanics, revised edition, 1995.

[12] Bose. Plancks gesetz und lichtquantenhypothese. *Zeitschrift für Physik*, 26(1):178–181, Dec 1924.

[13] F. LONDON. The λ-phenomenon of liquid helium and the bose-einstein degeneracy. *Nature*, 141(3571):643–644, Apr 1938.

[14] M. H. Anderson, J. R. Ensher, M. R. Matthews, C. E. Wieman, and E. A. Cornell. Observation of bose-einstein condensation in a dilute atomic vapor. *Science*, 269(5221):198–201, 1995.

[15] William D. Oliver, Yang Yu, Janice C. Lee, Karl K. Berggren, Leonid S. Levitov, and Terry P. Orlando. Mach-zehnder interferometry in a strongly driven superconducting qubit. *Science*, 310(5754):1653–1657, 2005.

[16] T. P. Harty, D. T. C. Allcock, C. J. Ballance, L. Guidoni, H. A. Janacek, N. M. Linke, D. N. Stacey, and D. M. Lucas. High-fidelity preparation, gates, memory, and readout of a trapped-ion quantum bit. *Phys. Rev. Lett.*, 113:220501, Nov 2014.

[17] S. Rosenblum, Y. Y. Gao, P. Reinhold, C. Wang, C. J. Axline, L. Frunzio, S. M. Girvin, Liang Jiang, M. Mirrahimi, M. H. Devoret, and R. J. Schoelkopf. A cnot gate between multiphoton qubits encoded in two cavities. *Nature Communications*, 9(1):652, Feb 2018.

[18] Morten Kjaergaard, Mollie E. Schwartz, Ami Greene, Gabriel O. Samach, Andreas Bengtsson, Michael O'Keeffe, Christopher M. McNally, Jochen Braumüller, David K. Kim, Philip Krantz, Milad Marvian, Alexander Melville, Bethany M. Niedzielski, Youngkyu Sung, Roni Winik, Jonilyn Yoder, Danna Rosenberg, Kevin Obenland, Seth Lloyd, Terry P. Orlando, Iman Marvian, Simon Gustavsson, and William D. Oliver. Programming a quantum computer with quantum instructions, 2020.

[19] Yuan Xu, Ji Chu, Jiahao Yuan, Jiawei Qiu, Yuxuan Zhou, Libo Zhang, Xinsheng Tan, Yang Yu, Song Liu, Jian Li, Fei Yan, and Dapeng Yu. High-fidelity, high-scalability two-qubit gate scheme for superconducting qubits. *Phys. Rev. Lett.*, 125:240503, Dec 2020.

[20] Frank Arute, Kunal Arya, Ryan Babbush, Dave Bacon, Joseph C. Bardin, Rami Barends, Rupak Biswas, Sergio Boixo, Fernando G. S. L. Brandao, David A. Buell, Brian Burkett, Yu Chen, Zijun Chen, Ben Chiaro, Roberto Collins, William

Courtney, Andrew Dunsworth, Edward Farhi, Brooks Foxen, Austin Fowler, Craig Gidney, Marissa Giustina, Rob Graff, Keith Guerin, Steve Habegger, Matthew P. Harrigan, Michael J. Hartmann, Alan Ho, Markus Hoffmann, Trent Huang, Travis S. Humble, Sergei V. Isakov, Evan Jeffrey, Zhang Jiang, Dvir Kafri, Kostyantyn Kechedzhi, Julian Kelly, Paul V. Klimov, Sergey Knysh, Alexander Korotkov, Fedor Kostritsa, David Landhuis, Mike Lindmark, Erik Lucero, Dmitry Lyakh, Salvatore Mandrà, Jarrod R. McClean, Matthew McEwen, Anthony Megrant, Xiao Mi, Kristel Michielsen, Masoud Mohseni, Josh Mutus, Ofer Naaman, Matthew Neeley, Charles Neill, Murphy Yuezhen Niu, Eric Ostby, Andre Petukhov, John C. Platt, Chris Quintana, Eleanor G. Rieffel, Pedram Roushan, Nicholas C. Rubin, Daniel Sank, Kevin J. Satzinger, Vadim Smelyanskiy, Kevin J. Sung, Matthew D. Trevithick, Amit Vainsencher, Benjamin Villalonga, Theodore White, Z. Jamie Yao, Ping Yeh, Adam Zalcman, Hartmut Neven, and John M. Martinis. Quantum supremacy using a programmable superconducting processor. *Nature*, 574(7779):505–510, Oct 2019.

[21] Morten Kjaergaard, Mollie E. Schwartz, Jochen Braumüller, Philip Krantz, Joel I.-J. Wang, Simon Gustavsson, and William D. Oliver. Superconducting qubits: Current state of play. *Annual Review of Condensed Matter Physics*, 11(1):369–395, 2020.

[22] P.T.H. Fisk, M.J. Sellars, M.A. Lawn, and G. Coles. Accurate measurement of the 12.6 ghz "clock" transition in trapped /sup 171/yb/sup +/ ions. *IEEE Transactions on Ultrasonics, Ferroelectrics, and Frequency Control*, 44(2):344–354, 1997.

[23] C. Langer, R. Ozeri, J. D. Jost, J. Chiaverini, B. DeMarco, A. Ben-Kish, R. B. Blakestad, J. Britton, D. B. Hume, W. M. Itano, D. Leibfried, R. Reichle, T. Rosenband, T. Schaetz, P. O. Schmidt, and D. J. Wineland. Long-lived qubit memory using atomic ions. *Phys. Rev. Lett.*, 95:060502, Aug 2005.

[24] A. P. VanDevender, Y. Colombe, J. Amini, D. Leibfried, and D. J. Wineland. Efficient fiber optic detection of trapped ion fluorescence. *Phys. Rev. Lett.*, 105:023001, Jul 2010.

[25] Loïc Henriet, Lucas Beguin, Adrien Signoles, Thierry Lahaye, Antoine Browaeys, Georges-Olivier Reymond, and Christophe Jurczak. Quantum computing with neutral atoms. *Quantum*, 4:327, 2020.

[26] Han-Sen Zhong, Hui Wang, Yu-Hao Deng, Ming-Cheng Chen, Li-Chao Peng, Yi-Han Luo, Jian Qin, Dian Wu, Xing Ding, Yi Hu, Peng Hu, Xiao-Yan Yang, Wei-Jun Zhang, Hao Li, Yuxuan Li, Xiao Jiang, Lin Gan, Guangwen Yang, Lixing

You, Zhen Wang, Li Li, Nai-Le Liu, Chao-Yang Lu, and Jian-Wei Pan. Quantum computational advantage using photons. *Science*, 370(6523):1460–1463, 2020.

[27] Lieven M. K. Vandersypen, Matthias Steffen, Gregory Breyta, Costantino S. Yannoni, Mark H. Sherwood, and Isaac L. Chuang. Experimental realization of shor's quantum factoring algorithm using nuclear magnetic resonance. *Nature*, 414(6866):883–887, Dec 2001.

[28] Chao-Yang Lu, Daniel E. Browne, Tao Yang, and Jian-Wei Pan. Demonstration of a compiled version of shor's quantum factoring algorithm using photonic qubits. *Phys. Rev. Lett.*, 99:250504, Dec 2007.

[29] Mikael C. Rechtsman, Julia M. Zeuner, Yonatan Plotnik, Yaakov Lumer, Daniel Podolsky, Felix Dreisow, Stefan Nolte, Mordechai Segev, and Alexander Szameit. Photonic floquet topological insulators. *Nature*, 496(7444):196–200, Apr 2013.

[30] Antoine Browaeys and Thierry Lahaye. Many-body physics with individually controlled rydberg atoms. *Nature Physics*, 16(2):132–142, Feb 2020.

[31] Ming Gong, Shiyu Wang, Chen Zha, Ming-Cheng Chen, He-Liang Huang, Yulin Wu, Qingling Zhu, Youwei Zhao, Shaowei Li, Shaojun Guo, Haoran Qian, Yangsen Ye, Fusheng Chen, Chong Ying, Jiale Yu, Daojin Fan, Dachao Wu, Hong Su, Hui Deng, Hao Rong, Kaili Zhang, Sirui Cao, Jin Lin, Yu Xu, Lihua Sun, Cheng Guo, Na Li, Futian Liang, V. M. Bastidas, Kae Nemoto, W. J. Munro, Yong-Heng Huo, Chao-Yang Lu, Cheng-Zhi Peng, Xiaobo Zhu, and Jian-Wei Pan. Quantum walks on a programmable two-dimensional 62-qubit superconducting processor. *Science*, 372(6545):948–952, 2021.

[32] Peng Xu, Wei Zheng, and Hui Zhai. Topological micromotion of floquet quantum systems. *Phys. Rev. B*, 105:045139, Jan 2022.

[33] Dominic V. Else, Bela Bauer, and Chetan Nayak. Floquet time crystals. *Phys. Rev. Lett.*, 117:090402, Aug 2016.

[34] Markus Heyl. Dynamical quantum phase transitions: A brief survey. 125(2):26001, feb 2019.

[35] Ryusuke Hamazaki. Exceptional dynamical quantum phase transitions in periodically driven systems. *Nature Communications*, 12(1):5108, Sep 2021.

[36] Jirawat Tangpanitanon, Supanut Thanasilp, Marc-Antoine Lemonde, Ninnat Dangiam, and Dimitris G Angelakis. Quantum supremacy in driven quantum many-body systems. *arXiv preprint arXiv:2002.11946*, 2020.

[37] Rodrigo Martínez-Peña, Gian Luca Giorgi, Johannes Nokkala, Miguel C. Soriano, and Roberta Zambrini. Dynamical phase transitions in quantum reservoir computing. *Phys. Rev. Lett.*, 127:100502, Aug 2021.

[38] M. P. Estarellas, T. Osada, V. M. Bastidas, B. Renoust, K. Sanaka, W. J. Munro, and K. Nemoto. Simulating complex quantum networks with time crystals. *Sci. Adv.*, 6(42):eaay8892, 2020.

[39] Soham Pal, Naveen Nishad, T. S. Mahesh, and G. J. Sreejith. Temporal order in periodically driven spins in star-shaped clusters. *Phys. Rev. Lett.*, 120:180602, May 2018.

[40] J. Smits, L. Liao, H. T. C. Stoof, and P. van der Straten. Observation of a space-time crystal in a superfluid quantum gas. *Phys. Rev. Lett.*, 121:185301, Oct 2018.

[41] Jared Rovny, Robert L. Blum, and Sean E. Barrett. Observation of discrete-time-crystal signatures in an ordered dipolar many-body system. *Phys. Rev. Lett.*, 120:180603, May 2018.

[42] J. Randall, C. E. Bradley, F. V. van der Gronden, A. Galicia, M. H. Abobeih, M. Markham, D. J. Twitchen, F. Machado, N. Y. Yao, and T. H. Taminiau. Observation of a many-body-localized discrete time crystal with a programmable spin-based quantum simulator. 2021.

[43] Xiao Mi, Matteo Ippoliti, Chris Quintana, Ami Greene, Zijun Chen, Jonathan Gross, Frank Arute, Kunal Arya, Juan Atalaya, Ryan Babbush, Joseph C. Bardin, Joao Basso, Andreas Bengtsson, Alexander Bilmes, Alexandre Bourassa, Leon Brill, Michael Broughton, Bob B. Buckley, David A. Buell, Brian Burkett, Nicholas Bushnell, Benjamin Chiaro, Roberto Collins, William Courtney, Dripto Debroy, Sean Demura, Alan R. Derk, Andrew Dunsworth, Daniel Eppens, Catherine Erickson, Edward Farhi, Austin G. Fowler, Brooks Foxen, Craig Gidney, Marissa Giustina, Matthew P. Harrigan, Sean D. Harrington, Jeremy Hilton, Alan Ho, Sabrina Hong, Trent Huang, Ashley Huff, William J. Huggins, L. B. Ioffe, Sergei V. Isakov, Justin Iveland, Evan Jeffrey, Zhang Jiang, Cody Jones, Dvir Kafri, Tanuj Khattar, Seon Kim, Alexei Kitaev, Paul V. Klimov, Alexander N. Korotkov, Fedor Kostritsa, David Landhuis, Pavel Laptev, Joonho Lee, Kenny Lee, Aditya Locharla, Erik Lucero, Orion Martin, Jarrod R. McClean, Trevor McCourt, Matt McEwen, Kevin C. Miao, Masoud Mohseni, Shirin Montazeri, Wojciech Mruczkiewicz, Ofer Naaman, Matthew Neeley, Charles Neill, Michael Newman, Murphy Yuezhen Niu, Thomas E. OBrien, Alex Opremcak, Eric Ostby, Balint Pato, Andre Petukhov, Nicholas C. Rubin, Daniel Sank, Kevin J. Satzinger, Vladimir Shvarts, Yuan Su,

Doug Strain, Marco Szalay, Matthew D. Trevithick, Benjamin Villalonga, Theodore White, Z. Jamie Yao, Ping Yeh, Juhwan Yoo, Adam Zalcman, Hartmut Neven, Sergio Boixo, Vadim Smelyanskiy, Anthony Megrant, Julian Kelly, Yu Chen, S. L. Sondhi, Roderich Moessner, Kostyantyn Kechedzhi, Vedika Khemani, and Pedram Roushan. Observation of time-crystalline eigenstate order on a quantum processor. 2021.

[44] Philipp Frey and Stephan Rachel. Realization of a discrete time crystal on 57 qubits of a quantum computer, 2022.

[45] A. Sakurai, V. M. Bastidas, W. J. Munro, and Kae Nemoto. Chimera time-crystalline order in quantum spin networks. *Phys. Rev. Lett.*, 126:120606, Mar 2021.

[46] Yann LeCun, Léon Bottou, Yoshua Bengio, and Patrick Haffner. Gradient-based learning applied to document recognition. *Proceedings of the IEEE*, 86(11):2278–2324, 1998.

[47] C. N. Yang and T. D. Lee. Statistical theory of equations of state and phase transitions. i. theory of condensation. *Phys. Rev.*, 87:404–409, Aug 1952.

[48] T. D. Lee and C. N. Yang. Statistical theory of equations of state and phase transitions. ii. lattice gas and ising model. *Phys. Rev.*, 87:410–419, Aug 1952.

[49] Paul Adrien Maurice Dirac. Relativistic quantum mechanics. *Proceedings of the Royal Society of London. Series A, Containing Papers of a Mathematical and Physical Character*, 136(829):453–464, 1932.

[50] T. D. Lee and G. C. Wick. Space inversion, time reversal, and other discrete symmetries in local field theories. *Phys. Rev.*, 148:1385–1404, Aug 1966.

[51] Vedika Khemani, Achilleas Lazarides, Roderich Moessner, and S. L. Sondhi. Phase structure of driven quantum systems. *Phys. Rev. Lett.*, 116:250401, Jun 2016.

[52] Krzysztof Sacha and Jakub Zakrzewski. Time crystals: a review. *Rep. Prog. Phys.*, 81(1):016401, jan 2018.

[53] Vedika Khemani, Roderich Moessner, and S. L. Sondhi. A brief history of time crystals, 2019.

[54] Dominic V Else, Christopher Monroe, Chetan Nayak, and Norman Y Yao. Discrete time crystals. *arXiv:1905.13232*, 2019.

[55] C. N. Yang and R. L. Mills. Conservation of isotopic spin and isotopic gauge invariance. *Phys. Rev.*, 96:191–195, Oct 1954.

[56] J. Bardeen, L. N. Cooper, and J. R. Schrieffer. Theory of superconductivity. *Phys. Rev.*, 108:1175–1204, Dec 1957.

[57] Peter W. Higgs. Broken symmetries and the masses of gauge bosons. *Phys. Rev. Lett.*, 13:508–509, Oct 1964.

[58] Subir Sachdev. *Quantum phase transitions*. Cambridge university press, 2011.

[59] Frank Wilczek. Quantum Time Crystals. *Phys. Rev. Lett.*, 109(16):160401, Oct 2012.

[60] Patrick Bruno. Impossibility of spontaneously rotating time crystals: A no-go theorem. *Phys. Rev. Lett.*, 111:070402, Aug 2013.

[61] Frank Wilczek. Superfluidity and space-time translation symmetry breaking. *Phys. Rev. Lett.*, 111:250402, Dec 2013.

[62] Ryosuke Yoshii, Satoshi Takada, Shunji Tsuchiya, Giacomo Marmorini, Hisao Hayakawa, and Muneto Nitta. Fulde-ferrell-larkin-ovchinnikov states in a superconducting ring with magnetic fields: Phase diagram and the first-order phase transitions. *Phys. Rev. B*, 92:224512, Dec 2015.

[63] Haruki Watanabe and Masaki Oshikawa. Absence of quantum time crystals. *Phys. Rev. Lett.*, 114:251603, Jun 2015.

[64] Vedika Khemani, Roderich Moessner, and S. L. Sondhi. A comment on "discrete time crystals: rigidity, criticality, and realizations", 2021.

[65] Denis M Basko, Igor L Aleiner, and Boris L Altshuler. Metal-insulator transition in a weakly interacting many-electron system with localized single-particle states. *Annals of physics*, 321(5):1126–1205, 2006.

[66] DM Basko, IL Aleiner, and BL Altshuler. On the problem of many-body localization. *Problems of Condensed Matter Physics*, pages 50–70, 2006.

[67] Vadim Oganesyan and David A. Huse. Localization of interacting fermions at high temperature. *Phys. Rev. B*, 75:155111, Apr 2007.

[68] Toma ž Prosen. Time evolution of a quantum many-body system: Transition from integrability to ergodicity in the thermodynamic limit. *Phys. Rev. Lett.*, 80:1808–1811, Mar 1998.

[69] Toma ž Prosen. Ergodic properties of a generic nonintegrable quantum many-body system in the thermodynamic limit. *Phys. Rev. E*, 60:3949–3968, Oct 1999.

[70] Luca D'Alessio and Anatoli Polkovnikov. Many-body energy localization transition in periodically driven systems. *Ann. Phys. (N. Y.)*, 333:19–33, 2013.

[71] Achilleas Lazarides, Arnab Das, and Roderich Moessner. Equilibrium states of generic quantum systems subject to periodic driving. *Phys. Rev. E*, 90:012110, Jul 2014.

[72] Luca D'Alessio and Marcos Rigol. Long-time behavior of isolated periodically driven interacting lattice systems. *Phys. Rev. X*, 4:041048, Dec 2014.

[73] Marin Bukov, Luca D'Alessio, and Anatoli Polkovnikov. Universal high-frequency behavior of periodically driven systems: from dynamical stabilization to floquet engineering. *Adv. Phys.*, 64(2):139–226, 2015.

[74] Pedro Ponte, Anushya Chandran, Z Papić, and Dmitry A Abanin. Periodically driven ergodic and many-body localized quantum systems. *Ann. Phys. (N. Y.)*, 353:196–204, 2015.

[75] Marin Bukov, Sarang Gopalakrishnan, Michael Knap, and Eugene Demler. Prethermal floquet steady states and instabilities in the periodically driven, weakly interacting bose-hubbard model. *Phys. Rev. Lett.*, 115:205301, Nov 2015.

[76] David J Luitz, Yevgeny Bar Lev, and Achilleas Lazarides. Absence of dynamical localization in interacting driven systems. *SciPost Phys*, 3:029, 2017.

[77] Maksym Serbyn, Z. Papić, and Dmitry A. Abanin. Universal slow growth of entanglement in interacting strongly disordered systems. *Phys. Rev. Lett.*, 110:260601, Jun 2013.

[78] Bela Bauer and Chetan Nayak. Area laws in a many-body localized state and its implications for topological order. *Journal of Statistical Mechanics: Theory and Experiment*, 2013(09):P09005, 2013.

[79] David A. Huse, Rahul Nandkishore, and Vadim Oganesyan. Phenomenology of fully many-body-localized systems. *Phys. Rev. B*, 90:174202, Nov 2014.

[80] Francisco Machado, Gregory D. Kahanamoku-Meyer, Dominic V. Else, Chetan Nayak, and Norman Y. Yao. Exponentially slow heating in short and long-range interacting floquet systems. *Phys. Rev. Research*, 1:033202, Dec 2019.

[81] Tomotaka Kuwahara, Takashi Mori, and Keiji Saito. Floquet–magnus theory and generic transient dynamics in periodically driven many-body quantum systems. *Annals of Physics*, 367:96–124, 2016.

[82] Takashi Mori, Tomotaka Kuwahara, and Keiji Saito. Rigorous bound on energy absorption and generic relaxation in periodically driven quantum systems. *Phys. Rev. Lett.*, 116:120401, Mar 2016.

[83] Dmitry Abanin, Wojciech De Roeck, Wen Wei Ho, and François Huveneers. A rigorous theory of many-body prethermalization for periodically driven and closed quantum systems. *Commun. Math. Phys.*, 354(3):809–827, Sep 2017.

[84] Dmitry A. Abanin, Wojciech De Roeck, Wen Wei Ho, and Fran çois Huveneers. Effective hamiltonians, prethermalization, and slow energy absorption in periodically driven many-body systems. *Phys. Rev. B*, 95:014112, Jan 2017.

[85] Dominic V. Else, Bela Bauer, and Chetan Nayak. Prethermal phases of matter protected by time-translation symmetry. *Phys. Rev. X*, 7:011026, Mar 2017.

[86] Subir Sachdev. *Quantum phase transitions*. Cambridge university press, 2011.

[87] William Berdanier, Michael Kolodrubetz, S. A. Parameswaran, and Romain Vasseur. Strong-disorder renormalization group for periodically driven systems. *Phys. Rev. B*, 98:174203, Nov 2018.

[88] Norman Y. Yao, Andrew C. Potter, Ionut-Dragos Potirniche, and Ashvin Vishwanath. Reply to comment on "discrete time crystals: Rigidity criticality and realizations", 2021.

[89] Yonatan Sharabi, Eran Lustig, and Mordechai Segev. Disordered photonic time crystals. *Phys. Rev. Lett.*, 126:163902, Apr 2021.

[90] Marko Medenjak, Berislav Buča, and Dieter Jaksch. Isolated heisenberg magnet as a quantum time crystal. *Phys. Rev. B*, 102:041117, Jul 2020.

[91] Krzysztof Giergiel, Alexandre Dauphin, Maciej Lewenstein, Jakub Zakrzewski, and Krzysztof Sacha. Topological time crystals. *New Journal of Physics*, 21(5):052003, may 2019.

[92] Achilleas Lazarides and Roderich Moessner. Fate of a discrete time crystal in an open system. *Phys. Rev. B*, 95:195135, May 2017.

[93] James O'Sullivan, Oliver Lunt, Christoph W Zollitsch, MLW Thewalt, John JL Morton, and Arijeet Pal. Dissipative discrete time crystals. *arXiv:1807.09884*, 2018.

[94] Bihui Zhu, Jamir Marino, Norman Y Yao, Mikhail D Lukin, and Eugene A Demler. Dicke time crystals in driven-dissipative quantum many-body systems. *New Journal of Physics*, 21(7):073028, jul 2019.

[95] F. Iemini, A. Russomanno, J. Keeling, M. Schirò, M. Dalmonte, and R. Fazio. Boundary time crystals. *Phys. Rev. Lett.*, 121:035301, Jul 2018.

[96] D. Porras and J. I. Cirac. Effective quantum spin systems with trapped ions. *Phys. Rev. Lett.*, 92:207901, May 2004.

[97] A. C. Lee, J. Smith, P. Richerme, B. Neyenhuis, P. W. Hess, J. Zhang, and C. Monroe. Engineering large stark shifts for control of individual clock state qubits. *Phys. Rev. A*, 94:042308, Oct 2016.

[98] Y Kuramoto and D Battogtokh. Coexistence of coherence and incoherence in nonlocally coupled phase oscillators. *Nonlinear Phenom. Complex Syst.*, 5(4):380–385, 2002.

[99] V. M. Bastidas, I. Omelchenko, A. Zakharova, E. Schöll, and T. Brandes. Quantum signatures of chimera states. *Phys. Rev. E*, 92:062924, Dec 2015.

[100] Daniel M. Abrams and Steven H. Strogatz. Chimera states for coupled oscillators. *Phys. Rev. Lett.*, 93:174102, Oct 2004.

[101] Mark J Panaggio and Daniel M Abrams. Chimera states: coexistence of coherence and incoherence in networks of coupled oscillators. *Nonlinearity*, 28(3):R67–R87, feb 2015.

[102] Aaron M. Hagerstrom, Thomas E. Murphy, Rajarshi Roy, Philipp Hövel, Iryna Omelchenko, and Eckehard Schöll. Experimental observation of chimeras in coupled-map lattices. *Nature Physics*, 8(9):658–661, Sep 2012.

[103] A. P. Young and H. Rieger. Numerical study of the random transverse-field ising spin chain. *Phys. Rev. B*, 53:8486–8498, Apr 1996.

[104] Glen Bigan Mbeng, Lorenzo Privitera, Luca Arceci, and Giuseppe E. Santoro. Dynamics of simulated quantum annealing in random ising chains. *Phys. Rev. B*, 99:064201, Feb 2019.

[105] Manuel Gessner, Victor Manuel Bastidas, Tobias Brandes, and Andreas Buchleitner. Semiclassical excited-state signatures of quantum phase transitions in spin chains with variable-range interactions. *Phys. Rev. B*, 93:155153, Apr 2016.

[106] Ryszard Horodecki, Paweł Horodecki, Michał Horodecki, and Karol Horodecki. Quantum entanglement. *Rev. Mod. Phys.*, 81:865–942, Jun 2009.

[107] J. Eisert, M. Cramer, and M. B. Plenio. Colloquium: Area laws for the entanglement entropy. *Rev. Mod. Phys.*, 82:277–306, Feb 2010.

[108] Don N. Page. Average entropy of a subsystem. *Phys. Rev. Lett.*, 71:1291–1294, Aug 1993.

[109] Jonas A. Kjäll, Jens H. Bardarson, and Frank Pollmann. Many-body localization in a disordered quantum ising chain. *Phys. Rev. Lett.*, 113:107204, Sep 2014.

[110] Xiaofang Zhang, Xiaoli Lin, and Rana Aamir Raza Ashfaq. Impact of different random initializations on generalization performance of extreme learning machine. *J. Comput.*, 13(7):805–822, 2018.

[111] W Rossmann. An introduction through linear groups. *Lie Groups, Oxford Graduate Texts in Mathematics*, 5, 2001.

[112] Achilleas Lazarides and Roderich Moessner. Fate of a discrete time crystal in an open system. *Phys. Rev. B*, 95:195135, May 2017.

[113] Andreu Riera-Campeny, Maria Moreno-Cardoner, and Anna Sanpera. Time crystallinity in open quantum systems. *Quantum*, 4:270, May 2020.

[114] Chu-hui Fan, D. Rossini, Han-Xiao Zhang, Jin-Hui Wu, M. Artoni, and G. C. La Rocca. Discrete time crystal in a finite chain of rydberg atoms without disorder. *Phys. Rev. A*, 101:013417, Jan 2020.

[115] Achilleas Lazarides, Sthitadhi Roy, Francesco Piazza, and Roderich Moessner. Time crystallinity in dissipative floquet systems. *Phys. Rev. Research*, 2:022002, Apr 2020.

[116] Hans Keßler, Phatthamon Kongkhambut, Christoph Georges, Ludwig Mathey, Jayson G. Cosme, and Andreas Hemmerich. Observation of a dissipative time crystal. *Phys. Rev. Lett.*, 127:043602, Jul 2021.

[117] Crispin Gardiner and Peter Zoller. *Quantum Noise*, volume 56. Springer, 2004.

[118] Carlos Alexandre Brasil, Felipe Fernandes Fanchini, and Reginaldo de Jesus Napolitano. A simple derivation of the lindblad equation. *Revista Brasileira de Ensino de Física*, 35(1):01–09, Mar 2013.

[119] Daniel Manzano. A short introduction to the lindblad master equation. *AIP Adv.*, 10(2):025106, 2020.

[120] Toma ž Prosen. Exact nonequilibrium steady state of a strongly driven open xxz chain. *Phys. Rev. Lett.*, 107:137201, Sep 2011.

[121] Berislav Buča and Tomaž Prosen. A note on symmetry reductions of the lindblad equation: transport in constrained open spin chains. 14(7):073007, jul 2012.

[122] Victor V. Albert and Liang Jiang. Symmetries and conserved quantities in lindblad master equations. *Phys. Rev. A*, 89:022118, Feb 2014.

[123] Marko Žnidarič. Relaxation times of dissipative many-body quantum systems. *Phys. Rev. E*, 92:042143, Oct 2015.

[124] G. Vidal and R. F. Werner. Computable measure of entanglement. *Phys. Rev. A*, 65:032314, Feb 2002.

[125] Soojoon Lee, Dong Pyo Chi, Sung Dahm Oh, and Jaewan Kim. Convex-roof extended negativity as an entanglement measure for bipartite quantum systems. *Phys. Rev. A*, 68:062304, Dec 2003.

[126] Naoyuki Shibata and Hosho Katsura. Quantum Ising chain with boundary dephasing. *Progress of Theoretical and Experimental Physics*, 2020(12), 08 2020. 12A108.

[127] M. V. Medvedyeva and S. Kehrein. Power-law approach to steady state in open lattices of noninteracting electrons. *Phys. Rev. B*, 90:205410, Nov 2014.

[128] Alastair Kay. Perfect coding for dephased quantum state transfer. *Phys. Rev. A*, 97:032317, Mar 2018.

[129] Merab Malishava, Ihor Vakulchyk, Mikhail Fistul, and Sergej Flach. Floquet anderson localization of two interacting discrete time quantum walks. *Phys. Rev. B*, 101:144201, Apr 2020.

[130] Richard P. Feynman. Simulating physics with computers. *International Journal of Theoretical Physics*, 21(6):467–488, Jun 1982.

[131] Paul Benioff. The computer as a physical system: A microscopic quantum mechanical hamiltonian model of computers as represented by turing machines. *Journal of Statistical Physics*, 22(5):563–591, May 1980.

[132] David Deutsch. Quantum theory, the church-turing principle and the universal quantum computer. 400:97–117, 1985.

[133] Michael A Nielsen and Isaac L Chuang. Quantum computation and quantum information. *Phys. Today*, 54(2):60, 2001.

[134] Peter W. Shor. Algorithms for quantum computation: Discrete logarithms and factoring, 1994.

[135] Lov K Grover. A fast quantum mechanical algorithm for database search. In *Proceedings of the twenty-eighth annual ACM symposium on Theory of computing*, pages 212–219, 1996.

[136] Asher Peres. Reversible logic and quantum computers. *Phys. Rev. A*, 32:3266–3276, Dec 1985.

[137] Peter W. Shor. Scheme for reducing decoherence in quantum computer memory. *Phys. Rev. A*, 52:R2493–R2496, Oct 1995.

[138] Subhash C Kak. Quantum neural computing. *Advances in imaging and electron physics*, 94:259–313, 1995.

[139] Ronald Chrisley. Quantum learning. In *New directions in cognitive science: Proceedings of the international symposium, Saariselka*, volume 4, 1995.

[140] Alberto Peruzzo, Jarrod McClean, Peter Shadbolt, Man-Hong Yung, Xiao-Qi Zhou, Peter J. Love, Alán Aspuru-Guzik, and Jeremy L. O'Brien. A variational eigenvalue solver on a photonic quantum processor. *Nature Communications*, 5(1):4213, Jul 2014.

[141] Nathan Wiebe, Ashish Kapoor, and Krysta M. Svore. Quantum deep learning, 2015.

[142] Siddhant Garg and Goutham Ramakrishnan. Advances in quantum deep learning: An overview, 2020.

[143] Michael Lubasch, Jaewoo Joo, Pierre Moinier, Martin Kiffner, and Dieter Jaksch. Variational quantum algorithms for nonlinear problems. *Phys. Rev. A*, 101:010301, Jan 2020.

[144] Dmitry A. Fedorov, Bo Peng, Niranjan Govind, and Yuri Alexeev. Vqe method: A short survey and recent developments, 2021.

[145] M. Cerezo, Andrew Arrasmith, Ryan Babbush, Simon C. Benjamin, Suguru Endo, Keisuke Fujii, Jarrod R. McClean, Kosuke Mitarai, Xiao Yuan, Lukasz Cincio, and Patrick J. Coles. Variational quantum algorithms. *Nature Reviews Physics*, 3(9):625–644, Sep 2021.

[146] Keisuke Fujii and Kohei Nakajima. Harnessing disordered-ensemble quantum dynamics for machine learning. *Phys. Rev. Applied*, 8:024030, Aug 2017.

[147] Danijela Marković and Julie Grollier. Quantum neuromorphic computing. *Applied Physics Letters*, 117(15):150501, 2020.

[148] Sanjib Ghosh, Tanjung Krisnanda, Tomasz Paterek, and Timothy C. H. Liew. Realising and compressing quantum circuits with quantum reservoir computing. *Communications Physics*, 4(1):105, May 2021.

[149] Adrian Parra-Rodriguez, Pavel Lougovski, Lucas Lamata, Enrique Solano, and Mikel Sanz. Digital-analog quantum computation. *Phys. Rev. A*, 101:022305, Feb 2020.

[150] Christopher John Cornish Hellaby Watkins. Learning from delayed rewards. 1989.

[151] Junyan Hu, Hanlin Niu, Joaquin Carrasco, Barry Lennox, and Farshad Arvin. Voronoi-based multi-robot autonomous exploration in unknown environments via deep reinforcement learning. *IEEE Transactions on Vehicular Technology*, 69(12):14413–14423, 2020.

[152] Warren S. McCulloch and Walter Pitts. A logical calculus of the ideas immanent in nervous activity. *The bulletin of mathematical biophysics*, 5(4):115–133, Dec 1943.

[153] Frank Rosenblatt. The perceptron: a probabilistic model for information storage and organization in the brain. *Psychological review*, 65(6):386, 1958.

[154] G. Cybenko. Approximation by superpositions of a sigmoidal function. *Mathematics of Control, Signals and Systems*, 2(4):303–314, Dec 1989.

[155] Sho Sonoda and Noboru Murata. Neural network with unbounded activation functions is universal approximator. *Applied and Computational Harmonic Analysis*, 43(2):233–268, 2017.

[156] Corinna Cortes and Vladimir Vapnik. Support-vector networks. *Machine learning*, 20(3):273–297, 1995.

[157] Simon Haykin. *Neural networks and learning machines, 3/E*. Pearson Education India, 2010.

[158] Elizabeth C Behrman, John Niemel, James E Steck, and Steve R Skinner. A quantum dot neural network. In *Proceedings of the 4th Workshop on Physics of Computation*, pages 22–24, 1996.

[159] MV Altaisky. Quantum neural network. *arXiv preprint quant-ph/0107012*, 2001.

[160] Michail Zak and Colin P. Williams. Quantum neural nets. *International Journal of Theoretical Physics*, 37(2):651–684, Feb 1998.

[161] Francesco Tacchino, Panagiotis Barkoutsos, Chiara Macchiavello, Ivano Tavernelli, Dario Gerace, and Daniele Bajoni. Quantum implementation of an artificial feed-forward neural network. 5(4):044010, oct 2020.

[162] K. Mitarai, M. Negoro, M. Kitagawa, and K. Fujii. Quantum circuit learning. *Phys. Rev. A*, 98:032309, Sep 2018.

[163] Abhinav Kandala, Antonio Mezzacapo, Kristan Temme, Maika Takita, Markus Brink, Jerry M. Chow, and Jay M. Gambetta. Hardware-efficient variational quantum eigensolver for small molecules and quantum magnets. *Nature*, 549(7671):242–246, Sep 2017.

[164] Jarrod R. McClean, Sergio Boixo, Vadim N. Smelyanskiy, Ryan Babbush, and Hartmut Neven. Barren plateaus in quantum neural network training landscapes. *Nature Communications*, 9(1):4812, Nov 2018.

[165] Zoë Holmes, Kunal Sharma, M. Cerezo, and Patrick J. Coles. Connecting ansatz expressibility to gradient magnitudes and barren plateaus, 2021.

[166] Hsin-Yuan Huang, Michael Broughton, Masoud Mohseni, Ryan Babbush, Sergio Boixo, Hartmut Neven, and Jarrod R. McClean. Power of data in quantum machine learning. *Nature Communications*, 12(1):2631, May 2021.

[167] Maria Schuld. Supervised quantum machine learning models are kernel methods. *arXiv preprint arXiv:2101.11020*, 2021.

[168] Takeru Kusumoto, Kosuke Mitarai, Keisuke Fujii, Masahiro Kitagawa, and Makoto Negoro. Experimental quantum kernel trick with nuclear spins in a solid. *npj Quantum Information*, 7(1):94, Jun 2021.

[169] Kohei Nakajima, Helmut Hauser, Rongjie Kang, Emanuele Guglielmino, Darwin Caldwell, and Rolf Pfeifer. A soft body as a reservoir: case studies in a dynamic model of octopus-inspired soft robotic arm. *Frontiers in Computational Neuroscience*, 7:91, 2013.

[170] Sanjib Ghosh, Andrzej Opala, Michał Matuszewski, Tomasz Paterek, and Timothy C. H. Liew. Quantum reservoir processing. *npj Quantum Information*, 5(1):35, Apr 2019.

[171] Kohei Nakajima. Physical reservoir computing—an introductory perspective. 59(6):060501, may 2020.

[172] Sanjib Ghosh, Andrzej Opala, Michał Matuszewski, Tomasz Paterek, and Timothy C. H. Liew. Reconstructing quantum states with quantum reservoir networks. *IEEE Transactions on Neural Networks and Learning Systems*, 32(7):3148–3155, 2021.

[173] Kohei Nakajima, Keisuke Fujii, Makoto Negoro, Kosuke Mitarai, and Masahiro Kitagawa. Boosting computational power through spatial multiplexing in quantum reservoir computing. *Phys. Rev. Applied*, 11:034021, Mar 2019.

[174] L. C. G. Govia, G. J. Ribeill, G. E. Rowlands, H. K. Krovi, and T. A. Ohki. Quantum reservoir computing with a single nonlinear oscillator. *Phys. Rev. Research*, 3:013077, Jan 2021.

[175] Guang-Bin Huang, Qin-Yu Zhu, and Chee-Kheong Siew. Extreme learning machine: Theory and applications. *Neurocomputing*, 70(1):489–501, 2006. Neural Networks.

[176] Guang-Bin Huang, Xiaojian Ding, and Hongming Zhou. Optimization method based extreme learning machine for classification. *Neurocomputing*, 74(1):155–163, 2010. Artificial Brains.

[177] Guang-Bin Huang, Hongming Zhou, Xiaojian Ding, and Rui Zhang. Extreme learning machine for regression and multiclass classification. *IEEE Transactions on Systems, Man, and Cybernetics, Part B (Cybernetics)*, 42(2):513–529, 2012.

[178] Jian Wang, Siyuan Lu, Shui-Hua Wang, and Yu-Dong Zhang. A review on extreme learning machine. *Multimedia Tools and Applications*, May 2021.

[179] Pere Mujal, Rodrigo Martínez-Peña, Johannes Nokkala, Jorge García-Beni, Gian Luca Giorgi, Miguel C. Soriano, and Roberta Zambrini. Opportunities in quantum reservoir computing and extreme learning machines. *Advanced Quantum Technologies*, 4(8):2100027, 2021.

[180] W. D. Kalfus, G. J. Ribeill, G. E. Rowlands, H. K. Krovi, T. A. Ohki, and L. C. G. Govia. Neuromorphic computing with a single qudit, 2021.

[181] Albert B Novikoff. On convergence proofs for perceptrons. Technical report, STANFORD RESEARCH INST MENLO PARK CA, 1963.

[182] Phuc Q. Le, Fangyan Dong, and Kaoru Hirota. A flexible representation of quantum images for polynomial preparation, image compression, and processing operations. 10(1), 2011.

[183] Yue Ruan, Hanwu Chen, Zhihao Liu, and Jianing Tan. Quantum image with high retrieval performance. *Quantum Information Processing*, 15(2):637–650, Feb 2016.

[184] Salvador E Venegas-Andraca and Sougato Bose. Storing, processing, and retrieving an image using quantum mechanics. In Eric Donkor, Andrew R. Pirich, and Howard E. Brandt, editors, *Quantum Information and Computation*, volume 5105, pages 137 – 147. International Society for Optics and Photonics, SPIE, 2003.

[185] Suresh Prasad Kannojia and Gaurav Jaiswal. Ensemble of hybrid cnn-elm model for image classification. In *2018 5th International Conference on Signal Processing and Integrated Networks (SPIN)*, pages 538–541, 2018.

[186] Saqib Ali, Jianqiang Li, Yan Pei, Muhammad Saqlain Aslam, Zeeshan Shaukat, and Muhammad Azeem. An effective and improved cnn-elm classifier for handwritten digits recognition and classification. *Symmetry*, 12(10), 2020.

[187] David H Hubel and Torsten N Wiesel. Receptive fields of single neurones in the cat's striate cortex. *The Journal of physiology*, 148(3):574–591, 1959.

[188] Yulin Wu, Wan-Su Bao, Sirui Cao, Fusheng Chen, Ming-Cheng Chen, Xiawei Chen, Tung-Hsun Chung, Hui Deng, Yajie Du, Daojin Fan, Ming Gong, Cheng Guo, Chu Guo, Shaojun Guo, Lianchen Han, Linyin Hong, He-Liang Huang, Yong-Heng Huo, Liping Li, Na Li, Shaowei Li, Yuan Li, Futian Liang, Chun Lin, Jin Lin, Haoran Qian, Dan Qiao, Hao Rong, Hong Su, Lihua Sun, Liangyuan Wang, Shiyu Wang, Dachao Wu, Yu Xu, Kai Yan, Weifeng Yang, Yang Yang, Yangsen Ye, Jianghan Yin, Chong Ying, Jiale Yu, Chen Zha, Cha Zhang, Haibin Zhang, Kaili Zhang, Yiming Zhang, Han Zhao, Youwei Zhao, Liang Zhou, Qingling Zhu, Chao-Yang Lu, Cheng-Zhi Peng, Xiaobo Zhu, and Jian-Wei Pan. Strong quantum computational advantage using a superconducting quantum processor. *Phys. Rev. Lett.*, 127:180501, Oct 2021.

[189] Sergio Boixo, Sergei V. Isakov, Vadim N. Smelyanskiy, Ryan Babbush, Nan Ding, Zhang Jiang, Michael J. Bremner, John M. Martinis, and Hartmut Neven. Characterizing quantum supremacy in near-term devices. *Nature Physics*, 14(6):595–600, Jun 2018.

[190] Rowan Killip and Rostyslav Kozhan. Matrix models and eigenvalue statistics for truncations of classical ensembles of random unitary matrices. *Communications in Mathematical Physics*, 349(3):991–1027, Feb 2017.

[191] Janusz E. Jacak, Witold A. Jacak, Wojciech A. Donderowicz, and Lucjan Jacak. Quantum random number generators with entanglement for public randomness testing. *Scientific Reports*, 10(1):164, Jan 2020.

[192] Ludovic Arnaud and Daniel Braun. Efficiency of producing random unitary matrices with quantum circuits. *Phys. Rev. A*, 78:062329, Dec 2008.

[193] Francesco Mezzadri. How to generate random matrices from the classical compact groups. *arXiv preprint math-ph/0609050*, 2006.

[194] E Miles Stoudenmire and David J Schwab. Supervised learning with quantum-inspired tensor networks. *arXiv preprint arXiv:1605.05775*, 2016.

[195] Xavier Glorot and Yoshua Bengio. Understanding the difficulty of training deep feedforward neural networks. 9:249–256, 13–15 May 2010.

[196] Kaiming He, Xiangyu Zhang, Shaoqing Ren, and Jian Sun. Delving deep into rectifiers: Surpassing human-level performance on imagenet classification. In *Proceedings of the IEEE International Conference on Computer Vision (ICCV)*, December 2015.

[197] Rigui Zhou and Qiulin Ding. Quantum m-p neural network. *International Journal of Theoretical Physics*, 46(12):3209–3215, Dec 2007.

[198] John Martyn, Guifre Vidal, Chase Roberts, and Stefan Leichenauer. Entanglement and tensor networks for supervised image classification. *arXiv preprint arXiv:2007.06082*, 2020.

[199] Iordanis Kerenidis and Alessandro Luongo. Classification of the mnist data set with quantum slow feature analysis. *Phys. Rev. A*, 101:062327, Jun 2020.

[200] Curtis G. Northcutt, Anish Athalye, and Jonas Mueller. Pervasive label errors in test sets destabilize machine learning benchmarks, 2021.

[201] Richard P Feynman, Robert B Leighton, and Matthew Sands. Feynman lectures on physics 5. quantum mechanics. 6. 2015.

[202] Shu Tanaka, Ryo Tamura, and Bikas K Chakrabarti. *Quantum spin glasses, annealing and computation*. Cambridge University Press, 2017.

[203] LD Landau and EM Lifshitz. Chapter i–the fundamental principles of statistical physics. *Course of Theoretical Physics*, pages 1–33, 1980.

[204] JW Gibbs. Elementary principles in statistical mechanics (new york: Charles scribner's sons). 1902.

[205] John von Neumann. *Mathematical Foundations of Quantum Mechanics: New Edition*. Princeton University Press, 2018.

[206] Richard Chace Tolman. *The principles of statistical mechanics*. Courier Corporation, 1979.

[207] J. M. Deutsch. Quantum statistical mechanics in a closed system. *Phys. Rev. A*, 43:2046–2049, Feb 1991.

[208] Marcos Rigol, Vanja Dunjko, and Maxim Olshanii. Thermalization and its mechanism for generic isolated quantum systems. *Nature*, 452(7189):854–858, Apr 2008.

[209] R. V. Jensen and R. Shankar. Statistical behavior in deterministic quantum systems with few degrees of freedom. *Phys. Rev. Lett.*, 54:1879–1882, Apr 1985.

[210] Mark Srednicki. Chaos and quantum thermalization. *Phys. Rev. E*, 50:888–901, Aug 1994.

[211] Luca D'Alessio, Yariv Kafri, Anatoli Polkovnikov, and Marcos Rigol. From quantum chaos and eigenstate thermalization to statistical mechanics and thermodynamics. *Advances in Physics*, 65(3):239–362, 2016.

[212] Wilhelm Magnus. On the exponential solution of differential equations for a linear operator. *Communications on pure and applied mathematics*, 7(4):649–673, 1954.

[213] S. Blanes, F. Casas, J.A. Oteo, and J. Ros. The magnus expansion and some of its applications. *Physics Reports*, 470(5):151–238, 2009.

[214] Dominic W. Berry, Andrew M. Childs, Yuan Su, Xin Wang, and Nathan Wiebe. Time-dependent hamiltonian simulation withl1-norm scaling. *Quantum*, 4:254, Apr 2020.

[215] C. M. Dai, Z. C. Shi, and X. X. Yi. Floquet theorem with open systems and its applications. *Phys. Rev. A*, 93:032121, Mar 2016.

[216] Tatsuhiko N. Ikeda and Anatoli Polkovnikov. Fermi's golden rule for heating in strongly driven floquet systems. *Physical Review B*, 104(13), Oct 2021.